Photonic Entanglement Certification and Distribution Based on Single Photons

Caspar, Patrik

Université de Genève
Section de physique
Département de physique appliquée

Faculté des Sciences
Professeur Hugo Zbinden
Docteur Rob Thew

Photonic Entanglement Certification and Distribution Based on Single Photons

Thèse

présentée à la Faculté des sciences de l'Université de Genève
pour obtenir le grade de Docteur ès sciences, mention Physique

par

Patrik Caspar

de

Schmitten (GR)

Thèse N° 5733

Genève
2023

UNIVERSITÉ DE GENÈVE
FACULTÉ DES SCIENCES

DOCTORAT ÈS SCIENCES, MENTION PHYSIQUE

Thèse de Monsieur Patrik CASPAR

intitulée :

«Photonic Entanglement Certification and Distribution Based on Single Photons»

La Faculté des sciences, sur le préavis de Monsieur H. ZBINDEN, professeur associé et directeur de thèse (Département de physique appliquée), Monsieur R. THEW, docteur et codirecteur de thèse (Département de physique appliquée), Madame T. BRYDGES, docteure (Département de physique appliquée), Monsieur R. WARBURTON, professeur (Department of Physics, University of Basel, Basel) et Monsieur N. SANGOUARD, professeur (CEA, Paris-Saclay, Paris, France), autorise l'impression de la présente thèse, sans exprimer d'opinion sur les propositions qui y sont énoncées.

Genève, le 19 juin 2023

Thèse - 5733 -

Le Doyen

N.B. - La thèse doit porter la déclaration précédente et remplir les conditions énumérées dans les "Informations relatives aux thèses de doctorat à l'Université de Genève".

To my beloved parents,
who passed away far too early.

Abstract

Over the past decades, the field of quantum technologies has been developed from fundamental quantum mechanical experiments. The ability to control and manipulate physical systems at the level of single quanta is at the heart of the modern-day quantum revolution, enabling the use of quantum mechanical systems and phenomena for communication and computation. In particular, quantum entanglement, and protocols based thereon, are key ingredients for the real-world implementation of future quantum networks. In this thesis, I concentrate on heralded single-photon sources as a key quantum technology for use in quantum optics experiments, as well as the certification and distribution of photonic entanglement in quantum networks.

The first part of this thesis focusses on single-photon sources as they become increasingly important in quantum technologies. A benchmark for single-photon sources is presented, which is based on the outcome of an autocorrelation measurement. From such a measurement, the probability of the source to emit a single photon can be bounded, which is a natural benchmark for the quality of the source. This is then experimentally demonstrated using a heralded single-photon source. Further, an improved heralded single-photon source is developed by replacing the original heralding detector by a photon-number-resolving detector. In this way, multi-photon emissions are filtered out, leading to a reduction in the heralded second-order autocorrelation function of $(26.9 \pm 0.1)\,\%$.

In the remainder of the thesis, I focus on the certification and distribution of photonic entanglement for use in quantum networks. First, an improved entanglement witness for genuine multipartite single-photon path entanglement is presented and demonstrated with local measurements for an 8-partite state. In this way, large multipartite W states can be certified through the estimation of only three observables. This has a vastly improved scaling over previously developed entanglement witnesses or other protocols, such as state tomography.

Following this, I discuss the implementation of two different protocols for the distribution of entanglement at telecommunication wavelength. This is integral in overcoming the inherent loss present in optical fibres, which currently limits direct transmission distances. The first protocol employs two weakly pumped non-degenerate photon-pair sources to herald the distribution of single-photon path entanglement. By actively phase stabilising an interferometer with arm length of 1 km, entanglement is distributed and certified by local measurements at a heralding rate of 1.6 kcps.

The second protocol, in conjunction with on-demand single-photon sources, is proposed for device-independent quantum key distribution and heralds the distribution of two polarisation-

entangled photons. Here, a variant of the protocol is demonstrated, where four input photons originate from two degenerate down-converted photon pairs, and the state is characterised after four-fold post-selection. The experimental challenges in this implementation and the expected performances for the case of the heralded distribution of polarisation entanglement are discussed.

Résumé

Au cours des dernières décennies, le domaine des technologies quantiques s'est développé à partir d'expériences fondamentales de mécanique quantique. La capacité à contrôler et manipuler des systèmes physiques au niveau de quanta uniques est au cœur de la révolution quantique moderne. Elle permet l'utilisation de systèmes et de phénomènes de mécanique quantique pour la communication et le calcul. En particulier, l'intrication quantique et les protocoles basés sur celle-ci sont des ingrédients clés pour la mise en œuvre dans le monde réel de futurs réseaux quantiques.

La première partie de cette thèse se concentre sur les sources de photons uniques car elles deviennent de plus en plus importantes dans les technologies quantiques. Un test pour les sources de photons uniques est présenté. Il est basé sur le résultat d'une mesure d'autocorrélation. A partir d'une telle mesure, la probabilité que la source émette un photon unique peut être bornée, ce qui donne un repère naturel pour la qualité de la source. Ceci est ensuite démontré expérimentalement à l'aide d'une source de photons uniques annoncés. En outre, une source de photons uniques annoncés améliorée est développée en remplaçant le détecteur d'annonce d'origine par un détecteur à résolution du nombre de photons. De cette manière, les émissions multiphotoniques sont filtrées, ce qui entraîne une réduction de la fonction d'autocorrélation de second ordre annoncée de $(26.9 \pm 0.1)\,\%$.

Dans le reste de la thèse, je me concentre sur la certification et la distribution de l'intrication photonique pour une utilisation dans les réseaux quantiques. Tout d'abord, un témoin d'intrication amélioré pour l'intrication "genuine" multipartite en chemin à photon unique est présenté et démontré avec des mesures locales pour un état à 8 parties. De cette façon, de grands états W multipartites peuvent être certifiés par l'estimation de seulement trois observables. Cela a une mise à l'échelle considérablement améliorée par rapport aux témoins d'intrication développés précédemment ou à d'autres protocoles, tels que la tomographie d'état.

Je discute ensuite de la mise en œuvre de deux protocoles différents pour la distribution d'intrication à la longueur d'onde des télécommunications. Ceci est essentiel pour surmonter la perte inhérente aux fibres optiques, qui limite actuellement les distances de transmission directe. Le premier protocole utilise deux sources de paires de photons non dégénérés faiblement pompées pour annoncer la distribution d'intrication en chemin à photon unique. En stabilisant activement la phase d'un interféromètre avec une longueur de bras de 1 km, l'intrication est distribuée et certifiée par des mesures locales à un taux d'annonce de 1.6 kcps.

Le deuxième protocole, en conjonction avec des sources de photons uniques à la demande, est proposé pour la distribution de clé quantique indépendante de l'appareil et annonce la distribution de deux photons intriqués en polarisation. Ici, une variante du protocole est

démontrée, où quatre photons d'entrée proviennent de deux paires de photons dégénérés obtenues par conversion paramétrique descendante spontanée, et l'état est caractérisé après une post-sélection quadruple. Les défis expérimentaux de cette implémentation et les performances attendues pour le cas de la distribution annoncée de l'intrication en polarisation sont discutés.

Contents

Acronyms

BS Beam splitter. 17, 29, 36, 37, 39, 41, 42, 43, 48, 49, 50, 51, 55, 57, 60, 63, 65, 66, 67, 71, 72, 75, 77, 81, 83, 84

BSM Bell state measurement. 75, 77, 78, 79, 80, 83, 84, 85, 86

DWDM Dense wavelength division multiplexing. 14, 15, 22, 29, 51, 63, 69, 81

FWHM Full width at half maximum. 10, 15, 23, 33, 65, 66

DFG Difference frequency generation. 51, 55, 61, 63, 64, 67, 71

DI-QKD Device-independent quantum key distribution. 4, 5, 6, 75

EPC Electronic polarisation controller. 53, 55, 56, 57, 65

EOIM Electro-optic intensity modulator. 51, 63, 73

HOM Hong-Ou-Mandel. 83, 84, 86, 89

HSPS Heralded single-photon source. 7, 10, 11, 17, 22, 25, 26, 27, 29, 32, 33, 36, 49, 50, 51

HWP Half-wave plate. 39, 72, 75, 77, 78, 79, 80, 81, 85

ITU International Telecommunication Union. 14, 30, 53, 63, 81

JSA Joint spectral amplitude. 10, 11, 12, 15, 28

JSI Joint spectral intensity. 16, 23, 29

MZI Mach-Zehnder interferometer. 61, 62, 63, 65, 66, 67, 68, 69, 71, 72, 73, 84, 85, 89

PBS Polarising beam splitter. 16, 23, 30, 39, 63, 64, 65, 67, 68, 72, 75, 77, 79, 81, 83, 85, 86, 89

PNR Photon-number-resolving. 25, 26, 27, 28, 29, 30, 31, 32, 33, 42, 48, 59, 88

POVM Positive operator-valued measure. 17, 20, 28, 37, 38, 39, 40, 44

PPKTP Periodically-poled potassium titanyl phosphate. 14, 16, 22, 33, 51, 53, 55, 65, 81

PPLN Periodically-poled lithium niobate. 51, 53, 55, 65, 67, 74

PPT Positive partial transpose. 37, 41, 42, 43, 44, 69

P-SNSPD Parallel superconducting nanowire single-photon detector. 26, 27, 28, 29, 30, 31, 32, 33, 60, 63, 66, 88

QKD Quantum key distribution. 4, 5, 71, 90

QWP Quarter-wave plate. 81, 85

SNSPD Superconducting nanowire single-photon detector. 23, 25, 29, 33, 51, 53, 73, 81, 83, 87, 89, 90

SPDC Spontaneous parametric down-conversion. 7, 9, 10, 11, 13, 16, 25, 27, 31, 32, 61, 63, 64, 71, 74, 75, 79, 80, 81, 86, 88, 89, 90

1. Introduction

As quantum mechanics revolutionised physics a century ago, its applications are about to revolutionise technology in the present. Allegedly, at the end of the 19th century, Lord Kelvin stated: "There is nothing new to be discovered in physics now. All that remains is more and more precise measurement". In the following decades, Einstein developed the special and general theories of relativity [1, 2] and, together with Planck and Bohr, laid the foundation of quantum mechanics [3–5]. In the mid 1920s, with Heisenberg's uncertainty principle and Schrödinger's wave mechanics, modern quantum mechanics was born [6, 7]. This theory was so different from the known classical physics that it completely changed the understanding of nature at its small scales and triggered new research and technological developments.

The first quantum revolution, based on the understanding of quantum mechanics, lead to devices such as the transistor, first demonstrated in the late 1940s by Bardeen, Brattain and Shockley [8, 9], and the first laser built in 1960 by Maiman [10]. Clearly, those inventions revolutionised computation and communication, and with that, all domains of technology. Further technological advances allowed for probing and controlling systems at the quantum level, often referred to as the second quantum revolution [11]. Investigating the usage of such quantum systems for computing and communication tasks lead to the field of quantum information. As it turns out, using quantum systems for computing allows for an algorithm that can find the prime factors of an integer, which is the underlying problem of the used RSA public-key cryptography protocol [12], exponentially faster than any currently known classical algorithm [13]. Fortunately, quantum cryptography protocols offer a solution to the threat posed by quantum computers and can guarantee information-theoretically secure communication [14].

In 2022, Aspect, Clauser and Zeilinger were awarded the Nobel prize in physics "for experiments with entangled photons, establishing the violation of Bell inequalities and pioneering quantum information science". These ground-breaking experiments clearly confirmed that quantum mechanics with its implications such as Bell nonlocality [15–18] or quantum teleportation [19, 20] not only is a beautiful theory, but also accurately describes physics.

First, in Sec. 1.1, we introduce the basic concept of quantum states and quantum entanglement to lay the basis for the theory sections in this thesis. Then, in Sec. 1.2, a brief overview of the field of quantum communication is given, followed by the outline of this thesis in Sec. 1.3.

1.1. Quantum states and entanglement

A quantum system is described by a wave function or *quantum state*. Mathematically, those quantum states can be described as elements of a Hilbert space over the complex numbers, that is an inner product space which is complete with respect to the norm defined by the inner product. The simplest example of a quantum state is the quantum bit or *qubit*, the quantum equivalent of the classical bit. In the Dirac notation, that is $|\psi\rangle = \alpha\,|0\rangle + \beta\,|1\rangle$, where $\alpha, \beta \in \mathbb{C}$ are normalised coefficients such that $|\alpha|^2 + |\beta|^2 = 1$, and $|0\rangle$, $|1\rangle$ are orthogonal states of the system ($\langle 0|1\rangle = 0$). A global phase factor $e^{\mathrm{i}\delta}$ multiplied to the state does not have any physical effect. Therefore, a qubit state can be parametrised with the two real angles $\theta \in [0, \pi]$ and $\phi \in [0, 2\pi)$

$$|\psi\rangle = \cos\left(\frac{\theta}{2}\right)|0\rangle + e^{\mathrm{i}\phi}\sin\left(\frac{\theta}{2}\right)|1\rangle \tag{1.1}$$

and graphically represented in the so called Bloch sphere, as shown in Fig. 1.1. This state is called a pure qubit state, and for $\theta \notin \{0, \pi\}$, it is in a coherent superposition between the two basis states $|0\rangle$ and $|1\rangle$.

In reality, qubits are usually subject to environmental noise and can decay ($|1\rangle \to |0\rangle$) and loose their coherent superposition. This results in states that are statistical mixtures of pure states, described by a density matrix. For example, the density matrix corresponding to the pure state in Eq. (1.1) is $\rho = |\psi\rangle\langle\psi|$ and the fully mixed state at the origin of the Bloch sphere is $\rho = (|0\rangle\langle 0| + |1\rangle\langle 1|)/2$. The purity of an arbitrary state ρ is defined as $\mathcal{P} = \mathrm{tr}(\rho^2)$ with $\frac{1}{d} \leq \mathcal{P} \leq 1$, where d is the dimension of the Hilbert space on which the state is defined. We note that all states on the surface of the Bloch sphere are pure states, i.e. $\mathcal{P} = 1$, and states inside the sphere are mixed, with the maximally mixed state at its centre. The density matrix of a qubit state ρ is related to its Bloch vector $\vec{v}$ according to

$$\rho = \frac{1}{2}(\mathbb{1} + \vec{v}\cdot\vec{\sigma}), \tag{1.2}$$

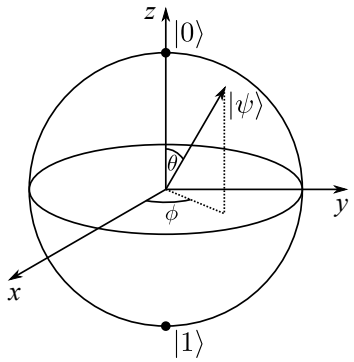

Figure 1.1.: Bloch sphere representation of a qubit state $|\psi\rangle$.

where $\vec{\sigma} = (\sigma_x, \sigma_y, \sigma_z)^T$ is the vector of Pauli matrices

$$\sigma_x = \begin{pmatrix} 0 & 1 \\ 1 & 0 \end{pmatrix}, \qquad \sigma_y = \begin{pmatrix} 0 & -\mathrm{i} \\ \mathrm{i} & 0 \end{pmatrix}, \qquad \sigma_z = \begin{pmatrix} 1 & 0 \\ 0 & -1 \end{pmatrix}. \tag{1.3}$$

Physically, a qubit can be realised, for example, with nuclear spin states of an atom $\{|\uparrow\rangle, |\downarrow\rangle\}$, with the polarisation states of a photon $\{|H\rangle, |V\rangle\}$ or with photon number states, where $|0\rangle$ denotes the electromagnetic vacuum state and $|1\rangle$ the single-photon state. We will encounter the two latter realisations in this thesis.

If we want to describe the state of not only one, but multiple quantum systems, the full state space can be described by the tensor product space of the individual systems. As the simplest example, let us consider a two-qubit state. In that case, the local Hilbert spaces are spanned by the basis $\{|0\rangle, |1\rangle\}$ and the joint space is spanned by the basis $\{|00\rangle, |01\rangle, |10\rangle, |11\rangle\}$, where e.g. $|10\rangle = |1\rangle_1 \otimes |0\rangle_2$ is a tensor product of the basis states of systems 1 and 2. If we have two systems in pure quantum states $|\psi_1\rangle$ and $|\psi_2\rangle$, then the overall state is described by $|\Psi\rangle = |\psi_1\rangle \otimes |\psi_2\rangle$, which is an example of a separable state. However, multipartite quantum states can be non-separable or *entangled*, which is a purely quantum-mechanical feature. An example of entangled two-qubit states are the four Bell states

$$|\Phi^{\pm}\rangle = \frac{1}{\sqrt{2}}\big(\,|00\rangle \pm |11\rangle\,\big), \qquad |\Psi^{\pm}\rangle = \frac{1}{\sqrt{2}}\big(\,|01\rangle \pm |10\rangle\,\big), \tag{1.4}$$

which are maximally entangled and also form a basis of the two-qubit state space. In general, a state ρ_e of N systems, described by the Hilbert space $\mathcal{H}_1 \otimes \cdots \otimes \mathcal{H}_N$, is called *entangled* if it cannot be written as a convex combination of product states [21, 22]

$$\rho_e \neq \sum_i p_i \, \rho_1^{(i)} \otimes \cdots \otimes \rho_N^{(i)}, \tag{1.5}$$

where $\sum_i p_i = 1$. Moreover, an N-partite state ρ_s is said to be separable with respect to a partition $G_1|...|G_m$ of $\{\mathcal{H}_1, ..., \mathcal{H}_N\}$ if it can be expressed as [23]

$$\rho_s = \sum_i p_i \, \rho_{G_1}^{(i)} \otimes \cdots \otimes \rho_{G_m}^{(i)}. \tag{1.6}$$

An N-partite state is called *genuinely k-partite entangled* if it cannot be written as a convex combination of states, each of which is separable with respect to at least one partition $G_1|G_2|...$ of $\{\mathcal{H}_1, ..., \mathcal{H}_N\}$ with $|G_j| \leq k-1$, for all j [24]. Further, an N-partite state is *genuinely entangled* if it is genuinely N-partite entangled.

Given a state in an experiment that is supposed to be entangled, the question arises of how one can certify the entanglement. One approach would be to experimentally reconstruct the density matrix of the state via state tomography [25, 26]. This provides all information about the state ρ. If a particular state $|\psi\rangle$ is desired, then with the reconstructed density

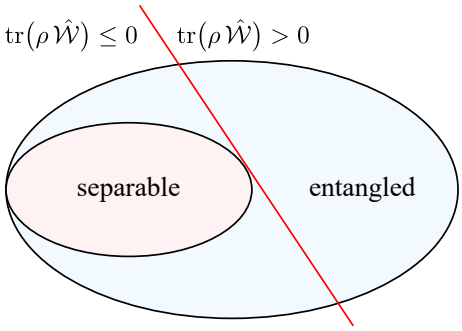

Figure 1.2.: Schematic representation of the convex set of all separable states inside the set of entangled states. The red line connects all the states ρ for which the expectation value of the witness $\mathrm{tr}\left(\rho\hat{\mathcal{W}}\right) = 0$.

matrix ρ, the *fidelity* of the target state $|\psi\rangle$ in ρ can then be calculated according to $\mathcal{F} = \langle\psi|\,\rho\,|\psi\rangle$. While this approach can be useful to better understand the inner workings of the system which generates the state, the measurement settings required for state tomography scale exponentially with the number of parties. It can also be that it is not necessary to know all information about the state, but enough to know whether entanglement is present. Therefore, a more efficient and practical way to certify entanglement are entanglement witnesses, which do not require knowledge about the density matrix of the state. An observable $\hat{\mathcal{W}}$ is called an *entanglement witness*, if its expectation value $\mathrm{tr}\left(\rho_s\hat{\mathcal{W}}\right) \leq 0$ for all separable states ρ_s and $\mathrm{tr}\left(\rho_e\hat{\mathcal{W}}\right) > 0$ for at least one entangled state ρ_e [27]. A graphical representation of an entanglement witness is shown in Fig. 1.2. A simple example of a witness for two-qubit states, targeted to detect the state $|\Psi^+\rangle$, is

$$\hat{\mathcal{W}} = \left|\Psi^+\right\rangle\!\left\langle\Psi^+\right| - \frac{1}{2}\mathbb{1}_4 = \frac{1}{4}(\sigma_x \otimes \sigma_x + \sigma_y \otimes \sigma_y - \sigma_z \otimes \sigma_z - \mathbb{1}_4), \tag{1.7}$$

for further details on the construction see Sec. 6 in Ref. [27]. Given the Werner state $\rho = p\,|\Psi^+\rangle\langle\Psi^+| + (1-p)\mathbb{1}_4/4$, this witness correctly detects the entanglement, i.e. $\mathrm{tr}\left(\rho\hat{\mathcal{W}}\right) > 0$, for $p > \frac{1}{3}$. In general, for multipartite systems it is often challenging to find the optimal witness that maximally separates the target state from the set of separable states.

1.2. Quantum communication

Quantum communication is the art of transferring a quantum state from one location to another [28]. The task of distributing entangled states between two or more parties lies at the heart of quantum communication. It enables applications such as quantum teleportation, distributed quantum computing or device-independent quantum key distribution (DI-QKD) [29]. Quantum key distribution (QKD), the art of distributing a secret key between to distant parties by means of quantum states, in particular has immensely progressed during the past four decades since the invention of the first protocol by Bennett and Brassard in 1984 [30]. Since future quantum computers represent a threat to the

security of currently applied classical cryptographic protocols [13], QKD protocols are of great interest because they can guarantee information-theoretical security [14, 31]. State of the art implementations of *prepare and measure* QKD protocols with weak coherent states, employing the decoy method to prevent photon-number-splitting attacks, achieve transmission distances through optical fibre over 420 km [32] and high secret key rates of more than 60 Mbps over 10 km of fibre [33, 34]. Implementations of the newer twin-field QKD protocol are experimentally more challenging since the optical phase in the fibre links needs to be stabilised or kept track of [35]. Nevertheless, recent implementations of this protocol are approaching the 1000 km fibre link distance [36–40].

When it comes to the distribution of bipartite entangled states, in recent years, distances of over 190 km in optical fibre [41, 42] and over 1200 km via a satellite downlink [43] have been demonstrated for polarisation-entangled photons with post-selection, i.e. by only considering events as part of the state where both parties detected a photon. However, the challenge remains to distribute high-fidelity entangled states over long distances, at high rates and in a heralded way in order to make use of the entanglement. In matter systems, the heralded entanglement distribution using single-photon schemes has been achieved over short distances with atoms [44], quantum dots [45, 46] and nitrogen-vacancy (NV) centres [47], in the latter system even for tripartite states [48]. Usually, higher fidelities but lower entanglement generation probabilities are achieved with two-photon schemes [49–52]. In this way, the seminal experiments demonstrating the loophole-free Bell inequality violation [53] were realised in 2015 with NV centres over a distance of 1.3 km [54] (at about the same time with the photonic demonstrations [55, 56]) and in 2017 with atoms [57]. Furthermore, the first experiments of DI-QKD, where a secret key is shared between two parties based on the the violation of Bell's inequality, were demonstrated in 2022 with independently trapped strontium ions [58] and rubidium atoms [59]. However, in order to increase the communication distance and to herald entanglement over long fibre links, it is necessary for most matter systems to frequency-convert the travelling photons, since usually their optical transitions are not at telecommunication wavelengths. In this way, entanglement was recently distributed between two rubidium atomic ensemble quantum memories [60], between two rear-earth-doped crystals [61] and between two single rubidium atoms [62].

From all these experiments, it becomes clear that in order to distribute entanglement over long distances, the carriers or constituents of the quantum state need to be photons for the transmission part, and in the case of fibre networks, the photons need to be at telecommunication wavelengths to reduce the transmission loss to 0.18 dB/km. Even so, the direct transmission from a central source, which generates the entangled state, to the distant parties is not an option due to transmission losses. In contrast to classical communication, where optical amplifiers are applied to compensate for transmission losses, they cannot be used when transmitting quantum states due to the no-cloning theorem [63]. Therefore, repeater protocols based on entanglement swapping need to be applied [64, 65]. In the context of photonic entanglement distribution, several interesting questions can be

asked. Which physical system should be used to encode the qubit states? Which protocol should be used for the distribution and what are the experimental challenges? For the single-photon protocols, how can we certify the distributed single-photon entanglement with local measurements? And how difficult is their implementation due to the phase stability requirement? We will address these questions in this thesis. Moreover, as single-photon sources are becoming increasingly important for various protocols and applications in quantum technology, we will investigate how we can benchmark single-photon sources in general and how already well established heralded single-photon sources can be improved.

1.3. Thesis outline

In Chapter 2, the theory and an implementation of a heralded single-photon source based on spontaneous parametric down-conversion are described. Further, a benchmark for general single-photon sources based on the outcome of a autocorrelation measurement is presented and demonstrated, which gives a lower bound on the probability that the source emits a single photon. Moreover, an improved heralded single-photon source is demonstrated, where the heralding detector exhibits photon-number resolution which leads to an increase in the single-photon purity of the heralded state.

In Chapter 3, the concept of single-photon path entanglement is presented and a scalable entanglement witness to certify multipartite single-photon path-entangled states with local measurements is introduced. This is followed by a section on the experimental implementation of the multipartite entanglement witness, where it is applied to certify 8-partite entanglement. Further, a scheme to distribute and certify single-photon path entanglement in a repeater-like architecture is demonstrated and the experimental challenges are discussed.

In Chapter 4, a protocol to distribute polarisation-entangled photons is implemented with probabilistic photon-pair sources and the experimental challenges and limitations are discussed. Together with deterministic single-photon sources that produce indistinguishable photons, this protocol is a promising candidate for DI-QKD.

Finally, the results of this thesis are summarised in Chapter 5 and future research directions are discussed.

2. Single-photon sources

A photon is a single excitation of the electromagnetic field [66]. The concept of quantised excitations of electromagnetic energy was first introduced by Planck in 1900 in his derivation of the black-body radiation law [3]. A few years later, in 1905, Einstein used photons to explain the photoelectric effect [4]. It then took almost seven decades until the first experimental demonstration of single-photon behaviour by Clauser in 1974 [67]. Further development on a source of entangled photon pairs by Grangier, Roger and Aspect [18] then lead to an experiment in 1986 where the source was explicitly used and characterised as a source of single photons for the first time [68]. In the same year, the first demonstration of a single-photon source using spontaneous parametric down-conversion was achieved by Hong and Mandel [69]. In the current development of quantum technologies, single-photon sources play a key role [70]. Single photons are a non-classical resource which is required for many quantum applications ranging from boson sampling [71–79] over the generation of single-photon entangled states [80–83] and cluster states [84, 85] to protocols for entanglement distribution [86, 87].

An *ideal single-photon source* is a fictional device which emits one (and only one) photon in a single optical mode (pure quantum state) with unit efficiency at a well defined time (*deterministically*) or upon request (*on-demand*). Furthermore, photons emitted at different times are *indistinguishable*, that is identical in all their degrees of freedom – frequency distribution, spatial mode, polarisation, momentum and emission time with respect to the trigger. A *real single-photon source* never has unit efficiency and usually suffers from multi-photon emissions. Further, the emitted state might not be in a spectrally pure state and the emitted spectrum can vary from one emission to another or slowly drift over time. Single-photon sources can be divided into two categories: heralded single-photon sources (HSPS) and deterministic single-photon sources, however, the border between the two categories is blurred. In the first case, usually an optically nonlinear interaction is used to generate a two-mode squeezed vacuum state where a detection in one mode heralds the presence of a state close to a single-photon state in the other mode. Due to the spontaneous nature of the nonlinear interaction, spontaneous parametric down-conversion (SPDC) or spontaneous four-wave mixing, the time of the heralding detection is probabilistic. As the pump power cannot be increased arbitrarily due to multi-pair emission, the probabilistic nature limits the application of these sources to cases where only few photons are required simultaneously. Therefore, deterministic single-photon sources are a crucial ingredient in order to enable high-repetition rate multi-photon applications. These sources can be obtained either by multiplexing heralded single-photon sources and pushing them into the

quasi-deterministic regime [88], or by using isolated systems as single-photon emitters. In the past two decades, enormous progress, in terms of photon extraction efficiency and indistinguishability, has been made in the development of solid-state quantum dot single-photon sources [89–92].

With the further development of these sources, it is important to have the right tools in hand to characterise how they perform. The standard way of determining the single-photon character of single-photon sources is to measure the second-order autocorrelation function by carrying out a Hanbury Brown-Twiss experiment [70, 93]. This allows to bound the multi-photon contribution in the state, however, does not give any information on the efficiency of the source, which needs to be characterised separately. For many applications it is essential for the source to fulfil both simultaneously, high efficiency and low multi-photon emission. In this thesis work, we therefore develop and demonstrate a benchmark that allows to extract a lower bound on the single-photon probability from an autocorrelation measurement.

In this chapter, we start with presenting the concepts of heralded single-photon sources based on spontaneous parametric down-conversion in Sec. 2.1. The experimental parameters of the used heralded single-photon source employing a periodically poled potassium titanyl phosphate crystal are discussed in Sec. 2.2. Then we introduce the single-photon source benchmark in Sec. 2.3, where we also show the link of the outcome of an autocorrelation measurement to the Wigner negativity of the measured state. Finally, in Sec. 2.4 we show how to mitigate multi-photon emissions in a heralded single-photon source by employing a photon-number resolving detector as a heralding detector. The articles that resulted from this work are attached in P.3 and P.4.

2.1. Theory of heralded single-photon sources

2.1.1. Spontaneous parametric down-conversion

In a classical description, an electro-magnetic field will induce an electric polarisation when interacting with a dielectric medium, since the charges are displaced from their equilibrium positions. To the first order, this polarisation $\vec{P} = (P_1, P_2, P_3)^T$ is linear in the driving electric field $\vec{E} = (E_1, E_2, E_3)^T$, however, weaker non-linear terms can be present (see Ch. 11.2 of Ref. [70])

$$P_i = \varepsilon_0 \Big(\sum_j \chi^{(1)}_{ij} E_j + \sum_{jk} \chi^{(2)}_{ijk} E_j E_k + \sum_{jkl} \chi^{(3)}_{ijkl} E_j E_k E_l + ... \Big), \tag{2.1}$$

where ε_0 is the vacuum permittivity, $\chi^{(1)}$ is the linear susceptibility, $\chi^{(2)}$ and $\chi^{(3)}$ are the second- and third-order susceptibility tensors of the medium. The non-linear interaction can therefore cause electro-magnetic waves with different frequencies to interact and

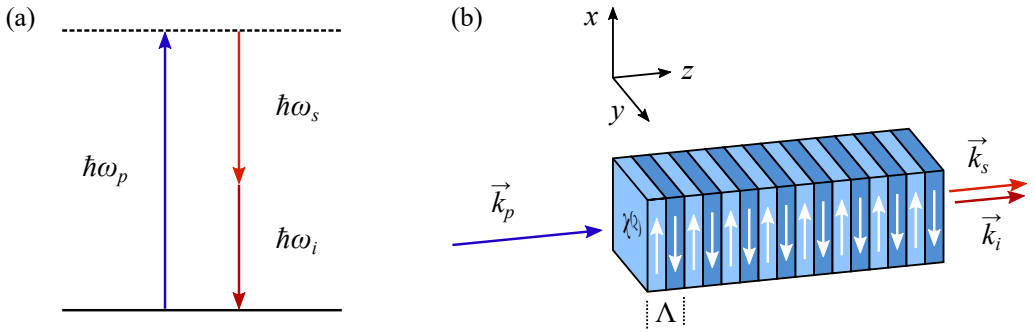

Figure 2.1.: Spontaneous parametric down-conversion (SPDC) in a $\chi^{(2)}$ non-linear medium. (a) Energy conservation: the down-converted signal and idler photons must conserve the energy of the pump photon. (b) Collinear quasi-phase-matching in a periodically poled crystal with poling period Λ.

frequency conversion can occur. Materials with broken inversion symmetry exhibit a non-zero $\chi^{(2)}$ which allows for spontaneous parametric down-conversion (SPDC), a three-wave mixing process where a higher energy *pump* photon is converted into two lower energy daughter photons, called *signal* and *idler* (lowest energy of the three). This is a parametric process, meaning that the energy levels of the interaction medium remains unchanged before and after the down-conversion. The process must conserve energy and momentum, as graphically shown in Fig. 2.1

$$\hbar\omega_p = \hbar\omega_s + \hbar\omega_i, \tag{2.2}$$

$$\vec{k}_p = \vec{k}_s + \vec{k}_i, \tag{2.3}$$

where $\hbar$ is the reduced Planck constant, ω is the angular frequency and $\vec{k}$ the wave vector of the corresponding photon.

Since in a dielectric medium the refractive index n is dependent on the wavelength λ, and therefore the wave number becomes $|\vec{k}| = 2\pi n(\lambda)/\lambda$, Eq. (2.3) referred to as the *phase-matching* condition is usually not fulfilled. However, it can be achieved, for example, in a birefringent crystal, where the refractive index is not only dependent on the wavelength, but also on the polarisation and incident angle of the wave. There exist different types of phase-matching: in type-0 phase-matching, the polarisation of all three photons is the same; in type-I phase-matching, signal and idler photons have the same polarisation, but orthogonal to the pump photon; in type-II phase-matching, signal and idler photons have orthogonal polarisation, one parallel and one orthogonal to the pump photon. Another aspect of the phase-matching condition is the orientation of the wave vectors. We now consider the case of collinear phase-matching, that is, the pump, signal and idler photons' wave vectors all point in the same direction. By introducing alternating ferroelectric domains in the crystal with a poling period Λ, the vector $2\pi\vec{z}/\Lambda$ is effectively added to the r.h.s. of Eq. (2.3). This technique, known as quasi-phase-matching (see [94] and Ch. 11.4.1 of Ref. [70]), reduces the conversion efficiency due to the remaining wave vector mismatch in each poled region,

but allows for collinear phase-matching.

In a quantum-mechanical picture, the interaction Hamiltonian is given by (see Ch. 11.2 of Ref. [70] for the full derivation)

$$\hat{H}_{\mathrm{SPDC}} \propto \chi^{(2)} \int_{-L/2}^{L/2} \mathrm{d}z \hat{E}_p^{(+)}(z,t) \hat{E}_s^{(-)}(z,t) \hat{E}_i^{(-)}(z,t) + h.c., \tag{2.4}$$

where L is the interaction length and the field operators are defined as as

$$\hat{E}_x^{(+)}(z,t) = \hat{E}_x^{(-)\dagger}(z,t) \propto \int \mathrm{d}\omega_x \exp\big(\mathrm{i}(k_x(\omega_x)z - \omega_x t)\big) \hat{a}_x(\omega_x) \tag{2.5}$$

with the photon annihilation operator $\hat{a}_x(\omega_x)$. By calculating the state in the Schrödinger picture and neglecting terms with more than two photons, one obtains

$$|\psi\rangle_{\mathrm{SPDC}} = \exp\Big(-\frac{\mathrm{i}}{\hbar}\int_{t_0}^{t} \mathrm{d}t' \hat{H}_{\mathrm{SPDC}}(t')\Big)\,|0\rangle \tag{2.6}$$

$$\approx |0\rangle + C \iint \mathrm{d}\omega_s \mathrm{d}\omega_i f(\omega_s,\omega_i) \hat{a}_s^\dagger(\omega_s) \hat{a}_i^\dagger(\omega_i)\,|0\rangle \tag{2.7}$$

with $C \propto E_p L$ depending linearly on the pump field amplitude E_p and the interaction length L. The important function here is $f(\omega_s,\omega_i)$, known as the joint spectral amplitude (JSA), and is defined by the pump envelope function $\alpha(\omega)$ and the phase-matching function $\phi(\omega_s,\omega_i)$ according to

$$f(\omega_s,\omega_i) = \alpha(\omega_s+\omega_i)\,\phi(\omega_s,\omega_i) = \alpha(\omega_s+\omega_i)\,\mathrm{sinc}\left(\frac{L}{2}\Delta k(\omega_s,\omega_i)\right), \tag{2.8}$$

where $\Delta k(\omega_s,\omega_i) = k_p(\omega_s+\omega_i) - k_s(\omega_s) - k_s(\omega_s) - 2\pi/\Lambda$, and the sinc function comes from the integration along the z-axis over the interaction length. We see that the length of the crystal determines the width of the phase-matching function. Note that in our case of a Ti:sapphire pump laser, the pump envelope function can be approximated by $\alpha(\omega_s+\omega_i) = \mathrm{sech}\big((\omega_s+\omega_i-\omega_p)\ln\big(3+2\sqrt{2}\big)/\Delta\omega_p\big)$, where $\Delta\omega_p$ denotes the angular frequency full width at half maximum (FWHM) of the pump power spectrum.

SPDC based heralded single-photon source

In the following, we want to investigate the case where SPDC is used for a heralded single-photon source (HSPS) by detecting the photons in one mode and therefore heralding the presence of a photon in the other mode. Here, we closely follow the derivation in [95]. To simplify the calculations, we can rewrite the JSA as a sum of orthogonal modes

$$f(\omega_s,\omega_i) = \sum_k \sqrt{\lambda_k} q_k(\omega_s) r_k(\omega_i), \tag{2.9}$$

which is known as the *Schmidt decomposition* [96]. The *Schmidt coefficients* $\sqrt{\lambda_k}$ are positive real numbers and in case $f(\omega_s, \omega_i)$ is normalised, they fulfil $\sum_k \lambda_k = 1$ and the *Schmidt modes* $q_k(\omega_s)$ and $r_k(\omega_i)$ are orthonormal single-photon spectral functions. For practical purposes, we assume the coefficients to be sorted, where $\lambda_1 \leq 1$ is the largest one. By introducing the orthonormal states in the signal and idler subspaces

$$|q_k\rangle_s = \int \mathrm{d}\omega q_k(\omega) \, |\omega\rangle_s \,, \qquad |r_k\rangle_i = \int \mathrm{d}\omega r_k(\omega) \, |\omega\rangle_i \,, \tag{2.10}$$

where $\langle q_k | q_{k'} \rangle_s = \delta_{kk'}$ and $\langle r_k | r_{k'} \rangle_i = \delta_{kk'}$, we can rewrite the two-photon term in Eq. (2.7)

$$|\psi_2\rangle_{\mathrm{SPDC}} = \sum_k \sqrt{\lambda_k} \, |q_k\rangle_s \, |r_k\rangle_i \,. \tag{2.11}$$

We proceed by modelling the detector on the idler mode in the HSPS with a flat frequency response by the projector

$$\hat{\pi}_i = \int \mathrm{d}\omega \, |\omega\rangle_i \, \langle\omega|_i = \sum_k |r_k\rangle_i \, \langle r_k|_i \,. \tag{2.12}$$

The heralded state in the signal mode is then obtained by the Born rule and tracing over the idler mode

$$\rho_s = \mathrm{tr}_i \Big(|\psi\rangle \, \langle\psi|_{\mathrm{SPDC}} \, (\mathbb{1}_s \otimes \hat{\pi}_i) \Big) = \sum_k \lambda_k \, |q_k\rangle_s \, \langle q_k|_s \,. \tag{2.13}$$

We note that if $\lambda_1 < 1$, which corresponds to a non-factorable JSA as seen from Eq. (2.9), this state is a mixed state of different spectral modes.

2.1.2. Spectral purity

In the case where a single photon is used in an application where it interferes with other states, it is required to have a high spectral purity in order to achieve a high interference visibility. For the heralded single-photon state ρ_s given in Eq. (2.13), the spectral purity is defined by

$$\mathcal{P} = \mathrm{tr}\big(\rho_s^2\big) = \sum_k \lambda_k^2. \tag{2.14}$$

Clearly, $\mathcal{P}$ is independent of which of the two modes is used as the heralding mode, but only depends on the JSA of the SPDC state. In order to obtain high-purity heralded single photons, it is therefore crucial to engineer the JSA $f(\omega_s, \omega_i) = \alpha(\omega_s + \omega_i) \, \phi(\omega_s, \omega_i)$ such that it is as close as possible to a factorable function. In fact, it has been shown that Gaussian pump envelope and phase-matching functions are the only functions that can make the JSA seperable, i.e. $\lambda_1 = 1$ [97].

One possibility to increase the spectral purity of a heralded single photon is to spectrally filter on the heralding mode before detection. In this way, non-factorable contributions to the JSA can be filtered out, however, it comes at a price. Since spectral filtering acts at the intensity level, it can destroy photon-number correlations between the two modes [95] and additionally reduce the heralding rate. Another possibility, although more complicated, is to directly shape the pump envelope function $\alpha(\omega)$ by using pulse-shaping techniques [98] as well as the phase-matching function $\phi(\omega_s, \omega_i)$ by group velocity matching and non-linearity-shaping methods [95].

Experimentally, the spectral purity can be determined or bounded by different techniques, discussed in Ref. [99]: scanning monochromator measurements, a variant of Fourier transform spectroscopy, dispersive fibre spectroscopy, stimulated-emission-based measurement, second-order autocorrelation measurement for one of the two photons, and two-source Hong-Ou-Mandel interferometry.

2.1.3. Coupling efficiency

For many applications in quantum technology, it is important to keep the loss on the generated single photon low. For example, as we will see in Ch. 3, loss degrades a single-photon path-entangled state and therefore reduces the shared correlations. Another example is quantum cryptography based on the violation of a Bell inequality [15, 16], where a loophole opens up if loss exceeds a certain threshold [100]. Here, we consider a pulsed photon-pair source where the down-converted photons are deterministically separated and coupled into single-mode optical fibre. One can divide the total system efficiency of the source into the detection efficiency η_d, the transmission efficiency η_t and the coupling efficiency η_c. The *coupling efficiency* η_c is the probability that one photon of the pair couples to the detected mode given the other photon of the pair has coupled to the detected mode. Contrary to the simpler loss contributions η_d and η_t, the coupling efficiency η_c is inherent to the quantum state and has a more complex structure, see [101] for details.

In the regime where the pair generation probability per pump pulse $p_{si} \lll 1$ and noise as well as dark counts are negligible, the rate of signal photon detections R_s, idler photon detections R_i and coincidence detections R_{si} can be approximated by

$$R_s = R_p p_{si} \eta_{c,s} \eta_{t,s} \eta_{d,s}, \tag{2.15}$$

$$R_i = R_p p_{si} \eta_{c,i} \eta_{t,i} \eta_{d,i}, \tag{2.16}$$

$$R_{si} = R_p p_{si} \eta_{c,s} \eta_{t,s} \eta_{d,s} \eta_{c,i} \eta_{t,i} \eta_{d,i}, \tag{2.17}$$

where R_p is the pump rate, η_d the detection efficiency, η_t the optical transmission efficiency and η_c the coupling efficiency, where the second subscript denotes the signal (s) or idler (i) mode. Inversely, the coupling efficiencies can be calculated from the measured rates,

the detection and transmission efficiencies according to

$$\eta_{c,s} = \frac{R_{si}}{R_i \eta_{t,s} \eta_{d,s}}, \qquad \eta_{c,i} = \frac{R_{si}}{R_s \eta_{t,i} \eta_{d,i}}, \qquad \eta_c = \sqrt{\eta_{c,s} \eta_{c,i}}, \tag{2.18}$$

where we introduced the *correlated-mode coupling efficiency* η_c which is symmetric with respect to signal and idler modes.

Experimentally, it is usually hard to accurately determine the transmission efficiencies and furthermore those efficiencies also belong to the source and need to be included to asses the actual performance of the source. Therefore, the experimentally more relevant *heralding efficiencies* can be estimated from

$$\eta_{h,s} = \frac{R_{si}}{R_i \eta_{d,s}}, \qquad \eta_{h,i} = \frac{R_{si}}{R_s \eta_{d,i}}, \qquad \eta_h = \sqrt{\eta_{h,s} \eta_{h,i}} = \eta_c \sqrt{\eta_{t,s} \eta_{t,i}}, \tag{2.19}$$

where η_h is the symmetric heralding efficiency. Here, we only need the knowledge about the detector efficiencies.

For completeness, we see that from the measured single and coincidence rates, we can easily estimate the pair generation probability per pump pulse

$$p_{si} = \frac{R_s R_i}{R_{si} R_p}, \tag{2.20}$$

in the case where double pairs are negligible, i.e. $p_{si} \lll 1$.

2.2. Heralded single-photon source based on PPKTP

In the past two decades, efforts have been made to understand and simulate the limitations of SPDC sources as practical single-photon sources in terms of coupling efficiency and spectral purity and the theoretical models were experimentally tested [101–108]. It has been shown that for a plane wave pump, projecting the idler mode on a spatially Gaussian state also leaves the signal in a Gaussian state, which is the fundamental spatial mode of an optical fibre [107, 109]. Therefore, in this case it is theoretically possible to obtain unit coupling efficiency hinting that it is favourable to work with weakly focused pump beams. Nevertheless, it has been shown that also for tighter focused pump beams it is possible to obtain high coupling efficiencies if the focal parameters of the collection modes are chosen accordingly [102, 104]. The source used in Ch. 2 and 3 of this thesis is based on the source discussed in [108] optimised for simultaneously high spectral purity and high coupling efficiency. Before rebuilding the source for the experiment presented in Ch. 4, the source parameters were optimised using a recently developed online simulation tool [110] based on [101, 104] and further experimental changes have been made as described in the following.

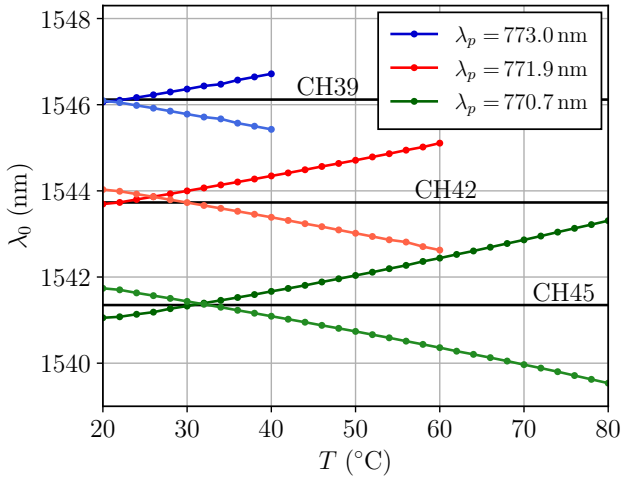

Figure 2.2.: Changing the phase-matching condition by temperature tuning. The central wavelength of the down-converted signal and idler photons is plotted as a function of the set PPKTP crystal temperature for different pump wavelengths. The central wavelength λ_0 is obtained for each T from a Gaussian fit of the measured counts as function of the set wavelength of the tunable grating filter in the path of the corresponding down-converted photon. The horizontal black lines correspond to the central wavelengths of the DWDM channels $\lambda_{\mathrm{CH39}} = 1546.12\,\mathrm{nm}$, $\lambda_{\mathrm{CH42}} = 1543.73\,\mathrm{nm}$ and $\lambda_{\mathrm{CH45}} = 1541.35\,\mathrm{nm}$.

Source	Phase-matching	$w_{0,p}$ (μm)	$w_{0,s} = w_{0,i}$ (μm)
Ref. [108]	$772.00\,\mathrm{nm} \rightarrow 1544.0\,\mathrm{nm} + 1544.0\,\mathrm{nm}$	296	187
Ch. 2,3	$771.85\,\mathrm{nm} \rightarrow 1541.3\,\mathrm{nm} + 1546.1\,\mathrm{nm}$	296	187
Ch. 4	$771.85\,\mathrm{nm} \rightarrow 1543.7\,\mathrm{nm} + 1543.7\,\mathrm{nm}$	265	135

Table 2.1.: PPKTP source parameters. In Ch. 2 and 3 of this thesis, the same pump waist $w_{0,p}$ and collections waists for signal (idler) $w_{0,s(i)}$ are used as in Ref. [108]. After a setup rebuild, those parameters are changed for the experiment in Ch. 4.

The source employs a $L = 30\,\mathrm{mm}$ long, 1 mm wide and 2 mm high periodically poled potassium titanyl phosphate (PPKTP) bulk non-linear crystal with poling period $\Lambda = 46.2\,\mu\mathrm{m}$ for type-II phase-matching. This crystal length leads to a JSA where the phase-matching bandwidth is similar to the bandwidth $\Delta\lambda_{p,\mathrm{FWHM}} = 0.4\,\mathrm{nm}$ of the Ti:sapphire pump laser (Coherent Mira Optima 900-P pumped by a Coherent Verdi-V8) in the picosecond pulsed configuration. The phase-matching condition can be changed by tuning the temperature of the crystal, as shown in Fig. 2.2. For all the experiments, the phase-matching was chosen such that signal and idler photons are compatible with the dense wavelength division multiplexing (DWDM) grid defined by the International Telecommunication Union (ITU). The pump and collection waists for the sources are given in Tab. 2.1.

We simulate the behaviour of the spectral purity and the coupling efficiency for our source using the simulator from Ref. [110]. As shown in Fig. 2.3(a), the spectral purity is expected

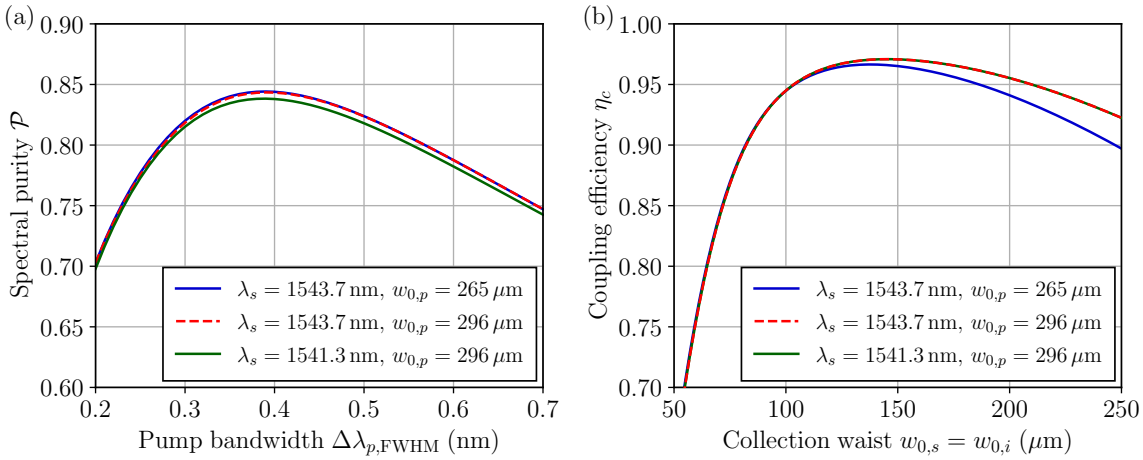

Figure 2.3.: Source parameter simulation for a pump wavelength of $\lambda_p = 771.85\,\mathrm{nm}$ using the online simulator from Ref. [110]. (a) Spectral purity as a function of the pump bandwidth for the different phase-matching conditions and pump waists. For a pump waist of $w_{0,p} = 265\,\mu\mathrm{m}$ we use a collection waist of $w_{0,s(i)} = 135\,\mu\mathrm{m}$ whereas for $w_{0,p} = 296\,\mu\mathrm{m}$ the collection waist is set to $w_{0,s(i)} = 135\,\mu\mathrm{m}$. (b) Coupling efficiency as a function of the collection waist.

to reach $\mathcal{P} = 0.84$ for a pump bandwidth of $\Delta\lambda_p = 0.39\,\mathrm{nm}$. It is important to note that in order to obtain accurate results for the purity when deducing it from a JSA simulation or measurement, the span of the signal and idler frequencies has to cover many times the phase-matching bandwidth in case of a sinc-shaped phase-matching function. If that is not the case, an incorrectly high purity will be obtained, see Ref. [95] for the full discussion. Further simulations show that in the case where a spectral top-hat filter is applied on the heralding mode, the purity can be increased drastically. For a commercial 200 GHz DWDM corresponding to a measured FWHM of 1.24 nm, a purity of $\mathcal{P} = 0.987$ can be achieved, where for a narrower 100 GHz DWDM $\mathcal{P} = 0.996$ is possible. However, this comes at the expense of a reduced heralding rate due to the filtering and the added loss. Commercially available DWDMs have an insertion loss of typically 0.8 dB.

In Fig. 2.3(b), the dependence of the coupling efficiency as a function of the collection waist is shown for the two pump waists used. For a pump waist of $w_{0,p} = 296\,\mu\mathrm{m}$, the maximal coupling efficiency is $\eta_c = 0.971$ at a collection waist of $w_{0,s(i)} = 145\,\mu\mathrm{m}$. This value is slightly different from the optimal collection waist reported in Ref. [108]. Therefore, we change the target collection waist before rebuilding the setup for the experiment discussed in Ch. 4. Moreover, since the maximal coupling efficiency only slightly decreases with a tighter focus, we target a pump waist of $w_{0,p} = 265\,\mu\mathrm{m}$ together with an optimal collection waist of $w_{0,s(i)} = 135\,\mu\mathrm{m}$ which should yield a coupling efficiency of $\eta_c = 0.966$. Compared to the previous waists, this new settings increase the expected coincidence counts per second at the same pump power by a factor of 1.39.

Apart from changing the pump and collections waist, further changes were made to the

Source	Phase-matching	$\mathcal{P}$	η_h
Ch. 2,3	$771.85\,\text{nm} \rightarrow 1541.3\,\text{nm} + 1546.1\,\text{nm}$	0.84	0.75(2)
Ch. 4	$771.85\,\text{nm} \rightarrow 1543.7\,\text{nm} + 1543.7\,\text{nm}$	0.84	0.80(2)

Table 2.2.: PPKTP source characterisation. Spectral purity $\mathcal{P}$ and symmetric heralding efficiency η_h. The uncertainty on η_h comes from the uncertainty of the detector characterisation, see Supplemental Material of Ref. [111] for the setup characterisation.

source. In order to optimally couple a Gaussian mode into fibre and not to induce any ellipticity, it is important that the mode travels through the exact centre of the focusing lens. Therefore, the coupling mounts are changed, such that the fibre can be moved independently of the lens after setting it such that the beam hits the same spot behind the lens with and without it in the beam path. Another modification is made regarding the fibres to which the photons are coupled. The previously used single-mode fibres with a mode field diameter (MFD) of $9.5\,\mu$m are replaced by thermally-expanded core fibres with MFD of $19\,\mu$m to make the coupling stages less sensitive to movements and potentially increase the long-term stability.

The source is characterised in terms of spectral purity and heralding efficiency and the values are given in Tab. 2.2. The spectral purity is deduced from a joint spectrum intensity (JSI) measurement by measuring the signal-idler coincidence counts while sweeping a 0.2 nm wide tunable grating filter (JDS Uniphase TB9) in the signal and idler path, respectively. The heralding efficiency is calculated according to Eq. (2.19) from a measurement of the single and coincidence count rates. An additional measurement of the transmission efficiencies of the used optical components leads to the following values: half the length of the PPKTP crystal 99.3 %, dichroic mirror 97.3 %, long-pass filter and collimation lens 98.4 %, polarising beam splitter (PBS) 96.4 % and three dielectric mirrors all together 98.9 %. In total this amounts to 90.6 % transmission efficiency, excluding the loss of the coupling lens and possible reflections at the air-fibre interface. Therefore, the coupling efficiency of the modified source is $\eta_c = \eta_h/\eta_t = (88 \pm 2)\,\%$. The gap between this number and the simulated maximal coupling efficiency $\eta_c = 96.6\,\%$ for the chosen parameters is most likely coming from the additional uncharacterised loss in the system as well as experimental imperfections, which manifest in spatial mode deformations.

State-of-the-art SPDC sources based on PPKTP that are optimised for high symmetric heralding efficiencies perform better and achieve $\eta_h \approx 84\,\%$ [112] and $\eta_h \approx 89\,\%$ ($\eta_c \approx 95\,\%$) [113], even for the generation of polarisation-entangled photons. To obtain similar high values, the transmission losses of the elements in our source have to be reduced and the alignment technique and precision further refined.

2.3. Benchmarking single-photon sources

In this section, we present and demonstrate a method to benchmark single-photon sources from the experimental outcome of an autocorrelation measurement. From such a measurement, the probability of the single-photon component can be lower-bounded, which is natural benchmark for single-photon sources. Furthermore, if the state is in a single optical mode, a relation between the single-photon probability and the Wigner-negativity is derived and used to construct a witness and measure of Wigner-negativity. Here, the experiment is performed using a HSPS, however, the method is general and applies to all types of single-photon sources.

2.3.1. Autocorrelation measurement

The measurement apparatus we consider to benchmark an unknown photonic input state ρ consists of a beam splitter (BS) followed by two non-photon-number-resolving detectors of efficiency η_d. We describe the measurement with the two element positive operator-valued measure (POVM) $\{E_0, E_c\}$ corresponding to a no-click (0) and click (c) outcome. In the case the measurement acts on a single mode described by the bosonic annihilation and creation operators $\hat{a}$ and $\hat{a}^\dagger$, the POVM elements are given by (Ch. 2.3 of Ref. [70] and [114])

$$E_0 = \sum_{n=0}^{\infty} (1-\eta_d)^n \, |n\rangle\langle n| = (1-\eta_d)^{\hat{a}^\dagger \hat{a}}, \qquad E_c = \mathbb{1} - E_0. \tag{2.21}$$

After the BS with power transmittance t and reflectance r, the four possible outcomes of the two detector can be described by the POVM elements

$$E_{00} = (1-\eta_d)^{\hat{a}^\dagger \hat{a}}, \qquad E_{c0} = (1-\eta_d t)^{\hat{a}^\dagger \hat{a}} - (1-\eta_d)^{\hat{a}^\dagger \hat{a}}, \tag{2.22}$$

$$E_{0c} = (1-\eta_d r)^{\hat{a}^\dagger \hat{a}} - (1-\eta_d)^{\hat{a}^\dagger \hat{a}}, \qquad E_{cc} = \mathbb{1} - E_{00} - E_{c0} - E_{0c}, \tag{2.23}$$

where first (second) subscript corresponds to the detector after the reflected (transmitted) output of the BS. Furthermore, the events where a fixed detector does not click are modelled by the two POVM elements

$$E_{0\_} = E_{00} + E_{0c} = (1-\eta_d r)^{\hat{a}^\dagger \hat{a}}, \tag{2.24}$$

$$E_{\_0} = E_{00} + E_{c0} = (1-\eta_d t)^{\hat{a}^\dagger \hat{a}}. \tag{2.25}$$

Note that the case where the two detectors do not have the same efficiency $\eta_{d_r} \neq \eta_{d_t}$ can be accounted for by replacing r with $r' = \frac{r\eta_{d_r}}{t\eta_{d_t} + r\eta_{d_r}}$, t with $t' = \frac{t\eta_{d_t}}{t\eta_{d_t} + r\eta_{d_r}}$, and setting $\eta = r\eta_{d_r} + t\eta_{d_t}$ in the equations above.

With the described measurement, for any input state ρ, a probability vector with the

corresponding outcome probabilities can be defined

$$\vec{p} = (p_{00}, p_{c0}, p_{0c}, p_{cc}) \tag{2.26}$$

and further $p_{0\_} = p_{00} + p_{0c}$ and $p_{\_0} = p_{00} + p_{c0}$.

2.3.2. Bounding the single-photon probability P1

From a measured probability vector $\vec{p}$ as in Eq. (2.26), we now want to bound the probability of having a single photon in ρ. For the sake of clarity, let us restrict to the case of unit detection efficiency $\eta_d = 1$, a balanced beam splitter, i.e. $r = t$ and assume that in each round of the measurement, the same state ρ is produced. Let $P_n = \langle n| \rho |n\rangle$ be the weight of the n-photon Fock state component of the measured state. We note that since $r = t$, we have $p_{c0} = p_{0c}$ and because $\eta_d = 1$ we end up with $E_{00} = |0\rangle\langle 0|$. Therefore, we know that $p_{00} = P_0$ and from Eq. (2.24) we get $p_{0\_} = \sum_n P_n/2^n$.

We now ask the question: what are the points $(p_{0\_}, p_{00})$ that can be obtained by states ρ which fulfil $P_1 \leq P$, for some parameter $P \in [0, 1]$?

First, we note that by definition $p_{0\_} \geq p_{00}$ and the points $(1, 1)$ and $(0, 0)$ are attained by the vacuum and the state with infinitely many photons, respectively. Thus, the line $p_{0\_} = p_{00}$ is also attainable by mixtures of those states. For a fixed p_{00}, the maximum value of $p_{0\_}$ is then obtained by solving

$$p_{0\_}^{\max}(p_{00}, P) = \max_{\rho} \sum_n P_n \frac{1}{2^n} \qquad \text{such that} \quad P_1 \leq P \text{ and } P_0 = p_{00}. \tag{2.27}$$

Since $1/2^n$ is decreasing with n, the maximum is attained by saturating the values of P_n starting with P_0. Hence, we obtain

$$p_{0\_} \leq p_{0\_}^{\max}(p_{00}, P) = \begin{cases} \frac{1+p_{00}}{2} & \text{for } 1 - p_{00} \leq P \\ \frac{1+P+3p_{00}}{4} & \text{for } 1 - p_{00} > P \end{cases} \tag{2.28}$$

The set of possible values $(p_{0\_}, p_{00})$ is thus included in a convex polytope with four vertices $\boldsymbol{Q}_P = \text{Polytope}\{(0,0), \left(\frac{1+P}{4}, 0\right), \left(\frac{2-P}{2}, 1-P\right), (1,1)\}$, as shown in Fig 2.4. The only non-trivial facet of this polytope is the edge connecting $\left(\frac{1+P}{4}, 0\right)$ and $\left(\frac{2-P}{2}, 1-P\right)$ which is associated to the inequality $4p_{0\_} - 3p_{00} - 1 \leq P$. Thus, without loss of generality, the condition $\langle 1| \rho |1\rangle \leq P$ implies that the elements of $\vec{p}$ satisfy the linear constraint

$$\hat{P}_1^T(\vec{p}) = 4p_{0\_} - 3p_{00} - 1 \leq P. \tag{2.29}$$

Conversely, by measuring the pair $(p_{0\_}, p_{00})$ and by computing the resulting value of $\hat{P}_1^T$, we can guarantee that for any value of P such that $\hat{P}_1^T > P$ the inequality $\langle 1| \rho |1\rangle > P$ holds,

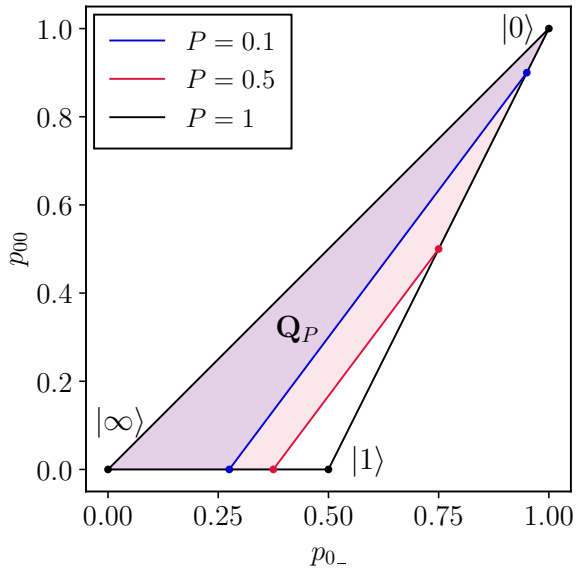

Figure 2.4.: Graphical representation of the single-photon source benchmark. The set of possible values $(p_{0\_}, p_{00})$ for states satisfying $P_1 \leq P$ and $P_0 = p_{00}$ is included in the polytope $\boldsymbol{Q}_P$ with four vertices $\{(0,0), \left(\frac{1+P}{4}, 0\right), \left(\frac{2-P}{2}, 1-P\right), (1,1)\}$, defined after Eq. (2.28). Three polytopes are shown for the values $P \in \{0.1, 0.5, 1\}$. The points $(1,1)$, $(0.5,0)$ and $(0,0)$ are attained by the states $|0\rangle$, $|1\rangle$ and $|\infty\rangle$, respectively.

which means we get a lower bound on the probability that the source to be benchmarked produces exactly a single photon.

Now we want to relax the initial assumptions. We consider the case where the beam splitter has an unknown reflectance r and transmittance $t = 1 - r$ and the two detectors have different efficiencies η_{d_r} and η_{d_t}. In this case, the observed statistics are equivalent to the case where the beam splitter has reflectance $r' = \frac{r\eta_{d_r}}{t\eta_{d_t} + r\eta_{d_r}}$, transmittance $t' = 1 - r'$ and two detectors with the same efficiency $\eta_d = t\eta_{d_t} + r\eta_{d_r}$. The measurement can therefore be modelled by a loss channel with transmission efficiency η_d, an unbalanced beam splitter with reflectance r' and two unit efficiency detectors. We still have $p_{00} = P_0$, but $p_{0\_} = p_{00} + p_{0c}$ and $p_{\_0} = p_{00} + p_{c0}$ are no longer the same. They are now given by $p_{0\_} = \sum_n P_n (1 - r')^n$ and $p_{\_0} = \sum_n P_n (1 - t')^n$ and are therefore no longer directly connected to the quantity $\sum_n P_n / 2^n$. Nevertheless, we find the relation $\sum_n P_n / 2^n \geq \min(p_{0\_}, p_{\_0})$. In analogy to Eq. (2.29) we define

$$\hat{P}_1^T(\vec{p}) = 4p_{0c} + 3p_{00} - 1, \tag{2.30}$$

$$\hat{P}_1^R(\vec{p}) = 4p_{c0} + 3p_{00} - 1 \tag{2.31}$$

and conclude that the quantity

$$\hat{P}_1(\vec{p}) = \min(\hat{P}_1^T(\vec{p}), \hat{P}_1^R(\vec{p})) \tag{2.32}$$

is a benchmark for single-photon sources, without assumptions on the detector efficiencies

and the balance of the beam splitter.

The analysis can be further extended to the experimentally relevant case where the detector efficiencies and the splitting ratio of the beam splitter are characterised and not considered to be part of the state. We assume upper bounds on the detection efficiencies $\eta_{d_{r(t)}} \leq \hat{\eta}_{d_{r(t)}}$ and bounds on the beam splitter reflectance $r \in [1-\hat{t}, \hat{r}]$. In that case, Eqs. (2.30 - 2.31) are replaced by

$$\hat{P}_1^{T*}(\vec{p}) = C_1(\hat{t}, \hat{\eta}_{d_t})\, p_{0c} - C_2(\hat{t}, \hat{\eta}_{d_t}, \hat{\eta}_{d_r})\, p_{cc}, \tag{2.33}$$

$$\hat{P}_1^{R*}(\vec{p}) = C_1(\hat{r}, \hat{\eta}_{d_r})\, p_{c0} - C_2(\hat{r}, \hat{\eta}_{d_r}, \hat{\eta}_{d_t})\, p_{cc}, \tag{2.34}$$

where the coefficients C_1 and C_2, defined as

$$C_1(x, \eta) = \frac{1}{x\,\eta}, \qquad C_2(x, \eta_1, \eta_2) = \frac{1}{x\,\eta_1}\left(\frac{2 - x\,\eta_1}{2(1-x)\eta_2} - 1\right), \tag{2.35}$$

$$\tag{2.36}$$

have been optimised such that $\hat{P}_1^{T*}(\vec{p})$ and $\hat{P}_1^{R*}(\vec{p})$ give the tightest bound on P. One can then choose the best among the two bounds, giving rise to the benchmark

$$\hat{P}_1^{*}(\vec{p}) = \max\{\hat{P}_1^{T*}(\vec{p}), \hat{P}_1^{R*}(\vec{p})\} \leq P_1 \tag{2.37}$$

for the single-photon probability, which takes the additional experimental knowledge into account.

Multimode input state

Note that so far the derivation assumed the measurement to be performed on a single optical mode, see Eqs. (2.21 - 2.25). In the case of a multimode state, where the mode k is associated with the annihilation operator $\hat{a}_k$ satisfying the commutation relation $[\hat{a}_k, \hat{a}_l^\dagger] = \delta_{kl}$, the POVM elements are generalised to $E_0 = \bigotimes_k (1-\eta_d)^{\hat{a}_k^\dagger \hat{a}_k}$ and $E_c = \mathbb{1} - E_0$, where a detector does not click only if none of the modes triggers a detection. To the multimode state ϱ, one associates the distribution P_n of the total photon number operator $\hat{n} = \sum_k \hat{a}_k^\dagger \hat{a}_k$. By assuming that the beam splitter and the detectors act identically on all modes k, the measurement apparatus is only sensitive to the total photon number $\hat{n}$. Therefore, the POVM elements $\{E_{00}, E_{c0}, E_{0c}, E_{cc}\}$ in the multimode case are still given by Eqs. (2.22 - 2.23) when replacing $\hat{a}_k^\dagger \hat{a}_k$ by $\hat{n}$. We conclude that $\hat{P}_1(\vec{p})$ as in Eq. (2.32) can readily be used to benchmark the probability that a multimode source emits a single photon

$$P_1 = \mathrm{tr}\left(\varrho \sum_k \hat{a}_k^\dagger\, |0\rangle\langle 0|\, \hat{a}_k\right). \tag{2.38}$$

It is worth emphasising that a high $\hat{P}_1(\vec{p})$ for a multimode source does not guarantee that the single-photon probability is high in any of the individual modes. The single-mode character of the source therefore needs to be evaluated separately.

However, given a lower bound $(1-\varepsilon)$ on the probability that all the modes but one are empty, i.e.

$$\mathrm{tr}(\varrho\,(\mathbb{1}_1 \otimes |0\rangle\langle 0|_2 \otimes \cdots \otimes |0\rangle\langle 0|_N)) \geq 1-\varepsilon, \tag{2.39}$$

we can lower bound the *single-mode* single-photon probability by

$$P_1^{[1]} = \mathrm{tr}(\rho_1\ |1\rangle\langle 1|_1) \geq P_1 - \varepsilon, \tag{2.40}$$

since the maximal contribution to P_1 from the other modes is ε. Here, $\rho_1 = \mathrm{tr}_{2,\ldots,N}(\varrho)$ denotes the marginal state in the first mode.

2.3.3. Wigner negativity

In the case where the generated state can be assumed to be *single-mode*, we can relate the measured value of $\hat{P}_1(\vec{p})$ to the non-classicality of the source. Concretely we show that the knowledge of P_1 can reveal Wigner-negativity [115], the strongest form of non-classicality for a bosonic mode. Thus, if the measured state from a source is Wigner-negative, then we know for sure that the source produces non-classical light.

The Wigner function is a representation of a single-mode state ρ defined by the following quasi-probability distribution [116]

$$W_\rho(\beta) = \frac{2}{\pi}\,\mathrm{tr}\left(D(\beta)(-1)^{a^\dagger a}D^\dagger(\beta)\,\rho\right), \tag{2.41}$$

with the normalisation $\int \mathrm{d}\beta^2 W_\rho(\beta) = 1$, where $D(\beta) = \exp\left(\beta a^\dagger - \beta^* a\right)$ is the displacement operator with a complex amplitude β. Applying Eq. (2.41) to a Fock state gives [117]

$$W_{|n\rangle\langle n|}(\beta) = \frac{2(-1)^n}{\pi}\exp\left(-2|\beta|^2\right)L_n\left(4|\beta|^2\right) \tag{2.42}$$

where L_n is the Laguerre polynomial. Note that $L_1(x) = 1-x$ and the following bound on the Laguerre polynomials $e^{-x/2}|L_n(x)| \leq 1$, see e.g. Eq. (18.14.8) in [118], leads to a bound on the Wigner function of Fock states $|W_{|n\rangle\langle n|}(\beta)| \leq \frac{2}{\pi}$.

Witness of Wigner-negativity

With the Eq. (2.42), the definition of the Laguerre polynomial $L_1(x)$ and the upper bound on the Wigner function of Fock states, it can be seen that the Wigner function of any

mixture of Fock states $\rho = \sum P_n \, |n\rangle\langle n|$ satisfies

$$W_\rho(\beta) = P_1 W_{|1\rangle\langle 1|}(\beta) + \sum_{n\neq 1} P_n W_{|n\rangle\langle n|}(\beta) \tag{2.43}$$

$$\leq \frac{2}{\pi}\big(- P_1 e^{-2|\beta|^2}(1-4|\beta|^2) + (1-P_1)\big). \tag{2.44}$$

At the origin $\beta = 0$, we obtain $W_\rho(0) \leq \frac{2}{\pi}(1-2P_1)$ which is negative if $P_1 > \frac{1}{2}$. Hence, if from the measurement of $\vec{p}$ one concludes that $\hat{P}_1(\vec{p}) > \frac{1}{2}$, then the measured state is Wigner-negative, under the assumption that ρ is a single-mode state.

Measure of Wigner-negativity

To quantify the negativity of the Wigner representation of a given state ρ, we measure the total quasi-probability for which the function $W_\rho(\beta)$ takes negative values [119], i.e.

$$N_W(\rho) = \int \mathrm{d}\beta^2 \frac{|W_\rho(\beta)| - W_\rho(\beta)}{2}. \tag{2.45}$$

The function $N_W(\rho)$ is non-increasing under Gaussian operations (see Appendix E in P.3), which justifies its use as a measure of Wigner-negativity. With the use of Ineq. (2.44), we show that

$$N_W(\rho) \geq F(P_1) = \begin{cases} \frac{3(1-P_1)\left(4w^2+3\right)}{8w} + P_1 - 2 & \text{for } P_1 > \frac{1}{2} \\ 0 & \text{for } P_1 \leq \frac{1}{2} \end{cases} \tag{2.46}$$

$$\text{with} \quad w = w_0\left(\frac{\sqrt{e}}{2}\frac{1-P_1}{P_1}\right),$$

where w_0 is the principal branch of the Lambert W function. The function $F(P_1)$ is non-decreasing and therefore, from the measurement of $\vec{p}$, we get a lower bound $\hat{P}_1(\vec{p})$ on P_1 which can be used to lower bound $N_W(\rho) \geq F(\hat{P}_1(\vec{p}))$. The bound in Ineq. (2.46) is tight by construction in the ideal case $N_W(|1\rangle\langle 1|) = F(1) = \frac{9}{4\sqrt{e}} - 1 \approx 0.36$.

2.3.4. Experimental benchmark of the heralded-single photon source

We demonstrate the benchmark as well as the measure of Wigner-negativity by using the HSPS presented in Sec. 2.1 and shown in Fig. 2.5. The PPKTP non-linear crystal is pumped at a repetition rate of 76.2 MHz with a pair generation probability per pump pulse of about 1×10^{-3}. The phase-matching condition is set such that $\lambda_p = 771.85\,\mathrm{nm} \rightarrow 1541.3\,\mathrm{nm} + 1546.1\,\mathrm{nm}$.

In order to make sure that the heralded signal photon is in a spectrally pure state, we filter the heralding idler photon with a 100 GHz DWDM corresponding to a central fil-

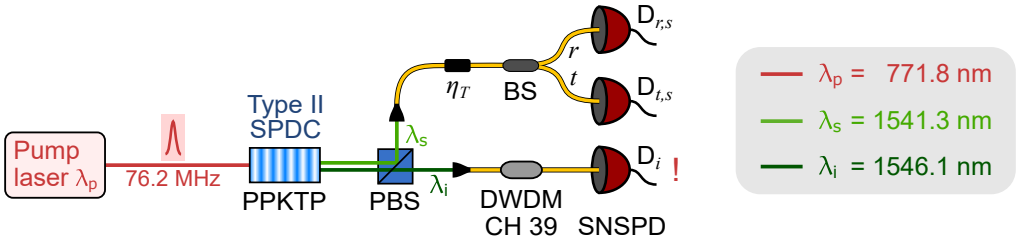

Figure 2.5.: Experimental setup for the autocorrelation measurement to demonstrate the benchmark for single-photon sources and the Wigner negativity of the heralded single-photon state. A variable optical attenuator (JDS Uniphase MV47W) allows for adding loss on the heralded signal photon corresponding to a transmission efficiency of η_T.

ter wavelength of 1546.1 nm with a measured FWHM of 0.6 nm. The spectral purity of the heralded state is experimentally determined by a JSI measurement and is calculated to be $\mathcal{P} = \sum_k \lambda_k^2 = (98.59 \pm 0.04)\,\%$ where the largest Schmidt coefficient is $\lambda_1 = (99.29 \pm 0.02)\,\%$. These values are obtained from the Schmidt decomposition of a 2D Gaussian fit to the measured JSI and the uncertainty is calculated with the Monte Carlo method over 10^4 JSI samples assuming Poissonian count statistics. The polarisation purity is ensured by the fact that the signal and idler photons are deterministically separated by a PBS with extinction ratio of about 10^3 (10^2) for the transmitted (reflected) port, therefore a heralded signal photon detection in the wrong polarisation mode is expected to occur with a probability of less than 10^{-5} since it is further suppressed by the polarisation dependence of the MoSi superconducting nanowire single-photon detectors (SNSPD). Furthermore, we assume that the spatial mode purity is guaranteed by coupling the photons into single-mode fibre.

The total efficiency of the heralded signal photons is $\eta_{s,\mathrm{tot}} = 62\,\%$, where the heralding efficiency including the insertion loss of the fibre beam splitter is $\eta_{h,s} = 70\,\%$ and the two detectors have efficiencies $\eta_{d_{r,s}} = 92\,\%$ and $\eta_{d_{t,s}} = 85\,\%$. For the calibration-dependent benchmark, we upper-bound the detector efficiencies by $(\hat{\eta}_{d_{r,s}}, \hat{\eta}_{d_{t,s}}) = (95\,\%, 88\,\%)$ and the beam splitter coefficients by $\hat{r} \in [0.49, 0.50]$. The heralding idler photons have a lower total transmission of 25 % due to spectral filtering and the lower detection efficiency $\eta_{d_i} = 75\,\%$.

The source therefore produces high-purity signal photons at a heralding rate of 19.1 kcps. In order to evaluate $\vec{p} = (p_{00}, p_{c0}, p_{0c}, p_{cc})$ for the signal photons after the 50/50 beam splitter, data are acquired for 200 s. The dark count probabilities of the used detectors for the autocorrelation measurement per heralding detection are lower than 4×10^{-7}. In fact, dark counts can be completely neglected in our experiment since the calculated corrections to the benchmark are more than two orders of magnitude lower than the statistical noise.

The results of the measurement are graphically shown in Fig. 2.6 for different added attenuation on the signal photon to mimic lower heralding efficiencies. The numerical results for the benchmark and the Wigner-negativity measure are given in Tab. 2.3. We see that in the case of no added attenuation on the heralded single-photon state ($\eta_{s,\mathrm{tot}} = 62\,\%$), we

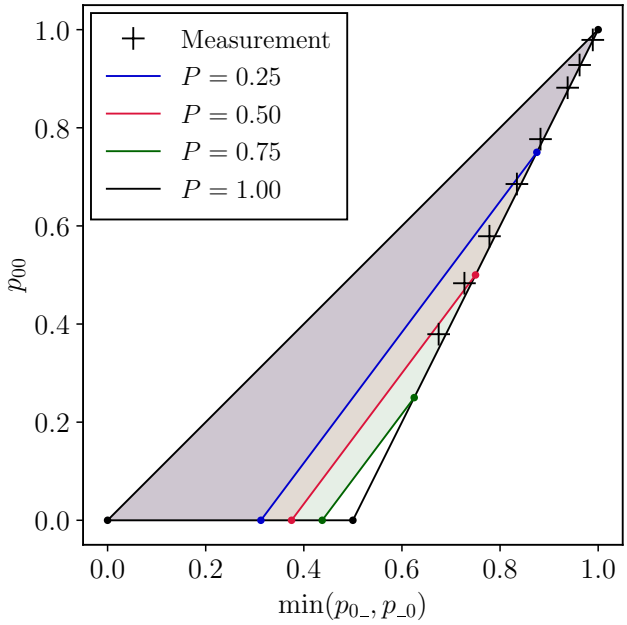

Figure 2.6.: Results of the measurement for the single-photon source benchmark. Four polytopes are shown for the values $P \in \{0.25, 0.5, 0.75, 1\}$. The black crosses are measurements for a heralded single photon undergoing different added attenuation corresponding to transmission efficiencies of $\eta_T \in \{1.0, 0.83, 0.68, 0.51, 0.36, 0.19, 0.12, 0.034\}$.

$\eta_{s,\text{tot}}$	$\hat{P}_1^T$	$\hat{P}_1^R$	$\hat{q}_\alpha$	$\hat{P}_1^{T*}$	$\hat{P}_1^{R*}$	$\hat{q}_\alpha^*$	$n\hat{w}_\alpha$	$n\hat{w}_\alpha^*$
62 %	0.561	0.678	0.554	0.658	0.683	0.677	0.0046	0.053
52 %	0.460	0.573	0.453	0.544	0.573	0.566	0	0.0072
42 %	0.376	0.465	0.369	0.444	0.466	0.459	0	0

Table 2.3.: Results of the measurement for the three highest transmission efficiencies $\eta_{s,\text{tot}}$ of the heralded single-photon state. The values for $\hat{P}_1^T$ and $\hat{P}_1^R$ are calculated according to Eqs. (2.30 - 2.31). For the finite statistics analysis we calculate the one-sided confidence interval $\hat{q}_\alpha$ on $\hat{P}_1$ where a confidence level of $1 - \alpha = 1 - 10^{-10}$ is applied throughout this table. All the variables with a * are calculated from Eqs. (2.33 - 2.34) which take the detector efficiencies and beam splitter ratio into account. The measure of Wigner-negativity $n\hat{w}_\alpha = F(\hat{q}_\alpha) \leq N_W(\rho)$ is only positive for the highest transmission, since $\hat{q}_\alpha < \frac{1}{2}$ for the cases where attenuation was added. This changes for $n\hat{w}_\alpha^*$ where detector inefficiencies are taken into account. Remember that for a single photon, $N_W(|1\rangle\langle 1|) = F(1) \approx 0.36$.

estimate a single-photon probability of $\hat{P}_1 = 0.561$ and in the case where the detector efficiencies are taken into account, this becomes $\hat{P}_1^* = 0.683$. For the finite statistics analysis (see Sec. 4 in P.3), we calculate the one-sided confidence intervals $\hat{q}_\alpha = 0.554$ on $\hat{P}_1$ and $\hat{q}_\alpha^* = 0.677$ on $\hat{P}_1^*$ for a confidence level of $1 - \alpha = 1 - 10^{-10}$.

Note that in order to make a conclusion about the Wigner negativity of the state, we needed to assume a single-mode state which is not the case in the experiment. However, we can estimate a lower bound on the spectrally single-mode single-photon component of the state by taking the spectral purity into account, and obtain with the help of Ineq. (2.40) $P_1^{[1]} \geq P_1 - (1 - \lambda_1 + 3\sigma_{\lambda_1}) = P_1 - 0.0076$. The Wigner-negativity is then calculated from this value corresponding to the spectrally single-mode state. As argued above, we assume the state to be single-mode in all the other degrees of freedom.

2.3.5. Conclusion

Autocorrelation measurements are commonly used to check that a given source does not emit more than one photon. Here, we showed that the statistics obtained from such a measurement are actually richer and can be used to lower bound the probability that a given source produces a single photon. This quantity is naturally a good benchmark for single-photon sources, since it captures its quality and its efficiency simultaneously, both crucial parameters of such a source. Further, we have shown that if the mode purity of a source can be estimated, the single-photon emission probability can be used to quantify the negativity of the Wigner function associated to the generated state.

Since the development of single-photon sources for quantum technology applications is currently ongoing at a high pace, the analysis of the outcome of an autocorrelation measurement presented here hopefully helps to assess these sources.

2.4. Improved heralded single-photon source

In this section, an improved HSPS is presented, where the heralding detector is a photon-number-resolving (PNR) parallel SNSPD. In this source, a successful heralding detection consists in a single-photon detection event with all higher-order detection events discarded. In this way, the generated higher-order photon pairs, which would contribute to the heralded state in case of a threshold heralding detector, can be suppressed. In theory, such a source, based on SPDC or spontaneous four-wave mixing, can achieve a heralding probability per pump pulse up to 25 %, limited by the thermal photon-number statistics of the heralding state [88].

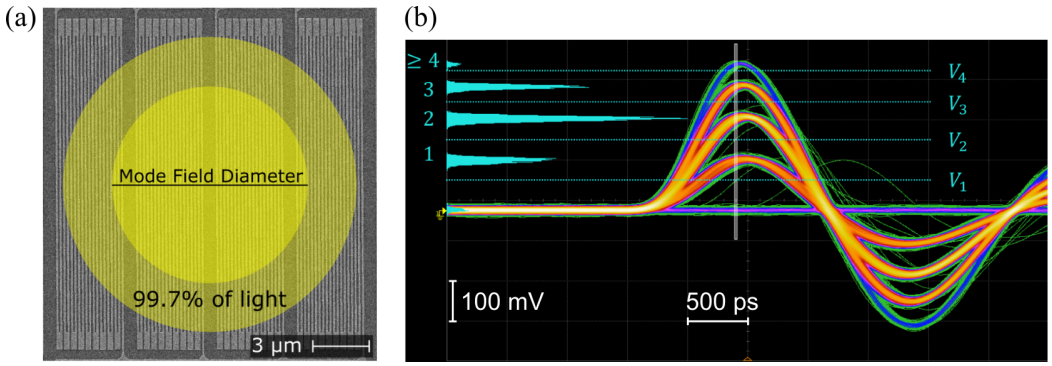

Figure 2.7.: P-SNSPD used as a heralding detector. (a) Image of the four-pixel detector with a photosensitive area of $16\,\mu\text{m} \times 16\,\mu\text{m}$. (b) Oscilloscope traces of the amplified electrical signal output by the P-SNSPD when photons are incident. The four different amplitudes, corresponding to events where 1, 2, 3 and 4 pixels are triggered, can be discriminated by selecting the threshold accordingly. Images are taken from Ref. [121].

2.4.1. Photon-number-resolving detector

The key ingredient to improve the heralded photon-number statistics of a single HSPS is to have high transmission, coupling and detection efficiency for the heralding photon, as well as the capability to distinguish a single photon from a higher-photon-number state. Regarding the capability to correctly identify a certain photon-number state incident on the detector, three different categories of detectors are found in the literature: threshold, pseudo PNR and true PNR detectors. Ideal threshold detectors (sometimes referred to as click, binary or non-PNR detectors) fire whenever there is one or more photons sent to the detector. Ideal true PNR detectors can perfectly distinguish between all different photon-number states. The pseudo PNR category lies in between, meaning that these detectors have PNR capability, however, the detection mechanism inherently prevents them to perfectly distinguish between all different photon-number states, even if the detector has unit efficiency.

In our case, we use a four-pixel MoSi parallel superconducting nanowire single-photon detector (P-SNSPD), as shown in Fig. 2.7(a) and described in Ref. [120]. As the names suggests, the four pixels are electrically connected in parallel and signal is read out via a single coaxial cable. Originally this detector was developed to achieve high count rates, however, the amplitude of the readout signal is dependent on how many pixels clicked in a detection event and thus this detector also exhibits photon-number resolution, see Fig. 2.7(b) and Ref. [121] for the detector model and characterisation. Since more than one photon can end up on the same pixel in a detection event, which would then be only registered as a single-photon event, this detector falls in the category of pseudo PNR detectors. In fact, this is true for all pixel detectors, but by increasing the number of pixels and using designs where all the pixels have the same click probability, one can reach high photon-number resolution.

In order to characterise the P-SNSPD in terms of efficiency and PNR capability, we apply the method described in Ref. [121] to determine the matrix of probabilities $\mathbf{P}$, where the element P_{nm} describes the probability that n out of N pixels click if an m-photon state is incident on the detector. The characterisation method uses a coherent state with known Poissonian photon-number statistics to reconstruct $\mathbf{P}$ from the measured output statistics. For an ideal PNR detector, $\mathbf{P} = \mathbb{1}$, i.e. the probability of detecting n photons when n are incident is 1, otherwise $\mathbf{P}$ is an upper-triangle matrix where the columns sum up to 1. In theory, the column index m can take an infinite value, but in practice it can be truncated to stop at a finite value M. An initial photon-number probability distribution $\vec{p} = (p_0, ..., p_M)^T$ is then connected to the probability of an n-click detection event by $q_n = \sum_{m=0}^{M} P_{nm} p_m$. By inverting the detector specific matrix $\mathbf{P}$ and measuring the output distribution $\vec{q} = (q_0, ..., q_N)^T$, one can calculate the incident photon number distribution $\vec{p} = (p_0, ..., p_M)^T$. In our case for $N = 4$ and $M = 9$, we measured $P_{11} = 84\,\%$, $P_{12} = 55\,\%$, $P_{13} = 31\,\%$, $P_{14} = 17\,\%$ and $P_{22} = 42\,\%$.

For our application, it is only important that we can distinguish between $m = 1$ and $m \geq 2$ photon events, i.e. we ideally want $P_{0m} = P_{1m} = 0$ for $m \geq 2$. The most crucial element is P_{22} since in a realistic HSPS $p_2 \gg p_3$, and therefore it is important to detect a two-photon state with a high probability. In our case, $P_{22} = 42\,\%$ is only limited to some extent by the efficiency of the device since $P_{11}^2 = 71\,\%$. An important contribution to P_{12} comes from the fact that a two-photon state has still a high probability, even if no photon is lost, to only make one pixel click. The probabilities for a single photon to hit a certain pixel are $(0.526, 0.386, 0.061, 0.027)$, where the two higher efficiency ones correspond to the pixels in the centre of the photosensitive area.

2.4.2. Theoretical model

The state generated by the SPDC process can be described in the photon-number basis by a two-mode squeezed vacuum state (TMSV) [122]

$$|\Psi\rangle_{si} = \sqrt{1-\lambda^2} \sum_{n=0}^{\infty} \lambda^n |nn\rangle_{si} = \sum_{n=0}^{\infty} \sqrt{\frac{\mu^n}{(\mu+1)^{n+1}}} |nn\rangle_{si}\,, \tag{2.47}$$

where $\lambda = \tanh(r)$ with the squeezing parameter r and the mean photon number $\mu = \sinh^2(r) = \lambda^2/(1-\lambda^2)$. The marginal states of the signal (s) and idler (i) modes are thermal states with photon-number probability distribution

$$p_n = \frac{\mu^n}{(\mu+1)^{n+1}}. \tag{2.48}$$

To obtain analytical equations describing the single and coincidence detection probabilities per pump pulse, we consider a configuration as shown in Fig. 2.8 and use the approach of Ref. [123]. In this formalism, the TMSV state $\rho = |\Psi\rangle\langle\Psi|_{si}$ can be expressed by a 4×4

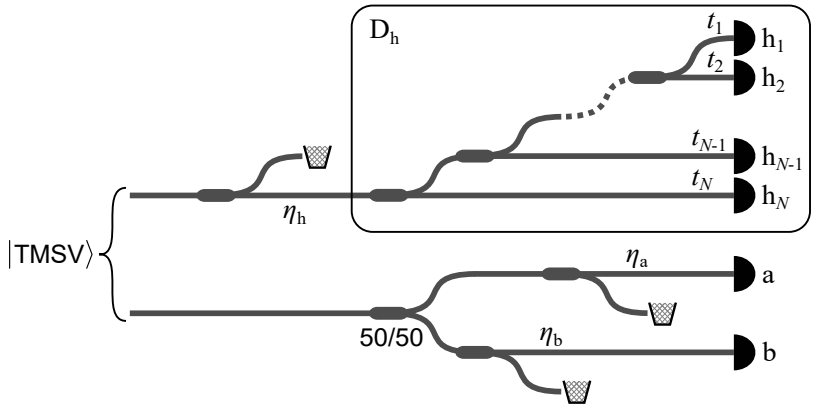

Figure 2.8.: Schematic representation of the theory model to calculate the single and coincidence detection probabilities. The heralding mode of the two-mode squeezed vacuum (TMSV) state is subject to loss, where the transmission efficiency is denoted by η_h. The PNR detector $\mathrm{D_h}$ is then modelled by a cascade of beam splitters where the states in the N output modes with normalised transmittance t_k are detected by threshold detectors ($\mathrm{h_1}$ to h_N), corresponding to the individual pixels. The other mode of the TMSV state is sent to a 50/50 beam splitter and further undergoes loss channels (η_a and η_b) before reaching the threshold detectors a and b.

covariance matrix with μ as a single free parameter. Furthermore, the action of beam splitters can be modelled by Gaussian unitary operations. The formalism additionally allows modes to be traced out, and so we are able to model transmission loss on a given mode by introducing an auxiliary mode, applying a beam splitter operation between the two modes, and finally tracing out the auxiliary mode. Moreover, the formalism also allows for calculation of the expectation value of a given Gaussian state after projection onto vacuum. Therefore, we can model threshold detectors described by POVM elements $E_0 = |0\rangle\langle 0|$ corresponding to a no-click outcome and $E_c = \mathbb{1} - |0\rangle\langle 0|$ to a click outcome. To obtain a model for the P-SNSPD, we note that each of the N pixels of the detector is a threshold detector. Thus, a physically intuitive model for the P-SNSPD consists of a sequence of beam splitters, with splitting ratios corresponding to the characterised pixel efficiencies, and N threshold detectors.

This model then allows the calculation of the probabilities per pump pulse to get a (single-click) detection on one of the detectors: $p_\mathrm{h} = \sum_{k=1}^{N} \mathrm{tr}\left(\rho\left(\mathbb{1}_a \otimes \mathbb{1}_b \otimes E_{c,\mathrm{h}_k} \otimes E_{0,\mathrm{h}_{\neg k}}^{\otimes(N-1)}\right)\right)$ for the heralding PNR detector $\mathrm{D_h}$, $p_\mathrm{a} = \mathrm{tr}\left(\rho\left(E_{c,\mathrm{a}} \otimes \mathbb{1}_b \otimes \mathbb{1}_{\mathrm{h}_k}^{\otimes N}\right)\right)$ for the threshold detector $\mathrm{D_a}$ and similarly for p_b. Moreover, we can also obtain the coincidence probabilities p_ha, p_hb, p_hab and p_ab between the corresponding detectors. In the case where we operate the heralding detector in the threshold mode, i.e. we only discriminate at the lowest threshold V_1, we can use the same model with the number of pixels $N = 1$.

The explicit formulas for the calculated probabilities are given in Appendix A of P.4, where we further assume the state to be in multiple Schmidt modes, and therefore account for sources with a non-factorable JSA. With the help of these probabilities, which can

be measured in a Hanbury Brown-Twiss experiment, we then approximate the heralded second-order autocorrelation function by

$$g_{\mathrm{h}}^{(2)}(0) \approx \frac{p_{\mathrm{h}} p_{\mathrm{hab}}}{p_{\mathrm{ha}} p_{\mathrm{hb}}} \tag{2.49}$$

and the unconditional second-order autocorrelation function of the state after the 50/50 beam splitter according to

$$g_{\mathrm{unc}}^{(2)}(0) \approx \frac{p_{\mathrm{ab}}}{p_{\mathrm{a}} p_{\mathrm{b}}}. \tag{2.50}$$

We note that in the case where we have direct access to the photon-number probability distribution p_n of the state by measuring it with a PNR detector, one can also directly use the definition of the second-order auto correlation function (see Ch. 2.2 of Ref. [122])

$$g^{(2)}(0) = \frac{\langle \hat{n}(\hat{n}-1) \rangle}{\langle \hat{n} \rangle^2} = \frac{\sum_n n(n-1) p_n}{\left(\sum_n n p_n \right)^2} \tag{2.51}$$

to calculate its value. An ideal single-photon state has $g^{(2)}(0) = 0$ and a thermal state gives $g^{(2)}(0) = 2$.

2.4.3. Experiment

We perform two experiments, as schematically shown in Fig. 2.9. In the first one, the P-SNSPD is used as the heralding detector of the HSPS and operated in the threshold as well as in the PNR mode ($\eta_{d,\mathrm{h}} = P_{11} = 84\,\%$). The heralded idler photons are sent to a 50/50 BS and detected by two MoSi threshold SNSPDs with efficiencies of about $\eta_{d,\mathrm{a}} = 85\,\%$ for $\mathrm{D_a}$ and $\eta_{d,\mathrm{b}} = 83\,\%$ for $\mathrm{D_b}$ to determine $g_{\mathrm{h}}^{(2)}(0)$ according to Eq. (2.50). We measure total efficiencies of $\eta_{h,\mathrm{h}}\eta_{d,\mathrm{h}} = 63.5\,\%$, $\eta_{h,\mathrm{a}}\eta_{d,\mathrm{a}} r = 31.5\,\%$ and $\eta_{h,\mathrm{b}}\eta_{d,\mathrm{b}} t = 29.0\,\%$ at low pump power ($\mu \approx 5 \times 10^{-4}$), where r ($t = 1 - r$) is the power reflectance (transmittance) of the BS. In the second experiment, we determine the unconditional $g^{(2)}(0)$ in the idler mode by using the P-SNSPD to reconstruct the photon-number distribution p_n and compare it to the value obtained with the standard method of using a 50/50 BS and two threshold detectors, see Eqs. (2.50 - 2.51).

In both experiments, we vary the power of the pump laser by means of a variable neutral density filter (NDF) and therefore vary the mean photon number of the generated state, see Eq. (2.47). In the first experiment, we want to show the full potential of the improved HSPS and therefore do not spectrally filter, which would add loss and reduce the quality of the heralded state. However, we measure the JSI of the generated state and determine the Schmidt coefficients λ_k, which are taken into account in our model, see Appendix A of P.4. The calculated purity amounts to $\mathcal{P} = \sum_k \lambda_k^2 \approx 0.84$. In the second experiment we additionally filter the idler mode with a DWDM in order to herald spectrally pure photons and suppress leaking signal photons due to the extinction ratio of around 10^3 for

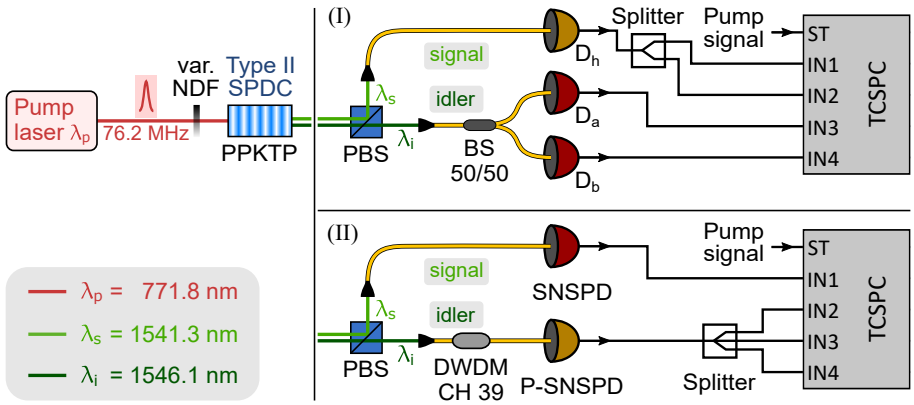

Figure 2.9.: Experimental setup for the two performed experiments. (I) The heralding signal photons are detected by the P-SNSPD while the idler photons are sent to a 50/50 BS and detected by threshold SNSPDs. (II) The idler photons are spectrally filtered by a 100 GHz DWDM at ITU channel 39 and detected by the P-SNSPD for the reconstruction of the thermal photon number statistics. Electrical signals are represented by solid black lines. BS, beam splitter; DWDM, dense wavelength division multiplexer; PBS, polarising beam splitter; PPKTP, periodically poled potassium titanyl phosphate; P-SNSPD, parallel superconducting nanowire single-photon detector; SNSPD, superconducting nanowire single-photon detector; SPDC, spontaneous parametric down-conversion; TCSPC, time-correlated single photon counting (ID Quantique ID900).

the transmitted port of the PBS which separates the signal and idler photons.

The results of the first experiment are shown in Fig. 2.10. The analysis is done for the case where the P-SNSPD operates in threshold mode (all detections are considered heralding events) or in PNR mode (only $n = 1$ click events are successful heralds). The mean photon number μ is calculated from the measured probability of detecting a heralding photon, p_h, in the threshold configuration together with the characterised total efficiency of the heralding photons $\eta_\mathrm{h} = \eta_{h,\mathrm{h}}\eta_{d,\mathrm{h}}$ and the Schmidt coefficients λ_k obtained from a fit of Eq. (2.50) to the corresponding measured data. The weighted average of the data for the ratio shown in Fig. 2.10(b) is $g^{(2)}_{\mathrm{h,thr}}(0)/g^{(2)}_{\mathrm{h,PNR}}(0) = 1.368 \pm 0.003$ which is the factor by which the heralding rate can be increased when switching from threshold to PNR heralding mode while keeping a fixed $g^{(2)}_\mathrm{h}(0) \ll 1$. Inversely this corresponds to a reduction in $g^{(2)}_\mathrm{h}(0)$ of $(26.9 \pm 0.2)\,\%$ for the same heralding rate. Note that in this demonstration, no spectral filtering of the heralding photons has been performed, in order to show the maximum achievable improvement in $g^{(2)}_\mathrm{h}(0)$ with our PNR detector.

The results obtained in the second experiment, where the P-SNSPD is used to measure the unconditional autocorrelation function on the idler mode, are shown in Fig. 2.11. The values of $g^{(2)}_\mathrm{unc}(0) \approx 2$ confirm the thermal nature of our source and the results between the two measurement methods agree. The error bars for the measurement with the P-SNSPD were calculated through a Monte Carlo method with 10^3 iterations. In each iteration, the Poissonian input state used for the detector characterisation is randomly picked from

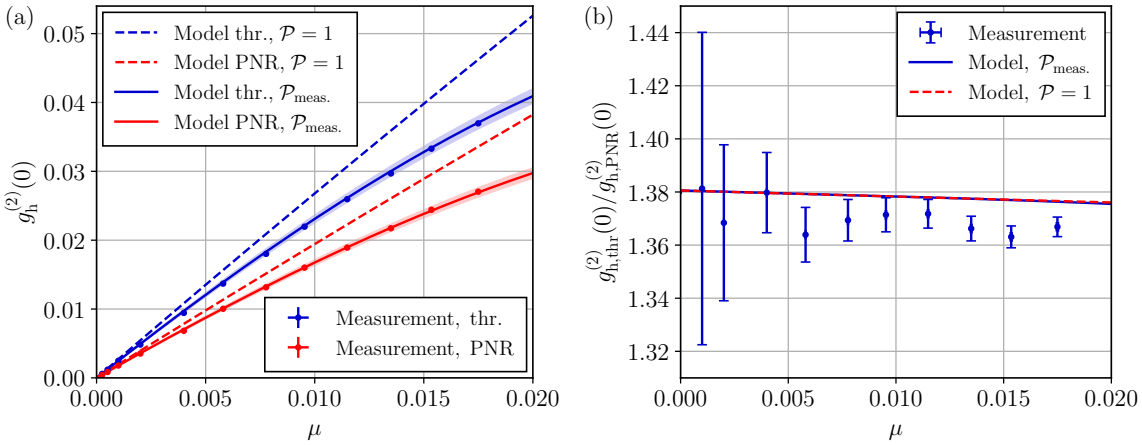

Figure 2.10.: Results of experiment (I). (a) Heralded second-order autocorrelation function as a function of the mean photon number μ. The blue points correspond to the case where the P-SNSPD operates in threshold mode (thr.), whereas the red points show the measurements for the PNR mode. The solid lines are obtained from the theoretical model with the same purity as in the experiment, where the shaded areas mark the spectral purity interval of $\pm 4\,\%$. The dashed lines show the behaviour for a source with purity $\mathcal{P} = 1$. (b) Ratio between the heralded second-order autocorrelation functions when the heralding detector is operated in the threshold and the PNR configuration.

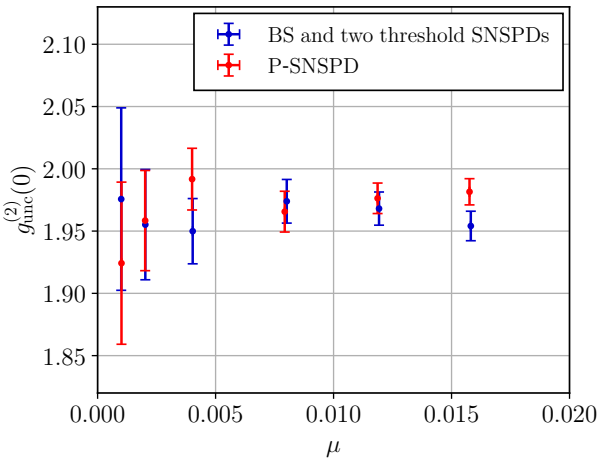

Figure 2.11.: Results of experiment (II). Unconditional second-order autocorrelation measurement on the spectrally filtered idler mode of the SPDC source as a function of the mean photon number μ. The red data correspond to the measurement with the P-SNSPD, whereas the blue data are obtained with the standard method using a beam splitter and two threshold detectors. The blue error bars are calculated from the counts by assuming Poissonian statistics and the red errorbars are obtained from a Monte Carlo simulation.

a Gaussian distribution centred at the set value of $\mu = 1$ with a standard deviation of $\sigma = 0.05$. In this way, the uncertainty of our characterisation setup is taken into account. The obtained matrix $\mathbf{P}$ is then used to reconstruct the light input statistics p_n from the experimental photon-counting distribution measured by the P-SNSPD. As a last step in each iteration, the value $g^{(2)}_{\mathrm{unc}}(0)$ is computed from the reconstructed statistics according to Eq. (2.51).

2.4.4. Discussion and outlook

The most important parameters for improving the HSPS are the PNR capability of the detector and the total efficiency η_{h}, i.e. transmission through optical elements, coupling, and detection efficiency of the heralding photons. As shown in Fig. 2.12, for a pure SPDC source combined with an ideal PNR heralding detector ($\mathbf{P} = \mathbb{1}$), the reduction in $g^{(2)}_{\mathrm{h}}(0)$, that is $1 - g^{(2)}_{\mathrm{h,PNR}}(0)/g^{(2)}_{\mathrm{h,thr}}(0)$, reaches 100 % for $\eta_{\mathrm{h}} = 1$. It achieves a value of 50 % for $\eta_{\mathrm{h}} = 0.67$ and surpasses 90 % for $\eta_{\mathrm{h}} = 0.95$. For $\eta_{\mathrm{h}} = 0.635$, as measured in our experiment, a perfect PNR detector would achieve a reduction of 46.5 %, however, our reported value of (26.9 ± 0.1) % lies significantly lower. This is due to the fact that the PNR capability of the detector to correctly detect an incoming higher-photon-number state is still limited by the non-resolvability of two photons hitting the same pixel. A 2-photon state, for example, is correctly detected with 41.7 % probability, is missed because both photons hit the same

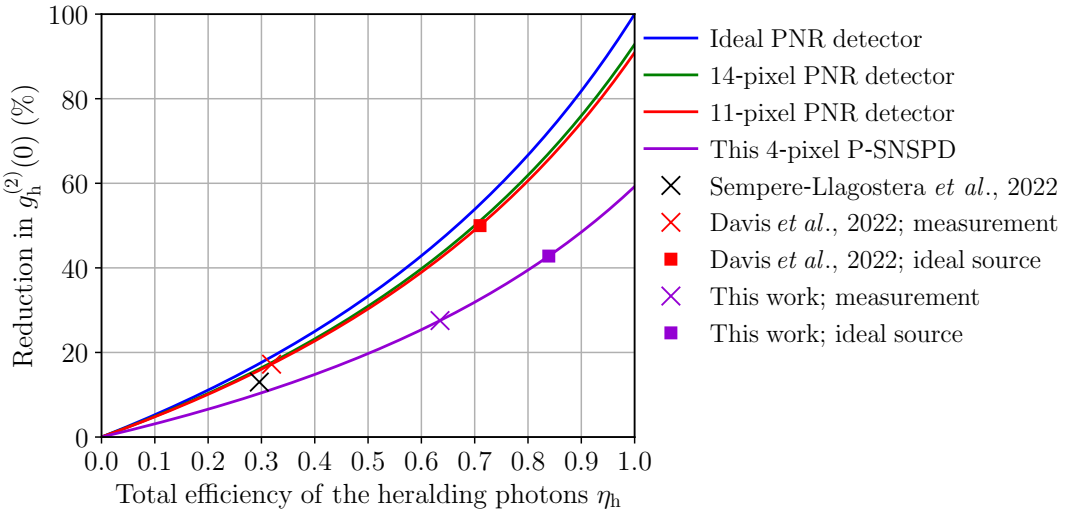

Figure 2.12.: Calculation of the reduction in $g^{(2)}_{\mathrm{h}}(0)$ as a function of the total efficiency of the heralding photons η_{h}. The solid lines are obtained from the theoretical model for a spectrally pure source with fixed $\mu = 10^{-3}$. For the 14- and 11- pixel PNR detectors, we assume uniform light distribution across the pixels. We further compare our results with the ones from Refs. [124, 125]. The crosses are calculated from the measured values and the squares are obtained by assuming unit efficiency on the source side, i.e. the total efficiency of the heralding photons is only limited by the single-photon detection efficiency ($\eta_{\mathrm{h}} = P_{11}$).

pixel with 28.7 % probability, and is missed due to the limited pixel efficiencies with 29.6 % probability. If the light would be uniformly distributed over the 4 pixels, these probabilities would be 52.8 %, 17.6 % and 29.6 %, respectively. In order to increase the PNR capability of our P-SNSPD, the number of pixels needs to be increased while still maintaining good amplitude discrimination of the electrical readout signal between different photon-number detection events. Additionally, a uniform light distribution over the pixels could further mitigate the problem and can be obtained by exploiting a detector design with interleaved nanowires [126, 127].

Another important aspect of a HSPS is the spectral purity of the heralded photon, since many single-photon applications relying on interference require high purity. The standard approach of spectral filtering presents a viable solution also in the case of a PNR heralding detector, given the insertion loss of the spectral filter is sufficiently low. Commercially available narrow linewidth (2 nm FWHM) band-pass filters already have transmission efficiencies of more than 90 % (Edmund Optics 12-514).

In our source, with increasing pump power we observe a decrease in purity due to spectral broadening of the pump light caused by the non-linearity of the spatial mode cleaning fibre (Coherent 780-HP, 9 cm long) before the PPKTP crystal. We take this into account in the model by fitting Eq. (2.50) to the experimental data with the purity $\mathcal{P}$ as a fit parameter. This issue could be solved by replacing the standard fibre for spatial mode cleaning by a photonic crystal fibre, where nonlinear effects are largely suppressed.

Two similar implementations of an improved HSPS have recently been shown, where the photon-number dependent slew rate of the readout signal of a single-meander SNSPD is exploited [124, 125]. Compared to those sources, we achieve a larger improvement in $g^{(2)}(0)$ mainly thanks to our high total efficiency, η_{h}, which is roughly twice as high as in the other sources. Further, the short recovery time of our P-SNSPD (< 40 ns) allows the source to be operated at a high pump repetition rate and therefore achieve significantly higher heralding rates.

In the second experiment we showed that P-SNSPDs can perform $g^{(2)}(0)$ measurements and therefore replace a beam splitter and two threshold detectors as used in the standard method, hence simplifying the overall experimental apparatus.

3. Detection and distribution of single-photon path entanglement

Single-photon path entanglement is a fundamentally interesting concept first introduced in the context of Bell non-locality [15] by Tan, Walls and Collet in 1991 [128] and further investigated by Hardy in 1994 [129]. Although the proposed schemes to demonstrate non-locality received criticism and objection [130–132], the striking underlying concept of a single photon exhibiting entanglement was further explored theoretically [80, 133–141]. Experiments followed quickly, demonstrating quantum teleportation [142, 143] and entanglement swapping based on single-photon entanglement [144]. With the development of the displacement-based measurement for path-entangled states [114], implementations that can be applied in a distributed scenario became possible. This lead to the demonstration of an entanglement witness [83], EPR steering [145] and the heralded amplification of path-entangled states [146] using local measurements only.

Currently, single-photon path entanglement is a promising candidate for long-distance entanglement distribution since there exist schemes which are more robust against transmission and detection loss compared to two-photon schemes [65]. Further applications for multipartite single-photon entangled states include quantum conference key agreement [147] or, more exotically, improving the sensitivity of long-baseline telescopes [148, 149]. The challenge in implementations of path-entangled states, however, is to fulfil the requirement of optical phase stability. Another downside concerns the measurement: while it is simple to access the z-basis with a single-photon detector, it is not straightforward to measure in other bases.

In this chapter, an introduction to the generation and the displacement-based measurement of single-photon path entanglement, which allows access to other measurement bases, is given in Sec. 3.1. Furthermore, we introduce a scalable genuine multipartite entanglement witness that employs the displacement-based measurement and can be applied in distributed scenarios. This is followed by the experimental detection of genuine multipartite entanglement in Sec. 3.2, where we take advantage of the developed scalable entanglement witness. Finally, in Sec. 3.3, a scheme with two weakly pumped photon-pair sources is demonstrated to herald the distribution of bipartite single-photon path entanglement. The phase-stability requirement is solved by phase-locking a fibre interferometer with arm length of up to 1 km. In our implementation, the distance is mainly limited by the signal-to-noise ratio of the heralding photons. The publications which resulted from this work are attached in P.1 and P.2.

3.1. Single-photon path entanglement

A single-photon path-entangled state corresponds to a single photon delocalised over two or more spatial modes. The qubit state space is spanned by the vacuum and single-photon Fock state, i.e. $\{|0\rangle, |1\rangle\}$, and the parties correspond to the spatial modes, also referred to as paths. For the bipartite case, this is one of the simplest entangled states to generate, achieved by sending a heralded single photon on a 50/50 beam splitter (BS), as sketched in Fig. 3.1. The resulting state in the Fock basis is given by

$$|\psi\rangle = \frac{1}{\sqrt{2}}(\hat{a}_1^\dagger + e^{\mathrm{i}\theta_{12}}\hat{a}_2^\dagger)\,|0\rangle = \frac{1}{\sqrt{2}}\Big(\,|1\rangle_1\,|0\rangle_2 + e^{\mathrm{i}\theta_{12}}\,|0\rangle_1\,|1\rangle_2\,\Big), \tag{3.1}$$

where $\hat{a}_1^\dagger$ and $\hat{a}_2^\dagger$ are the bosonic creation operators corresponding to the spatial output modes of the BS and θ_{12} is the relative optical phase picked up by the photons in the two paths. By adding more BSs, multipartite states can easily be generated in the same manner. Therefore, single-photon path entanglement can be generated at the same high rates as single photons can be created, and by using an HSPS, the state is heralded.

In the presence of loss, i.e. $|1\rangle\langle 1| \xrightarrow{\eta} (1-\eta)\,|0\rangle\langle 0| + \eta\,|1\rangle\langle 1|$, the state will degrade. This is due to the fact that the overall vacuum state $|0\rangle\langle 0|_1 \otimes |0\rangle\langle 0|_2$ still lies within the state space. The density matrix of the state given in Eq. (3.1) after local loss channels with transmission efficiencies η_1 and η_2 is

$$|\psi\rangle\langle\psi| \xrightarrow{\eta_a,\eta_b} \rho = \frac{1}{2}\begin{pmatrix} 2-\eta_1-\eta_2 & 0 & 0 & 0 \\ 0 & \eta_2 & e^{\mathrm{i}\theta_{12}}\sqrt{\eta_1\eta_2} & 0 \\ 0 & e^{-\mathrm{i}\theta_{12}}\sqrt{\eta_1\eta_2} & \eta_1 & 0 \\ 0 & 0 & 0 & 0 \end{pmatrix}, \tag{3.2}$$

where the standard Kronecker product is applied. Here, we see that the coherence terms $\langle 01|\,\rho\,|10\rangle$ and $\langle 10|\,\rho\,|01\rangle$ scale linearly with the transmission efficiency $\sqrt{\eta_1\eta_2}$, which is an advantage over two-photon states ($\propto \eta_1\eta_2$).

Besides the simplicity of generating single-photon path-entangled states at high rates, it is not straightforward to detect this type of entanglement. In the following, we discuss the displacement-based measurement which allows access to bases other than the z-basis.

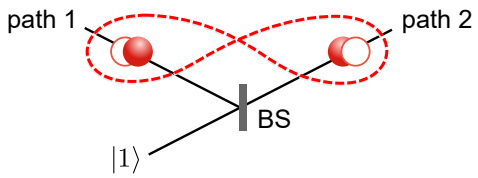

Figure 3.1.: Generation of a single-photon path-entangled state by sending a single photon to a 50/50 beam splitter (BS).

We then discuss an entanglement witness that applies this measurement together with the positive partial transpose (PPT) criterion. Further, an improved entanglement witness is presented that can detect genuine multipartite entanglement in single-photon states in a scalable way.

3.1.1. Displacement-based measurement

In order to have access to the coherence terms in a quantum state, it is necessary to measure in a complementary basis. While this is easy for e.g. polarisation qubits, it is not a straightforward task for single-photon states. However, it has been shown that local displacement operations on a single-photon path-entangled state gives access to the state's coherence and can be used to test non-locality [138]. The displacement operation is realised by interfering the input state with a coherent state on a highly imbalanced BS [150–152]. Here, we follow the description of the measurement presented in Ref. [114].

The displacement operator is defined by (see Ch. 2.3 in Ref. [122])

$$\hat{D}(\alpha) = \exp\left(\alpha\hat{a}^\dagger - \alpha^*\hat{a}\right), \tag{3.3}$$

where $\alpha = |\alpha|e^{\mathrm{i}\delta}$ is the complex displacement amplitude and $\hat{a}^\dagger$ and $\hat{a}$ are the creation and annihilation operators. By acting on the vacuum state, this operator generates a coherent state $\hat{D}(\alpha)\,|0\rangle = |\alpha\rangle = e^{-|\alpha|^2/2}\sum_n \frac{\alpha^n}{\sqrt{n!}}\,|n\rangle$ with mean photon number $\bar{n} = |\alpha|^2$. We further describe unit efficiency click detectors with the POVM elements $E_0 = |0\rangle\langle 0|$ corresponding to a no-click outcome and $E_c = \mathbb{1} - |0\rangle\langle 0|$ for a click outcome. To calculate the outcome probabilities for a general input state ρ after undergoing a displacement operation $\hat{D}(\alpha)$, we apply the Born rule and obtain

$$p_0 = \mathrm{tr}\left(\hat{D}(\alpha)\rho\hat{D}^\dagger(\alpha)\,E_0\right) = \mathrm{tr}\left(\rho\,\hat{D}^\dagger(\alpha)E_0\hat{D}(\alpha)\right), \tag{3.4}$$

$$p_c = \mathrm{tr}\left(\rho\,\hat{D}^\dagger(\alpha)E_c\hat{D}(\alpha)\right) = \mathrm{tr}\left(\rho\,\hat{D}^\dagger(\alpha)(\mathbb{1} - E_0)\hat{D}(\alpha)\right) = 1 - p_0, \tag{3.5}$$

where we used that the trace is cyclic. The POVM for the displacement-based measurement is therefore given by

$$P_0^\alpha = \hat{D}^\dagger(\alpha)E_0\hat{D}(\alpha) = |-\alpha\rangle\langle-\alpha| \tag{3.6}$$

$$P_c^\alpha = \hat{D}^\dagger(\alpha)E_c\hat{D}(\alpha) = \mathbb{1} - |-\alpha\rangle\langle-\alpha|\,, \tag{3.7}$$

where we used the property $\hat{D}^\dagger(\alpha) = \hat{D}(-\alpha)$. Moreover, if we attribute the value $+1$ to a no-click outcome and -1 to a click outcome, the observable of the displacement-based measurement is given by

$$\sigma_\alpha = P_0^\alpha - P_c^\alpha = \hat{D}^\dagger(\alpha)(2\,|0\rangle\langle 0| - \mathbb{1})\hat{D}(\alpha) = 2\,|-\alpha\rangle\langle-\alpha| - \mathbb{1}, \tag{3.8}$$

Note that for $|\alpha| = 0$ this observable becomes the Pauli matrix for the measurement along

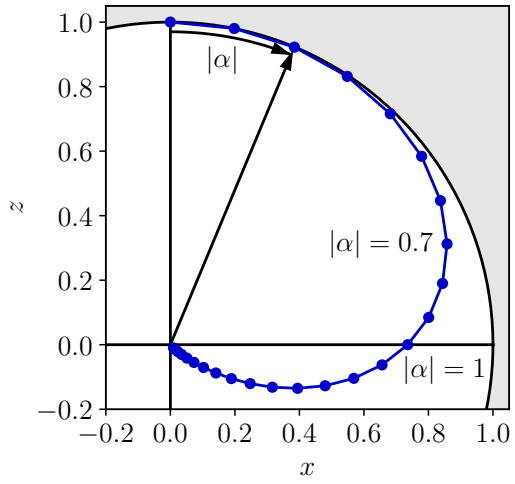

Figure 3.2.: Bloch sphere representation of the POVM element P_0^α corresponding to the no-click outcome. Here, α is assumed to be real, therefore the vector lies in the x-z plane. The blue points mark the direction of the vector for increasing $|\alpha|$ from 0 to 2.5 in steps of 0.1. The maximum component in the x direction is achieved for $|\alpha| = 1/\sqrt{2} \approx 0.7$ and the z component vanishes for $|\alpha| = 1$.

the z-axis, i.e. $\sigma_0 = \sigma_z$. This observable is the basis for what will follow to demonstrate entanglement in single-photon path-entangled states.

In order to understand σ_α better, it is instructive to have a look at the POVM element P_0^α in matrix form in the qubit subspace

$$P_0^\alpha = \begin{pmatrix} e^{-|\alpha|^2} & -\alpha^* e^{-|\alpha|^2} \\ -\alpha e^{-|\alpha|^2} & |\alpha|^2 e^{-|\alpha|^2} \end{pmatrix} = \begin{pmatrix} e^{-|\alpha|^2} & -|\alpha| e^{-|\alpha|^2 - \mathrm{i}\delta} \\ -|\alpha| e^{-|\alpha|^2 + \mathrm{i}\delta} & |\alpha|^2 e^{-|\alpha|^2} \end{pmatrix}, \tag{3.9}$$

which corresponds to a projector in the direction of

$$\vec{n} = e^{-|\alpha|^2} \begin{pmatrix} -2\,\mathrm{Re}(\alpha) \\ 2\,\mathrm{Im}(\alpha) \\ 1 - |\alpha|^2 \end{pmatrix} \tag{3.10}$$

on the Bloch sphere with the probability $(|\alpha|^2 + 1)e^{-|\alpha|^2}$, see Ref. [114] for details. A graphical representation is given in Fig. 3.2.

With the help of Eq. (3.9) and a general single-photon input state

$$\rho = \begin{pmatrix} \sin^2(\varphi) & |d| e^{-\mathrm{i}\theta} \\ |d| e^{\mathrm{i}\theta} & \cos^2(\varphi) \end{pmatrix}, \tag{3.11}$$

where $\theta \in [0, 2\pi)$, $\varphi \in [0, \frac{\pi}{2}]$ and $|d| \leq |\sin(\varphi)\cos(\varphi)|$, we can now explicitly calculate p_0

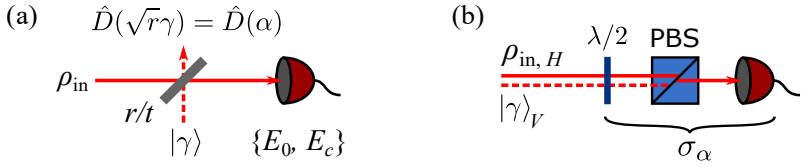

Figure 3.3.: Implementation of the displacement-based measurement. (a) Interfering the input state ρ_{in} with a coherent state $|\gamma\rangle$ on an imbalanced beam splitter with power reflectance r (transmittance $t \gg r$) implements a displacement operation with parameter $\alpha = \sqrt{r}\gamma$. The output is then detected by a click detector described by the POVM $\{E_0, E_c\}$. (b) The same measurement can be implemented in a tunable manner by using orthogonal linear polarisation states ($\rho_{\text{in},H}$ and $|\gamma\rangle_V$) and rotating them with a half-wave plate (HWP) before projecting onto horizontal polarisation by means of a polarising beam splitter (PBS) or polariser.

from Eq. (3.4) and obtain

$$p_0 = \text{tr}(\rho\, P_0^\alpha) = e^{-|\alpha|^2}\big(\sin^2(\varphi) + |\alpha|^2\cos^2(\varphi) - 2|\alpha||d|\cos(\delta-\theta)\big). \tag{3.12}$$

We see that this outcome probability varies as a function of the phase difference between the displacement field (phase δ) and the coherence term of the single-photon state (phase θ). Hence, the amplitude $2|\alpha||d|$, and thus information on the coherence, can be extracted by measuring p_0 and varying the phase of the displacement field, given the displacement amplitude is well known.

There are still two open questions at this point: first, how can we perform such a displacement-based measurement experimentally and second, is it enough to only consider the case of a unit efficiency detector or do we need a more general POVM which replaces $\{E_0, E_c\}$?

To answer the first question, we notice that by inputting a coherent state $|\gamma\rangle$ to a BS, we have $|\alpha\rangle = |\sqrt{r}\gamma\rangle$ in the reflected output port, where r is the reflectance of the BS. Therefore, by sending the input state ρ_{in} to the other input port and using a highly imbalanced BS with $t \gg r$, the transmitted state is displaced, i.e. $\hat{D}(\alpha)\rho_{\text{in},t}\hat{D}^\dagger(\alpha)$, as shown in Fig. 3.3(a). The displacement-based measurement is then completed by detecting the output mode with a click detector. An equivalent implementation, shown in Fig. 3.3(b), can be obtained if the input state and the coherent state co-propagate in the same spatial mode, but in different orthogonal linear polarisation modes. Using a half-wave plate (HWP) and a polarising element, the two orthogonal input modes are projected on the same output mode where the transmission can be tuned by rotating the HWP.

The second question can be answered twofold. Either, the non-unit detector efficiency η_d is taken into account and treated separately by replacing $\{E_0, E_c\}$ with $\{(1-\eta_d)^{\hat{a}^\dagger\hat{a}}, \mathbb{1} - (1-\eta_d)^{\hat{a}^\dagger\hat{a}}\}$ as done in Sec. 2.3.1 and discussed in Ref. [114] or, more conservatively, the detector inefficiency is considered as loss on the state. To see that this can be done, we have a look at no-click outcome probability of a general input state ρ_a after undergoing the displacement operation $\hat{D}_a(\alpha) = e^{\alpha\hat{a}^\dagger - \alpha^*\hat{a}}$ followed by a loss channel with efficiency η_d.

We describe the loss channel by the beam splitter unitary operator $\hat{U} = e^{\xi(\hat{a}^\dagger \hat{c} - \hat{a}\hat{c}^\dagger)}$, where $\hat{c}$ and $\hat{c}^\dagger$ are the annihilation and creation operator of the auxiliary mode and $\eta_d = \cos^2(\xi)$. The no-click outcome probability then is

$$\begin{aligned} p_0 &= \mathrm{tr}\left(\mathrm{tr}_c\{\hat{U}(\hat{D}_a(\alpha)\rho_a\hat{D}_a^\dagger(\alpha)\otimes|0\rangle\langle 0|_c)\hat{U}^\dagger\}\ |0\rangle\langle 0|_a\right) \\ &= \mathrm{tr}\left(\hat{U}\hat{D}_a(\alpha)(\rho_a\otimes|0\rangle\langle 0|_c)\hat{D}_a^\dagger(\alpha)\hat{U}^\dagger\ |0\rangle\langle 0|_a\otimes\mathbb{1}_c\right) \\ &= \mathrm{tr}\left(\hat{D}_c\big(\alpha\sqrt{1-\eta_d}\big)\hat{D}_a(\alpha\sqrt{\eta_d})\hat{U}(\rho_a\otimes|0\rangle\langle 0|_c)\hat{U}^\dagger\hat{D}_a^\dagger(\alpha\sqrt{\eta_d})\hat{D}_c^\dagger\big(\alpha\sqrt{1-\eta_d}\big)\ |0\rangle\langle 0|_a\otimes\mathbb{1}_c\right) \\ &= \mathrm{tr}\Big(\underbrace{\mathrm{tr}_c\{\hat{U}(\rho_a\otimes|0\rangle\langle 0|_c)\hat{U}^\dagger\}}_{\rho_a^{\mathrm{loss}}}\hat{D}_a^\dagger(\alpha\sqrt{\eta_d})\ |0\rangle\langle 0|_a\,\hat{D}_a(\alpha\sqrt{\eta_d})\Big) \end{aligned} \tag{3.13}$$

where we used that the trace is cyclic, applied the definition of the partial trace in the second and fourth lines and in the third line we made use of the proposition 3.35 [1] in Ref. [153]. The last line corresponds to first acting with the loss channel on the input state ρ_a and then displacing the lossy state with a reduced displacement parameter $\alpha\sqrt{\eta_d}$. Thus, it is possible to keep the introduced POVM $\{E_0, E_c\} = \{|0\rangle\langle 0|, \mathbb{1} - |0\rangle\langle 0|\}$ describing a unit-efficiency click detector and treating the detection loss as loss on the state before the displacement operation.

3.1.2. Bipartite entanglement witness using the PPT criterion

Building upon the displacement-based measurement we construct an entanglement witness which is then used in Sec. 3.3 to certify the bipartite entanglement of our path-entangled state. To start with, we consider two spatial modes $i = 1, 2$, where we can measure the observable $\sigma_{\alpha_i}^{(i)}$ as defined in Eq. (3.8). We then define the operator

$$\hat{\mathcal{W}} = \sigma_{\alpha_1}^{(1)}\otimes\sigma_{\alpha_2}^{(2)} = (P_0^{\alpha_1} - P_c^{\alpha_1})\otimes(P_0^{\alpha_2} - P_c^{\alpha_2}) \tag{3.14}$$

and, by assuming that from experimental run to run the global phase of the displacement parameters α_1 and α_2 are arbitrary (which we guarantee in our implementations), we actually measure the phase-averaged observable

$$\begin{aligned} \hat{W} &= \frac{1}{2\pi}\int_0^{2\pi}\mathrm{d}\phi\Big(e^{\mathrm{i}\phi\sum_{i=1}^2\hat{a}_i^\dagger\hat{a}_i}\Big)\hat{\mathcal{W}}\Big(e^{-\mathrm{i}\phi\sum_{i=1}^2\hat{a}_i^\dagger\hat{a}_i}\Big) \\ &= P_{00}^{\alpha_1\alpha_2} - P_{0c}^{\alpha_1\alpha_2} - P_{c0}^{\alpha_1\alpha_2} + P_{cc}^{\alpha_1\alpha_2}, \end{aligned} \tag{3.15}$$

where we introduced the bipartite phase-averaged POVM elements $P_{kl}^{\alpha_1\alpha_2}$ corresponding to the outcome kl with $k, l \in \{0, c\}$. This phase-averaging puts all coherence terms between

1. As a consequence we have the relation $e^X e^Y e^{-X} = e^{Y+[X,Y]+\frac{1}{2!}[X,[X,Y]]+\dots} = e^{Y+\sum_{n=1}^\infty\frac{1}{n!}[X^{(n)},Y]}$, where $[X^{(n)}, Y] = [X,[X,[\dots[X,Y]]$ denotes the nested commutator where X occurs n times. In our case of $X = \xi(a^\dagger c - c^\dagger a)$ and $Y = (\alpha a^\dagger - \alpha^* a)$, we obtain $[X^{(2n)}, Y] = (-\xi^2)^n(\alpha a^\dagger - \alpha^* a)$ and $[X^{(2n+1)}, Y] = -\xi(-\xi^2)^n(\alpha c^\dagger - \alpha^* c)$. Together with the series definitions of $\sin(\xi)$ and $\cos(\xi)$ we end up with $e^X e^Y e^{-X} = \hat{U}\hat{D}_a(\alpha)\hat{U}^\dagger = \hat{D}_c(-\alpha\sin\xi)\hat{D}_a(\alpha\cos\xi)$ and with $\cos(\xi) = \sqrt{\eta_d}$ the equality $\hat{U}\hat{D}_a(\alpha) = \hat{D}_c(\alpha\sqrt{1-\eta_d})\hat{D}_a(\alpha\sqrt{\eta_d})\hat{U}$ follows.

basis states with different total photon number in $\hat{\mathcal{W}}$ to 0.

In order to obtain an intuition about this observable, we have a look at its matrix representation in the two-qubit subspace

$$\hat{W}_{\text{qubit}} = \begin{pmatrix} f(\alpha_1)f(\alpha_2) & 0 & 0 & 0 \\ 0 & f(\alpha_1)h(\alpha_2) & g(\alpha_1)^* g(\alpha_2) & 0 \\ 0 & g(\alpha_1)g(\alpha_2)^* & h(\alpha_1)f(\alpha_2) & 0 \\ 0 & 0 & 0 & h(\alpha_1)h(\alpha_2) \end{pmatrix}, \tag{3.16}$$

where we defined

$$f(\alpha) = 2e^{-|\alpha|^2} - 1, \qquad g(\alpha) = 2\alpha e^{-|\alpha|^2}, \qquad h(\alpha) = 2|\alpha|^2 e^{-|\alpha|^2} - 1. \tag{3.17}$$

Note that for the experimentally relevant case of $|\alpha| = \sqrt{\ln 2} \approx 0.83$ we simply have $f(\alpha) = 0$, $g(\alpha) = \alpha$ and $h(\alpha) = |\alpha|^2 - 1$. It becomes obvious that $\hat{W}_{\text{qubit}}$ is a natural candidate to detect a single-photon path-entangled state, since the only remaining coherence terms are the ones between $|01\rangle$ and $|10\rangle$. The expectation value when measuring the lossy bipartite path-entangled state ρ introduced in Eq. (3.2) is then

$$\begin{aligned} \text{tr}\left(\rho\, \hat{W}_{\text{qubit}}\right) = &\left(1 - \frac{\eta_1}{2} - \frac{\eta_2}{2}\right) f(\alpha_1)f(\alpha_2) + \frac{\eta_2}{2} f(\alpha_1)h(\alpha_2) + \frac{\eta_1}{2} h(\alpha_1)f(\alpha_2) \\ &+ 8\frac{\sqrt{\eta_1\eta_2}}{2} |\alpha_1||\alpha_2| e^{-|\alpha_1|^2 - |\alpha_2|^2} \cos(\theta_{12} - (\delta_2 - \delta_1)), \end{aligned} \tag{3.18}$$

where we again defined $\alpha_1 = |\alpha_1| e^{\mathrm{i}\delta_1}$ and $\alpha_2 = |\alpha_2| e^{\mathrm{i}\delta_2}$. We see that the last term ($\propto \sqrt{\eta_1\eta_2}$), which comes from the coherence terms in ρ, is varying as a function of the phase term $\theta_{12} - (\delta_2 - \delta_1)$. This term can be probed by varying the phase difference between the displacement parameters $\delta_2 - \delta_1$. It also becomes clear, that the coherence terms of the state can only be fully retrieved if the difference between the path-entangled state's phase difference θ_{12} and the one of the displacement parameters $\delta_2 - \delta_1$ does not fluctuate during the measurement. If the state is generated directly by sending a single photon to one or several BSs, the phase stability can be guaranteed by co-propagating the coherent state used for the displacement operation in the orthogonal polarisation mode and then implementing the measurement as depicted in Fig. 3.3(b).

In order to demonstrate entanglement, we use the Peres-Horodecki criterion [154, 155], which states that if the bipartite state ρ is separable, then all the eigenvalues of its partial transpose ρ^{T_1} are non-negative. This criterion is also referred to as the positive partial transpose (PPT) criterion, where the partial transpose of a state $\rho = \sum_{ijkl} c_{ijkl} \left|i\right\rangle\!\left\langle j\right|_1 \otimes \left|k\right\rangle\!\left\langle l\right|_2$ is defined as

$$\rho^{T_1} = (T \otimes I)(\rho) = \sum_{ijkl} c_{ijkl} (\left|i\right\rangle\!\left\langle j\right|_1)^T \otimes \left|k\right\rangle\!\left\langle l\right|_2 = \sum_{ijkl} c_{jikl} \left|i\right\rangle\!\left\langle j\right|_1 \otimes \left|k\right\rangle\!\left\langle l\right|_2 . \tag{3.19}$$

If $\rho^{T_1} \geq 0$, it corresponds to a physical state, also referred to as the PPT state. In

the case of a qubit-qubit or qubit-qutrit system, the PPT criterion is not only necessary but also sufficient, i.e. if all eigenvalues ρ^{T_1} are non-negative, then ρ is separable [155]. Or formulated differently, if ρ^{T_1} has at least one negative eigenvalue, then ρ is entangled. Using the observable $\hat{W}$ together with the knowledge of the diagonal elements of the density matrix from a z-basis measurement, we can calculate the maximum expectation value for a separable two-qubit state ρ_{qubit}

$$\begin{aligned} w_{\text{ppt}} = \max_{\rho_{\text{qubit}}} \operatorname{tr}\left(\rho_{\text{qubit}}\hat{W}\right) \\ \text{such that} \quad (i)\ (\rho_{\text{qubit}})^{T_1} \geq 0, \\ (ii)\ (\rho_{\text{qubit}})_{ii} = p_{ii}. \end{aligned} \tag{3.20}$$

The condition (i) imposes the separability on ρ_{qubit} and (ii) ensures that we use all our knowledge of the diagonal elements of the density matrix. This is equivalent to considering an optimised witness constructed from all possible linear combinations of $\sigma_{\alpha_1}^{(1)} \otimes \sigma_{\alpha_2}^{(2)}$, $\sigma_0^{(1)} \otimes \sigma_0^{(2)}$, $\sigma_0^{(1)} \otimes \mathbb{1}$ and $\mathbb{1} \otimes \sigma_0^{(2)}$, which can detect more entangled states than a fixed linear combination. If we restrict ourselves to qubit states, the probabilities p_{ii} are given by the measured quantities $p_{00} = p_{00}$, $p_{11} = p_{0c}$, $p_{22} = p_{c0}$ and $p_{33} = p_{cc}$ without displacement fields. If the measured value of $\langle\hat{W}\rangle$ is larger than w_{ppt}, we can make the conclusion that our qubit state is entangled, also referred to as a witness violation. Explicitly, the bound is given by

$$\begin{aligned} w_{\text{ppt}} = p_{00}\, f(\alpha_1)f(\alpha_2) + p_{0c}\, f(\alpha_1)h(\alpha_2) + p_{c0}\, h(\alpha_1)f(\alpha_2) \\ + p_{cc}h(\alpha_1)h(\alpha_2) + \sqrt{p_{00}p_{cc}}\,(g(\alpha_1)g(\alpha_2)^* + g(\alpha_1)^* g(\alpha_2)). \end{aligned} \tag{3.21}$$

In an experiment, first we might encounter varying displacement amplitudes over the measurement duration due to power drifts of the lasers which generate the displacement field. Second, we must not assume that the state is a qubit state since, with a low probability, the source might produce multi-photon states. The first problem is tackled by tracking the displacement amplitude and taking this into account when calculating w_{ppt} according to Eq. (3.20) which leads to $\widetilde{w}_{\text{ppt}} \geq w_{\text{ppt}}$. To mitigate the effect, we choose the mean displacement amplitudes such that $\partial^2 w_{\text{ppt}}/\partial\alpha_1\alpha_2 = 0$ which is achieved for $|\alpha_1| = |\alpha_2| \approx 0.83$. Regarding the second point, we remove the assumption on the state dimension by experimentally bounding the contributions from outside the qubit subspace and adding them to the separable bound $\widetilde{w}_{\text{ppt}}$ (for the derivation see Sec. III in the Supplemental Material of P.1)

$$\begin{aligned} w_{\text{ppt}}^{\max} = \widetilde{w}_{\text{ppt}} + p_1^* + p_2^* \\ + 4|\alpha_1||\alpha_2|e^{-|\alpha_1|^2-|\alpha_2|^2}\sqrt{2(|\alpha_1|^4 + |\alpha_2|^4)(p_1^* + p_2^*)(1 - p_1^* - p_2^*)} \end{aligned} \tag{3.22}$$

where p_i^* denotes the upper bound on the probability of having more than one photon in mode $i \in \{1, 2\}$. The latter can be bounded in practice by measuring twofold coincidences after a 50/50 BS or with a PNR detector. In the case of a 50/50 BS, we can calculate the

twofold coincidence probability in mode i after the BS

$$p_{\text{coinc}}^{(i)} = \sum_{n=2}^{\infty} \Big(1 - \frac{1}{2^{n-1}}\Big) p_n^{(i)} \geq \frac{1}{2} \sum_{n=2}^{\infty} p_n^{(i)} \quad \Rightarrow \quad p_i^* = 2p_{\text{coinc}}^{(i)} \geq \sum_{n=2}^{\infty} p_n^{(i)}, \tag{3.23}$$

where $p_n^{(i)}$ is the probability of having n photons in mode i before the 50/50 BS.

We can therefore make the conclusion that an arbitrary state ρ is entangled if the measured expectation value of the witness is larger than the maximum PPT bound

$$w_\rho^{\text{exp}} = p_{00}^{\alpha_1\alpha_2} - p_{0c}^{\alpha_1\alpha_2} - p_{c0}^{\alpha_1\alpha_2} + p_{cc}^{\alpha_1\alpha_2} > w_{\text{ppt}}^{\max}. \tag{3.24}$$

3.1.3. Analytical genuine multipartite entanglement witness

So far we have considered bipartite single-photon path-entangled states and discussed a witness to detect this entanglement. Now we want to generalise this to multipartite single-photon path-entangled states, that is an equal superposition of the photon being in one of the N parties, which can be described by the W state [156]

$$|W_N\rangle = \frac{1}{\sqrt{N}} \sum_{i=1}^{N} |0_1, ..., 0_{i-1}, 1_i, 0_{i+1}, ..., 0_N\rangle \,. \tag{3.25}$$

In Ref. [83], a fidelity-based entanglement witness of the form $(2^N |W_N\rangle\langle W_N| - \mathbb{1})$ is presented and approximated by the operator

$$\hat{\mathcal{Z}} = \sum_{m=1}^{N} (N - 2m)\sigma_0^{\otimes m} \otimes \mathbb{1}^{\otimes(N-m)} + 4 \sum_{m=0}^{N-2} \sigma_0^{\otimes m} \otimes \mathbb{1}^{\otimes(N-m-2)} \otimes \sigma_\alpha \otimes \sigma_\alpha + \text{ sym.}, \tag{3.26}$$

where "sym." includes all terms corresponding to permutations of parties. The separable bound is then calculated by considering an N-qubit state ρ_{qubit} that has a PPT with respect to a single party, i.e. $(\rho_{\text{qubit}})^{T_1} \geq 0$, and maximising the expectation values of the witness over all such states. This maximisation problem can be solved efficiently with semi-definite programming techniques, however, is still limited to a few tens of parties due to the size of the $2^N \times 2^N$ density matrix. Contributions from outside the N-qubit subspace need to bounded and added to the separable bound, like in the two-qubit case. Further, the number of measurements settings to estimate the phase averaged expectation value of $\hat{\mathcal{W}}$ scales quadratically $(N^2/2 - N/2 + 1)$ with the number of parties N (1 setting for the first term in Eq. (3.26) corresponding to $\sigma_0^{\otimes N}$ and $N(N-1)/2$ settings for the rest). Especially, the witness includes terms which require measuring two parties with displacement $\sigma_\alpha \otimes \sigma_\alpha$ and the rest of the parties in the z-basis $\sigma_0^{\otimes N-2}$ which is not straightforward to implement in the case the single-photon and coherent states co-propagate in orthogonal polarisation modes.

An improved multipartite entanglement witness

Here, we develop a witness to reveal genuine multipartite single-photon path entanglement building upon the displacement-based measurement, that eliminates the shortcomings of the witness in Ref. [83]. First, the measurement settings for our witness is reduced to a constant number of $2+$ the setting to estimate the probability of having two or more photons in the state, which eases the experiment for many parties N enormously. Second, the two measurement settings which are required are global measurements, that is, either measuring all parties in the z-basis or with the displacement operation, but no combinations thereof. Third and last, the separable bound is calculated analytically without the help of the PPT criterion which is achieved by reducing the analysis to the subspace containing one photon at maximum and bounding the contributions from outside this subspace. This leads to an eigenvalue problem of an $N \times N$ matrix, which can be computed efficiently and presents a vast improvement compared to the previous witness, where a semi-definite programming problem for a $2^N \times 2^N$ density matrix has to be solved.

As a multipartite extension of the bipartite operator given in Eq. (3.14), we see that

$$\hat{\mathcal{O}}_{\vec{\alpha}} = \sum_{i \neq j} \sigma_{\alpha_i}^{(i)} \otimes \sigma_{\alpha_j}^{(j)} \otimes \mathbb{1}_{\neg\{i,j\}}^{\otimes(N-2)} \tag{3.27}$$

picks up all the coherence terms $|0_i, 1_j\rangle\langle 1_i, 0_j| + h.c.$ in the state $|W_N\rangle$ and is therefore a good candidate to witness the entanglement. Here, we introduced the vector describing the local displacement parameters $\vec{\alpha} = (\alpha_1, ..., \alpha_N)$ and the term $\mathbb{1}_{\neg\{i,j\}}^{\otimes(N-2)}$ which is the tensor product of identity operators in all modes except modes i and j. Again, we consider the experimentally relevant case where the displacement parameters are not phase-locked to the input state and thus the displacement parameters are only defined up to an arbitrary global phase $e^{\mathrm{i}\phi}\vec{\alpha}$, leading to the phase averaged operator

$$\hat{O}_{\vec{\alpha}} = \frac{1}{2\pi} \int_0^{2\pi} \mathrm{d}\phi \Big(e^{\mathrm{i}\phi \sum_{i=1}^N \hat{a}_i^\dagger \hat{a}_i} \Big) \hat{\mathcal{O}}_{\vec{\alpha}} \Big(e^{-\mathrm{i}\phi \sum_{i=1}^N \hat{a}_i^\dagger \hat{a}_i} \Big), \tag{3.28}$$

which acts orthogonally on subspaces with different total photon numbers $n = \langle \sum_{i=1}^N \hat{a}_i^\dagger \hat{a}_i \rangle$ and therefore we can write it as a direct sum $\hat{O}_{\vec{\alpha}} = \bigoplus_{n=0}^{\infty} \hat{O}_{\vec{\alpha}}^{(n)}$.

Since $\hat{O}_{\vec{\alpha}} = \hat{O}_{\vec{\alpha}}^{n\leq 1} \oplus \hat{O}_{\vec{\alpha}}^{n\geq 2}$ is also sensitive to higher photon number contributions $n \geq 2$, which are not part of the target state, we need to make sure that such contributions in a state cannot increase the expectation value of our witness. To this end, we define in mode i the local projector on all states with two or more photons $\hat{\Pi}_{n\geq 2}^{(i)} = \sum_{n\geq 2} |n_i\rangle\langle n_i|$ and the POVM element $E_{n\geq 2}$ corresponding to the probability of having an outcome where $n \geq 2$ detectors click when measuring in the z-basis. With $\hat{\Pi}_{n\geq 2}$ we further denote the projector on all combinations of Fock states containing at least two photons in total and see that

the following inequality holds

$$\hat{\Pi}_{n\geq 2} \leq E_{n\geq 2} + \sum_{i=1}^{N} \hat{\Pi}^{(i)}_{n\geq 2}. \tag{3.29}$$

Hence, the term on the right-hand side, which can be experimentally accessed, upper-bounds the probability of having $n \geq 2$ photons in the state. For the expected state close to $|W_N\rangle$, we have $\mathrm{tr}\left(\rho\,\hat{\Pi}_{n\geq 2}\right) \approx 0$ and since the operator norm $||\hat{O}_{\vec{\alpha}}|| \leq N(N-1)$ and $||\hat{\Pi}_{n\geq 2}|| = 1$, we can bound

$$\hat{O}_{\vec{\alpha}} - N(N-1)\hat{\Pi}_{n\geq 2} = \hat{O}^{n\leq 1}_{\vec{\alpha}} \oplus \underbrace{(\hat{O}^{n\geq 2}_{\vec{\alpha}} - N(N-1)\hat{\Pi}_{n\geq 2})}_{\leq 0} \leq \hat{O}^{n\leq 1}_{\vec{\alpha}} \tag{3.30}$$

by an operator supported on a subspace with one photon at most. We now define our witness

$$\begin{aligned}
\hat{W}_{\vec{\alpha}} &= \hat{O}_{\vec{\alpha}} + M_{n\leq 1} - N(N-1)\hat{\Pi}_{n\geq 2} - \mu E_{n\geq 2} && (3.31)\\
&= \left(\hat{O}^{n\leq 1}_{\vec{\alpha}} + M_{n\leq 1}\right) \oplus \left(\hat{O}^{n\geq 2}_{\vec{\alpha}} - N(N-1)\hat{\Pi}_{n\geq 2} - \mu E_{n\geq 2}\right) && (3.32)\\
&\overset{(3.30)}{\leq} \left(\hat{O}^{n\leq 1}_{\vec{\alpha}} + M_{n\leq 1}\right) \oplus (-\mu E_{n\geq 2}) = \widetilde{W}_{\vec{\alpha}}, && (3.33)
\end{aligned}$$

where μ is a positive real parameter that one can tune to penalise states which contain more than one photon in total and $M_{n\leq 1}$ an operator in the sector with not more than one photon which we define by

$$M_{n\leq 1} = \lambda\,|\bar{0}\rangle\langle\bar{0}| - \sum_{i\neq j} f(\alpha_i)f(\alpha_j)\Big(\,|\bar{0}\rangle\langle\bar{0}| + \sum_{k\neq i,j} |1_k\rangle\langle 1_k|\,\Big). \tag{3.34}$$

Here, $|\bar{0}\rangle$ denotes the vacuum state in all involved modes, $|1_k\rangle = a_k^\dagger\,|\bar{0}\rangle$ the state with one photon in mode k and vacuum elsewhere, λ is another positive real parameter that one can tune and $f(\alpha)$ the function as defined in Eq. (3.17). The operator $M_{n\leq 1}$ is chosen such that

$$\begin{aligned}
\hat{O}^{n\leq 1}_{\vec{\alpha}} + M_{n\leq 1} = \lambda\,|\bar{0}\rangle\langle\bar{0}| + \sum_{i\neq j}\Big(&g(\alpha_i)g(\alpha_j)^*\,|1_i\rangle\langle 1_j| + g(\alpha_i)^*g(\alpha_j)\,|1_j\rangle\langle 1_i|\\
&+ h(\alpha_i)f(\alpha_j)\,|1_i\rangle\langle 1_i| + f(\alpha_i)h(\alpha_j)\,|1_j\rangle\langle 1_j|\,\Big).
\end{aligned} \tag{3.35}$$

This expression picks up exactly the coherence terms in $|W_N\rangle$ and λ allows the optimisation of the weight of the projection on the overall vacuum. Again, $g(\alpha)$ and $h(\alpha)$ are the functions as defined in Eq. (3.17).

We note that in the experiment we can access $\hat{W}_{\vec{\alpha}}$ as defined in Eq. (3.31), whereas for the calculation of the separable bound we make use of $\widetilde{W}_{\vec{\alpha}}$ from Eq. (3.33), which will simplify the calculations enormously.

Calculation of the separable bound

We now calculate the biseparable bound, i.e. the maximum expectation value that our witness takes on any biseparable state

$$w_{\text{bisep}} = \max_{\varrho_{\text{bisep}}} \operatorname{tr}\left(\varrho_{\text{bisep}} \hat{W}_{\vec{\alpha}}\right). \tag{3.36}$$

where a general biseparable state is a mixture of product states on some bipartitions (partitions of all modes into two groups G_1 and G_2). Explicitly, it is defined by

$$\varrho_{\text{bisep}} = \sum_{G_1|G_2} p(G_1|G_2)\rho_{G_1|G_2}, \tag{3.37}$$

where the sum runs over all partitions $G_1|G_2$ of the N parties with $G_1 \cup G_2 = \{1, 2, \ldots, N\}$ and $G_1 \cap G_2 = \emptyset$. The probabilities of different partitions are normalised $\sum_{G_1|G_2} p(G_1|G_2) = 1$ and $\rho_{G_1|G_2}$ is a separable state with respect to the partition $G_1|G_2$. We note that since the set of biseparable states is convex, the maximum value that an observable takes on any biseparable state ϱ_{bisep}, including mixed states, is attained for a pure state $|\Psi\rangle = |\Psi_1\rangle_{G_1} |\Psi_2\rangle_{G_2}$ on some partition. Together with Ineq. (3.33), we get

$$w_{\text{bisep}} = \max_{G_1,G_2,|\Psi\rangle} \langle\Psi| \hat{W}_{\vec{\alpha}} |\Psi\rangle \leq \max_{G_1,G_2,|\Psi\rangle} \langle\Psi| \widetilde{W}_{\vec{\alpha}} |\Psi\rangle . \tag{3.38}$$

Since operator $\widetilde{W}_{\vec{\alpha}}$ is block diagonal, and its restriction to the sector with two or more photons $-\mu E_{n\geq 2}$ is negative, we can restrict the maximisation to states $|\Psi_k\rangle_{G_k}$ which contain one photon at most, that is without loss of generality

$$|\Psi_k\rangle_{G_k} = \cos(\theta_k) |\bar{0}\rangle_{G_k} + \sin(\theta_k) \sum_{i=1|j_i\in G_k}^{|G_k|} v_i^{(k)} a_{j_i}^\dagger |\bar{0}\rangle_{G_k} , \tag{3.39}$$

where we introduced the parameter θ_k and the normalised vector $\vec{v}^{(k)} \in \mathbb{C}^{|G_k|}$. To simplify the notation, lets define $s_k = \sin(\theta_k)$, $c_k = \cos(\theta_k)$, $\vec{v}^{(1)} = \vec{v}$ and $\vec{v}^{(2)} = \vec{w}$. The biseparable state can then be written as

$$\begin{aligned} |\Psi\rangle = c_1 c_2 |\bar{0}\rangle + s_1 s_2 \sum_{i\in G_1} \sum_{j\in G_2} v_i w_j |1_i\rangle_{G_1} |1_j\rangle_{G_2} \\ + s_1 c_2 \sum_{i\in G_1} v_i |1_i\rangle_{G_1} + c_1 s_2 \sum_{j\in G_2} w_j |1_j\rangle_{G_2} . \end{aligned} \tag{3.40}$$

By defining a vector $\vec{L} = \begin{pmatrix} c_1 s_2 \vec{w} \\ s_1 c_2 \vec{v} \end{pmatrix}$ we end up with a compact expression for the upper

bound on the expectation value that our witness can take for any biseparable state

$$\begin{aligned}\langle\Psi|\,\widetilde{W}_{\vec{\alpha}}\,|\Psi\rangle &= \lambda c_1^2 c_2^2 - \mu s_1^2 s_2^2 + \vec{L}^T \underbrace{\begin{pmatrix} M_w & M_c \\ M_c^T & M_v \end{pmatrix}}_{M} \vec{L} \\ &= \begin{pmatrix} s_2\vec{w} \\ c_2\vec{v} \end{pmatrix}^T \underbrace{\begin{pmatrix} c_1^2 M_w - s_1^2\mu\mathbb{1} & c_1 s_1 M_c \\ c_1 s_1 M_c^T & M_v + c_1^2\lambda\mathbb{1} \end{pmatrix}}_{\mathbb{M}(\lambda,\mu,\vec{\alpha},\theta_1)} \begin{pmatrix} s_2\vec{w} \\ c_2\vec{v} \end{pmatrix},\end{aligned} \tag{3.41}$$

where λ and μ are the witness parameters as defined in Eqs. (3.31, 3.34). By arranging the entries of the matrix M according to the defined bipartition (M_v corresponds to G_1 and M_w to G_2), we can explicitly write down the diagonal matrix elements $M_{ii} = 2\sum_{k\neq i} f(\alpha_k)h(\alpha_i)$ and the off-diagonal elements $M_{ij} = 2g(\alpha_i)g(\alpha_j)^*$ with the functions f, g and h as defined in Eq. (3.17). Finally, we can reduce Eq. (3.41) to a single parameter eigenvalue problem

$$\langle\Psi|\,\widetilde{W}_{\vec{\alpha}}\,|\Psi\rangle \leq \widetilde{w}_{G_1,G_2} = \max_{\theta_1\in[0,2\pi]} (\max \mathrm{eig}(\mathbb{M}(\lambda,\mu,\vec{\alpha},\theta_1))) \tag{3.42}$$

and obtain the separable bound according to Eq. (3.38)

$$w_{\mathrm{bisep}} \leq \widetilde{w}_{\mathrm{bisep}} = \max_{G_1,G_2} (\widetilde{w}_{G_1,G_2}). \tag{3.43}$$

Thus, if a state exceeds this bound, i.e. $\mathrm{tr}\left(\rho\,\hat{W}_{\vec{\alpha}}\right) > \widetilde{w}_{\mathrm{bisep}}$, we can make the conclusion that the state ρ can not be written in the biseparable form as defined in Eq. (3.37) and is therefore genuinely multipartite entangled.

Estimating the witness

In reality, the displacement parameters $\vec{\alpha}$ can fluctuate, e.g. due to power drifts and fluctuations of the generating lasers, and the range needs to be experimentally bounded $\vec{\alpha} \in A$. This impacts the measured and calculated values in the following way. The expectation value of the witness $\hat{W}_{\vec{\alpha}}$ on a state ρ depends on $\vec{\alpha}$ directly through the term $\hat{O}_{\vec{\alpha}}$, which is obtained from the measurement with displacement on all modes, as well as algebraically through the term $M_{n\leq 1}$ where the knowledge of $\vec{\alpha}$ together with the outcomes of the measurement in the z-basis is needed. Furthermore, the separable bound calculated from the maximum eigenvalue of the matrix $\mathbb{M}(\lambda,\mu,\vec{\alpha},\theta_1)$ also depends on $\vec{\alpha}$.

To ensure that those effects do not lead to false violations of the witness, we consider the worst-case scenario for the bound

$$w_{\mathrm{bisep}}^{\max} = \max_{\vec{\alpha}\in A} \left(\widetilde{w}_{\mathrm{bisep}}(\vec{\alpha})\right). \tag{3.44}$$

Then, defining the operator $\overline{W}_{\vec{\alpha}}$, where $M_{n\leq 1}$ is replaced by $\bar{M}_{n\leq 1} = \min_{\vec{\alpha}\in A}(M_{n\leq 1}(\vec{\alpha}))$ in the witness $\hat{W}_{\vec{\alpha}}$ as defined in Eq. (3.31), implies

$$\hat{W}_{\vec{\alpha}} - w_{\text{bisep}} \geq \overline{W}_{\vec{\alpha}} - w_{\text{bisep}}^{\max}. \tag{3.45}$$

To prove genuine multipartite entanglement in a state ρ, it suffices to show that, over all measurement rounds with fluctuating $\vec{\alpha}$, the average expectation value of $w_\rho^{\text{exp}} = \langle \overline{W}_{\vec{\alpha}} \rangle$ exceeds the constant $w_{\text{bisep}}^{\max}$. In Appendix C of P.2, we show that $\langle \overline{W}_{\vec{\alpha}} \rangle$ can be estimated by combining the average values of three different observables measured independently in different runs of the experiment:

$$\overline{W}_{\vec{\alpha}} = \hat{O}_{\vec{\alpha}} + \mathcal{Z} - N(N-1)\Sigma_{n\geq 2} \tag{3.46}$$

with

- $\hat{O}_{\vec{\alpha}}$, as defined in Eq. (3.28), measured with displacement operations on all modes,
- $\mathcal{Z} = \lambda \left|\bar{0}\right\rangle\!\left\langle\bar{0}\right| - \sum_{i\neq j} \max\{0, \max_{\vec{\alpha}\in A} f(\alpha_i) f(\alpha_j)\} \left|00\right\rangle\!\left\langle 00\right|_{ij} - (N(N-1)+\mu)E_{n\geq 2}$, measured without displacement operations and one detector per mode, but with the knowledge about the displacement amplitudes,
- $\Sigma_{n\geq 2} = \sum_i \Pi_{n_i\geq 2}^{(i)}$, measured on a single mode with a 50/50 BS and two detectors (see Eq. (3.23)) or a PNR detector.

Finally, in Appendix D of P.2 we analyse the statistical significance of the observed violation of the witness. To this end, we make use of Hoeffding's theorem (1963) [157] to upper bound the p-value for the null-hypothesis that the state ρ is biseparable.

Scaling of the improved multipartite witness

A few words are prudent on how the presented witness scales as a function of the number of parties N. First, we stress that the witness only requires three measurement settings, independent of N. In the case where PNR detectors are used, this could even be reduced to two settings, one with displacement and one without. However, the displacement amplitude also needs to be known and bounded, which can be done in a separate additional measurement setting. Still, this represents a vast improvement compared to the witness in Ref. [83], which scales polynomially in N, and is in sharp contrast to state tomography, which scales exponentially in N. That being said, state tomography fully reconstructs the density matrix and can therefore not be compared with our entanglement witness in terms of knowledge about the state.

Second, an important aspect which can limit the application of the witness to large N is the computational resources needed for the calculation of the separable bound. Our method is based on the computation of the maximum eigenvalue of an $N \times N$ matrix, which scales polynomially in N and can therefore be efficiently computed, for each bipartition of the N parties in two groups. The number of bipartitions $G_1|G_2$ of a set of N modes is given by

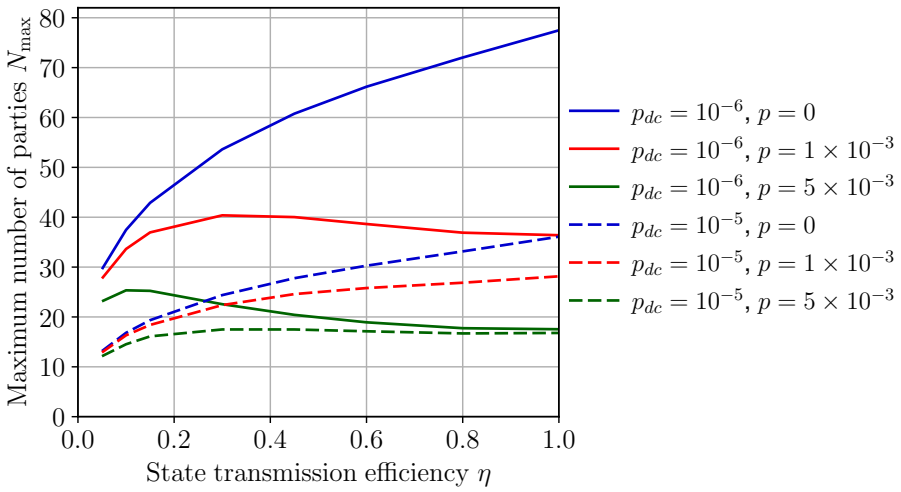

Figure 3.4.: Maximum number of parties $N_{\max}$ for which the witness is still violated as a function of η for a state ρ_η which is obtained by sending $\rho = (|1\rangle\langle 1| + p\,|2\rangle\langle 2|)/(1+p)$ through a loss channel with transmission efficiency η. The scaling behaviour is shown for input states $\rho = (|1\rangle\langle 1| + p\,|2\rangle\langle 2|)/(1+p)$ with $p \in \{0, 1\times 10^{-3}, 5\times 10^{-3}\}$ that are measured with detectors suffering from dark counts with probabilities per heralding event of $p_{dc} \in \{10^{-6}, 10^{-5}\}$.

the Stirling number of the second kind $S(N,2) = 2^{N-1} - 1$ and scales exponentially with N. However, if the displacement parameter on each mode α_i can be assumed to be equal for all the modes, the number of bipartitions to evaluate reduces to $\lfloor N/2 \rfloor$.

Third and last, the question arises of how much experimental imperfections such as dark counts or multi-photon contributions in the state affect the scalability of the witness. Since for an increasing number of parties N, the probability of the single photon being in one party decreases as $1/N$, dark counts of the detectors become more important. Also, multi-photon contributions reduce the expectation value of the witness through the terms $-N(N-1)\hat{\Pi}_{n\geq 2} - \mu E_{n\geq 2}$ and prohibit its violation if they become too important. In order to quantify these effects, we calculate the maximum number of parties $N_{\max}$ for which we still see a violation of the witness given a state $\rho = (|1\rangle\langle 1| + p\,|2\rangle\langle 2|)/(1+p)$ undergoing a loss channel with transmission efficiency η (leading to the state ρ_η) and then input on a N-port BS. We assume that the detectors suffer from dark counts with a probability of p_{dc} per detection window (triggered by the heralding detection in the case of a HSPS). The displacement operation is assumed to be identical on all modes with amplitude $|\alpha| = \sqrt{\ln 2} \approx 0.83$. The result of this calculation as a function of the transmission efficiency η of the state is shown in Fig. 3.4 for different values of p and p_{dc}. For details on the dark count model, see Appendix F in P.2. We see that for the simulated values, our witness is able to detect genuine multipartite entanglement for a few tens of parties.

3.2. Local and scalable detection of genuine multipartite single-photon path entanglement

Multipartite entangled states are not only conceptually fascinating, but lie at the heart of quantum networks and are therefore potentially useful. In the case of single-photon path entanglement, a multipartite entangled state could be distributed by giving each party a weakly pumped photon-pair source and combining one mode from each party on a multi-port BS at a central station, as schematically shown in Fig. 3.5(a). This would lead to a state close to a $|W_N\rangle$ state as defined in Eq. (3.25). The goal here is to experimentally certify such a state by means of local measurements on the state. To this end, we consider a scenario as depicted in Fig. 3.5(b), where a heralded single photon is delocalised over 8 modes.

Apart from the simplicity of the generation, the question about certification of such a state is more complicated, as discussed in Sec. 3.1.3. For an N-qubit state, the number of measurement settings required to fully reconstruct the density matrix via quantum state tomography scales exponentially with N. Therefore, this technique becomes quickly experimentally infeasible. Furthermore, in our case of single-photon path entanglement, one can not a priori assume that locally, the state is a qubit state. Thus, the certification method needs to take into account that the state is in principle infinite dimensional.

In the past, experiments have been carried out where single-photon path-entangled states are certified interferometrically by the recombination of the modes [81, 158]. In a realistic network scenario, this approach is not applicable any longer. A first experimental certification of a tripartite state with local measurements was then presented in [83] as discussed in the beginning of Sec. 3.1.3. Here, we demonstrate multipartite single-photon path entanglement for 8 parties by means of the improved multipartite entanglement witness described in Sec. 3.1.3. Apart from the improvement on the theoretical side, we also implement the displacement operation in an all-fibre configuration which leads to a com-

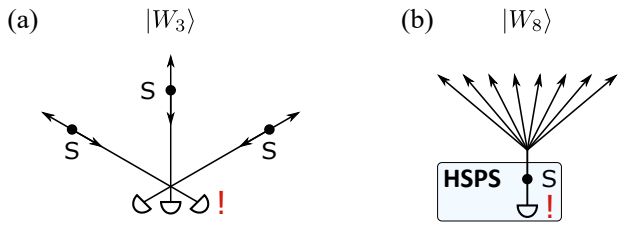

Figure 3.5.: Heralded multipartite single-photon path entanglement. (a) Entanglement is distributed between three parties, each holding a weakly pumped signal-idler photon-pair source (S). The idler modes are combined on a three-port symmetric beam splitter (tritter) and the detection of a single photon after this beam splitter projects the signal modes into a single-photon entangled state. (b) Conceptual schematic of the state generation in the experimental detection of genuine multipartite entanglement. A single photon generated by a heralded single-photon source (HSPS) is split into multiple spatial output modes.

pact and scalable setup. In principle, the number of modes could still have been increased beyond 8, however, we were limited on the detector side by our 8 cryostat readout channels for the high-efficiency SNSPDs.

3.2.1. Experimental setup

The setup for the demonstration of 8-partite single-photon path entanglement is shown in Fig. 3.6. It can be grouped into four parts: HSPS, coherent state generation, path entanglement generation, and measurement part as described in the following.

The HSPS based on type-II quasi-phase-matching in a PPKTP crystal is described in Sec. 2.2. The pair creation probability per pump pulse is kept low at approximately 2.7×10^{-3} to minimise double-pair emissions. In order to herald signal photons with high spectral purity, we filter the heralding photons with a commercial 100 GHz DWDM at channel 39 (= 1546.1 nm). Then, the heralding photons are detected by an InGaAs single-photon avalanche diode (ID Quantique ID210) in gated mode with a detection efficiency of around 20 %. The gate trigger signal is provided by the fast photodiode inside the pump laser, so synchronising the detection and the state generation. In this way, we obtain a heralding rate of 11.5 kcps whereof 0.6 kcps are attributed to dark counts, which effectively adds loss to the heralded state.

To generate the coherent state with the same spectral and temporal properties as the signal photon, we use difference frequency generation (DFG) between the pump and a seed laser in a type-II periodically poled lithium niobate (PPLN) crystal. The seed laser is a distributed feedback laser at $\lambda_i = 1546.1$ nm, emitting long pulses of around 0.7 ns, with the pump laser photodiode used to trigger the seed laser. It is driven from well below to above the lasing threshold in each cycle to randomise the phase of the coherent state. In order to reach the required displacement amplitude, we amplify the pulses with an erbium doped fibre amplifier (EDFA). Together with the pump pulses we then stimulate a DFG process in the PPLN nonlinear crystal. After the crystal, we couple into single-mode optical fibre and go through a motorised delay line (Newport MDL 560 ps) to fine-adjust the time delay between the coherent state and the signal photon. Furthermore, to avoid saturation of the detectors, we select the coherent state pulses by passing them through an electro-optic intensity modulator (EOIM) with an extinction ratio of around 30 dB triggered by a 5 ns gate upon successful detection of a heralding photon. Residual seed laser light is then filtered with a 200 GHz DWDM at channel 45 (= 1541.3 nm).

For the entangled state generation, the heralded signal photon is input to a cascade of 50/50 BSs. The coherent state is input to the second port of the first 50/50 BS and co-propagated with the single-photon state. This passively guarantees stability of the relative optical phase for the later displacement. To ensure orthogonal polarisations between coherent and single-photon states, manual paddle polarisation controllers (PC) are used before the first 50/50 BS.

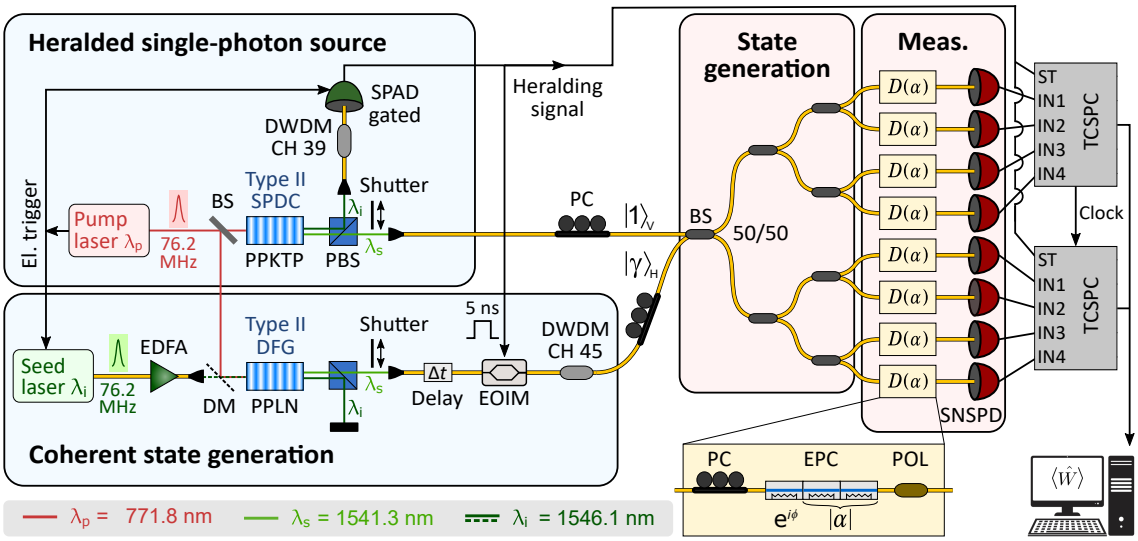

Figure 3.6.: Setup for the detection of genuine multipartite single-photon path entanglement. The state produced by a heralded single-photon source is delocalised by a cascade of 50/50 fibre BSs to generate an 8-partite path-entangled state. Coherent states in orthogonal polarisation modes are co-propagated with the single-photon state to locally perform displacement-based measurements. On each mode, the state is detected by a MoSi SNSPD and time-correlated single photon counting (TCSPC) is used to obtain the 8-bit click/no-click detection outcome. Electrical signals are represented by solid black lines.
BS, beam splitter; DFG, difference frequency generation; DM, dichroic mirror; DWDM, dense wavelength division multiplexer; EDFA, erbium-doped fibre amplifier; EOIM, electro-optic intensity modulator; EPC, electronic polarisation controller; PBS, polarising beam splitter; PC, polarisation controller; POL, polariser; PPKTP, periodically poled potassium titanyl phosphate; PPLN, periodically poled lithium niobate; SNSPD, superconducting nanowire single-photon detector; SPAD, single-photon avalanche diode; SPDC, spontaneous parametric down-conversion.

The measurement part of the setup consist of fibre components (yellow box in Fig. 3.6), which perform the displacement operation in the case where the coherent state is present at the input, and high-efficiency MoSi SNSPDs (75 – 82 %). The implementation for the displacement operation is a fibre version of the one shown in Fig. 3.3(b) and works as follows. The incoming orthogonal states are aligned with a PC on the fast and slow optical axes of the first segment of an electronic polarisation controller (EPC). This EPC (Phoenix Photonics PSC) consists of three segments of polarisation maintaining fibre, where the fibre in the middle is spliced at 45° with respect to the other fibres. In each segment, the refractive index difference between the fast and slow optical axis can be tuned via ohmic heating with a relative phase difference range of $> 2\pi$. In this way, with the first EPC segment we can tune the relative phase between the coherent and single-photon states. With the second and third EPC segments we choose the polarisation state such that we get the desired displacement amplitudes. In theory, a very high transmission for the single-photon state would be optimal. However, in practice we are limited by the polarisation extinction ratio of the polariser (> 28 dB), and therefore set a normalised transmission of 95 % (5 %) for the single-photon state (coherent state). Shutters in the bulk part of the setup allow different measurement settings to be chosen: single-photon state only (z-basis), single-photon and coherent states (α-basis) or only coherent state to determine the displacement amplitudes.

Finally, the detector readout signals are discriminated by two clock-synchronised programmable time-to-digital converters (ID Quantique ID900). Conditioned on a successful heralding detection (connected to the "Start" input), the time stamps for all input channels are saved for the later evaluation of the 8-bit click/no-click outcomes.

3.2.2. Characterisation, alignment and measurement sequence

In order for the entanglement certification to work properly, several things need to be characterised and aligned. Most importantly, the coherent state used for the displacement operation needs to be as indistinguishable as possible from the single-photon state. The indistinguishability in the spatial degree of freedom is guaranteed by the single mode optical fibre, therefore only the spectral and temporal degree of freedom need to be characterised and aligned. The wavelengths are chosen such that idler and signal photons generated in the PPKTP crystal are centred in the ITU channels 39 and 45, respectively. We then choose the phase-matching conditions in the PPLN crystal such that the same pump together with the distributed feedback laser at the idler wavelength generates a coherent state at the signal wavelength. We verify the spectral overlap by sweeping a 0.2 nm bandwidth tunable grating filter (JDS Uniphase TB9) before the single-photon detector and compare the spectra of the coherent state and the heralded single photon, as shown in Fig. 3.7(a). From the Gaussian fits, the Hong-Ou-Mandel visibility due to the non-unit spectral overlap is calculated to be 99.2 % (see Eq. (5.14) in [159]).

To make sure that the coherent and single-photon states are temporally aligned, we also

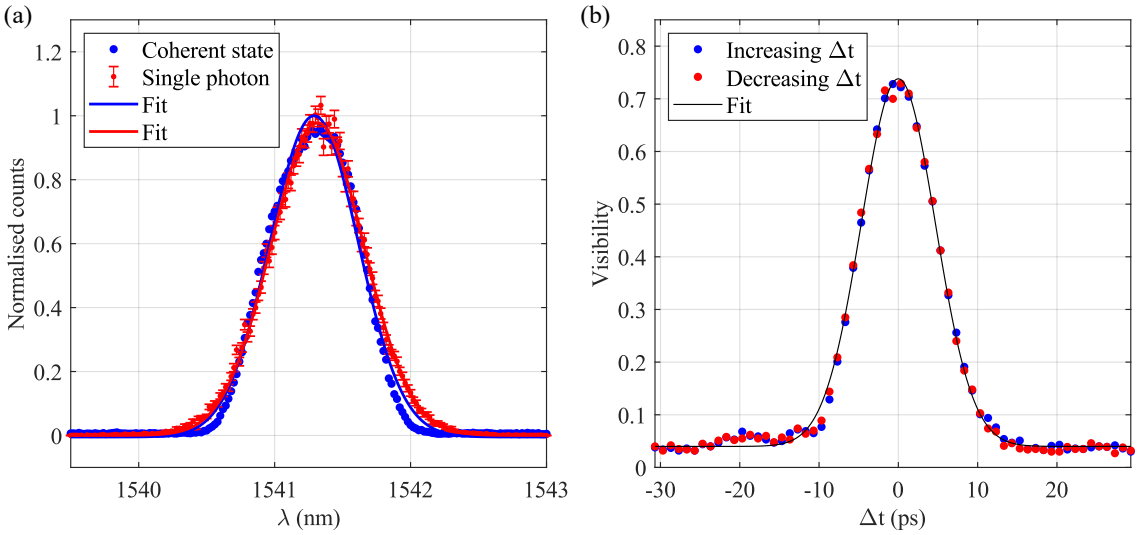

Figure 3.7.: Characterisation and alignment of the coherent state and the single-photon state. (a) Spectral overlap. (b) Temporal alignment.

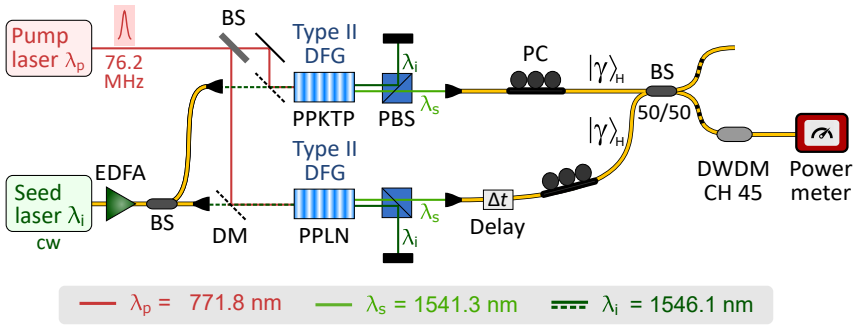

Figure 3.8.: Schematic of the temporal setup alignment. BS, beam splitter; DFG, difference frequency generation; DM, dichroic mirror; DWDM, dense wavelength division multiplexer; EDFA, erbium-doped fibre amplifier; PC, polarisation controller.

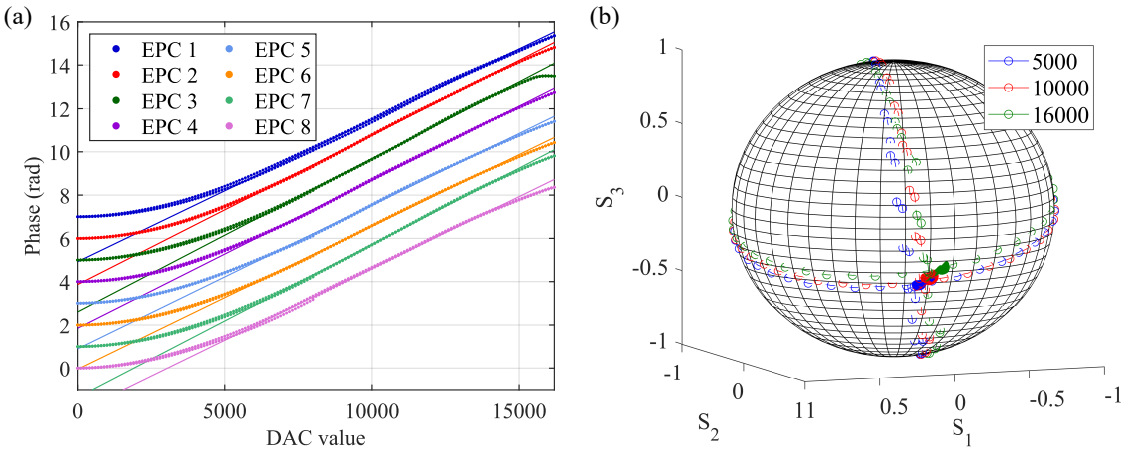

Figure 3.9.: Characterisation of the electronic polarisation controllers (EPC). (a) Induced phase difference with the first segment of the EPC as a function of the applied voltage to the ohmic heating element. The voltage is indicated in values of the 14-bit digital-to-analog (DAC) converter of the control electronics. Low DAC values correspond to more heating, which explains the saturation effect. A linear fit is applied to the data between the DAC values 6000 and 15000. (b) Output polarisation on the Poincaré sphere for the qualitative characterisation of the cross talk between EPC segments. The input light is aligned on axis with the first segment, i.e. different settings for the first segment should not alter the measured output state. The three different colours correspond to different DAC values, which are set for the first segment and kept for 30 min. In between the three settings, the second and third segments are fully swept (in 20 s) to see the direction of polarisation change (2nd segment: left-right; 3rd segment: up-down), and then brought back to the fixed DAC values of 16000 and 10000, respectively. Different temperatures on the first EPC segment mainly influences the second segment and therefore we see the state moving to the right.

stimulate a DFG process in the PPKTP crystal by splitting the seed laser output, as shown in Fig. 3.8. The two coherent states, originating from DFG processes with the same seed pulse in the PPKTP and PPLN crystals, are then combined on the first 50/50 BS of the cascade in the same polarisation mode. In one of the 8 output modes, we measure the output power with a power meter and calculate the interference visibility from the observed minimum and maximum values over a 20 s interval. As shown in Fig. 3.7(b), by changing the delay Δt in the coherent state path we find and set the delay such that the interference visibility is maximal.

Regarding the displacement-based measurement, we need to be able to locally control the phase between the coherent and single-photon state (see Eq. (3.12)), which we achieve by tuning the first segments of the EPCs and align the polarisation of the incoming states on the fast and slow axes, as described above. In Fig. 3.9(a), we show the characterisation of the induced phase difference as a function of the applied voltage (indicated in values of the 14-bit digital-to-analog (DAC) converter) to the ohmic heating element of the EPCs' first segments. This is measured with light input to the EPCs in a polarisation state which is

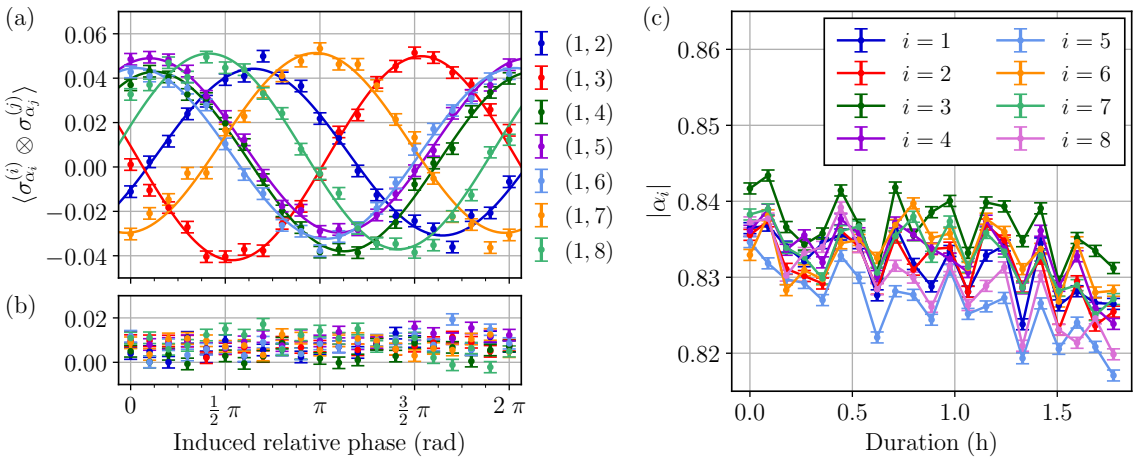

Figure 3.10.: (a) Phase alignment between mode 1 and all seven other modes. The single-photon state is displaced with $|\alpha| \approx 0.83$ and the first segments of the EPCs 2 - 7 are swept over their full range from 0 to 2π. Sinusoidal curves are fitted to the data for expectation values of the pairwise correlators $\langle \sigma_{\alpha_i}^{(i)} \otimes \sigma_{\alpha_j}^{(j)} \rangle = p_{00}^{\alpha_i\alpha_j} - p_{0c}^{\alpha_i\alpha_j} - p_{c0}^{\alpha_i\alpha_j} + p_{cc}^{\alpha_i\alpha_j}$. (b) Same measurement without the presence of the single-photon state. (c) Measurement of the displacement amplitude $|\alpha_i|$ in mode i (1 min per point) during the data acquisition for the entanglement witness. Error bars correspond to one standard deviation assuming Poissonian count statistics.

split equally between the fast and slow axes of the EPCs' first segments and a polarimeter at the output. The EPCs are then operated in the linear regime (between DAC values 6000 and 15000) and the phase is calculated from the slope of the corresponding linear fit function.

Our fibre implementation of the displacement operation is compact and can easily be scaled up to more parties. However, the drawback of the chosen EPC is the thermal crosstalk between adjacent segments. When changing the temperature of the first segment, for example, not only the phase of the displacement, but also the amplitude is affected, as shown in Fig. 3.9(b). Therefore, the settings have to be adjusted in an iterative way to reach the final alignment. Enough waiting time has to be left in between iterations to ensure that the device has reached a thermal equilibrium, which makes the full alignment process slow (several tens of minutes to hours). This problem could be solved by using piezo-actuated fibre squeezers instead.

The measurement results of the phase alignment are shown in Fig. 3.10(a). First, the displacement amplitude is set to $|\alpha| \approx 0.83$ for all modes, corresponding to a heralded no-click probability locally of $p_0 = e^{-|\alpha|^2} = 0.5$, by changing the temperature of the second and third EPC segments. Then, we additionally input the single-photon state and sweep the first segments of the EPCs 2 - 7 over the full range. The same measurement without single-photon state at the input leads to the result shown in Fig. 3.10(b), where no phase-dependence is observed, as expected. The phases are then aligned by setting the first EPC segments such that the expectation values of the pairwise correlators $\langle \sigma_{\alpha_1}^{(1)} \otimes \sigma_{\alpha_i}^{(i)} \rangle$ are

maximised.

After the alignment of the relative phases between the output modes, data for the witness are acquired in 20 sequences of 5 min. Each sequence measures the displacement amplitudes (1 min), as shown in Fig. 3.10(c), followed by the measurement of the state in the α-basis and then in the z-basis (2 min). This leads to more than 27×10^6 evaluations for the α- and the z-basis, respectively. The observed drifts and fluctuations in the displacement amplitudes reduce the violation of the 8-partite witness by 2.4 %. In order to estimate the probability of having more than one photon locally, we additionally perform a heralded autocorrelation measurement on one output mode by inserting a 50/50 BS before the detectors and acquire data for 6 h corresponding to more than 365×10^6 heralding events.

3.2.3. Results for a genuinely 8-partite entangled state

The results of the measurement on the 8-partite state are given in Fig. 3.11. From the counts in the z-basis we deduce the normalised splitting ratio of the state, as shown in Fig. 3.11(a). All the output modes have a normalised splitting ratio of (12.5 ± 0.8) %. The probability of measuring in one or more clicks on all 8 detectors combined, conditioned on a heralding event, is 26.8 %. Apart from the heralding efficiency of the source (75 %) and the detector efficiencies (75 – 82 %), this is mainly due to the loss of the 50/50 BSs (~ 0.5 dB per BS) for the state generation, the EPC (~ 0.8 dB), and the polariser (~ 0.5 dB) used for the displacement-based measurement, which amounts to a transmission efficiency of ~ 52 %

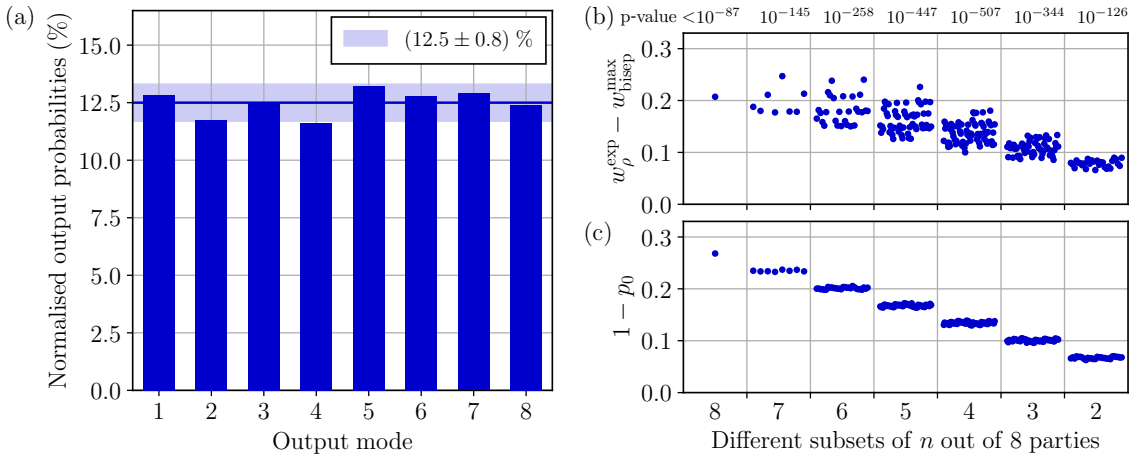

Figure 3.11.: Results for the measured 8-partite state. (a) Normalised probabilities of detecting a photon in output mode $i \in \{1, ..., 8\}$ from the measurement without displacement (z-basis). (b) Witness violation $w_\rho^{\text{exp}} - w_{\text{bisep}}^{\text{max}}$ with the maximum p-value for each fixed number of subsets indicated on top. The witness is applied to all possible different subsets of $n \in \{2, ..., 8\}$ out of 8 parties where the discarded parties are traced out. (c) State efficiency $1 - p_0$ where p_0 is the probability of the overall vacuum component $|\bar{0}\rangle\langle\bar{0}|$ for each subset of parties.

p_0	P^1_{click}	P^2_{click}	P^3_{click}	p_1^*	p_*
0.7319(1)	0.2678(1)	$2.96(4)\cdot 10^{-4}$	$1.5(8)\cdot 10^{-7}$	$5.4(1)\cdot 10^{-6}$	$3.40(4)\cdot 10^{-4}$

Table 3.1.: Measured probability for the overall vacuum contribution p_0 and probabilities P^n_{click} that n detectors click. Further, p_1^* is an upper bound on the probability of having more than one photon locally in mode 1, and $p_* = 8p_1^* + \sum_{n=2}^{8} P^n_{\text{click}}$ is an upper bound on the probability of having in total more than one photon in the state.

λ	μ	$\overline{o}$	$\overline{z}$	$\overline{s}$	w_ρ^{exp}	$w_{\text{bisep}}^{\text{max}}$	p-value
8.29	151	2.5762	5.9915	-0.0024	8.565(4)	8.358	10^{-87}

Table 3.2.: Evaluation of the 8-partite witness with parameters λ and μ according to Eqs. (3.31) and (3.34). The mean values $\overline{o}$, $\overline{z}$ and $\overline{s}$ are associated to the observables $\hat{O}_{\vec{\alpha}}$, $\mathcal{Z}$ and $-N^2(N-1)\Pi^{(1)}_{n\geq 2}$, respectively, where $N = 8$. As defined in Eq. (3.46), we have $w_\rho^{\text{exp}} = \overline{o} + \overline{z} + \overline{s}$. Further, we calculate the biseparable bound $w_{\text{bisep}}^{\text{max}}$ according to Eq. (3.44), and the p-value for the null-hypothesis that the observed result is produced by a separable state due to finite statistics.

per mode. Further details on the state characterisation and multi-photon contributions are given in Tab. 3.1.

For the calculation of the witness described in Sec. 3.1.3, we consider all possible subsets of $n \in \{2, ..., 8\}$ out of 8 parties. For each subset, the expectation value and separable bound of the n-partite witness are calculated, as shown in Fig. 3.11(b). We observe that the witness violates the separable bound for all subsets. We further indicate the p-value for the null-hypothesis that the observed result is produced by a separable state due to finite statistics. The explicit calculation of the p-values is given in Appendix D of P.2. In Fig. 3.11(c) we plot the probability $(1 - p_0)$ of measuring in total one or more clicks on all n detectors for all sets of n out of 8 parties. The fewer parties we consider, i.e. the more parties we trace out, the lower the state efficiency becomes.

For each subset of modes, the witness is optimised such that the violation $(w_\rho^{\text{exp}} - w_{\text{bisep}}^{\text{max}})$ is maximised by tuning the parameters λ and μ, see Eqs. (3.31) and (3.34). The optimal values depend on the overall vacuum component of the state as well as the multi-photon components in the state. In the case of the 8-partite state, the optimal witness parameters and the corresponding evaluated values are given in Tab. 3.2. To visualise the behaviour of the witness as a function of λ and μ, the calculated witness violation for the state measured in the experiment is shown in Fig. 3.12. Note that we defined our witness such that values above 0 indicate the detection of entanglement. It becomes clear that especially λ, the weight of the projector on the overall vacuum state in the witness, is a crucial parameter to tune.

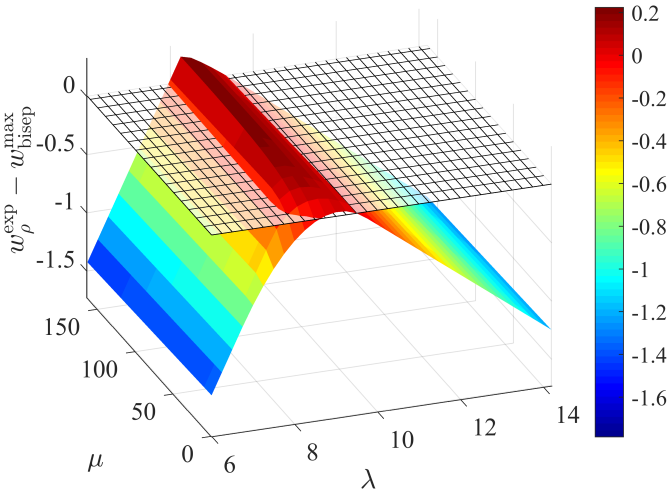

Figure 3.12.: Witness violation as a function of the parameters λ and μ, defined according to Eqs. (3.31) and (3.34), for the 8-partite state. Values greater than 0 indicate that the entanglement is detected by the witness with the corresponding parameters. For the evaluation, the parameters $\lambda = 8.29$ and $\mu = 151$ are chosen.

3.2.4. Conclusion

We have demonstrated that the developed witness presented in Sec. 3.1.3 is well suited for an efficient certification of multipartite single-photon path entanglement. Our demonstration was limited to 8-partite entanglement due to the 8 detector readout channels of the cryostat, but in principle much larger states can be certified with our witness, see Sec. 3.1.3. Not only has the calculation of the separable bound a favourable scaling with the number of parties since it does not rely on semi-definite programming techniques, but the number of measurement settings is also fixed to three. If PNR detectors are used, the local multi-photon components can be directly estimated from the z-basis measurement, which reduces the number of measurement settings to two. This makes it very practical and thanks to the local measurements, it can be applied in a distributed scenario and therefore possibly in future quantum networks.

Multipartite single-photon path-entangled states could be distributed at high rates in a scheme where each party holds a photon-pair source and one photon of each pair is sent to a central multi-port beam splitter which erases the which-path information. In this way, local losses can be kept low and the added distance between parties only reduces the heralding rate. In combination with quantum memories, such a scheme has potential for applications relying on distributed W states [147–149]. As will become clear in the next section, where such an implementation for the bipartite case is demonstrated, the main experimental challenge in such a scheme is the need for phase stability in long fibre links. To this end, lessons can be learned from an implementation where phase-sensitive multipartite entangled states are distributed [48].

3.3. Heralded distribution of single-photon path entanglement

As already mentioned in the previous section, single-photon path-entangled states can be distributed by giving each party a weakly pumped photon-pair source and combining one mode from each party on a multi-port BS at a central station. Based on the Duan-Lukin-Cirac-Zoller (DLCZ) protocol [160], in 2007 Simon et al. proposed a bipartite version of this scheme, combined with multimode quantum memories, to build a quantum repeater [161]. Compared to schemes where a two-photon entangled state is distributed, e.g. entangled in the polarisation degree of freedom of the photons, this single-photon scheme has a more favourable scaling with transmission loss. In the case of probabilistic photon-pair sources, the heralding rate of the entanglement distribution also has a more favourable scaling as a function of the pair creation probability, compared to two-photon schemes [65]. To illustrate this, let's consider a scenario as shown in Fig. 3.13, where two parties, Alice and Bob, have the ability to generate a resource state and finally want to share an entangled state. Given a transmission efficiency of η between Alice (Bob) and the central station, and a pair creation probability of p for both sources, the heralding rate in the two-photon scheme scales with $(p\eta)^2$ because two pairs need to be generated and two photons need to be transmitted to the central station. In the single-photon scheme, the scaling is $\propto p\eta$, since only one pair needs to be generated and transmitted. The downside of the single-photon scheme, however, is the phase-stability requirement which can be experimentally challenging.

Here, we demonstrate one part of the scheme proposed in Ref. [161], namely the heralded distribution of photonic entanglement. We certify the heralded single-photon entanglement by means of local displacement-based measurements and the entanglement witness discussed in Sec. 3.1.2. This work has already been partially presented and discussed in the PhD thesis of E. Verbanis in 2019 [162]. The therein described noise problems of the InGaAs single-photon avalanche diodes have been solved by replacing them with P-SNSPDs and reducing the repetition rate of the experiment. In the following, a complete description of the implementation is given, which does not require previous knowledge from Ref. [162].

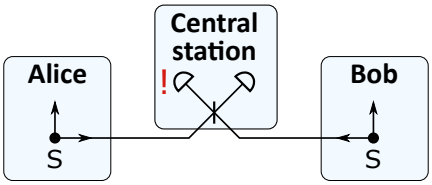

Figure 3.13.: Scheme for the heralded distribution of single-photon path entanglement. Alice and Bob both hold a weakly pumped signal-idler photon-pair source (S). The idler modes are combined on a beam splitter at the central station where the detection of a single photon projects the signal modes into a single-photon entangled state shared between Alice and Bob.

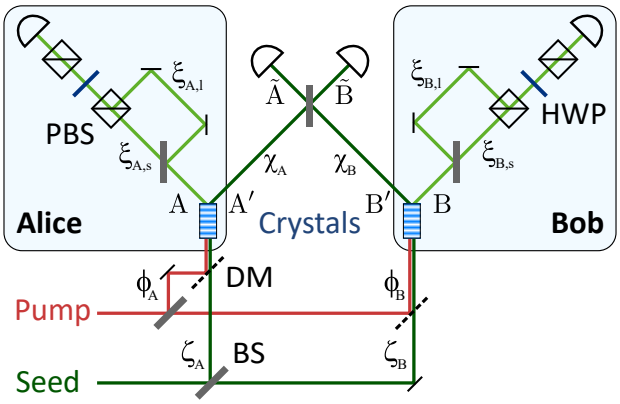

Figure 3.14.: Schematic of the experimental setup with the relevant phases ϕ, ζ, χ and ξ (see text). BS, 50/50 beam splitter; DM, dichroic mirror; HWP, half-wave plate; PBS, polarising beam splitter.

3.3.1. Scheme with two photon-pair sources

We consider a scheme as shown in Fig. 3.14, where Alice and Bob each holds a weakly pumped SPDC photon-pair source. Given a pair creation probability per pump pulse $p \ll 1$ for both sources, the generated state can be approximated by

$$|\psi\rangle = \left(\sqrt{1-p}\,|00\rangle_{AA'} + \sqrt{p}e^{\mathrm{i}\phi_A}\,|11\rangle_{AA'}\right) \otimes \left(\sqrt{1-p}\,|00\rangle_{BB'} + \sqrt{p}e^{\mathrm{i}\phi_B}\,|11\rangle_{BB'}\right) + O(p), \tag{3.47}$$

where $|0\rangle$ is the vacuum state, $|1\rangle$ the single-photon number state and $\phi_{A(B)}$ the phase of the pump laser at Alice's (Bob's) source. The idler photons from each source are sent to a 50/50 beam splitter at the central station, where they pick up a phase $\chi_{A(B)}$ on their way. The bosonic annihilation operators of the modes after the beam splitter are $a_{\tilde{A}} = \frac{1}{\sqrt{2}}(e^{-\mathrm{i}\chi_A}a_{A'} + e^{-\mathrm{i}\chi_B}a_{B'})$ and $a_{\tilde{B}} = \frac{1}{\sqrt{2}}(e^{-\mathrm{i}\chi_A}a_{A'} - e^{-\mathrm{i}\chi_B}a_{B'})$ [161]. By neglecting contributions from higher order pair creation probabilities $O(p)$, a detection of a single photon in mode $\tilde{A}$ then projects the state of the signal photons of Alice and Bob after the crystals into the single-photon path-entangled state

$$|\psi\rangle_{AB} = \frac{1}{\sqrt{2}}\left(|10\rangle_{AB} + e^{\mathrm{i}(\theta_B - \theta_A)}\,|01\rangle_{AB}\right) \tag{3.48}$$

with the phase $\theta_{A(B)} = \phi_{A(B)} + \chi_{A(B)}$.

In order to certify the entanglement, we make use of local displacement-based measurements. To this end, we generate coherent states by stimulating a DFG process in the nonlinear crystals using seed pulses, temporally alternating with the SPDC processes that generate the single-photon states. Before Alice's (Bob's) crystal, the seed pulses pick up a phase $\zeta_{A(B)}$ and, therefore, the coherent states in mode $A(B)$ after the crystal have a phase $\phi_{A(B)} - \zeta_{A(B)}$. Locally, the single-photon state and the coherent states are temporally combined in asymmetric Mach-Zehnder interferometers (MZI) with a delay equal to

the time difference between the single-photon and coherent states (13.1 ns). We consider the case where the single-photon state takes the long path and picks up a phase $\xi_{A(B),l}$, whereas the coherent state acquires a phase $\xi_{A(B),s}$ in the short path. To summarise, we have the following phases in our scheme

- ➢ $\phi_{A(B)}$, the phase of the pump laser at the source,
- ➢ $\zeta_{A(B)}$, the phase of the seed laser at the source,
- ➢ $\chi_{A(B)}$, the phase picked up between the source and the central station,
- ➢ $\xi_{A(B),l(s)}$, the phase from the crystal to the detector through the long (short) arm of the asymmetric MZI,

which leads to the phases

- ➢ $\phi_{A(B)} + \chi_{A(B)} + \xi_{A(B),l}$ for the single-photon state,
- ➢ $\phi_{A(B)} - \zeta_{A(B)} + \xi_{A(B),s}$ for the coherent state.

As shown in Sec. VI of the Supplemental Material of P.1, in our scheme this leads to the following phase stability requirement

$$\zeta_A + \chi_A + \xi_{A,l} - \xi_{A,s} = \zeta_B + \chi_B + \xi_{B,l} - \xi_{B,s} + \text{const.} \tag{3.49}$$

Interestingly, this shows that the phases of the pump before the crystals ϕ_A and ϕ_B cancel out since they contribute to the creation of both, the single-photon and the coherent states. The phase stability requirement of Eq. (3.49) can be achieved by phase-locking the central interferometer spanned by the seed laser such that

$$(\zeta_A + \chi_A) \mod 2\pi = \zeta_B + \chi_B \tag{3.50}$$

and the two asymmetric MZIs for the displacement-based measurement, either independently such that

$$(\xi_{A,l} - \xi_{A,s}) \mod 2\pi = 0, \qquad (\xi_{B,l} - \xi_{B,s}) \mod 2\pi = 0 \tag{3.51}$$

or, as we will see in our implementation, in a way that

$$(\xi_{A,l} + \xi_{B,s}) \mod 2\pi = \xi_{A,s} + \xi_{B,l}. \tag{3.52}$$

This stabilisation can be achieved by consecutively propagating laser pulses through both asymmetric MZIs (in the opposite direction of the signal) at a repetition rate of $f \leq \frac{c}{3\Delta\ell}$ with a duty cycle of $< \frac{f\Delta\ell}{c}$, where $\Delta\ell$ is the optical path length difference between the long and short paths in the asymmetric MZIs. In this way, the pulses taking the long-short and short-long paths will interfere and the detected signal amplitude can be used for the phase-locking.

3.3.2. Experimental implementation and characterisation

A schematic overview of the experimental implementation is shown in Fig. 3.15(a). We use the same two nonlinear crystals as in Sec. 3.2 for type-II SPDC, pumped by a pulsed laser (76 MHz repetition rate) at $\lambda_p = 771.8\,\text{nm}$ to create nondegenerate photons at $\lambda_s = 1541.3\,\text{nm}$ (signal) and $\lambda_i = 1546.1\,\text{nm}$ (idler). The photon pair creation probability per pump pulse for each source is kept at $p \approx 3 \times 10^{-3}$ in order to keep the probability of having double-pair emissions sufficiently low. Signal and idler modes are separated after their generation at the PBSs and coupled into single-mode optical fibres. The idler photons are then sent to a 50/50 BS and are spectrally filtered by a 100 GHz DWDM at ITU channel 39. In this way, we ensure high-purity heralded signal photons and achieve a spectral overlap of 99.9 % between idler photons originating from the two independent sources, as shown in Fig. 3.16(a).

For the displacement-based measurement, the coherent state with the same spectral, temporal and polarisation properties as the single-photon state is generated via DFG by stimulating the nonlinear crystals with a pulsed distributed feedback seed laser at a wavelength $\lambda_i = 1546.1\,\text{nm}$ and repetition rate 19 MHz. The seed laser is driven from well below to above the lasing threshold each cycle to phase-randomise the coherent state. The repetition rate of 19 MHz is chosen such that the state to detect is temporally separated by 39.4 ns ($= 1/(19\,\text{MHz}) - 1/(76\,\text{MHz})$) from the preceding (strong) coherent state, which ensures that the used detectors (P-SNSPDs) have enough time to recover. To further reduce the photon noise at the central station due to residual seed-pulse photons, and unwanted optical reflections, arriving before the heralding idler photons, a gate of 2 ns is generated by an EOIM to temporally filter before the detector. The EOIM has an insertion loss of 5.0 dB and an extinction ratio of 33 dB.

As shown in Fig. 3.15(b), the single-photon and the coherent states are temporally brought to coincidence on Alice's (Bob's) side in an asymmetric MZI, where we use a 50/50 BS at the input and the output BS is replaced by a PBS in order to fine-tune the displacement amplitude. Subsequently, a PBS projects the single-photon and the coherent states into the same polarisation mode. A fibre Bragg grating (FBG) with extinction ratio of $\sim 50\,\text{dB}$ is used to reject reflections from the locking laser at $\lambda_r = 1559.0\,\text{nm}$ (see below). Additionally, the spectral overlap between single-photon and coherent states, as shown in Figs. 3.16(b-c), is increased by locally filtering with a DWDM at ITU channel 45.

To fulfil the phase stability requirement, the central interferometer is phase-locked using the residual seed laser pulses at the central station. A piezo-electric fibre stretcher (PZT) with a half-wavelength voltage of $V_\pi = 0.18\,\text{V}$ and an optical delay range of about 0.57 ps (corresponding to an optical path length of 171 μm) is actively controlled by a microcontroller (PJRC Teensy 3.2) such that the seed power at the second output port of the 50/50 BS, measured with a fast photodiode, is maximised. This makes sure that Eq. (3.50) is fulfilled and at the same time minimises the seed power (in total 1.0 μW) that is sent to the heralding detector.

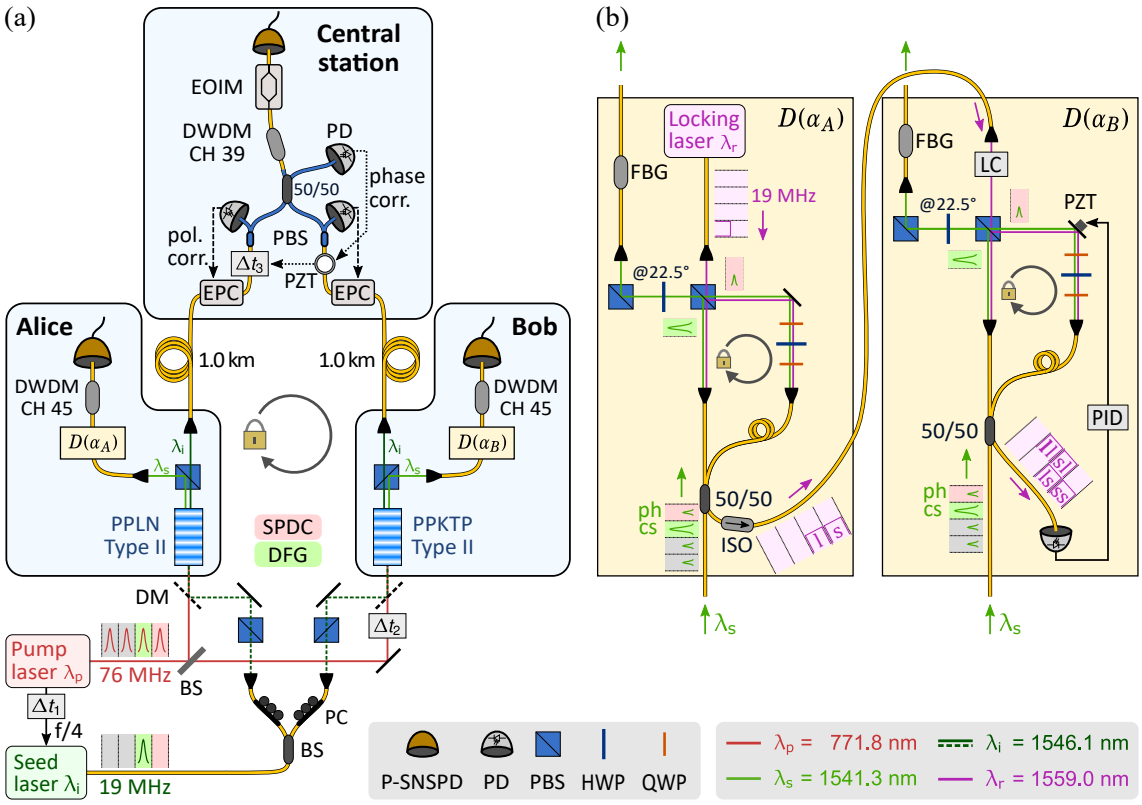

Figure 3.15.: Schematic of the experimental implementation of the heralded distribution and certification of single-photon path entanglement. (a) Alice and Bob each hold a weakly pumped nonlinear crystal, in which a signal-idler photon pair is generated with low probability via SPDC. Additionally, every fourth pump pulse is overlapped with a seed pulse at the idler wavelength to generate coherent states via DFG. The idler photons are then sent to the central station and herald the entanglement distribution. The signal photons and coherent states are kept by Alice and Bob, respectively, in order to perform the displacement-based measurement. Photons are detected by three P-SNSPDs. (b) Detailed implementation of the displacement-based measurement on Alice's and Bob's side. The separate single-photon and coherent states are temporally combined in asymmetric Mach-Zehnder interferometers where the output beam splitters are replaced by PBSs. The displacement takes place on subsequent PBSs where the single-photon and coherent states are projected onto the same polarisation mode. A pulsed reference laser is used to lock the relative phase difference which is picked up in the two interferometers.
BS, beam splitter; DFG, difference frequency generation; DM, dichroic mirror; DWDM, dense wavelength division multiplexer; EOIM, electro-optic intensity modulator; EPC, electronic polarisation controller; FBG, fibre Bragg grating; HWP, half-wave plate; ISO, isolator; LC, liquid crystal; PBS, polarising beam splitter; PC; polarisation controller; PD, photodiode; PID, proportional–integral–derivative controller; PPKTP, periodically poled potassium titanyl phosphate; PPLN, periodically poled lithium niobate; P-SNSPD, parallel superconducting nanowire single-photon detector; PZT, lead zirconate titanate (piezoelectric); QWP, quarter-wave plate; SPDC, spontaneous parametric down-conversion.

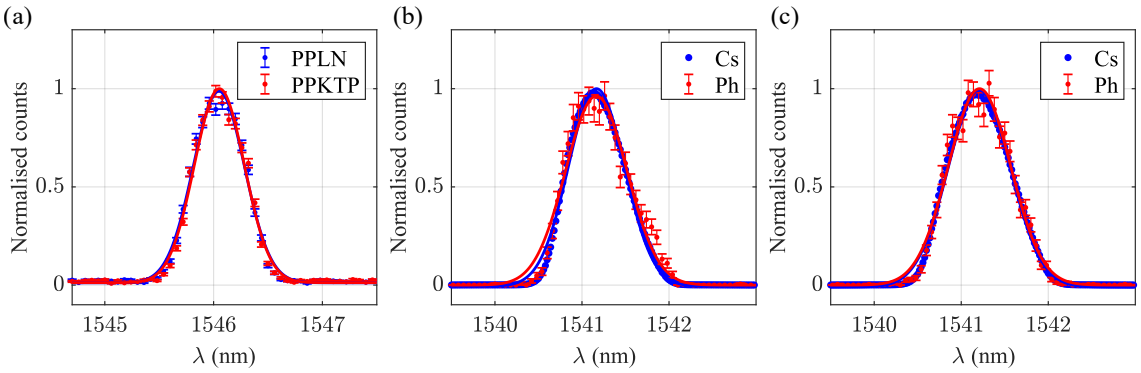

Figure 3.16.: Characterisation of the spectral overlap measured with a tunable grating filter with a FWHM of 0.2 nm before the corresponding detector. (a) Spectra of the idler photons at the central station originating from the PPLN crystal (Alice) and the PPKTP crystal (Bob). (b) Coherent state (Cs) and single photon (Ph) spectra for Alice and (c) for Bob.

Regarding the local measurements, we first note that in the common paths of the coherent state and the single-photon state, their short temporal separation of 13.1 ns intrinsically guarantees the phase stability since the phase changes occurring over this time scale are negligible. To stabilise the phase in the asymmetric MZIs and fulfil Eq. (3.52), we inject laser pulses at $\lambda_r = 1559.0\,\text{nm}$ of about 10 ns duration at a repetition rate of 19 MHz travelling in the reverse direction to the signal, first through Alice's asymmetric MZI, then through Bob's, as schematically shown in Fig. 3.15(b). The resulting signal is measured by a fast photodiode and shows 50 % visibility interference fringes as a function of the phase difference between the long-short and short-long paths in the asymmetric MZIs, which is kept at a constant set point by controlling a piezo-actuated mirror in the long arm of Bob's asymmetric MZI. In this way, the phase difference of the displacement fields between Alice and Bob can be set with a liquid crystal (LC; Thorlabs LCC1111T-C) in the locking laser path before Bob's asymmetric MZI. The LC allows us to induce a phase difference of up to π between orthogonal linear polarisation states, see Fig. 3.17 for the corresponding calibration measurement. The LC is aligned on-axis with the subsequent PBS in Bob's asymmetric MZI and therefore allows for selective retardation of the signal in the long arm with respect to the signal in the short arm of Bob's interferometer.

In order to demonstrate the feasibility of long-distance entanglement distribution, we extend the central interferometer arm lengths from initially $l = 42\,\text{m}$ to $l = 1.0\,\text{km}$ by inserting two fibre coils. This change additionally requires active polarisation control before the 50/50 BS as well as active compensation of slow relative drifts in optical path length between the two interferometer arms. Therefore, EPCs (Phoenix Photonics PSC) are inserted after the fibre coils to minimise the seed power at the second output ports of the fibre PBSs whose first output ports are connected to the polarisation maintaining 50/50 BS at the end of the central interferometer. The slow relative optical length drifts are compensated by actively setting Δt_3 with a motorised delay line (Newport MDL 560 ps) such that the voltage applied to the PZT is kept in range. In this way, we achieve

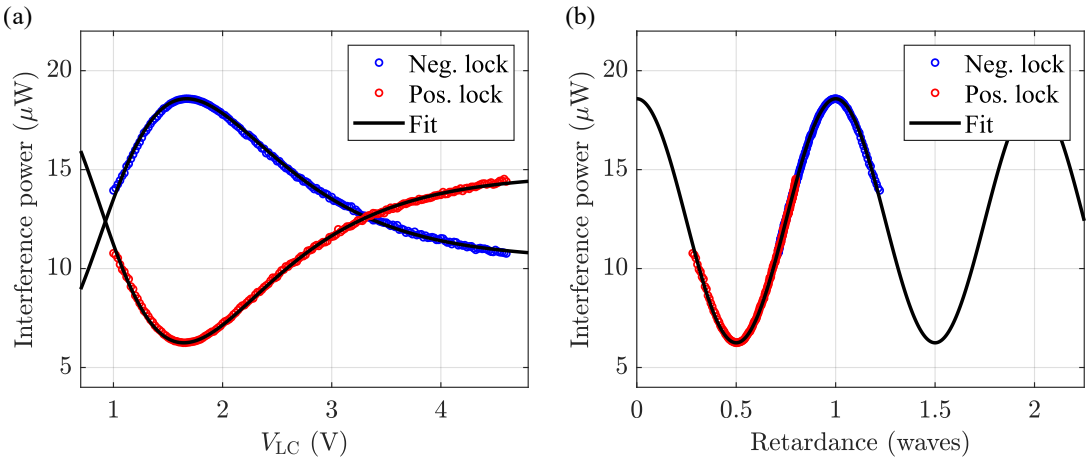

Figure 3.17.: Characterisation of the liquid crystal (LC) at a temperature of 40 °C. The asymmetric MZIs are phase-locked, as shown in Fig. 3.15(b), and seed pulses at 19 MHz are sequentially sent through Alice's and Bob's MZIs in the forward direction. The 50 % interference is then measured at Bob's output. (a) Interference power P measured as a function of the voltage V_{LC} applied to the LC for phase-locking with the PID controller on the negative and positive slope of the interference fringe. The function $P = \frac{(P_{\max}+P_{\min})}{2} + \frac{(P_{\max}-P_{\min})}{2}\sin(a_1 + a_2\exp(-a_3\cdot(V_{\mathrm{LC}})^{a_4}))$ with parameters a_1 to a_4 is fitted to the data. (b) Interference power as a function of the induced calibrated retardance $(a_1 + a_2\exp(-a_3\cdot(V_{\mathrm{LC}})^{a_4}))/(2\pi)$. [Negative lock: $a_1 = 5.96$, $a_2 = 5.72$, $a_3 = 0.555\,\mathrm{V}^{-1.35}$, $a_4 = 1.35$; positive lock: $a_1 = 6.68$, $a_2 = -5.94$, $a_3 = 0.576\,\mathrm{V}^{-1.32}$, $a_4 = 1.32$].

long-term phase stabilisation as shown in Fig. 3.18 for a duration of 8 h.

The photons are detected by three MoSi P-SNSPDs optimised for short recovery times and operated as click/no-click detectors, with efficiencies $\eta_d > 60\,\%$ and full recovery times $\tau_{\mathrm{rec}} < 35$ ns [120]. Those short recovery times make it possible to generate coherent states at the rate of 19 MHz. Time correlated single-photon counting (ID Quantique ID900) is used to register the events of a signal photon detected by Alice, by Bob, and coincidences conditioned on the detection of an idler photon at the central station within a 400 ps window with respect to the 19 MHz clock signal. In the α-basis, we monitor the displacement amplitudes by tracking the detection rates caused by coherent states arriving 1 cycle (52.5 ns) later than the expected signal photons.

Temporal setup alignment

The setup is temporally aligned by adjusting three different electronic and optical delays, labelled Δt_1 - Δt_3 in Fig. 3.15(a). This is done in the following way.

First, the seed laser is replaced by a broadband light source (EXFO M2103) in the telecom C-band with a FWHM of 50 nm. The motorised delay line at the central station is then used to adjust Δt_3 such that the observed interference visibility after the 50/50 BS is

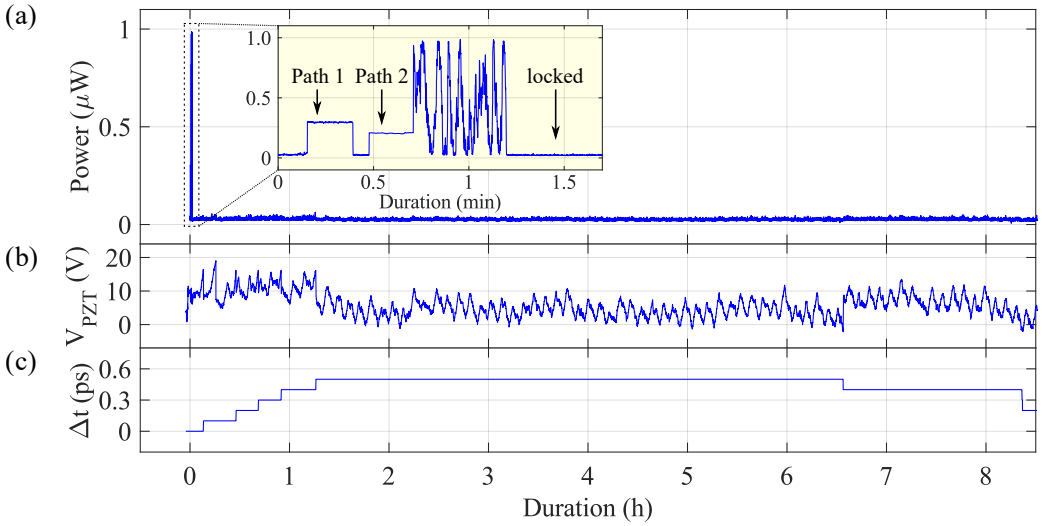

Figure 3.18.: Phase stabilisation of the central interferometer with arm length of $l = 1.0\,\mathrm{km}$ over a duration of 8 h. (a) Measured seed power at the 50/50 BS output port 1. The active feedback on the piezo-electric fibre stretcher and the time delay feedback are turned on after 1.2 min. Inset: during the initial 1.2 min, first path 1 of the interferometer is left open only, then path 2, and afterwards both paths are opened leading to interference. (b) Feedback voltage V_{PZT} to the piezo-electric fibre stretcher. (c) Time delay feedback Δt to the motorised delay line to correct for large drifts in optical path length. This ensures that V_{PZT} does not reach the limit of its range.

maximised. The observed maximum visibility drops to half its value if Δt_3 is changed by 0.25 ps, hence we achieve a precise alignment between the two arms of the central interferometer.

Second, we inject seed and pump laser pulses and adjust the electronic delay Δt_1 of the signal that triggers the seed laser pulses such that they overlap in the PPLN crystal on Alice's side. Therefore, DFG light can be observed at the signal wavelength λ_s in the reflected port of the PBS after the crystal.

Third, the seed laser is replaced by a cw laser at the signal wavelength λ_s and its polarisation is rotated to vertical before combining it with the vertically polarised pump laser. Thus, in both crystals we generate horizontally polarised DFG light pulses at the idler wavelength λ_i which interfere at the central station. A motorised delay stage in Bob's pump path is used to change Δt_2 such that the observed interference visibility after the 50/50 BS at the central station is maximised. Because of the path length difference in the pump + idler paths between Alice and Bob corresponding to 13.1 ns, the interfering pulse on Bob's side originates from a pump pulse that is generated one cycle earlier than the one on Alice's side. The alignment still works since consecutive pump pulses from the Ti:sapphire laser are coherent.

In a similar fashion, the asymmetric MZIs on Alice's and Bob's side are aligned. To this

end, the seed laser is switched to continuous-wave mode and coherent states at λ_s at a repetition rate of 76 MHz are generated. On both sides, the interference visibility after the second PBS is maximised by moving the coupling stage in the long arm of the MZI. After these steps, the setup is temporally aligned. Changing the fibre length or optical path length drifts in the central interferometer after the sources only require the repetition of the first alignment step.

Local efficiencies

Local losses on the state will increase the vacuum component and therefore deteriorate the distributed state. In our implementation, we additionally introduce losses on the state in our implementation of the displacement-based measurement such that the required amplitude of the coherent state for displacement is reduced. This is required as noise caused by the seed pulses in the detector at the central station prevents us from generating coherent states with much higher amplitudes. The total efficiencies of the photons for both

Source	p	$\eta_{\mathrm{tot},s}$	$\eta_{\mathrm{tot},i}$	R_h (cps)
PPLN (Alice)	$(2.3 \pm 0.1) \times 10^{-3}$	4.7 %	1.55 %	685
PPKTP (Bob)	$(3.2 \pm 0.1) \times 10^{-3}$	4.3 %	1.18 %	720

Table 3.3.: Characterisation of the pair creation probability per pump pulse p and the total efficiency $\eta_{\mathrm{tot},s(i)}$ for the signal (idler) photons including coupling, transmission and detection efficiency measured in the full setup with 1 km of fibre in each arm of the central interferometer. Additionally, the achieved heralding rate R_h for an effective pump rate of 19 MHz is given.

Element	Alice		Bob	
	short	long	short	long
50/50 BS (+ WPs)	48.5 %	43.1 %	44.1 %	40.4 %
1st PBS	97.0 %	96.3 %	95.9 %	95.3 %
2nd PBS	45.3 %	50.0 %	44.7 %	51.4 %
Fibre coupling	82.1 %	84.3 %	82.2 %	85.3 %
FBG	93.0 %		93.4 %	
DWDM	94.5 %		88.0 %	
Transmission	92.3 %		96.6 %	
Detector	63 %		60 %	
Total	**8.9 %**	**8.9 %**	**7.4 %**	**8.0 %**

Table 3.4.: Detailed characterisation of the efficiencies of the components in the asymmetric MZIs as well as the transmission (due to fibre connectors) and detection efficiencies.

crystals are given in Tab. 3.3 and a detailed characterisation of the efficiencies for the local measurements in Tab. 3.4. The difference between the total efficiencies in Tab. 3.4 for the long paths taken by the single-photon state and $\eta_{\mathrm{tot},s}$ in Tab. 3.3 comes from the additional loss on the photons due to filtering by the DWDMs and non-unit coupling efficiencies.

3.3.3. Results

A measurement of the bipartite entanglement witness discussed in Sec. 3.1.2 as a function of the relative phase between Alice's and Bob's displacement operations is shown in Fig. 3.19. After the relative phase is set to $(\theta_B - \theta_A) = 0$, counts were acquired in the α-basis for 1 h and subsequently in the z-basis for 2.5 h by blocking the coherent state in the short paths of the asymmetric MZIs. From the click/no-click events recorded by Alice and Bob, the corresponding joint probabilities are deduced, see Tab. 3.5. We separately determine an upper bound on the probability of having more than one photon locally in a Hanbury Brown-Twiss experiment for both Alice and Bob, see Eq. (3.23). Together with the joint probabilities measured in the z-basis as well as the displacement parameter amplitudes used in the α-basis measurement, we compute the maximal separable bound $w_{\mathrm{ppt}}^{\mathrm{max}}$ according to Eq. (3.22). The experimental value for the expectation value w_{ρ}^{exp} of the witness $\hat{W}$ is computed from the measured joint probabilities in the α-basis according to Eq. (3.24).

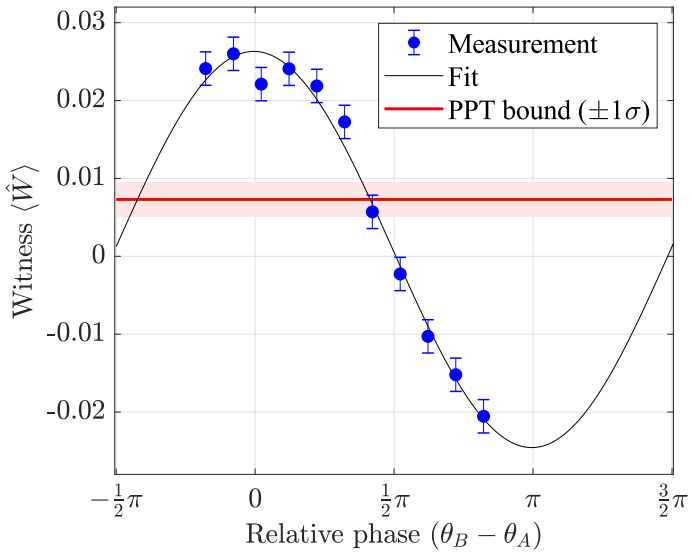

Figure 3.19.: Expectation value and PPT bound $w_{\mathrm{ppt}}^{\mathrm{max}}$ of the entanglement witness as a function of the relative phase $(\theta_B - \theta_A)$ between the displacement measurements for Alice and Bob with $l = 1.0\,\mathrm{km}$. Values of $\langle \hat{W} \rangle$ larger than $w_{\mathrm{ppt}}^{\mathrm{max}}$ demonstrate entanglement. For each phase setting, counts were acquired for 200 s in the α-basis with $|\alpha_1| = 0.818^{+0.004}_{-0.003}$ and $|\alpha_2| = 0.830^{+0.006}_{-0.007}$ indicating the mean, maximum and minimum displacement amplitudes. Error bars of the measured data represent 1 standard deviation.

l		p_{00}	p_{0c}	p_{c0}	p_{cc}	p_1^*	p_2^*
42 m	z	0.96935(5)	0.01515(3)	0.01550(3)	0.0000052(6)	$2.5(3) \times 10^{-6}$	$5.1(4) \times 10^{-6}$
	α	0.2715(2)	0.2504(2)	0.2393(2)	0.2388(2)		
1.0 km	z	0.96142(5)	0.01881(4)	0.01977(4)	0.0000059(6)	$3.2(4) \times 10^{-6}$	$1.25(8) \times 10^{-5}$
	α	0.2575(2)	0.2504(2)	0.2370(2)	0.2552(2)		

Table 3.5.: Measured joint probabilities in the z- and α-basis for different fibre lengths l in each arm of the central interferometer. The measured displacement amplitudes for $l = 42\,\mathrm{m}$ are $|\alpha_1| = 0.804^{+0.010}_{-0.009}$ and $|\alpha_2| = 0.819^{+0.003}_{-0.004}$, where for $l = 1.0\,\mathrm{km}$ we measured $|\alpha_1| = 0.819^{+0.005}_{-0.007}$ and $|\alpha_2| = 0.837^{+0.006}_{-0.007}$. The amplitudes $|\alpha_i|$ are the mean amplitudes for the α-basis measurement with bounds on the minimum and maximum obtained from the counts in 10 s intervals during the 3600 s of measurement. The probabilities of having more than one photon p_1^* on Alice's side and p_2^* on Bob's side are separately determined for each experimental run. The errors on all probabilities correspond to 1 standard deviation.

l	R_h (kcps)	SNR	w_ρ^{exp}	$w_{\mathrm{ppt}}^{\mathrm{max}}$	k
42 m	1.4	12	0.0206(8)	0.0071(16)	5.6
1.0 km	1.6	5	0.0253(7)	0.0071(22)	6.2

Table 3.6.: Measured value w_ρ^{exp} and calculated separable bound $w_{\mathrm{ppt}}^{\mathrm{max}}$ of the entanglement witness for fibres of length l in each arm of the central interferometer at an observed heralding rate R_h and signal-to-noise ratio (SNR). The witness is violated by $k = (w_\rho^{\mathrm{exp}} - w_{\mathrm{ppt}}^{\mathrm{max}})/(\sigma_{\mathrm{ppt}}^{\mathrm{max}} + \sigma_\rho^{\mathrm{exp}})$ standard deviations.

For the analysis of uncertainties on the separable bound $\sigma_{\text{ppt}}^{\max}$ and on the experimental value of the witness $\sigma_{\rho}^{\exp}$ we assume the coincidence probabilities to be independent and identically distributed (i.i.d.) random variables. The obtained results, as shown in Tab. 3.6, certify a violation of the entanglement witness by more than 5 standard deviations at a heralding rate of at least 1.4 kcps for fibre distances of $l = 42\,\text{m}$ and $l = 1.0\,\text{km}$ inserted in each arm of the central interferometer. For $l = 42\,\text{m}$ we measure a signal-to-noise ratio (SNR) for the heralding photons of 12, whereas this is decreased to 5 for $l = 1.0\,\text{km}$. This is due to noise caused by the strong seed laser pulses in the central interferometer. The higher total heralding rate in the case of $l = 1.0\,\text{km}$ is therefore due to this elevated noise contribution. The larger statistical significance of the result with $l = 1.0\,\text{km}$ compared to $l = 42\,\text{m}$ is mainly attributed to a different alignment setting in the measurement MZIs leading to an increase of the transmission on the entangled state (see p_{00} in the z-basis in Tab. 3.5).

3.3.4. Discussion

The successful implementation of the scheme required to overcome several challenges, as already described in Ref. [162]. One of them is the phase-locking of the central interferometer, which we achieve by actuating a piezo-electric fibre stretcher such that the detected power in the second output port of the central interferometer is maximised. In this way we demonstrate stable operation for several hours even for an interferometer with 1 km arm length. However, the variance of the phase noise is expected to increase linearly with the length of deployed fibre which sets limits to the phase stability [163]. Nevertheless, recent developments in twin-field QKD lead to demonstrations of phase-stabilised links over several hundred of kilometres with phase stabilisation techniques from work on frequency dissemination [164]. This shows that long-distance phase stabilised links are feasible.

Another challenge is noise caused by the seed laser leaking to the heralding detector which is linked to the phase stability of the central interferometer. We measure a seed power of about 500 nW in each arm before the BS at the central station, which corresponds to a mean number of 2×10^5 photons per pulse. This is opposed to roughly 5×10^{-4} photons per pulse in each arm for the single-photon state, given a pair generation probability per pump pulse of 3×10^{-3}. The problem with those different power levels is that even tiny reflections of the seed pulses that can occur in the setup might end up in the detection window of the single-photon state and therefore decrease the SNR. In longer fibre links, backward Brillouin scattered and forward reflected light might become a problem as well. In our implementation, the reduction in SNR at the central station due to the seed pulses is the main limiting factor which prevents us from generating higher intensity coherent states. A solution would be to use higher pump power levels for the DFG than for the SPDC. In this way, higher intensity coherent states could be produced while keeping the seed power low.

In future implementations, where higher intensity coherent states can be tolerated, the

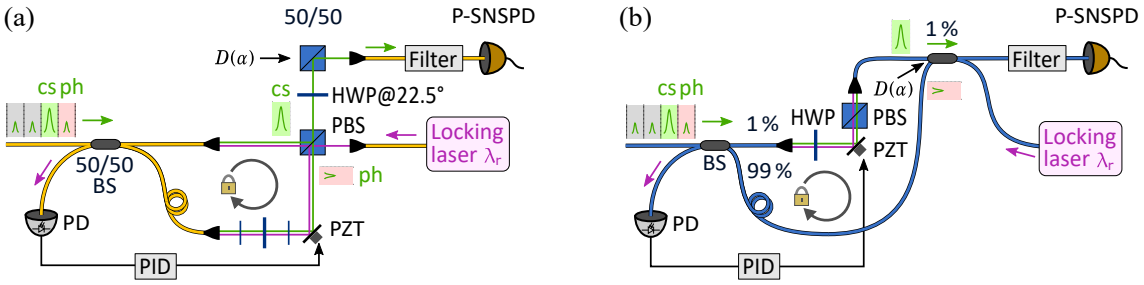

Figure 3.20.: Local displacement operation. (a) Similar setup as the one used in our implementation, where here the phase difference in the asymmetric MZI is stabilised locally. (b) Possible improved setup where two 99/1 beam splitters (BS) increase the transmission efficiency of the single-photon state (long path) towards the detector to 98 %. Polarisation-maintaining fibres ensure that the single-photon and coherent state for displacement are in the same polarisation mode. HWP, half-wave plate; PBS, polarising beam splitter;PD, photodiode; PID, proportional–integral–derivative controller; P-SNSPD, parallel superconducting nanowire single-photon detector; PZT, lead zirconate titanate (piezoelectric).

implementation of the local displacement operations could be adapted such that losses on the single-photon state are reduced. A possible variation of our implementation of the displacement-based measurement is shown in Fig. 3.20(a). Note that here, the phase-locking is done such that the phase difference in the asymmetric MZI is stabilised locally. Even without any additional losses (see Tab. 3.4), the single-photon state transmission efficiency is only 25 % due to the 50/50 BS and the PBS used for the displacement operation, which reflects 50 % of the single-photon state (and therefore 50 % of the coherent state). The setup could be improved and the single-photon state transmission efficiency increased to for example 98 %, as shown in Fig. 3.20(b). This could be achieved by using two 99/1 BSs, where on each BS the single photon state is transmitted towards the detector with 99 %. A piezo-actuated mirror in the coherent state path is used for phase-locking and a HWP and a PBS allow to set the displacement amplitude. Polarisation-maintaining fibres ensure that the single-photon and coherent state for displacement are in the same polarisation mode. The challenge with this implementation, however, would be that the interference visibility of the signal for phase-locking is only 2 % which could make accurate phase stabilisation more difficult. Moreover, another problem could be the strong coherent state with more than 6×10^3 photons per pulse on average, which takes the long path, and arrives after the displaced single-photon state at the detector. It needs to be ensured that this is not a problem for the detector and that it can recover fast enough to detect the next incoming displaced state.

3.3.5. Conclusion and outlook

Single-photon quantum repeater schemes are promising for fibre-based long-distance entanglement distribution because of their favourable transmission loss scaling, their robustness to memory and detector inefficiencies and the need for fewer resources than protocols based

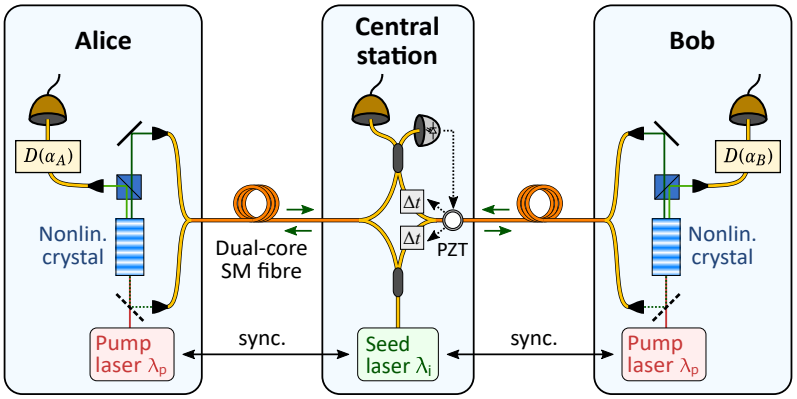

Figure 3.21.: Possible implementation of the scheme in a distributed scenario with dual-core single-mode (SM) fibres. The additionally required active polarisation control is not shown.

on two-photon detections [65]. We demonstrated the feasibility of such a scheme by actively stabilising the phase of an interferometer with arm lengths of 1.0 km and utilising local displacement-based measurements for entanglement certification by means of an entanglement witness. In our scheme the phase difference between the asymmetric MZIs also needs to be stabilised, however, in a quantum repeater these asymmetric MZIs could be replaced, and the displacement performed, by quantum memories [165, 166].

In principle, the scheme can be extended for real world applications by using two individual pump lasers, adding fibre before the sources to distribute the seed pulses, and further increasing the size of the central interferometer. Apart from the frequency-locking of the pump lasers and the synchronisation of all the lasers, the main technical challenge in such an implementation is the increase of phase noise in a larger central interferometer [163]. This would not only degrade the entanglement, but also increase the leakage of residual seed laser photons towards the heralding detector. Our solution to suppress them with an EOIM introduces unwanted loss on the heralding photons. Hence, a better solution would be to develop a gated SNSPD for the central station.

Another problem in a real-world implementation would be the optical path length drift in the central interferometer before the crystals. In our implementation, drifts mainly occur in the added fibres after the crystals, therefore the feedback to Δt_3 at the central station corrects for this and automatically ensures that the idler photons arriving at the central station do not drift out of their coherence time. This would not be the case any more if fibre is added before the crystals and drifts would be caused there as well. Thus, a more complicated stabilisation scheme would be required. A possibly simpler solution for that problem would be to distribute the seed from the central station through one core of a dual-core fibre to Alice (Bob) and send back the idler photons and seed pulses through the other core of the fibre, as shown in Fig. 3.21. Under the assumption that optical path length drifts in the dual-core fibre are the same for both cores, they could be compensated by delay lines at the central station which uniformly act on both cores of Bob's fibre. The

required phase and optical path length stability, as well as if the crosstalk between the two cores is tolerable, would need to be investigated.

Despite all these challenges, one of the main advantages of this protocol is that the pair sources can be designed such that they generate highly non-degenerate photons. In this way, the local photons can be directly interfaced with quantum memories, whereas the photons which are sent to the central station are at telecommunication wavelength. This has recently been demonstrated with two multimode praseodymium-doped solid-state quantum memories [61]. The used type-I cavity-enhanced SPDC sources based on PPLN crystals produce narrow-band photons at a wavelength of 606 nm for storage and at 1436 nm for transmission, with the entanglement heralded at a rate of 1.4 kcps, similar to the rate in our demonstration. Therefore, by further improving the heralding and memory efficiencies, this scheme holds promise for the realisation of a high-rate quantum repeater.

4. Distribution of polarisation entanglement

In the previous chapter, we discussed the heralded distribution of single-photon path entanglement with two weakly pumped photon-pair sources, based on the scheme of Ref. [161]. Another scheme for the distribution of entanglement would be the approach of Ref. [86] where locally, single photons are input on imbalanced BSs with high reflectance r, as shown schematically in Fig. 4.1(a). The modes with low transmittance t are then combined on a 50/50 BS to perform a Bell state measurement (BSM), which leaves the modes a and b in a single-photon entangled state. Although the scaling as a function of the transmission distance is favourable for single-photon entanglement, the requirement of phase stability and the difficulty of implementing distributed displacement-based measurements make real world implementations of such a scheme challenging.

Alternatively, as shown in Fig. 4.1(b), a high-fidelity polarisation-entangled state can be distributed between modes a and b by multiplexing the scheme in Fig. 4.1(a) for horizontally and vertically polarised input photons and heralding upon a coincidence detection of, for example, H in the first output port and V in the second output port at the BSM. In combination with on-demand single photon sources, this scheme has been proposed for photonic DI-QKD [87, 167]. However, experimentally it is hard to have highly imbalanced beam splitters with polarisation-independent splitting ratios, as required for a direct implementation of this scheme.

A different approach which similarly generates polarisation-entangled states with PBSs is schematically shown in Fig. 4.1(c). Four diagonally polarised photons are input to PBSs and the BSM is realised with a type-II fusion gate, where HWPs are used to rotate the PBS basis to 45°, i.e. diagonal polarisation states are transmitted and anti-diagonal states reflected [169]. This scheme has been previously demonstrated with a SPDC source in a double-pass configuration and 4-fold post-selection in a bulk setup [168], and more recently with two local quantum memories based on rare-earth ion doped crystals [170]. In a similar fashion, a two-hierarchy entanglement swapping scheme has been shown [171]. Interestingly, in the two-hierarchy scheme, the noise terms present in the swapped state of the one-hierarchy links (scheme in Fig. 4.1(c)) are filtered out by the connecting Bell state measurement.

Here, we consider the scheme as presented in Fig. 4.1(d), where polarisation-entangled states can be distributed in a heralded fashion. This can be seen as hybrid between the schemes in Figs. 4.1(b) and (c) since locally we use PBSs, but the BSM is realised with a BS to facilitate the alignment in a fibre implementation. In order to achieve a tunable

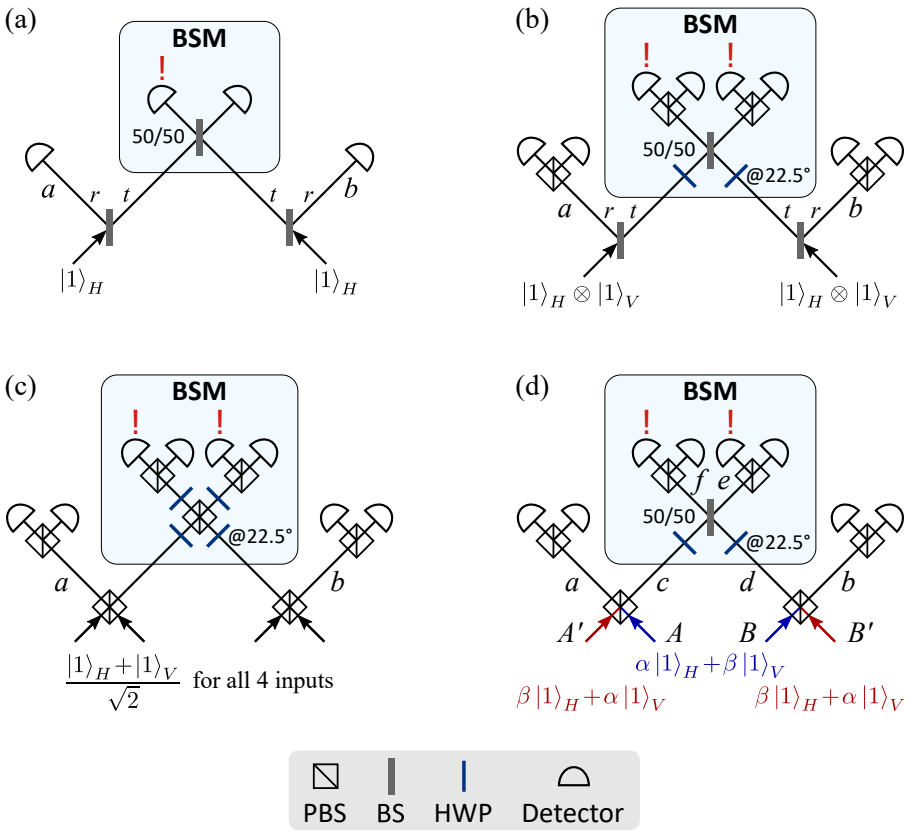

Figure 4.1.: Different schemes for the distribution of entanglement with the corresponding detection pattern (!) at the Bell state measurement (BSM). (a) Heralded distribution of single-photon path entanglement with two single photons input on imbalanced beam splitters (BS) and a 50/50 BS at the BSM, see Ref. [86]. (b) Heralded distribution of a polarisation-entangled two-photon state by inputting two orthogonally polarised single photons on each side, see Ref. [87]. Half-wave plates (HWP) at 22.5° are used to reduce unwanted heralding events. (c) Generation of polarisation-entangled states by using polarisation beam splitters (PBS) and a type-II fusion gate for the BSM, see Ref. [168]. (d) Heralded distribution of polarisation entanglement with linearly polarised states input to PBSs and the BSM employing a 50/50 BS.

effective imbalance between reflected and transmitted two-photon states, we consider linearly polarised input states which are biased from diagonal towards the horizontal and vertical polarisation state, respectively.

4.1. A scheme for photonic polarisation entanglement distribution

We now take a closer look at the scheme presented in Fig. 4.1(d) and calculate the heralded state. The goal is to distribute a state close to a maximally polarisation-entangled state in the spatial modes a and b upon a 2-fold coincidence detection at the Bell state measurement. With $\hat{a}_m^\dagger$ we denote the bosonic creation operator on mode m (polarisation and path, see Fig. 4.1(d) for the labelling). For the first input PBS, we assume the following input-output relations

$$\hat{a}_{HA}^\dagger \to \hat{a}_{Ha}^\dagger, \qquad \hat{a}_{HA'}^\dagger \to \hat{a}_{Hc}^\dagger, \tag{4.1}$$

$$\hat{a}_{VA}^\dagger \to \mathrm{i}\,\hat{a}_{Vc}^\dagger, \qquad \hat{a}_{VA'}^\dagger \to \mathrm{i}\,\hat{a}_{Va}^\dagger. \tag{4.2}$$

Similarly, by replacing the spatial modes $A \to B$, $a \to b$ and $c \to d$, the relations for the second input PBS are obtained. For the HWP in spatial mode c with its fast axis set at an angle θ_c with respect to the horizontal axis (and similarly for d), we model the input-output relations by (see p. 212 in Ref. [172])

$$\hat{a}_{Hc}^\dagger \to \Big(\cos(2\theta_c)\hat{a}_{Hc'}^\dagger + \sin(2\theta_c)\hat{a}_{Vc'}^\dagger\Big), \tag{4.3}$$

$$\hat{a}_{Vc}^\dagger \to \Big(\sin(2\theta_c)\hat{a}_{Hc'}^\dagger - \cos(2\theta_c)\hat{a}_{Vc'}^\dagger\Big). \tag{4.4}$$

Furthermore, the input-output relations for the spatial modes of the 50/50 BS at the BSM are given by [173]

$$\hat{a}_{c'}^\dagger \to \frac{1}{\sqrt{2}}\big(\hat{a}_e^\dagger + \mathrm{i}\,\hat{a}_f^\dagger\big), \qquad \hat{a}_{d'}^\dagger \to \frac{1}{\sqrt{2}}\big(\mathrm{i}\,\hat{a}_e^\dagger + \hat{a}_f^\dagger\big). \tag{4.5}$$

We now start with the calculation of the state after the input PBS, where we consider the single-photon polarisation state $\alpha\,|1\rangle_H + \beta\,|1\rangle_V$ input in the spatial mode A, and $\beta\,|1\rangle_H + \alpha\,|1\rangle_V$ in the spatial mode A'. Here, we take $\alpha, \beta \in \mathbb{R}$ with $\alpha^2 + \beta^2 = 1$. By applying the PBS transformation, the state in the spatial modes a and c is calculated to be

$$\begin{aligned}\big(\alpha\hat{a}_{HA}^\dagger + \beta\hat{a}_{VA}^\dagger\big)\big(\beta\hat{a}_{HA'}^\dagger + \alpha\hat{a}_{VA'}^\dagger\big)\,|\bar{0}\rangle \to \alpha\beta\overbrace{\big(\hat{a}_{Ha}^\dagger\hat{a}_{Hc}^\dagger - \hat{a}_{Va}^\dagger\hat{a}_{Vc}^\dagger\big)\,|\bar{0}\rangle}^{\sqrt{2}|\Phi^-\rangle_{ac}} \\ + \mathrm{i}\,\big(\alpha^2\hat{a}_{Ha}^\dagger\hat{a}_{Va}^\dagger + \beta^2\hat{a}_{Hc}^\dagger\hat{a}_{Vc}^\dagger\big)\,|\bar{0}\rangle\end{aligned} \tag{4.6}$$

and similarly for the spatial modes b and d. Here, $|\bar{0}\rangle$ denotes the vacuum state on all involved modes. We note that after post-selection of one photon in the spatial modes a and one photon in mode c, this state is the Bell state $|\Phi^-\rangle_{ac}$ in polarisation. However, without post-selection we have two additional terms corresponding to two orthogonally polarised photons in each of the spatial modes a and c, respectively.

We now consider the case of $\theta_c = \theta_d = 0°$ and calculate the final state. The terms after the BSM that contain *one* photon in the mode Ve and *one* in Hf (projecting on $|\Psi^-\rangle_{c'd'}$), are

$$\hat{a}^\dagger_{Ve}\hat{a}^\dagger_{Hf}\frac{1}{\sqrt{2}}\alpha^2\beta^2\Big(-\overbrace{\frac{1}{\sqrt{2}}\big(\hat{a}^\dagger_{Ha}\hat{a}^\dagger_{Vb}-\hat{a}^\dagger_{Va}\hat{a}^\dagger_{Hb}\big)|\bar{0}\rangle}^{|\Psi^-\rangle_{ab}}+\frac{\mathrm{i}}{\sqrt{2}}\big(\hat{a}^\dagger_{Ha}\hat{a}^\dagger_{Va}+\hat{a}^\dagger_{Hb}\hat{a}^\dagger_{Vb}\big)|\bar{0}\rangle\Big). \tag{4.7}$$

Besides the maximally polarisation-entangled state $|\Psi^-\rangle_{ab}$, we also have noise contributions corresponding to two orthogonally polarised photons in each of the modes a and b, respectively. Additionally, terms with at least three photons in total in the modes Ve and Hf (and at least one photon in each mode) occur with probability $\alpha^2\beta^6 + \frac{1}{4}\beta^8$. All these unwanted terms can still be suppressed by post-selecting on coincidence detections in a and b. However, we note that by setting the HWPs in the spatial modes c and d to $\theta = 22.5°$, the last term in the expression (4.6) becomes

$$\hat{a}^\dagger_{Hc}\hat{a}^\dagger_{Vc} \to \frac{1}{2}\Big(\big(\hat{a}^\dagger_{Hc'}\big)^2-\big(\hat{a}^\dagger_{Vc'}\big)^2\Big) \tag{4.8}$$

and similarly for the spatial mode d. In this case, the part of the final state where we detect *one* photon in the mode Ve and *one* in Hf at the BSM becomes

$$\begin{aligned}&\hat{a}^\dagger_{Ve}\hat{a}^\dagger_{Hf}\Big(\frac{1}{\sqrt{2}}\alpha^2\beta^2\overbrace{\frac{1}{\sqrt{2}}\big(\hat{a}^\dagger_{Ha}\hat{a}^\dagger_{Vb}-\hat{a}^\dagger_{Va}\hat{a}^\dagger_{Hb}\big)|\bar{0}\rangle}^{|\Psi^-\rangle_{ab}}+\frac{1}{2}\beta^4\hat{a}^\dagger_{He}\hat{a}^\dagger_{Vf}|\bar{0}\rangle\\&+\frac{1}{4}\alpha\beta^3\big(\hat{a}^\dagger_{He}\big(\hat{a}^\dagger_{Ha}+\hat{a}^\dagger_{Va}+\mathrm{i}\hat{a}^\dagger_{Hb}+\mathrm{i}\hat{a}^\dagger_{Vb}\big)-\hat{a}^\dagger_{Vf}\big(\mathrm{i}\hat{a}^\dagger_{Ha}-\mathrm{i}\hat{a}^\dagger_{Va}+\hat{a}^\dagger_{Hb}-\hat{a}^\dagger_{Vb}\big)\big)|\bar{0}\rangle\Big).\end{aligned} \tag{4.9}$$

We see that the coefficient of the term $|\Psi^-\rangle_{ab}$ is $\frac{1}{\sqrt{2}}\alpha^2\beta^2$, as is the case for the HWPs set at $\theta = 0°$. However, now we have one unwanted term with coefficient $\frac{1}{2}\beta^4$ and 8 terms with coefficient $\frac{1}{4}\alpha\beta^3$ and therefore we can reduce their contribution to the heralded state by setting $\alpha^2 = (1-\beta^2) \to 1$. Also, we note that all the unwanted contributions lead to detections in the modes He and/or Vf and could therefore be reduced by heralding only upon a 2-fold coincidence detection in the modes Ve and Hf (excluding 3- and 4-fold coincidences at the BSM). However, in the case of loss between the local parties and the BSM, this only partially works because, for example, missing one photon in an event that would lead to a 3-fold coincidence could lead to the 2-fold coincidence detection we are looking for.

We now have a closer look at the outcome probability of the wanted output state $|\Psi^-\rangle_{ab}$. The probability of having a coincidence detection in the modes Ve and Hf together with

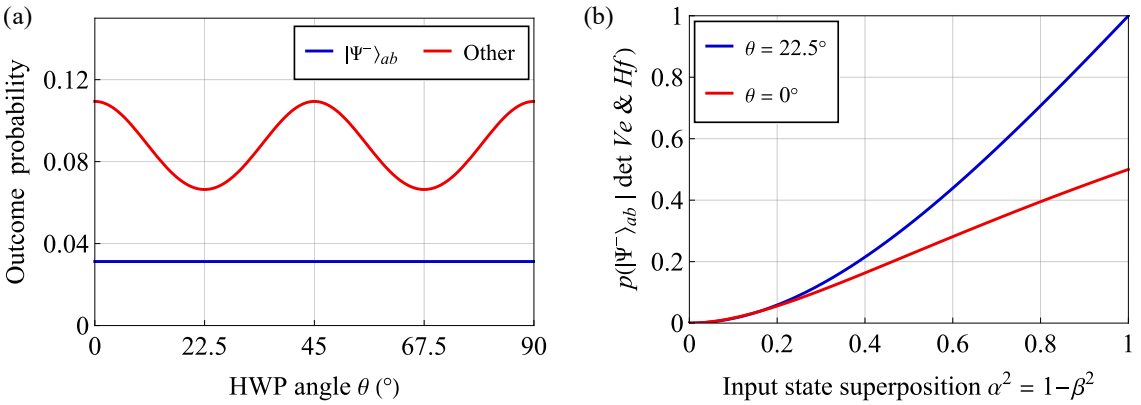

Figure 4.2.: Calculation of the outcome probabilities when four photons are input to the first PBSs and no loss is present in the system. (a) Overall outcome probability as a function of the HWP angle in the spatial modes c and d for diagonally polarised input states, i.e. $\alpha = \beta = \frac{1}{\sqrt{2}}$. The probability is shown for a heralding coincidence detection in the modes Ve, Hf and having the state $|\Psi^-\rangle_{ab}$ in the modes a and b in blue. In red is shown the probability of the heralding coincidence detection together with unwanted other terms, also including zero/one photons in the spatial modes a and b. (b) Normalised probability of heralding the state $|\Psi^-\rangle_{ab}$, without post-selection on coincidences in the modes a and b, when detecting coincidences in the modes Ve and Hf at the BSM. This probability is shown for the two extremal HWP settings as a function of α^2, which defines the four input states.

the state $|\Psi^-\rangle_{ab}$ in the modes a and b is $\frac{1}{2}\alpha^4\beta^4$. However, there are other unwanted terms which can lead to a coincidence detection in the modes Ve and Hf, but do not herald the state $|\Psi^-\rangle_{ab}$. As shown in Fig. 4.2(a), the probability of those terms varies as a function of the angle of the HWPs in the spatial modes c and d. Note that here we only consider the case where both HWPs have the same setting, since different settings reduce the probability of heralding the state $|\Psi^-\rangle_{ab}$. For $\theta = 22.5°$, those unwanted terms are the ones in expression (4.9) (with probability $\frac{1}{2}\alpha^2\beta^6 + \frac{1}{4}\beta^8$) as well as contributions with at least three photons in total in the modes Ve and Hf that occur with probability $\frac{1}{4}\alpha^2\beta^6 + \frac{1}{16}\beta^8$. The normalised probability of heralding the state $|\Psi^-\rangle_{ab}$ when detecting coincidences in the modes Ve and Hf without post-selection, i.e. without only considering 2-fold coincidence detections in the spatial modes a and b, is shown in Fig. 4.2(b). We see that for HWP settings of $\theta = 22.5°$, the probability of heralding the state $|\Psi^-\rangle_{ab}$ approaches unity for highly imbalanced input states, i.e. $\alpha^2 = (1-\beta^2) \to 1$.

4.2. Implementation with photon-pair sources

The scheme described in the previous section is implemented with a bidirectionally pumped photon-pair source based on degenerate SPDC. However, these sources generate photon pairs probabilistically and suffer from multi-pair generation which so far have not been

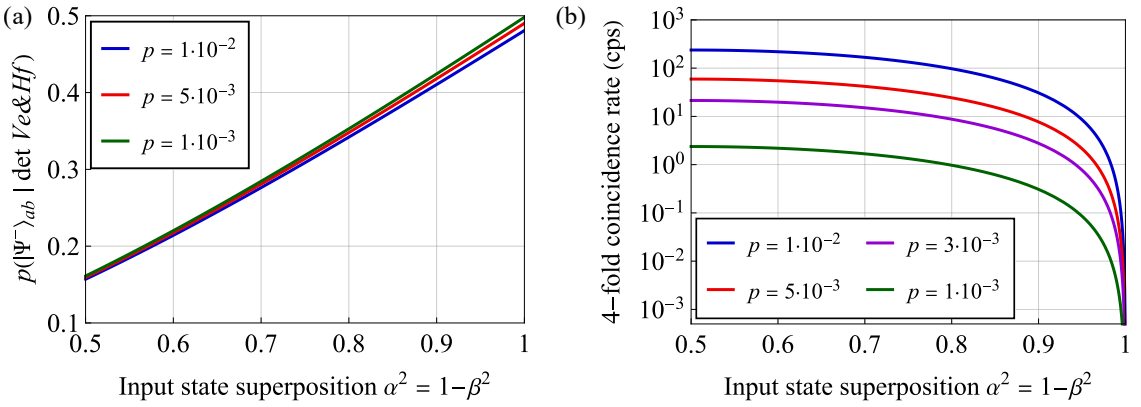

Figure 4.3.: Expected performance for a lossless implementation of the scheme with SPDC sources for different pair creation probabilities per pump pulse p. Here, a pump rate of 76 MHz is assumed and the HWPs in the modes c and d are set to $\theta = 22.5°$. (a) Normalised probability of heralding the state $|\Psi^-\rangle_{ab}$, without post-selection on coincidences in the modes a and b, given a coincidence detection in the modes Ve and Hf as a function of the input state coefficient α^2. (b) Four-fold coincidence detection rate in the modes Ve, Hf, a and b, as a function of α^2, with no loss.

considered. The first part of this section looks at the impact of double-pair generation on the scheme along with the rate trade-off which must be considered for the experimental implementation. In the remainder of the section, the actual experimental implementation is presented.

4.2.1. Expected rates and limitations from double-pair contributions

We calculate the expected performance of the scheme presented in Fig. 4.1(d) for the case where two weakly pumped photon-pair sources are used to generate the 4 input photons. For this calculation, we assume a pump repetition rate of 76 MHz, as in the experiment. In our model, each source emits a photon pair with probability p per pump pulse. Therefore, with probability p^2, a 4-photon state is generated. Contributions from one pair on each side are taken into account as well as double pair contributions on Alice's and on Bob's side, respectively. Furthermore, we consider events where one source emits a pair and the other source emits a double pair, which occurs with probability $2p^3$ in total, and triple pairs on either side. All other terms of order $\mathcal{O}(p^4)$ are neglected for this calculation.

We then calculate the probability of having the state $|\Psi^-\rangle_{ab}$ conditioned on a coincidence detection in the modes Ve and Hf. Here, we include all photon-number terms at the BSM, i.e. up to 6 photons which lead to a coincidence detection. Shown in Fig. 4.3(a) is this probability of heralding $|\Psi^-\rangle_{ab}$ as a function of the input states. This is analogous to Fig. 4.2(b), however, now with the inclusion of double pairs. Note that here, we only consider the case where the HWPs are set to $\theta = 22.5°$. Also, the calculation does not include losses in the system, which would decrease the probability of having the state

$|\Psi^-\rangle_{ab}$. The calculated probability shows a similar behaviour as in the case where no double pairs are present (see Fig. 4.2(b)), however, the maximum achievable probability is reduced to a value below 0.5, mainly due to one-sided double pair contributions, and decreases with increasing pair creation probability p.

Additionally, we calculate the lossless 4-fold coincidence rate between the detectors in the modes Ve, Hf, a and b. In Fig. 4.3(b), this is shown for different pair creation probabilities p as a function of the input state parameter α^2. We see that for increasing α^2, which increases the probability of heralding the wanted state $|\Psi^-\rangle_{ab}$, the 4-fold rate is drastically reduced and therefore, there is a trade-off between the rate and the probability of heralding the correct state. In a realistic implementation, the rate is further reduced due to non-unit heralding and detection efficiencies (η_h and η_d). To first order, multiplying the calculated lossless rate by a factor $(\eta_h\eta_d)^4$ gives an estimate of the rate that can be expected in the experiment.

4.2.2. Experiment

The experimental implementation of our scheme is shown in Fig. 4.4. We use a PPKTP nonlinear crystal with parameters as discussed in Sec. 2.2 for type-II SPDC. The crystal is bidirectionally pumped by a picosecond pulsed laser (76 MHz repetition rate) at $\lambda_p = 771.85\,\text{nm}$ to create degenerate photons at $\lambda_s = \lambda_i = 1543.7\,\text{nm}$. A delay stage in Alice's pump path allows one to induce a time delay Δt between the pairs generated in opposite directions. For both pump directions, the photon pair creation probability per pump pulse is kept at $p \approx 3 \times 10^{-3}$ in order to keep the probability of having double-pair emissions low. The orthogonal signal and idler modes are separated after their generation at the first PBSs. After that, we prepare the linearly polarised initial states by means of HWPs before they are input into the combining PBSs. There is a walk-off between the two orthogonally polarised photons of around 4.5 ps due to the birefringence of the PPKTP crystal. This is compensated for by positioning the combining PBSs such as to negate this by setting a 1.35 mm shorter path for the H photons than for the V photons.

Locally, on Alice's and Bob's side, we have a quarter-wave plate (QWP) and a HWP followed by a PBS and two SNSPDs on each output mode in order to measure the state in any basis. The other two modes are coupled into fibre and combined on a 50/50 fibre BS at the central station. The three wave plates on Alice's side before coupling into the fibre allow for relative phase control between the modes Hc and Vc, which suffices to adjust the phase ϕ in the wanted part of the heralded state $(|HV\rangle_{ab} + e^{i\phi}|VH\rangle_{ab})$. The polarisation controllers are used for polarisation alignment by inputting light in the reverse direction and measuring the polarisation state with a polarimeter in free space. Note that the polarisation alignment must be such that the unitary transformation of the polarisation state from Alice's side to the 50/50 fibre BS is the same as for the one on Bob's side. After the BS at the central station, we spectrally filter with 200 GHz DWDMs at ITU channel 42 (1543.73 nm) in order to herald photons on Alice's and Bob's side with high spectral

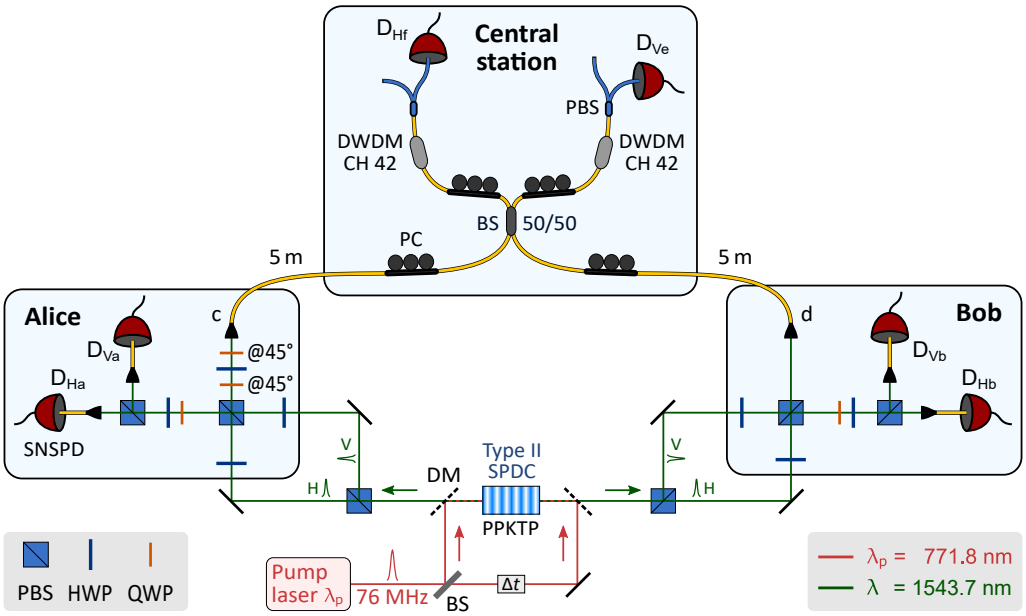

Figure 4.4.: Setup for the distribution of polarisation entanglement. The pulsed pump laser bidirectionally pumps the nonlinear crystal to create degenerate photon pairs, which are separated on each side by a PBS. The four photons are then recombined on subsequent PBSs in linear polarisation states. One part of the state is kept locally, whereas the other part of the state from each side is sent to the Bell state measurement at the central station where we detect coincidences between detectors D_{Ve} and D_{Hf}. BS, beam splitter; DM, dichroic mirror; DWDM, dense wavelength division multiplexer; HWP, half-wave plate; PBS, polarising beam splitter; PC, polarisation controller; PPKTP, periodically poled potassium titanyl phosphate; QWP, quarter-wave plate; SNSPD, superconducting nanowire single-photon detector; SPDC, spontaneous parametric down-conversion.

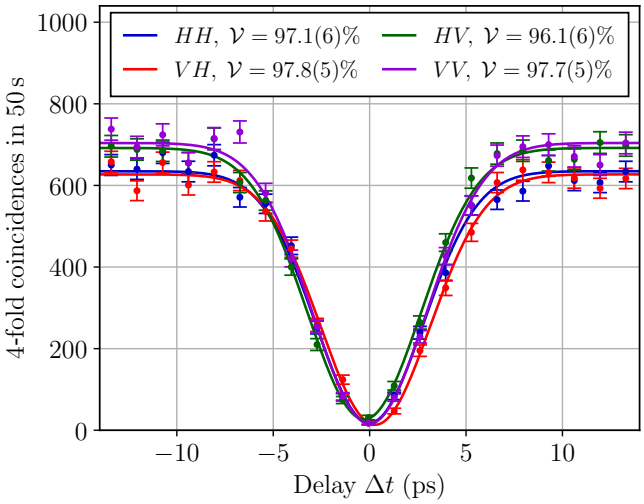

Figure 4.5.: Hong-Ou-Mandel (HOM) interference for all four combinations of photons (HH, HV, VH and VV) from Alice's and Bob's side sent to the 50/50 BS at the Bell state measurement. The 4-fold coincidences between the two local heralding detectors and the two detectors at the central station are recorded as a function of the delay Δt in Alice's pump path. The visibilities $\mathcal{V}$ are calculated for all four HOM dips from a weighted inverse Gaussian fit, where the weight of each data point is $1/\sigma$ under the assumption of Poissonian count statistics with standard deviation σ.

purity. We then employ fibre PBSs to project on the horizontal and vertical polarisation modes before detecting photons with SNSPDs. Due to the limited availability of detectors, we only use two SNSPDs, one in the mode Ve and one in Hf.

All SNSPDs used are MoSi single-meander detectors with detection efficiencies between 79 % and 90 %. When detecting directly after the fibre couplers in the spatial modes c and d, without going through the BSM setup, the heralding efficiencies for all modes are between 65 % and 75 % (including coupling and transmission efficiencies, excluding detection efficiencies). The symmetric coupling efficiency is measured to be around 90 %, whereas the transmission efficiencies through the optical elements are between 72 % and 83 %, depending on the path.

The impact of finite indistinguishability and spectral purity of the generated photons is quantified by measuring their Hong-Ou-Mandel (HOM) interference, as shown in Fig. 4.5. We send all four different combinations of horizontally/vertically polarised photons on Alice's and Bob's side to the 50/50 BS at the Bell state measurement, with the other photon of each pair detected locally. The wave plates on Alice's side before coupling into fibre are used to ensure that the polarisation of Alice's photons match those of Bob at the 50/50 BS. The 4-fold coincidences between the two local heralding detectors and the two detectors at the central station (in the modes He and Hf for HH and VH photons, or in the modes Ve and Vf for HV and VV photons) are recorded as a function of the delay Δt in Alice's pump path. We observe HOM visibilities of around 97 % for all four

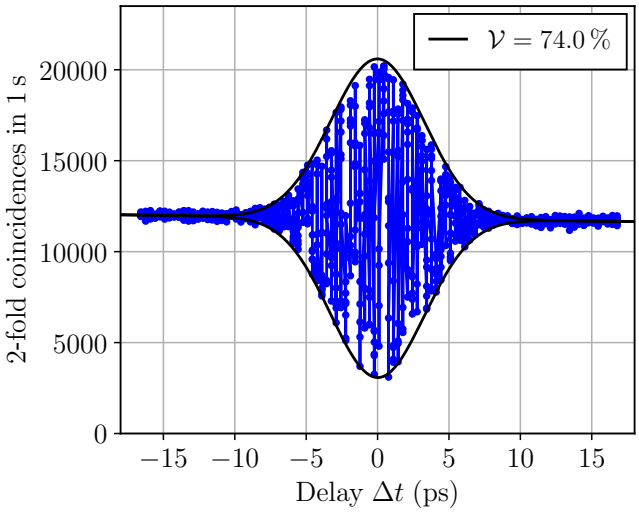

Figure 4.6.: Measurement of the 2-photon coincidence counts in the modes Ve and Hf, when sending H and V photons on Alice's and Bob's side to the central station, as a function of the delay Δt in Alice's pump path.

combinations. Moreover, we see that the photons from different input paths are temporally well aligned since all four HOM dips are centred around a delay of $\Delta t = 0\,\text{ps}$.

If the path length difference between Alice-BSM and Bob-BSM is changed, the temporal alignment can be regained by HOM interference, as shown in Fig. 4.5. Another possibility for faster temporal alignment, used in the experiment, is to send on each side both horizontally and vertically polarised photons to the central station and record 2-photon coincidences in the modes Ve and Hf, as shown in Fig. 4.6. Like this, a MZI is effectively spanned between the BS in the pump path and the BS at the central station, hence the coincidence counts depend on the phase difference between the two arms of the MZI if the photons from both sides temporally overlap. We can therefore temporally align the setup by setting the delay Δt such that the interference visibility is maximised. We acquire 10 points per delay setting with an integration time of 1 s per point. The low maximum interference visibility is attributed to phase fluctuations which occur over shorter time scales than 1 s. Using shorter integration times would increase the visibility, however, it would also lower the coincidence count rate and therefore increase the statistical error. For the same number of delay settings Δt, this measurement is five times faster than the one based on HOM interference shown in Fig. 4.5.

4.2.3. Results

Using the previously described experimental arrangement, we measure the distributed entanglement between Alice and Bob for a configuration where we input diagonally polarised states, i.e. $\frac{1}{\sqrt{2}}\left(\hat{a}_H^\dagger + \hat{a}_V^\dagger\right)|0\rangle$, on all four spatial input modes in order to achieve maximum count rates. We then characterise the entanglement by detecting 4-fold coincidences

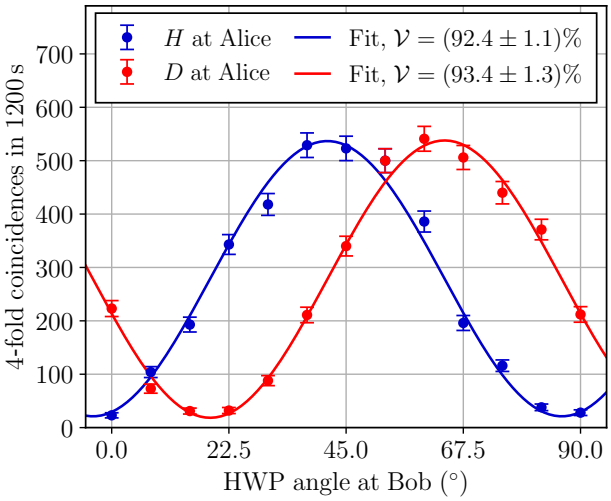

Figure 4.7.: Characterisation of the entangled state between Alice and Bob. Four-fold coincidences between the detectors in the modes Ha, Hb, Ve and Hf are recorded within 20 min as a function of the HWP setting on Bob's side. The measurement is performed for two different settings on Alice's side corresponding to the projection on the horizontal (blue) and diagonal (red) polarisation state. The visibilities $\mathcal{V}$ are calculated from a weighted sinusoidal fit, where the weight of each data point is $1/\sigma$ under the assumption of Poissonian count statistics with standard deviation σ.

between the BSM detectors (D_{Ve} and D_{Hf}) and the local detectors on the transmitted output ports of the PBSs (D_{Ha} and D_{Hb}). The coincidences as a function of the HWP angle on Bob's side are shown in Fig. 4.7 for two wave plate settings on Alice's side, corresponding to the projection on horizontal and diagonal polarisation states, respectively. For this measurement, we did not use any QWPs before the HWPs and the projecting PBSs, since only projections on linear polarisation states are measured. Moreover, since we measure 4-fold coincidences, we align the polarisation controllers at the central station such that no effective HWP is implemented for simplicity, and therefore measure the state given by the expression (4.7) .

In this way, we measure a mean 2-fold coincidence rate at the BSM of 3.0 kcps, however, the rate fluctuates as a function of the phase difference in the two paths of the effective MZI due to the interfering terms $\hat{a}^\dagger_{Hc}\hat{a}^\dagger_{Vc}$ and $\hat{a}^\dagger_{Hd}\hat{a}^\dagger_{Vd}$, see Fig. 4.6. In the 4-fold coincidence detections, those interfering terms drop out. The achieved maximum 4-fold coincidence rate is (0.45 ± 0.02) cps and the measured visibilities are $\mathcal{V} = (92.4 \pm 1.1)\,\%$ and $\mathcal{V} = (93.4 \pm 1.3)\,\%$, respectively. This corresponds to a fidelity to the state $|\Psi^-\rangle_{ab}$ of $\mathcal{F} \geq (1 + 3\mathcal{V})/4 = (94.3 \pm 0.8)\,\%$.

Further work towards a full implementation of the setup shown in Fig. 4.4 with imbalanced input states ($\alpha > \beta$) is currently ongoing.

4.3. Discussion and outlook

We have demonstrated a scheme for the distribution of polarisation entanglement, where the four input photons are separable in their polarisation degree of freedom. We achieve visibilities of more than 92 % in both bases, limited by the non-unit spectral purity of the photons, the different extinction ratios of the combining PBSs, as well as slight polarisation and temporal misalignment in the setup. It remains to quantify the corresponding contributions to the reduction in visibility and to estimate their impact on the scheme in the case where the input polarisation states of the photons are imbalanced, i.e. $\left(\alpha\hat{a}^{\dagger}_{HA} + \beta\hat{a}^{\dagger}_{VA}\right)|0\rangle$ and $\left(\beta\hat{a}^{\dagger}_{HA'} + \alpha\hat{a}^{\dagger}_{VA'}\right)|0\rangle$ with $\alpha > \beta$ (and the same input states on Bob's side).

In order to achieve long-distance entanglement distribution with this scheme, several changes have to be made. Most importantly, the probabilistic photon-pair sources based on SPDC need to be replaced by deterministic single-photon sources which have reduced double-pair generation issues. In this way high 4-photon generation rates can be achieved, without compromising the photon-number purity of the generated input states. A promising platform to achieve this is represented by semiconductor quantum dot single photon sources [89–91]. However, the challenge in such an implementation is to generate highly indistinguishable photons. While the two input photons on each side can be extracted from subsequently generated photons of the same quantum dot, photons produced by the two distant quantum dot sources also need to show high indistinguishability. Recent progress in the development of GaAs quantum dots lead to a HOM visibility of (90.9 ± 0.8) % for the two photons originating from two remote quantum dots [92]. Thus, this platform holds promise for the realisation of long-distance entanglement distribution. However, the downside of most state-of-the-art quantum dot sources is that they need to by operated at cryogenic temperatures, typically below 30 K, and that they emit photons which are not at telecommunication wavelengths. Thus, frequency conversion to telecommunication wavelengths is required for fibre-based long-distance entanglement distribution. Another option for sources in the quasi-deterministic regime, which can generate highly indistinguishable telecom photons and work at room temperature, would be multiplexed SPDC sources [174].

Furthermore, a real-world implementation for long-distance polarisation entanglement distribution might require active polarisation and optical path length stabilisation to correct for slow drifts which could make photons from Alice and Bob arrive at the BSM outside of their coherence time. Although a passively stable link over 192 km of submarine fibre cables has been demonstrated for several hours [41], field deployed fibres are usually subject to changes of the refractive index as a function of temperature and, due to the stress induced birefringence in the fibre, require active polarisation stabilisation [42, 175].

5. Conclusion and outlook

This thesis has presented resources and protocols for applications in the rapidly developing field of quantum technology. Specifically, we presented a tool to characterise single-photon sources and showed how to improve heralded single-photon sources. Moreover, we addressed the problem of certification and distribution of photonic entanglement.

In the first part of this thesis, we presented a benchmark for single-photon sources based on the outcome of an autocorrelation measurement, where a 50/50 beam splitter and two click/no-click detectors are used. The commonly used measurement of the second-order autocorrelation function gives information about the higher-order photon-number probabilities with respect to the single-photon probability. However, in many applications, single-photon sources are not only required to have a low emission probability of higher-order photon-number states, but also need to show a high efficiency. Therefore, the single-photon probability P_1 is a natural benchmark for such a source. We have shown how to obtain a lower bound on the probability of having exactly a single photon in the state, without assumptions on the beam splitter ratio or the detection efficiencies in the measurement apparatus. The analysis is extended to the case where the detection efficiencies and splitting ratio of the beam splitter are taken into account. In this way, the source can be characterised independently of the measurement apparatus. Furthermore, if the state is in a single optical mode or if the single-photon probability in one mode of a multimode state can be lower bounded, we can use the single-photon probability to witness and measure the Wigner negativity in the state, the strongest form of non-classicality. We experimentally demonstrated our benchmark with a heralded single-photon source, where the heralding idler photon is spectrally filtered to increase the spectral purity of the signal photon. Without assumptions on the measurement apparatus, we obtain a lower bound on P_1 of 0.554 with a confidence level of $(1 - 10^{-10})$ and witness Wigner negativity. With the imperfections of the measurement apparatus taken into account, the benchmark yields a lower bound on P_1 of 0.677. This benchmark will hopefully find use in the community which develops single-photon sources, along with other established characterisation tools.

Second, we improved the heralded single-photon source by employing a photon-number-resolving detector as the heralding detector, which filters out multi-photon heralding events. The photon-number resolution is achieved thanks to a recently developed parallel SNSPD without electrical thermal crosstalk between adjacent pixels [120, 121]. In the experimentally relevant low-squeezing regime, we achieve a reduction of the heralded $g^2(0)$ of $(26.9 \pm 0.1)\,\%$ compared to the case where we operate the detector in threshold mode.

Inversely, this corresponds to an increase of the heralding rate by a factor of 1.368 ± 0.002 when the heralded $g^2(0)$ is kept at the same value as in the threshold heralding mode. These values are achieved thanks to the high single-photon efficiency of the P-SNSPD of 84 % and the relatively high coupling and transmission efficiency of the heralding photons of 75 %. Those parameters are crucial for further improving the source. Another crucial parameter is the capability of the PNR detector to distinguish between a single photon and all multi-photon input states. Compared to other demonstrations [124, 125], our 4-pixel P-SNSPD is clearly limited in that regard, due to the limited number of pixels and the adjacent pixel geometry which results in the two centre pixels receiving more light than the two outer pixels. Therefore, further development of high-efficieny P-SNSPDs with a large number of pixels in an interleaved geometry for uniform light distribution is required, and is an active field of research. Nevertheless, we further demonstrated that our 4-pixel P-SNSPD is capable of correctly reconstructing the incoming photon-number probability distribution of the idler photons from the SPDC source, and in this way determine $g^2(0)$. Therefore, this detector can be readily used in quantum optics experiments to measure the $g^2(0)$ and replace the commonly used setup of a 50/50 beam splitter and two click/no-click detectors.

We then moved to implementations of single-photon path entanglement, and developed an entanglement witness to certify large multipartite states by means of local displacement-based measurements. The witness presented is scalable since, experimentally, it only requires the estimation of three observables and the problem of finding the separable bound is reduced to an eigenvalue problem of $N \times N$ matrices, where N is the number of parties. We experimentally certified an 8-partite single-photon path-entangled state, which we generated by delocalising a heralded single photon over 8 spatial modes. We estimate that with the heralding, transmission and detection efficiencies in our setup, our witness can detect up to 23-partite states, limited by the probability of having more than one photon in the heralded state. Compared to other methods where the certification of the entanglement is achieved by recombination of the modes [81, 158], our witness is applicable in a network scenario with distributed nodes. The heralded distribution of multipartite single-photon path-entangled states could be realised in a star network topology, where each party holds a weakly pumped photon-pair source and sends the idler photons to a multi-port beam splitter at the central node. By erasing the which-path information and phase-stabilising all the links in the network, a detection of a single photon at the central node after the beam splitter would project the signal modes of the parties into a state close to a multipartite single-photon path-entangled state. Such states could be useful for protocols such as quantum conference key agreement [147] or sensing applications such as increasing the resolution of long-baseline telescopes [148, 149].

In another experiment, we demonstrated the heralded distribution of single-photon path entanglement, as described above, for the bipartite case. In this implementation, we achieved a heralding rate of 1.6 kcps for phase-stabilised links of 1.0 km. This is realised by phase-stabilising a Mach-Zehnder interferometer with 1.0 km long arms spanned by seed laser

pulses which are used, together with the pump pulses, for the creation of the displacement fields via difference frequency generation. Thanks to the fast recovery time (< 35 ns) of the parallel SNSPDs [120], we were able to run the displacement field generation at a repetition rate of 19 MHz. Another crucial feature of the parallel SNSPDs in this implementation is their capability of tolerating relatively strong coherent light pulses, while nevertheless fully recovering. This is required in our implementation for the heralding detector at the central station as well as for the local detectors. There, the coherent state pulses, which take the long path in the asymmetric MZI also arrive at the detectors and can be strong in an optimised setup where the loss on the single-photon path-entangled state is reduced. However, in a quantum repeater these asymmetric MZIs could be replaced, and the displacement operation performed, by quantum memories [165, 166]. In the future, this scheme could be used to distribute entanglement between two distant quantum memories, either as recently demonstrated for a total fibre length of 75 m by employing cavity-enhanced SPDC sources [61] or by using microring resonator-based photon-pair sources [176], which directly emit highly non-degenerate photon pairs. Therefore, the signal photons are tailored to the absorption wavelength and bandwidth of the absorptive quantum memory, whereas the idler photons are at telecommunication wavelength for long-distance transmission in optical fibre.

Finally, we presented the experimental implementation of a scheme for the distribution of polarisation-entangled photons. In order to generate the four input photons, we employ a bidirectionally pumped type-II SPDC source and deterministically split the photons in each pair with a PBS. With diagonally polarised input states, we achieve a maximum 4-fold coincidence rate (two detections at the Bell state measurement, one on Alice's and one on Bob's side) of 0.4 cps and visibilities of over 92 %. As a next step, it would be interesting to test the scheme for imbalanced input superposition states and quantify the effects of experimental imperfections, such as limited PBS extinction ratio and non-unit HOM interference visibility of the input photons, on the fidelity of the distributed state. However, compared to $\alpha^2 = 0.5$ (given the input states in A and B: $\alpha\,|1\rangle_H + \sqrt{1-\alpha}\,|1\rangle_V$), the 4-fold coincidence rate for $\alpha^2 = 0.8$ will reduce to 41 %, for $\alpha^2 = 0.95$ to 3.6 % and for $\alpha^2 = 0.99$ to 0.157 %. This poses a problem when using SPDC sources for the generation of the photons, since 4 photons are created with probability p^2, where p is the pair creation probability per pump pulse. Since the contribution of additional unwanted double pairs scales with $\mathcal{O}(p^3)$, p has to be kept low ($p \approx 3 \times 10^{-3}$ in our experiment). Therefore, deterministic single-photon sources will be required when using highly imbalanced input superposition states ($\alpha^2 \sim 0.99$) to herald the distribution of polarisation-entangled photons.

Perspective

The generation of a single photon in a single optical mode is an outstanding task in quantum optics, however is desirable for many protocols in quantum information. Heralded

single-photon sources based on SPDC are an attractive solution: they can be operated at room temperature and the wavelength of the generated photons is tunable. Combined with high-efficiency photon-number-resolving heralding detectors, these sources can be pushed into the quasi-deterministic regime, up to the theoretical limit for the heralding probability per pump pulse of 25 % [88]. Superconducting transition-edge sensors have shown detection efficiencies at telecommunication wavelength of 95 % [177] and even 98 % at a wavelength of 850 nm [178] with excellent photon-number discrimination. However, these detectors have recovery times on the order of microseconds, which would limit the repetition rate of the source. Recently developed photon-number-resolving SNSPD arrays recover much faster, on the time scale of nanoseconds, and have system detection efficiencies of 78 % [179] or even 89.5 % [127]. With further development of those detectors, and optimised SPDC sources, total efficiencies above 90 % (coupling, transmission and detection of the heralding photons) are within reach which would improve the heralding rate by over a factor of 5 while keeping the same low value for the heralded $g^{(2)}(0)$. In combination with an adjustable delay line for the heralded photons [180, 181], deterministic single-photon sources could therefore be realised using such platforms. For applications where indistinguishable photons at telecommunication wavelengths are required, such sources represent a viable alternative to single-photon sources based on semiconductor quantum dots [174].

Sources which deterministically produce highly indistinguishable single photons could be employed for the heralded distribution of high-fidelity entangled states using a proposed scheme [87, 167]. Two-hierarchy entanglement swapping schemes, an example of which has been experimentally demonstrated with probabilistic photon-pair sources [171], would also benefit from deterministic single-photon sources to increase the heralding rate and thus, high-fidelity entanglement could be distributed in a heralded manner. At this point, the question about applications of distributed entanglement may arise. One application could be to link quantum information processing devices, and therefore allow for distributed quantum computing. With the entangled state as a resource, arbitrary qubit states can be transferred via quantum teleportation, as recently demonstrated for two non-neighbouring quantum nodes [182]. Another prominent application of distributed entanglement is device-independent QKD, which has been experimentally demonstrated recently [58, 59]. This presents the ultimate solution for the distribution of a secret key with minimal assumptions on the system. However, real-world implementations are extremely challenging and it is unclear if such schemes will ever find widespread use. If the devices can be trusted, standard QKD protocols are much simpler to realise and nowadays achieve secret key rates of more than 60 Mbps over a distance of 10 km of optical fibre [33, 34] and more than 6 bps over 400 km [32]. For long-distance fibre transmission, the more challenging implementations of the twin-field QKD protocol achieve distances over 830 km [38, 40].

With all that being said, it is exciting to see the pace at which the field of quantum technology is currently developing. Who knows what milestones are about to come and which quantum technology will be part of our everyday life in the future.

Acknowledgements

I am deeply indebted to my supervisors Hugo Zbinden and Rob Thew for giving me the unique opportunity to join their group. I am grateful for all the help and discussions during the four and a half years of my thesis work. Despite personal setbacks, the COVID-19 pandemic and the move from Pinchat to AEM in autumn 2021, with their input and guidance I managed to get the experiments up and running.

I am extremely grateful for getting to know Anthony Martin at the beginning of my time at GAP, who inspired me a lot with his problem-solving skills, his hands-on mentality and his hard-working attitude. Not only will I keep the moments in the lab in good memory, but also the nights out discussing while having some "chopes". Many thanks to Ephanielle Verbanis for introducing me to the lab and teaching me the basics of experimental optics! I would also like to express my deepest appreciation to my post-docs Nicolas Maring and Tiff Brydges for all the collaboration and great discussions. You helped me a lot with the problem-solving in the lab as well as the article and thesis writing! Special thanks to Claudio Barreiro for the technical support and the long explanations on electronics, you were always helping out immediately and lifted the spirits!

This thesis work would not have been possible without my theory collaborators Enky Oudot, Pavel Sekatski and Nicolas Sangouard. I am thankful for all the discussions we had, you made me learn a lot about physics. You always understood experimental issues and limitations, which made it very easy for me to convey the problems.

I would like to extend my sincere thanks to my friend and ex-colleague Fadri Grünenfelder whom I know already since primary school. Maybe it was our hike from Grisons to Geneva after our high school degree which made us end up there in the same research group, who knows? I thank you for all the years of high school, undergraduate and PhD studies that we spent together, where we got to know physics and pushed each other doing so. I am still inspired by your motivation and skill level in programming! Also in our leisure time, you were always open to enjoy some quality time together on the crag or under the wings. Thanks for all of that!

Special thanks to Moritz Businger, for all the years at ETH and at GAP, and all the time we spent together on the weekends! I am also grateful to Antonio Ortu for all the discussions including the ones about good music, to Davide Rusca for the excellent explanations and the many amazing conversations around Friday evening beers, to Farid Samara for letting me steal your lab equipment and for forgiving us for all the pranks we played on you,

and to Alberto Boaron for all the chats and help in the lab. I would like to extend my sincere thanks to Rebecka Sax, Giovanni Resta, Lorenzo Stasi, Dmitry Tabakaev, Joey Marcellino, Victor Moreno and Alberto Rolandi for enriching discussions, many bouldering and climbing sessions as well as some truly unique outdoor experiences!

Many thanks to my office colleagues Adrian Holzäpfel, Kris Kaczmarek, Misael Caloz and Théo Sanchez for the exchange and the fun during and after work! Thanks should also go to Matthieu Perrenoud, Emna Amri, Patrick Remy, Gaëtan Gras, Maria Pereira, Claire Autebert and Félix Bussières for all the discussions on the detectors and help in the lab. Moreover, I had the pleasure of working with the visiting students Laura dos Santos Martins and Vasiliki Angelopoulou whom I thank for the fruitful discussions.

Last, I could not have undertaken this journey without my sister Nicole and my brother Dominik who always stood by my side and supported me. The past five years were tough for all of us with the passing of our parents and a close friend of mine. Your resilience and optimism helped me to deal with the losses, and together we are an incredibly strong team, which can handle very difficult situations.

Bibliography

[1] A. Einstein. Zur Elektrodynamik bewegter Körper. *Annalen der Physik*, 322(10): 891–921, 1905. DOI: 10.1002/andp.19053221004. (Cited on page 1.)

[2] A. Einstein. Die Grundlage der allgemeinen Relativitätstheorie. *Annalen der Physik*, 354(7):769–822, 1916. DOI: 10.1002/andp.19163540702. (Cited on page 1.)

[3] M. Planck. Ueber das Gesetz der Energieverteilung im Normalspectrum. *Annalen der Physik*, 309(3):553–563, 1901. DOI: 10.1002/andp.19013090310. (Cited on pages 1 and 7.)

[4] A. Einstein. Über einen die Erzeugung und Verwandlung des Lichtes betreffenden heuristischen Gesichtspunkt. *Annalen der Physik*, 322(6):132–148, 1905. DOI: 10.1002/andp.19053220607. (Cited on pages 1 and 7.)

[5] N. Bohr. I. On the constitution of atoms and molecules. *The London, Edinburgh, and Dublin Philosophical Magazine and Journal of Science*, 26(151):1–25, 1913. DOI: 10.1080/14786441308634955. (Cited on page 1.)

[6] W. Heisenberg. Über den anschaulichen Inhalt der quantentheoretischen Kinematik und Mechanik. *Zeitschrift für Physik*, 43(3-4):172–198, 1927. DOI: 10.1007/BF01397280. (Cited on page 1.)

[7] E. Schrödinger. An Undulatory Theory of the Mechanics of Atoms and Molecules. *Physical Review*, 28(6):1049–1070, 1926. DOI: 10.1103/PhysRev.28.1049. (Cited on page 1.)

[8] J. Bardeen and W. H. Brattain. The Transistor, A Semi-Conductor Triode. *Physical Review*, 74(2):230–231, 1948. DOI: 10.1103/PhysRev.74.230. (Cited on page 1.)

[9] W. Shockley. The Theory of p-n Junctions in Semiconductors and p-n Junction Transistors. *Bell System Technical Journal*, 28(3):435–489, 1949. DOI: 10.1002/j.1538-7305.1949.tb03645.x. (Cited on page 1.)

[10] T. H. Maiman. Stimulated Optical Radiation in Ruby. *Nature*, 187(4736):493–494, 1960. DOI: 10.1038/187493a0. (Cited on page 1.)

[11] J. P. Dowling and G. J. Milburn. Quantum technology: the second quantum revolution. *Philosophical Transactions of the Royal Society of London. Series A: Mathematical, Physical and Engineering Sciences*, 361(1809):1655–1674, 2003. DOI: 10.1098/rsta.2003.1227. (Cited on page 1.)

[12] R. L. Rivest, A. Shamir, and L. Adleman. A method for obtaining digital signatures and public-key cryptosystems. *Communications of the ACM*, 21(2):120–126, 1978. DOI: 10.1145/359340.359342. (Cited on page 1.)

[13] P. Shor. Algorithms for quantum computation: discrete logarithms and factoring. In *Proceedings 35th Annual Symposium on Foundations of Computer Science*, pages 124–134. IEEE Comput. Soc. Press, 1994. ISBN 0-8186-6580-7. DOI: 10.1109/SFCS.1994.365700. URL: `http://ieeexplore.ieee.org/document/365700/`. (Cited on pages 1 and 5.)

[14] N. Gisin, G. Ribordy, W. Tittel, and H. Zbinden. Quantum cryptography. *Reviews of Modern Physics*, 74(1):145–195, 2002. DOI: 10.1103/RevModPhys.74.145. (Cited on pages 1 and 5.)

[15] J. S. Bell. On the Einstein Podolsky Rosen paradox. *Physics*, 1(3):195–200, 1964. DOI: 10.1103/PhysicsPhysiqueFizika.1.195. (Cited on pages 1, 12, and 35.)

[16] J. F. Clauser, M. A. Horne, A. Shimony, and R. A. Holt. Proposed Experiment to Test Local Hidden-Variable Theories. *Physical Review Letters*, 23(15):880–884, 1969. DOI: 10.1103/PhysRevLett.23.880. (Cited on pages 1 and 12.)

[17] S. J. Freedman and J. F. Clauser. Experimental Test of Local Hidden-Variable Theories. *Physical Review Letters*, 28(14):938–941, 1972. DOI: 10.1103/PhysRevLett.28.938. (Cited on page 1.)

[18] A. Aspect, P. Grangier, and G. Roger. Experimental Tests of Realistic Local Theories via Bell's Theorem. *Physical Review Letters*, 47(7):460–463, 1981. DOI: 10.1103/PhysRevLett.47.460. (Cited on pages 1 and 7.)

[19] C. H. Bennett, G. Brassard, C. Crépeau, R. Jozsa, A. Peres, and W. K. Wootters. Teleporting an unknown quantum state via dual classical and Einstein-Podolsky-Rosen channels. *Physical Review Letters*, 70(13):1895–1899, 1993. DOI: 10.1103/PhysRevLett.70.1895. (Cited on page 1.)

[20] D. Bouwmeester, J.-W. Pan, K. Mattle, M. Eibl, H. Weinfurter, and A. Zeilinger. Experimental quantum teleportation. *Nature*, 390(6660):575–579, 1997. DOI: 10.1038/37539. (Cited on page 1.)

[21] R. F. Werner. Quantum states with Einstein-Podolsky-Rosen correlations admitting a hidden-variable model. *Physical Review A*, 40(8):4277–4281, 1989. DOI: 10.1103/PhysRevA.40.4277. (Cited on page 3.)

[22] R. Horodecki, P. Horodecki, M. Horodecki, and K. Horodecki. Quantum entanglement. *Reviews of Modern Physics*, 81(2):865–942, 2009. DOI: 10.1103/RevModPhys.81.865. (Cited on page 3.)

[23] M. Seevinck and J. Uffink. Sufficient conditions for three-particle entanglement and their tests in recent experiments. *Physical Review A*, 65(1):012107, 2001. DOI: 10.1103/PhysRevA.65.012107. (Cited on page 3.)

[24] M. Navascués, E. Wolfe, D. Rosset, and A. Pozas-Kerstjens. Genuine Network Multipartite Entanglement. *Physical Review Letters*, 125(24):240505, 2020. DOI: 10.1103/PhysRevLett.125.240505. (Cited on page 3.)

[25] J. Altepeter, E. Jeffrey, and P. Kwiat. Photonic State Tomography. In *Advances In Atomic, Molecular, and Optical Physics*, volume 52, pages 105–159. Academic Press, Cambridge, Massachusetts, 2005. DOI: 10.1016/S1049-250X(05)52003-2. URL: `https://linkinghub.elsevier.com/retrieve/pii/S1049250X05520032`. (Cited on page 3.)

[26] M. Paris and J. Řeháček, editors. *Quantum State Estimation*, volume 649 of *Lecture Notes in Physics*. Springer Berlin Heidelberg, Berlin, Heidelberg, 2004. ISBN 978-3-540-22329-0. DOI: 10.1007/b98673. (Cited on page 3.)

[27] O. Gühne and G. Tóth. Entanglement detection. *Physics Reports*, 474(1-6):1–75, 2009. DOI: 10.1016/j.physrep.2009.02.004. (Cited on page 4.)

[28] N. Gisin and R. Thew. Quantum communication. *Nature Photonics*, 1(3):165–171, 2007. DOI: 10.1038/nphoton.2007.22. (Cited on page 4.)

[29] V. Zapatero, T. van Leent, R. Arnon-Friedman, W.-Z. Liu, Q. Zhang, H. Weinfurter, and M. Curty. Advances in device-independent quantum key distribution. *npj Quantum Information*, 9(1):10, 2023. DOI: 10.1038/s41534-023-00684-x. (Cited on page 4.)

[30] C. H. Bennett and G. Brassard. Quantum cryptography: Public key distribution and coin tossing. *Theoretical Computer Science*, 560(P1):7–11, 2014. DOI: 10.1016/j.tcs.2014.05.025. (Cited on page 4.)

[31] H.-K. Lo, M. Curty, and K. Tamaki. Secure quantum key distribution. *Nature Photonics*, 8(8):595–604, 2014. DOI: 10.1038/nphoton.2014.149. (Cited on page 5.)

[32] A. Boaron, G. Boso, D. Rusca, C. Vulliez, C. Autebert, M. Caloz, M. Perrenoud, G. Gras, F. Bussières, M. J. Li, D. Nolan, A. Martin, and H. Zbinden. Secure Quantum Key Distribution over 421 km of Optical Fiber. *Physical Review Letters*, 121 (19):1–4, 2018. DOI: 10.1103/PhysRevLett.121.190502. (Cited on pages 5 and 90.)

[33] F. Grünenfelder, A. Boaron, G. V. Resta, M. Perrenoud, D. Rusca, C. Barreiro, R. Houlmann, R. Sax, L. Stasi, S. El-Khoury, E. Hänggi, N. Bosshard, F. Bussières, and H. Zbinden. Fast single-photon detectors and real-time key distillation enable high secret-key-rate quantum key distribution systems. *Nature Photonics*, 17(5): 422–426, 2023. DOI: 10.1038/s41566-023-01168-2. (Cited on pages 5 and 90.)

[34] W. Li, L. Zhang, H. Tan, Y. Lu, S.-K. Liao, J. Huang, H. Li, Z. Wang, H.-K. Mao, B. Yan, Q. Li, Y. Liu, Q. Zhang, C.-Z. Peng, L. You, F. Xu, and J.-W. Pan. High-rate quantum key distribution exceeding 110 Mb s–1. *Nature Photonics*, 2023. DOI: 10.1038/s41566-023-01166-4. (Cited on pages 5 and 90.)

[35] M. Lucamarini, Z. L. Yuan, J. F. Dynes, and A. J. Shields. Overcoming the

rate–distance limit of quantum key distribution without quantum repeaters. *Nature*, 557(7705):400–403, 2018. DOI: 10.1038/s41586-018-0066-6. (Cited on page 5.)

[36] M. Pittaluga, M. Minder, M. Lucamarini, M. Sanzaro, R. I. Woodward, M.-J. Li, Z. Yuan, and A. J. Shields. 600-km repeater-like quantum communications with dual-band stabilization. *Nature Photonics*, 15(7):530–535, 2021. DOI: 10.1038/s41566-021-00811-0. (Cited on page 5.)

[37] J.-P. Chen, C. Zhang, Y. Liu, C. Jiang, D.-F. Zhao, W.-J. Zhang, F.-X. Chen, H. Li, L.-X. You, Z. Wang, Y. Chen, X.-B. Wang, Q. Zhang, and J.-W. Pan. Quantum Key Distribution over 658 km Fiber with Distributed Vibration Sensing. *Physical Review Letters*, 128(18):180502, 2022. DOI: 10.1103/PhysRevLett.128.180502. (Cited on page 5.)

[38] S. Wang, Z.-q. Yin, D.-y. He, W. Chen, R.-Q. Wang, P. Ye, Y. Zhou, G.-J. Fan-Yuan, F.-x. Wang, W. Chen, Y.-g. Zhu, P. V. Morozov, A. V. Divochiy, Z. Zhou, G.-c. Guo, and Z.-F. Han. Twin-field quantum key distribution over 830-km fibre. *Nature Photonics*, 2022. DOI: 10.1038/s41566-021-00928-2. (Cited on pages 5 and 90.)

[39] L. Zhou, J. Lin, Y. Jing, and Z. Yuan. Twin-field quantum key distribution without optical frequency dissemination. *Nature Communications*, 14(1):928, 2023. DOI: 10.1038/s41467-023-36573-2. (Cited on page 5.)

[40] Y. Liu, W.-J. Zhang, C. Jiang, J.-P. Chen, C. Zhang, W.-X. Pan, D. Ma, H. Dong, J.-M. Xiong, C.-J. Zhang, H. Li, R.-C. Wang, J. Wu, T.-Y. Chen, L. You, X.-B. Wang, Q. Zhang, and J.-W. Pan. Experimental Twin-Field Quantum Key Distribution Over 1000 km Fiber Distance. *Preprint arXiv:2303.15795*, 2023. URL: `http://arxiv.org/abs/2303.15795`. (Cited on pages 5 and 90.)

[41] S. Wengerowsky, S. K. Joshi, F. Steinlechner, J. R. Zichi, B. Liu, T. Scheidl, S. M. Dobrovolskiy, R. van der Molen, J. W. N. Los, V. Zwiller, M. A. M. Versteegh, A. Mura, D. Calonico, M. Inguscio, A. Zeilinger, A. Xuereb, and R. Ursin. Passively stable distribution of polarisation entanglement over 192 km of deployed optical fibre. *npj Quantum Information*, 6(1):5, 2020. DOI: 10.1038/s41534-019-0238-8. (Cited on pages 5 and 86.)

[42] S. P. Neumann, A. Buchner, L. Bulla, M. Bohmann, and R. Ursin. Continuous entanglement distribution over a transnational 248 km fiber link. *Nature Communications*, 13(1):6134, 2022. DOI: 10.1038/s41467-022-33919-0. (Cited on pages 5 and 86.)

[43] J. Yin, Y. Cao, Y.-H. Li, S.-K. Liao, L. Zhang, J.-G. Ren, W.-Q. Cai, W.-Y. Liu, B. Li, H. Dai, G.-B. Li, Q.-M. Lu, Y.-H. Gong, Y. Xu, S.-L. Li, F.-Z. Li, Y.-Y. Yin, Z.-Q. Jiang, M. Li, J.-J. Jia, G. Ren, D. He, Y.-L. Zhou, X.-X. Zhang, N. Wang, X. Chang, Z.-C. Zhu, N.-L. Liu, Y.-A. Chen, C.-Y. Lu, R. Shu, C.-Z. Peng, J.-Y. Wang, and J.-W. Pan. Satellite-based entanglement distribution over 1200 kilometers. *Science*, 356(6343):1140–1144, 2017. DOI: 10.1126/science.aan3211. (Cited on page 5.)

[44] L. Slodička, G. Hétet, N. Röck, P. Schindler, M. Hennrich, and R. Blatt. Atom-Atom

Entanglement by Single-Photon Detection. *Physical Review Letters*, 110(8):083603, 2013. DOI: 10.1103/PhysRevLett.110.083603. (Cited on page 5.)

[45] A. Delteil, Z. Sun, W.-b. Gao, E. Togan, S. Faelt, and A. Imamoğlu. Generation of heralded entanglement between distant hole spins. *Nature Physics*, 12(3):218–223, 2016. DOI: 10.1038/nphys3605. (Cited on page 5.)

[46] R. Stockill, M. J. Stanley, L. Huthmacher, E. Clarke, M. Hugues, A. J. Miller, C. Matthiesen, C. Le Gall, and M. Atatüre. Phase-Tuned Entangled State Generation between Distant Spin Qubits. *Physical Review Letters*, 119(1):010503, 2017. DOI: 10.1103/PhysRevLett.119.010503. (Cited on page 5.)

[47] P. C. Humphreys, N. Kalb, J. P. J. Morits, R. N. Schouten, R. F. L. Vermeulen, D. J. Twitchen, M. Markham, and R. Hanson. Deterministic delivery of remote entanglement on a quantum network. *Nature*, 558(7709):268–273, 2018. DOI: 10.1038/s41586-018-0200-5. (Cited on page 5.)

[48] M. Pompili, S. L. N. Hermans, S. Baier, H. K. C. Beukers, P. C. Humphreys, R. N. Schouten, R. F. L. Vermeulen, M. J. Tiggelman, L. dos Santos Martins, B. Dirkse, S. Wehner, and R. Hanson. Realization of a multinode quantum network of remote solid-state qubits. *Science*, 372(6539):259–264, 2021. DOI: 10.1126/science.abg1919. (Cited on pages 5 and 59.)

[49] P. Maunz, S. Olmschenk, D. Hayes, D. N. Matsukevich, L.-M. Duan, and C. Monroe. Heralded Quantum Gate between Remote Quantum Memories. *Physical Review Letters*, 102(25):250502, 2009. DOI: 10.1103/PhysRevLett.102.250502. (Cited on page 5.)

[50] J. Hofmann, M. Krug, N. Ortegel, L. Gérard, M. Weber, W. Rosenfeld, and H. Weinfurter. Heralded Entanglement Between Widely Separated Atoms. *Science*, 891 (July):72–76, 2012. DOI: 10.1126/science.1221856. (Cited on page 5.)

[51] W. Pfaff, B. J. Hensen, H. Bernien, S. B. van Dam, M. S. Blok, T. H. Taminiau, M. J. Tiggelman, R. N. Schouten, M. Markham, D. J. Twitchen, and R. Hanson. Unconditional quantum teleportation between distant solid-state quantum bits. *Science*, 345(6196):532–535, 2014. DOI: 10.1126/science.1253512. (Cited on page 5.)

[52] D. Hucul, I. V. Inlek, G. Vittorini, C. Crocker, S. Debnath, S. M. Clark, and C. Monroe. Modular entanglement of atomic qubits using photons and phonons. *Nature Physics*, 11(1):37–42, 2015. DOI: 10.1038/nphys3150. (Cited on page 5.)

[53] J.-Å. Larsson. Loopholes in Bell inequality tests of local realism. *Journal of Physics A: Mathematical and Theoretical*, 47(42):424003, 2014. DOI: 10.1088/1751-8113/47/42/424003. (Cited on page 5.)

[54] B. Hensen, H. Bernien, A. E. Dréau, A. Reiserer, N. Kalb, M. S. Blok, J. Ruitenberg, R. F. L. Vermeulen, R. N. Schouten, C. Abellán, W. Amaya, V. Pruneri, M. W. Mitchell, M. Markham, D. J. Twitchen, D. Elkouss, S. Wehner, T. H. Taminiau, and R. Hanson. Loophole-free Bell inequality violation using electron spins separated by

1.3 kilometres. *Nature*, 526(7575):682–686, 2015. DOI: 10.1038/nature15759. (Cited on page 5.)

[55] L. K. Shalm, E. Meyer-Scott, B. G. Christensen, P. Bierhorst, M. A. Wayne, M. J. Stevens, T. Gerrits, S. Glancy, D. R. Hamel, M. S. Allman, K. J. Coakley, S. D. Dyer, C. Hodge, A. E. Lita, V. B. Verma, C. Lambrocco, E. Tortorici, A. L. Migdall, Y. Zhang, D. R. Kumor, W. H. Farr, F. Marsili, M. D. Shaw, J. A. Stern, C. Abellán, W. Amaya, V. Pruneri, T. Jennewein, M. W. Mitchell, P. G. Kwiat, J. C. Bienfang, R. P. Mirin, E. Knill, and S. W. Nam. Strong Loophole-Free Test of Local Realism. *Physical Review Letters*, 115(25):250402, 2015. DOI: 10.1103/PhysRevLett.115.250402. (Cited on page 5.)

[56] M. Giustina, M. A. Versteegh, S. Wengerowsky, J. Handsteiner, A. Hochrainer, K. Phelan, F. Steinlechner, J. Kofler, J.-Å. Larsson, C. Abellán, W. Amaya, V. Pruneri, M. W. Mitchell, J. Beyer, T. Gerrits, A. E. Lita, L. K. Shalm, S. W. Nam, T. Scheidl, R. Ursin, B. Wittmann, and A. Zeilinger. Significant-Loophole-Free Test of Bell's Theorem with Entangled Photons. *Physical Review Letters*, 115(25): 250401, 2015. DOI: 10.1103/PhysRevLett.115.250401. (Cited on page 5.)

[57] W. Rosenfeld, D. Burchardt, R. Garthoff, K. Redeker, N. Ortegel, M. Rau, and H. Weinfurter. Event-Ready Bell Test Using Entangled Atoms Simultaneously Closing Detection and Locality Loopholes. *Physical Review Letters*, 119(1):010402, 2017. DOI: 10.1103/PhysRevLett.119.010402. (Cited on page 5.)

[58] D. P. Nadlinger, P. Drmota, B. C. Nichol, G. Araneda, D. Main, R. Srinivas, D. M. Lucas, C. J. Ballance, K. Ivanov, E. Y.-Z. Tan, P. Sekatski, R. L. Urbanke, R. Renner, N. Sangouard, and J.-D. Bancal. Experimental quantum key distribution certified by Bell's theorem. *Nature*, 607(7920):682–686, 2022. DOI: 10.1038/s41586-022-04941-5. (Cited on pages 5 and 90.)

[59] W. Zhang, T. van Leent, K. Redeker, R. Garthoff, R. Schwonnek, F. Fertig, S. Eppelt, W. Rosenfeld, V. Scarani, C. C.-W. Lim, and H. Weinfurter. A device-independent quantum key distribution system for distant users. *Nature*, 607(7920):687–691, 2022. DOI: 10.1038/s41586-022-04891-y. (Cited on pages 5 and 90.)

[60] Y. Yu, F. Ma, X.-y. Luo, B. Jing, P.-f. Sun, R.-z. Fang, C.-w. Yang, H. Liu, M.-y. Zheng, X.-p. Xie, W.-J. Zhang, L.-x. You, Z. Wang, T.-y. Chen, Q. Zhang, X.-h. Bao, and J.-w. Pan. Entanglement of two quantum memories via fibres over dozens of kilometres. *Nature*, 578(7794):240–245, 2020. DOI: 10.1038/s41586-020-1976-7. (Cited on page 5.)

[61] D. Lago-Rivera, S. Grandi, J. V. Rakonjac, A. Seri, and H. de Riedmatten. Telecom-heralded entanglement between multimode solid-state quantum memories. *Nature*, 594(7861):37–40, 2021. DOI: 10.1038/s41586-021-03481-8. (Cited on pages 5, 74, and 89.)

[62] T. van Leent, M. Bock, F. Fertig, R. Garthoff, S. Eppelt, Y. Zhou, P. Malik, M. Seubert, T. Bauer, W. Rosenfeld, W. Zhang, C. Becher, and H. Weinfurter. Entangling single atoms over 33 km telecom fibre. *Nature*, 607(7917):69–73, 2022. DOI:

10.1038/s41586-022-04764-4. (Cited on page 5.)

[63] W. K. Wootters and W. H. Zurek. A single quantum cannot be cloned. *Nature*, 299 (5886):802–803, 1982. (Cited on page 5.)

[64] H. J. Briegel, W. Dür, J. I. Cirac, and P. Zoller. Quantum repeaters: The role of imperfect local operations in quantum communication. *Physical Review Letters*, 81 (26):5932–5935, 1998. DOI: 10.1103/PhysRevLett.81.5932. (Cited on page 5.)

[65] N. Sangouard, C. Simon, H. de Riedmatten, and N. Gisin. Quantum repeaters based on atomic ensembles and linear optics. *Reviews of Modern Physics*, 83(1):33–80, 2011. DOI: 10.1103/RevModPhys.83.33. (Cited on pages 5, 35, 60, and 73.)

[66] C. Cohen-Tannoudji, J. Dupont-Roc, and G. Grynberg. *Photons and Atoms-Introduction to Quantum Electrodynamics*. John Wiley & Sons, Hoboken, New Jersey, 1997. (Cited on page 7.)

[67] J. F. Clauser. Experimental distinction between the quantum and classical field-theoretic predictions for the photoelectric effect. *Physical Review D*, 9(4):853–860, 1974. DOI: 10.1103/PhysRevD.9.853. (Cited on page 7.)

[68] P. Grangier, G. Roger, and A. Aspect. Experimental Evidence for a Photon Anticorrelation Effect on a Beam Splitter: A New Light on Single-Photon Interferences. *Europhysics Letters (EPL)*, 1(4):173–179, 1986. DOI: 10.1209/0295-5075/1/4/004. (Cited on page 7.)

[69] C. K. Hong and L. Mandel. Experimental realization of a localized one-photon state. *Physical Review Letters*, 56(1):58–60, 1986. DOI: 10.1103/PhysRevLett.56.58. (Cited on page 7.)

[70] A. Migdall, S. V. Polyakov, J. Fan, and J. C. Bienfang, editors. *Experimental Methods in the Physical Sciences: Single-Photon Generation and Detection*. Academic Press, Cambridge, Massachusetts, 2013. ISBN 9780123876959. (Cited on pages 7, 8, 9, 10, and 17.)

[71] M. A. Broome, A. Fedrizzi, S. Rahimi-Keshari, J. Dove, S. Aaronson, T. C. Ralph, and A. G. White. Photonic Boson Sampling in a Tunable Circuit. *Science*, 339 (6121):794–798, 2013. DOI: 10.1126/science.1231440. (Cited on page 7.)

[72] J. B. Spring, B. J. Metcalf, P. C. Humphreys, W. S. Kolthammer, X.-M. Jin, M. Barbieri, A. Datta, N. Thomas-Peter, N. K. Langford, D. Kundys, J. C. Gates, B. J. Smith, P. G. R. Smith, and I. A. Walmsley. Boson Sampling on a Photonic Chip. *Science*, 339(6121):798–801, 2013. DOI: 10.1126/science.1231692. (Cited on page 7.)

[73] M. Tillmann, B. Dakić, R. Heilmann, S. Nolte, A. Szameit, and P. Walther. Experimental boson sampling. *Nature Photonics*, 7(7):540–544, 2013. DOI: 10.1038/nphoton.2013.102. (Cited on page 7.)

[74] A. Crespi, R. Osellame, R. Ramponi, D. J. Brod, E. F. Galvão, N. Spagnolo, C. Vitelli, E. Maiorino, P. Mataloni, and F. Sciarrino. Integrated multimode in-

terferometers with arbitrary designs for photonic boson sampling. *Nature Photonics*, 7(7):545–549, 2013. DOI: 10.1038/nphoton.2013.112. (Cited on page 7.)

[75] H. Wang, Y.-M. He, Y.-H. Li, Z.-E. Su, B. Li, H.-L. Huang, X. Ding, M.-C. Chen, C. Liu, J. Qin, J.-P. Li, Y.-M. He, C. Schneider, M. Kamp, C.-Z. Peng, S. Höfling, C.-Y. Lu, and J.-W. Pan. High-efficiency multiphoton boson sampling. *Nature Photonics*, 11(6):361–365, 2017. DOI: 10.1038/nphoton.2017.63. (Cited on page 7.)

[76] J. C. Loredo, M. A. Broome, P. Hilaire, O. Gazzano, I. Sagnes, A. Lemaitre, M. P. Almeida, P. Senellart, and A. G. White. Boson Sampling with Single-Photon Fock States from a Bright Solid-State Source. *Physical Review Letters*, 118(13):130503, 2017. DOI: 10.1103/PhysRevLett.118.130503. (Cited on page 7.)

[77] Y. He, X. Ding, Z.-E. Su, H.-L. Huang, J. Qin, C. Wang, S. Unsleber, C. Chen, H. Wang, Y.-M. He, X.-L. Wang, W.-J. Zhang, S.-J. Chen, C. Schneider, M. Kamp, L.-X. You, Z. Wang, S. Höfling, C.-Y. Lu, and J.-W. Pan. Time-Bin-Encoded Boson Sampling with a Single-Photon Device. *Physical Review Letters*, 118(19):190501, 2017. DOI: 10.1103/PhysRevLett.118.190501. (Cited on page 7.)

[78] H. S. Zhong, Y. Li, W. Li, L. C. Peng, Z. E. Su, Y. Hu, Y. M. He, X. Ding, W. Zhang, H. Li, L. Zhang, Z. Wang, L. You, X. L. Wang, X. Jiang, L. Li, Y. A. Chen, N. L. Liu, C. Y. Lu, and J. W. Pan. 12-Photon Entanglement and Scalable Scattershot Boson Sampling with Optimal Entangled-Photon Pairs from Parametric Down-Conversion. *Physical Review Letters*, 121(25):1–6, 2018. DOI: 10.1103/PhysRevLett.121.250505. (Cited on page 7.)

[79] H. Wang, J. Qin, X. Ding, M. C. Chen, S. Chen, X. You, Y. M. He, X. Jiang, L. You, Z. Wang, C. Schneider, J. J. Renema, S. Höfling, C. Y. Lu, and J. W. Pan. Boson Sampling with 20 Input Photons and a 60-Mode Interferometer in a 1014 -Dimensional Hilbert Space. *Physical Review Letters*, 123(25):250503, 2019. DOI: 10.1103/PhysRevLett.123.250503. (Cited on page 7.)

[80] M. S. Kim, W. Son, V. Bužek, and P. L. Knight. Entanglement by a beam splitter: Nonclassicality as a prerequisite for entanglement. *Physical Review A*, 65(3):032323, 2002. DOI: 10.1103/PhysRevA.65.032323. (Cited on pages 7 and 35.)

[81] S. B. Papp, K. S. Choi, H. Deng, P. Lougovski, S. J. van Enk, and H. J. Kimble. Characterization of Multipartite Entanglement for One Photon Shared Among Four Optical Modes. *Science*, 324(5928):764–768, 2009. DOI: 10.1126/science.1172260. (Cited on pages 7, 50, and 88.)

[82] O. Morin, J.-D. Bancal, M. Ho, P. Sekatski, V. D'Auria, N. Gisin, J. Laurat, and N. Sangouard. Witnessing Trustworthy Single-Photon Entanglement with Local Homodyne Measurements. *Physical Review Letters*, 110(13):130401, 2013. DOI: 10.1103/PhysRevLett.110.130401. (Cited on page 7.)

[83] F. Monteiro, V. C. Vivoli, T. Guerreiro, A. Martin, J.-D. Bancal, H. Zbinden, R. T. Thew, and N. Sangouard. Revealing Genuine Optical-Path Entanglement. *Physical Review Letters*, 114(17):170504, 2015. DOI: 10.1103/PhysRevLett.114.170504.

(Cited on pages 7, 35, 43, 44, 48, and 50.)

[84] R. Raussendorf, D. E. Browne, and H. J. Briegel. Measurement-based quantum computation on cluster states. *Physical Review A*, 68(2):022312, 2003. DOI: 10.1103/PhysRevA.68.022312. (Cited on page 7.)

[85] D. Istrati, Y. Pilnyak, J. C. Loredo, C. Antón, N. Somaschi, P. Hilaire, H. Ollivier, M. Esmann, L. Cohen, L. Vidro, C. Millet, A. Lemaître, I. Sagnes, A. Harouri, L. Lanco, P. Senellart, and H. S. Eisenberg. Sequential generation of linear cluster states from a single photon emitter. *Nature Communications*, 11(1):1–8, 2020. DOI: 10.1038/s41467-020-19341-4. (Cited on page 7.)

[86] N. Sangouard, C. Simon, J. Minář, H. Zbinden, H. de Riedmatten, and N. Gisin. Long-distance entanglement distribution with single-photon sources. *Physical Review A*, 76(5):050301, 2007. DOI: 10.1103/PhysRevA.76.050301. (Cited on pages 7, 75, and 76.)

[87] J. Kołodyński, A. Máttar, P. Skrzypczyk, E. Woodhead, D. Cavalcanti, K. Banaszek, and A. Acín. Device-independent quantum key distribution with single-photon sources. *Quantum*, 4:260, 2020. DOI: 10.22331/q-2020-04-30-260. (Cited on pages 7, 75, 76, and 90.)

[88] A. Christ and C. Silberhorn. Limits on the deterministic creation of pure single-photon states using parametric down-conversion. *Physical Review A*, 85(2):023829, 2012. DOI: 10.1103/PhysRevA.85.023829. (Cited on pages 8, 25, and 90.)

[89] P. Senellart, G. Solomon, and A. White. High-performance semiconductor quantum-dot single-photon sources. *Nature Nanotechnology*, 12(11):1026–1039, 2017. DOI: 10.1038/nnano.2017.218. (Cited on pages 8 and 86.)

[90] Y. Arakawa and M. J. Holmes. Progress in quantum-dot single photon sources for quantum information technologies: A broad spectrum overview. *Applied Physics Reviews*, 7(2):021309, 2020. DOI: 10.1063/5.0010193. (Cited on pages 8 and 86.)

[91] N. Tomm, A. Javadi, N. O. Antoniadis, D. Najer, M. C. Löbl, A. R. Korsch, R. Schott, S. R. Valentin, A. D. Wieck, A. Ludwig, and R. J. Warburton. A bright and fast source of coherent single photons. *Nature Nanotechnology*, 16(4):399–403, 2021. DOI: 10.1038/s41565-020-00831-x. (Cited on pages 8 and 86.)

[92] L. Zhai, G. N. Nguyen, C. Spinnler, J. Ritzmann, M. C. Löbl, A. D. Wieck, A. Ludwig, A. Javadi, and R. J. Warburton. Quantum interference of identical photons from remote GaAs quantum dots. *Nature Nanotechnology*, 17(8):829–833, 2022. DOI: 10.1038/s41565-022-01131-2. (Cited on pages 8 and 86.)

[93] R. Hanbury Brown and R. Q. Twiss. Correlation between Photons in two Coherent Beams of Light. *Nature*, 177(4497):27–29, 1956. DOI: 10.1038/177027a0. (Cited on page 8.)

[94] M. Fejer, G. Magel, D. Jundt, and R. Byer. Quasi-phase-matched second harmonic

generation: tuning and tolerances. *IEEE Journal of Quantum Electronics*, 28(11): 2631–2654, 1992. DOI: 10.1109/3.161322. (Cited on page 9.)

[95] F. Graffitti, J. Kelly-Massicotte, A. Fedrizzi, and A. M. Brańczyk. Design considerations for high-purity heralded single-photon sources. *Physical Review A*, 98(5): 053811, 2018. DOI: 10.1103/PhysRevA.98.053811. (Cited on pages 10, 12, and 15.)

[96] C. K. Law, I. A. Walmsley, and J. H. Eberly. Continuous Frequency Entanglement: Effective Finite Hilbert Space and Entropy Control. *Physical Review Letters*, 84(23): 5304–5307, 2000. DOI: 10.1103/PhysRevLett.84.5304. (Cited on page 11.)

[97] N. Quesada and A. M. Brańczyk. Gaussian functions are optimal for waveguided nonlinear-quantum-optical processes. *Physical Review A*, 98(4):043813, 2018. DOI: 10.1103/PhysRevA.98.043813. (Cited on page 11.)

[98] A. M. Weiner. Ultrafast optical pulse shaping: A tutorial review. *Optics Communications*, 284(15):3669–3692, 2011. DOI: 10.1016/j.optcom.2011.03.084. (Cited on page 12.)

[99] K. Zielnicki, K. Garay-Palmett, D. Cruz-Delgado, H. Cruz-Ramirez, M. F. O'Boyle, B. Fang, V. O. Lorenz, A. B. U'Ren, and P. G. Kwiat. Joint spectral characterization of photon-pair sources. *Journal of Modern Optics*, 65(10):1141–1160, 2018. DOI: 10.1080/09500340.2018.1437228. (Cited on page 12.)

[100] P. H. Eberhard. Background level and counter efficiencies required for a loophole-free Einstein-Podolsky-Rosen experiment. *Physical Review A*, 47(2):747–750, 1993. DOI: 10.1103/PhysRevA.47.R747. (Cited on page 12.)

[101] P. B. Dixon, D. Rosenberg, V. Stelmakh, M. E. Grein, R. S. Bennink, E. A. Dauler, A. J. Kerman, R. J. Molnar, and F. N. C. Wong. Heralding efficiency and correlated-mode coupling of near-IR fiber-coupled photon pairs. *Physical Review A*, 90(4): 043804, 2014. DOI: 10.1103/PhysRevA.90.043804. (Cited on pages 12 and 13.)

[102] D. Ljunggren and M. Tengner. Optimal focusing for maximal collection of entangled narrow-band photon pairs into single-mode fibers. *Physical Review A*, 72(6):062301, 2005. DOI: 10.1103/PhysRevA.72.062301. (Cited on page 13.)

[103] P. J. Mosley, J. S. Lundeen, B. J. Smith, P. Wasylczyk, A. B. U'Ren, C. Silberhorn, and I. A. Walmsley. Heralded generation of ultrafast single photons in pure quantum states. *Physical Review Letters*, 100(13):1–4, 2008. DOI: 10.1103/PhysRevLett.100.133601. (Cited on page 13.)

[104] R. S. Bennink. Optimal collinear Gaussian beams for spontaneous parametric down-conversion. *Physical Review A*, 81(5):053805, 2010. DOI: 10.1103/PhysRevA.81.053805. (Cited on page 13.)

[105] J.-l. Smirr, M. Deconinck, R. Frey, I. Agha, E. Diamanti, and I. Zaquine. Optimal photon-pair single-mode coupling in narrow-band spontaneous parametric downconversion with arbitrary pump profile. *Journal of the Optical Society of America B*, 30

(2):288, 2013. DOI: 10.1364/JOSAB.30.000288. (Cited on page 13.)

[106] M. D. Cunha Pereira, F. E. Becerra, B. L. Glebov, J. Fan, S. W. Nam, and A. Migdall. Demonstrating highly symmetric single-mode, single-photon heralding efficiency in spontaneous parametric downconversion. *Optics Letters*, 38(10):1609, 2013. DOI: 10.1364/OL.38.001609. (Cited on page 13.)

[107] T. Guerreiro, A. Martin, B. Sanguinetti, N. Bruno, H. Zbinden, and R. T. Thew. High efficiency coupling of photon pairs in practice. *Optics Express*, 21(23):27641, 2013. DOI: 10.1364/OE.21.027641. (Cited on page 13.)

[108] N. Bruno, A. Martin, T. Guerreiro, B. Sanguinetti, and R. T. Thew. Pulsed source of spectrally uncorrelated and indistinguishable photons at telecom wavelengths. *Optics Express*, 22(14):17246, 2014. DOI: 10.1364/OE.22.017246. (Cited on pages 13, 14, and 15.)

[109] S. P. Walborn, C. H. Monken, S. Pádua, and P. H. S. Ribeiro. Spatial correlations in parametric down-conversion. *Physics Reports*, 495(4-5):87–139, 2010. DOI: 10.1016/j.physrep.2010.06.003. (Cited on page 13.)

[110] L. K. Shalm, K. Garay, J. Palfree, A. L. Migdall, A. U'Ren, and S. Nam. Spontaneous parametric downconversion calculator. `http://www.spdcalc.org`, Last accessed: 2023-02-23. (Cited on pages 13, 14, and 15.)

[111] M. Caloz, M. Perrenoud, C. Autebert, B. Korzh, M. Weiss, C. Schönenberger, R. J. Warburton, H. Zbinden, and F. Bussières. High-detection efficiency and low-timing jitter with amorphous superconducting nanowire single-photon detectors. *Applied Physics Letters*, 112(6):061103, 2018. DOI: 10.1063/1.5010102. (Cited on page 16.)

[112] L. K. Shalm, Y. Zhang, J. C. Bienfang, C. Schlager, M. J. Stevens, M. D. Mazurek, C. Abellán, W. Amaya, M. W. Mitchell, M. A. Alhejji, H. Fu, J. Ornstein, R. P. Mirin, S. W. Nam, and E. Knill. Device-independent randomness expansion with entangled photons. *Nature Physics*, 17(4):452–456, 2021. DOI: 10.1038/s41567-020-01153-4. (Cited on page 16.)

[113] W.-Z. Liu, Y.-Z. Zhang, Y.-Z. Zhen, M.-H. Li, Y. Liu, J. Fan, F. Xu, Q. Zhang, and J.-W. Pan. Toward a Photonic Demonstration of Device-Independent Quantum Key Distribution. *Physical Review Letters*, 129(5):050502, 2022. DOI: 10.1103/PhysRevLett.129.050502. (Cited on page 16.)

[114] V. C. Vivoli, P. Sekatski, J.-D. Bancal, C. C. W. Lim, A. Martin, R. T. Thew, H. Zbinden, N. Gisin, and N. Sangouard. Comparing different approaches for generating random numbers device-independently using a photon pair source. *New Journal of Physics*, 17(2):023023, 2015. DOI: 10.1088/1367-2630/17/2/023023. (Cited on pages 17, 35, 37, 38, and 39.)

[115] E. Wigner. On the Quantum Correction For Thermodynamic Equilibrium. *Physical Review*, 40(5):749–759, 1932. DOI: 10.1103/PhysRev.40.749. (Cited on page 21.)

[116] A. Royer. Wigner function as the expectation value of a parity operator. *Phys. Rev. A*, 15:449–450, 1977. DOI: 10.1103/PhysRevA.15.449. (Cited on page 21.)

[117] W. Vogel and D.-G. Welsch. *Quantum optics*. John Wiley & Sons, Hoboken, New Jersey, 2006. DOI: 10.1002/3527608524. (Cited on page 21.)

[118] F. W. J. Olver, A. B. Olde Daalhuis, D. W. Lozier, B. I. Schneider, R. F. Boisvert, C. W. Clark, B. R. Miller, B. V. Saunders, H. S. Cohl, M. A. McClain, and eds. NIST digital library of mathematical functions. `http://dlmf.nist.gov/`, Release 1.1.3 of 2021-09-15. (Cited on page 21.)

[119] A. Kenfack and K. Zyczkowski. Negativity of the Wigner function as an indicator of non-classicality. *Journal of Optics B: Quantum and Semiclassical Optics*, 6(10): 396–404, 2004. DOI: 10.1088/1464-4266/6/10/003. (Cited on page 22.)

[120] M. Perrenoud, M. Caloz, E. Amri, C. Autebert, C. Schönenberger, H. Zbinden, and F. Bussières. Operation of parallel SNSPDs at high detection rates. *Superconductor Science and Technology*, 34(2):024002, 2021. DOI: 10.1088/1361-6668/abc8d0. (Cited on pages 26, 66, 87, and 89.)

[121] L. Stasi, G. Gras, R. Berrazouane, M. Perrenoud, H. Zbinden, and F. Bussières. Fast High-Efficiency Photon-Number-Resolving Parallel Superconducting Nanowire Single-Photon Detector. *Physical Review Applied*, 19(6):064041, 2023. DOI: 10.1103/PhysRevApplied.19.064041. (Cited on pages 26, 27, and 87.)

[122] D. Walls and G. J. Milburn, editors. *Quantum Optics*. Springer Berlin Heidelberg, Berlin, Heidelberg, 2008. ISBN 978-3-540-28573-1. DOI: 10.1007/978-3-540-28574-8. URL: `http://link.springer.com/10.1007/978-3-540-28574-8`. (Cited on pages 27, 29, and 37.)

[123] M. Takeoka, R.-B. Jin, and M. Sasaki. Full analysis of multi-photon pair effects in spontaneous parametric down conversion based photonic quantum information processing. *New Journal of Physics*, 17(4):043030, 2015. DOI: 10.1088/1367-2630/17/4/043030. (Cited on page 27.)

[124] S. Sempere-Llagostera, G. S. Thekkadath, R. B. Patel, W. S. Kolthammer, and I. A. Walmsley. Reducing g (2) (0) of a parametric down-conversion source via photon-number resolution with superconducting nanowire detectors. *Optics Express*, 30(2): 3138, 2022. DOI: 10.1364/OE.450172. (Cited on pages 32, 33, and 88.)

[125] S. I. Davis, A. Mueller, R. Valivarthi, N. Lauk, L. Narvaez, B. Korzh, A. D. Beyer, O. Cerri, M. Colangelo, K. K. Berggren, M. D. Shaw, S. Xie, N. Sinclair, and M. Spiropulu. Improved Heralded Single-Photon Source with a Photon-Number-Resolving Superconducting Nanowire Detector. *Physical Review Applied*, 18(6): 064007, 2022. DOI: 10.1103/PhysRevApplied.18.064007. (Cited on pages 32, 33, and 88.)

[126] W. Zhang, J. Huang, C. Zhang, L. You, C. Lv, L. Zhang, H. Li, Z. Wang, and X. Xie. A 16-Pixel Interleaved Superconducting Nanowire Single-Photon Detector

Array With A Maximum Count Rate Exceeding 1.5 GHz. *IEEE Transactions on Applied Superconductivity*, 29(5):1–4, 2019. DOI: 10.1109/TASC.2019.2895621. (Cited on page 33.)

[127] G. V. Resta, L. Stasi, M. Perrenoud, S. El-Khoury, T. Brydges, R. Thew, H. Zbinden, and F. Bussières. Gigahertz Detection Rates and Dynamic Photon-Number Resolution with Superconducting Nanowire Arrays. *Nano Letters*, 23(13):6018–6026, 2023. DOI: 10.1021/acs.nanolett.3c01228. (Cited on pages 33 and 90.)

[128] S. M. Tan, D. F. Walls, and M. J. Collett. Nonlocality of a single photon. *Physical Review Letters*, 66(3):252–255, 1991. DOI: 10.1103/PhysRevLett.66.252. (Cited on page 35.)

[129] L. Hardy. Nonlocality of a Single Photon Revisited. *Physical Review Letters*, 73(17): 2279–2283, 1994. DOI: 10.1103/PhysRevLett.73.2279. (Cited on page 35.)

[130] E. Santos. Comment on "Nonlocality of a single photon". *Physical Review Letters*, 68(6):894–894, 1992. DOI: 10.1103/PhysRevLett.68.894. (Cited on page 35.)

[131] D. M. Greenberger, M. A. Horne, and A. Zeilinger. Nonlocality of a Single Photon? *Physical Review Letters*, 75(10):2064–2064, 1995. DOI: 10.1103/PhysRevLett.75.2064. (Cited on page 35.)

[132] L. Vaidman. Nonlocality of a Single Photon Revisited Again. *Physical Review Letters*, 75(10):2063–2063, 1995. DOI: 10.1103/PhysRevLett.75.2063. (Cited on page 35.)

[133] M. Czachor. Bell theorem without inequalities: A single-particle formulation. *Physical Review A*, 49(4):2231–2240, 1994. DOI: 10.1103/PhysRevA.49.2231. (Cited on page 35.)

[134] D. Home and G. S. Agarwal. Quantum nonlocality of single photon states. *Physics Letters A*, 209(1-2):1–5, 1995. DOI: 10.1016/0375-9601(95)00825-5. (Cited on page 35.)

[135] A. Peres. Nonlocal Effects in Fock Space. *Physical Review Letters*, 74(23):4571–4571, 1995. DOI: 10.1103/PhysRevLett.74.4571. (Cited on page 35.)

[136] M. Revzen and A. Mann. Bell's inequality for a single particle. *Foundations of Physics*, 26(6):847–850, 1996. DOI: 10.1007/BF02058637. (Cited on page 35.)

[137] C. C. Gerry. Nonlocality of a single photon in cavity QED. *Physical Review A*, 53 (6):4583–4586, 1996. DOI: 10.1103/PhysRevA.53.4583. (Cited on page 35.)

[138] K. Banaszek and K. Wódkiewicz. Testing quantum nonlocality in phase space. *Physical Review Letters*, 82(10):2009–2013, 1999. DOI: 10.1103/PhysRevLett.82.2009. (Cited on pages 35 and 37.)

[139] G. Björk, P. Jonsson, and L. L. Sánchez-Soto. Single-particle nonlocality and entanglement with the vacuum. *Physical Review A*, 64(4):042106, 2001. DOI: 10.1103/PhysRevA.64.042106. (Cited on page 35.)

[140] S. J. van Enk. Single-particle entanglement. *Physical Review A*, 72(6):064306, 2005. DOI: 10.1103/PhysRevA.72.064306. (Cited on page 35.)

[141] J. Dunningham and V. Vedral. Nonlocality of a single particle. *Physical Review Letters*, 99(18):1–4, 2007. DOI: 10.1103/PhysRevLett.99.180404. (Cited on page 35.)

[142] D. Boschi, S. Branca, F. De Martini, L. Hardy, and S. Popescu. Experimental realization of teleporting an unknown pure quantum state via dual classical and einstein-podolsky-rosen channels. *Physical Review Letters*, 80(6):1121–1125, 1998. DOI: 10.1103/PhysRevLett.80.1121. (Cited on page 35.)

[143] E. Lombardi, F. Sciarrino, S. Popescu, and F. De Martini. Teleportation of a Vacuum–One-Photon Qubit. *Physical Review Letters*, 88(7):070402, 2002. DOI: 10.1103/PhysRevLett.88.070402. (Cited on page 35.)

[144] F. Sciarrino, E. Lombardi, G. Milani, and F. De Martini. Delayed-choice entanglement swapping with vacuum–one-photon quantum states. *Physical Review A*, 66(2): 024309, 2002. DOI: 10.1103/PhysRevA.66.024309. (Cited on page 35.)

[145] T. Guerreiro, F. Monteiro, A. Martin, J. B. Brask, T. Vértesi, B. Korzh, M. Caloz, F. Bussières, V. B. Verma, A. E. Lita, R. P. Mirin, S. W. Nam, F. Marsilli, M. D. Shaw, N. Gisin, N. Brunner, H. Zbinden, and R. T. Thew. Demonstration of Einstein-Podolsky-Rosen Steering Using Single-Photon Path Entanglement and Displacement-Based Detection. *Physical Review Letters*, 117(7):070404, 2016. DOI: 10.1103/PhysRevLett.117.070404. (Cited on page 35.)

[146] F. Monteiro, E. Verbanis, V. C. Vivoli, A. Martin, N. Gisin, H. Zbinden, and R. T. Thew. Heralded amplification of path entangled quantum states. *Quantum Science and Technology*, 2(2):024008, 2017. DOI: 10.1088/2058-9565/aa70ad. (Cited on page 35.)

[147] G. Murta, F. Grasselli, H. Kampermann, and D. Bruß. Quantum Conference Key Agreement: A Review. *Advanced Quantum Technologies*, 3(11):2000025, 2020. DOI: 10.1002/qute.202000025. (Cited on pages 35, 59, and 88.)

[148] D. Gottesman, T. Jennewein, and S. Croke. Longer-Baseline Telescopes Using Quantum Repeaters. *Physical Review Letters*, 109(7):070503, 2012. DOI: 10.1103/PhysRevLett.109.070503. (Cited on pages 35, 59, and 88.)

[149] E. T. Khabiboulline, J. Borregaard, K. De Greve, and M. D. Lukin. Optical Interferometry with Quantum Networks. *Physical Review Letters*, 123(7):070504, 2019. DOI: 10.1103/PhysRevLett.123.070504. (Cited on pages 35, 59, and 88.)

[150] S. Wallentowitz and W. Vogel. Unbalanced homodyning for quantum state measurements. *Physical Review A*, 53(6):4528–4533, 1996. DOI: 10.1103/PhysRevA.53.4528. (Cited on page 37.)

[151] K. Banaszek and K. Wódkiewicz. Direct Probing of Quantum Phase Space by Photon Counting. *Physical Review Letters*, 76(23):4344–4347, 1996. DOI: 10.1103/Phys-

RevLett.76.4344. (Cited on page 37.)

[152] M. G. Paris. Displacement operator by beam splitter. *Physics Letters A*, 217(2-3): 78–80, 1996. DOI: 10.1016/0375-9601(96)00339-8. (Cited on page 37.)

[153] B. C. Hall. *Lie Groups, Lie Algebras, and Representations*, volume 222 of *Graduate Texts in Mathematics*. Springer International Publishing, Cham, 2015. ISBN 978-3-319-13466-6. DOI: 10.1007/978-3-319-13467-3. (Cited on page 40.)

[154] A. Peres. Separability criterion for density matrices. *Physical Review Letters*, 77(8): 1413–1415, 1996. DOI: 10.1103/PhysRevLett.77.1413. (Cited on page 41.)

[155] M. Horodecki, P. Horodecki, and R. Horodecki. Separability of mixed states: necessary and sufficient conditions. *Physics Letters A*, 223(1-2):1–8, 1996. DOI: 10.1016/S0375-9601(96)00706-2. (Cited on pages 41 and 42.)

[156] W. Dür, G. Vidal, and J. I. Cirac. Three qubits can be entangled in two inequivalent ways. *Physical Review A*, 62(6):062314, 2000. DOI: 10.1103/PhysRevA.62.062314. (Cited on page 43.)

[157] W. Hoeffding. Probability Inequalities for Sums of Bounded Random Variables. *Journal of the American Statistical Association*, 58(301):13–30, 1963. DOI: 10.1080/01621459.1963.10500830. (Cited on page 48.)

[158] M. Gräfe, R. Heilmann, A. Perez-Leija, R. Keil, F. Dreisow, M. Heinrich, H. Moya-Cessa, S. Nolte, D. N. Christodoulides, and A. Szameit. On-chip generation of high-order single-photon W-states. *Nature Photonics*, 8(10):791–795, 2014. DOI: 10.1038/nphoton.2014.204. (Cited on pages 50 and 88.)

[159] P. J. Mosley. *Generation of Heralded Single Photons in Pure Quantum States*. PhD thesis, University of Oxford, 2007. (Cited on page 53.)

[160] L.-M. Duan, M. D. Lukin, J. I. Cirac, and P. Zoller. Long-distance quantum communication with atomic ensembles and linear optics. *Nature*, 414(6862):413–418, 2001. DOI: 10.1038/35106500. (Cited on page 60.)

[161] C. Simon, H. de Riedmatten, M. Afzelius, N. Sangouard, H. Zbinden, and N. Gisin. Quantum Repeaters with Photon Pair Sources and Multimode Memories. *Physical Review Letters*, 98(19):190503, 2007. DOI: 10.1103/PhysRevLett.98.190503. (Cited on pages 60, 61, and 75.)

[162] E. Verbanis. *Distribution and certification of photonic entanglement for quantum communication*. PhD thesis, Université de Genève, 2019. URL: `https://archive-ouverte.unige.ch/unige:119899`. (Cited on pages 60 and 71.)

[163] J. Minář, H. de Riedmatten, C. Simon, H. Zbinden, and N. Gisin. Phase-noise measurements in long-fiber interferometers for quantum-repeater applications. *Physical Review A*, 77(5):052325, 2008. DOI: 10.1103/PhysRevA.77.052325. (Cited on pages 71 and 73.)

[164] C. Clivati, A. Meda, S. Donadello, S. Virzì, M. Genovese, F. Levi, A. Mura, M. Pittaluga, Z. Yuan, A. J. Shields, M. Lucamarini, I. P. Degiovanni, and D. Calonico. Coherent phase transfer for real-world twin-field quantum key distribution. *Nature Communications*, 13(1):157, 2022. DOI: 10.1038/s41467-021-27808-1. (Cited on page 71.)

[165] P. Jobez. *Stockage multimode au niveau quantique pendant une milliseconde*. PhD thesis, Université de Genève, 2015. (Cited on pages 73 and 89.)

[166] K. Kutluer, E. Distante, B. Casabone, S. Duranti, M. Mazzera, and H. De Riedmatten. Time Entanglement between a Photon and a Spin Wave in a Multimode Solid-State Quantum Memory. *Physical Review Letters*, 123(3):30501, 2019. DOI: 10.1103/PhysRevLett.123.030501. (Cited on pages 73 and 89.)

[167] E. M. González-Ruiz, S. K. Das, P. Lodahl, and A. S. Sørensen. Violation of Bell's inequality with quantum-dot single-photon sources. *Physical Review A*, 106(1):1–16, 2022. DOI: 10.1103/PhysRevA.106.012222. (Cited on pages 75 and 90.)

[168] Q. Zhang, X.-H. Bao, C.-Y. Lu, X.-Q. Zhou, T. Yang, T. Rudolph, and J.-W. Pan. Demonstration of a scheme for the generation of "event-ready" entangled photon pairs from a single-photon source. *Physical Review A*, 77(6):062316, 2008. DOI: 10.1103/PhysRevA.77.062316. (Cited on pages 75 and 76.)

[169] D. E. Browne and T. Rudolph. Resource-Efficient Linear Optical Quantum Computation. *Physical Review Letters*, 95(1):010501, 2005. DOI: 10.1103/PhysRevLett.95.010501. (Cited on page 75.)

[170] X. Liu, J. Hu, Z. F. Li, X. Li, P. Y. Li, P. J. Liang, Z. Q. Zhou, C. F. Li, and G. C. Guo. Heralded entanglement distribution between two absorptive quantum memories. *Nature*, 594(7861):41–45, 2021. DOI: 10.1038/s41586-021-03505-3. (Cited on page 75.)

[171] P. Xu, H.-L. Yong, L.-K. Chen, C. Liu, T. Xiang, X.-C. Yao, H. Lu, Z.-D. Li, N.-L. Liu, L. Li, T. Yang, C.-Z. Peng, B. Zhao, Y.-A. Chen, and J.-W. Pan. Two-Hierarchy Entanglement Swapping for a Linear Optical Quantum Repeater. *Physical Review Letters*, 119(17):170502, 2017. DOI: 10.1103/PhysRevLett.119.170502. (Cited on pages 75 and 90.)

[172] A. Gerrard and J. M. Burch. *Introduction to Matrix Methods in Optics*. John Wiley & Sons, Hoboken, New Jersey, 1975. ISBN 978-0-471-29685-0. (Cited on page 77.)

[173] D. Makarov. Theory for the Beam Splitter in Quantum Optics: Quantum Entanglement of Photons and Their Statistics, HOM Effect. *Mathematics*, 10(24):4794, 2022. DOI: 10.3390/math10244794. (Cited on page 77.)

[174] E. Meyer-Scott, C. Silberhorn, and A. Migdall. Single-photon sources: Approaching the ideal through multiplexing. *Review of Scientific Instruments*, 91(4):041101, 2020. DOI: 10.1063/5.0003320. (Cited on pages 86 and 90.)

[175] Y.-Y. Ding, H. Chen, S. Wang, D.-Y. He, Z.-Q. Yin, W. Chen, Z. Zhou, G.-C. Guo, and Z.-F. Han. Polarization variations in installed fibers and their influence on quantum key distribution systems. *Optics Express*, 25(22):27923, 2017. DOI: 10.1364/OE.25.027923. (Cited on page 86.)

[176] X. Lu, Q. Li, D. A. Westly, G. Moille, A. Singh, V. Anant, and K. Srinivasan. Chip-integrated visible–telecom entangled photon pair source for quantum communication. *Nature Physics*, 15(4):373–381, 2019. DOI: 10.1038/s41567-018-0394-3. (Cited on page 89.)

[177] A. E. Lita, A. J. Miller, and S. W. Nam. Counting near-infrared single-photons with 95% efficiency. *Optics Express*, 16(5):3032, 2008. DOI: 10.1364/OE.16.003032. (Cited on page 90.)

[178] D. Fukuda, G. Fujii, T. Numata, K. Amemiya, A. Yoshizawa, H. Tsuchida, H. Fujino, H. Ishii, T. Itatani, S. Inoue, and T. Zama. Titanium Superconducting Photon-Number-Resolving Detector. *IEEE Transactions on Applied Superconductivity*, 21 (3):241–245, 2011. DOI: 10.1109/TASC.2010.2089953. (Cited on page 90.)

[179] I. Craiciu, B. Korzh, A. D. Beyer, A. Mueller, J. P. Allmaras, L. Narváez, M. Spiropulu, B. Bumble, T. Lehner, E. E. Wollman, and M. D. Shaw. High-speed detection of 1550 nm single photons with superconducting nanowire detectors. *Optica*, 10(2): 183, 2023. DOI: 10.1364/OPTICA.478960. (Cited on page 90.)

[180] F. Kaneda, B. G. Christensen, J. J. Wong, H. S. Park, K. T. McCusker, and P. G. Kwiat. Time-multiplexed heralded single-photon source. *Optica*, 2(12):1010, 2015. DOI: 10.1364/OPTICA.2.001010. (Cited on page 90.)

[181] F. Kaneda and P. G. Kwiat. High-efficiency single-photon generation via large-scale active time multiplexing. *Science Advances*, 5(10):eaaw8586, 2019. DOI: 10.1126/sciadv.aaw8586. (Cited on page 90.)

[182] S. L. N. Hermans, M. Pompili, H. K. C. Beukers, S. Baier, J. Borregaard, and R. Hanson. Qubit teleportation between non-neighbouring nodes in a quantum network. *Nature*, 605(7911):663–668, 2022. DOI: 10.1038/s41586-022-04697-y. (Cited on page 90.)

P. Published articles in peer-reviewed journals

1. **P. Caspar**, E. Verbanis, E. Oudot, N. Maring, F. Samara, M. Caloz, M. Perrenoud, P. Sekatski, A. Martin, N. Sangouard, H. Zbinden, and R. T. Thew. Heralded distribution of single-photon path entanglement. *Physical Review Letters*, 125(11):110506, 2020. DOI: 10.1103/PhysRevLett.125.110506.
2. **P. Caspar**, E. Oudot, P. Sekatski, N. Maring, A. Martin, N. Sangouard, H. Zbinden, and R. T. Thew. Local and scalable detection of genuine multipartite single-photon path entanglement. *Quantum*, 6:671, 2022. DOI: 10.22331/q-2022-03-22-671.
3. P. Sekatski, E. Oudot, **P. Caspar**, R. T. Thew, and N. Sangouard. Benchmarking single-photon sources from an auto-correlation measurement. *Quantum*, 6:875, 2022. DOI: 10.22331/q-2022-12-13-875.
4. L. Stasi, **P. Caspar**, T. Brydges, H. Zbinden, F. Bussières, and R. T. Thew. High-efficiency photon-number-resolving detector for improving heralded single-photon sources. *Quantum Science and Technology*, in press, 2023. DOI: 10.1088/2058-9565/ace54b.

P.1. Heralded distribution of single-photon path entanglement

Heralded Distribution of Single-Photon Path Entanglement

P. Caspar,[1] E. Verbanis,[1] E. Oudot,[1,2] N. Maring,[1] F. Samara,[1] M. Caloz,[1] M. Perrenoud,[1] P. Sekatski,[2] A. Martin,[1,*] N. Sangouard,[2,3] H. Zbinden,[1] and R. T. Thew[1,†]
[1]*Department of Applied Physics, University of Geneva, CH-1211 Genève, Switzerland*
[2]*Quantum Optics Theory Group, University of Basel, CH-4056 Basel, Switzerland*
[3]*Institut de physique théorique, Université Paris Saclay, CEA, CNRS, F-91191 Gif-sur-Yvette, France*

(Received 24 April 2020; accepted 30 July 2020; published 10 September 2020)

We report the experimental realization of heralded distribution of single-photon path entanglement at telecommunication wavelengths in a repeater-like architecture. The entanglement is established upon detection of a single photon, originating from one of two spontaneous parametric down-conversion photon pair sources, after erasing the photon's which-path information. In order to certify the entanglement, we use an entanglement witness which does not rely on postselection. We herald entanglement between two locations, separated by a total distance of 2 km of optical fiber, at a rate of 1.6 kHz. This work paves the way towards high-rate and practical quantum repeater architectures.

DOI: 10.1103/PhysRevLett.125.110506

Sharing photonic entanglement over long distances is a key resource for building a quantum communication network [1,2]. In order to distribute entanglement to two remote parties through optical fiber, quantum repeater schemes provide a solution to overcome the direct transmission loss [3]. The basic idea is to divide the whole distance into elementary links in each of which entanglement is independently established in a heralded way between two quantum memories. Finally, successive entanglement swapping operations between the links are used to extend the entanglement over the whole distance. Among the different quantum repeater schemes, those using single-photon path entanglement [4], where a single photon is delocalized into two modes, are promising candidates for establishing such a network since they require fewer resources as well as being less sensitive to memory and detector inefficiencies compared to other repeater schemes due to their linear, rather than quadratic, loss scaling [5].

A proposed postselection-free approach for entanglement distribution, based on the erasure of the heralding photon's which-path information, is a modification of the Duan-Lukin-Cirac-Zoller (DLCZ) protocol [6] that employs photon pair sources and multimode memories [7]. A practical implementation of this scheme, however, faces two major challenges. It requires first, stabilization and control of the optical phase between the two parties, and second, a practical implementation for entanglement certification. Experiments overcoming both challenges by employing individual matter qubits have been presented with ions [8], quantum dots [9,10], and nitrogen-vacancy centers [11]. However, in all those table-top demonstrations, entanglement was heralded by a photon outside the telecom band and thus will need to be frequency converted, which will further complicate the management of phase in the network. An approach combining an atomic ensemble quantum memory at near-infrared wavelengths and quantum frequency conversion to the telecom O-band has recently been reported [12], however, the entanglement was certified by recombining the entangled modes (single-photon interference) which is not applicable in a distributed scenario.

In this work we demonstrate a scheme for the heralded distribution of single-photon path entanglement at telecom wavelengths over a distance of 2×1.0 km of optical fiber, in a quantum repeater-like architecture (see Fig. 1). The detection of a single photon at the central station erases the which-path information about which one of the two photon pair sources it was emitted from, and heralds the distributed entangled state. The fiber connecting Alice and Bob is part of a phase stabilized interferometer. Another fiber (not shown), between Alice and Bob, closes the interferometer and is connected to a laser that is used to stabilize the interferometer. Inspired by an entanglement witness [13] using displacement-based photon detections [14], the

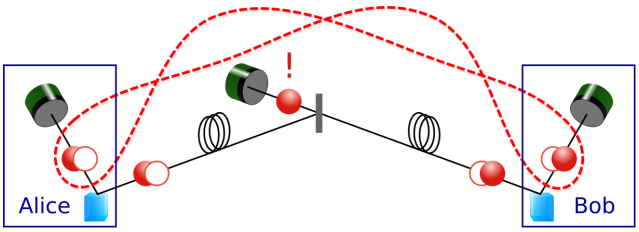

FIG. 1. Conceptual schematic of the experiment. A successful detection of a photon at the central station, originating from one of two photon pair sources, heralds the distribution of a single-photon path-entangled state between Alice and Bob.

distributed entanglement is measured locally and certified by an entanglement witness that is robust to loss, and does not make assumptions about the state itself.

Concept.—Each of the two spontaneous parametric down conversion (SPDC) photon pair sources, held by Alice and Bob, creates a two-mode squeezed vacuum state with low photon pair creation probability per pump pulse $P_{\mathrm{pair},A} = P_{\mathrm{pair},B} \ll 1$. Two modes, one from each source, are combined on a 50/50 beam splitter at the central station. By neglecting contributions from higher order pair creation probabilities $\mathcal{O}(P_{\mathrm{pair}})$, the resulting state shared between Alice and Bob, conditioned on the detection of a heralding photon, can be written as

$$|\psi\rangle_{AB} = \frac{1}{\sqrt{2}}(|10\rangle_{AB} + e^{i(\theta_B-\theta_A)}|01\rangle_{AB}), \tag{1}$$

where $|0\rangle$ denotes the vacuum state, $|1\rangle$ the single-photon number state, $\theta_{A(B)} = \phi_{A(B)} + \chi_{A(B)}$ with $\phi_{A(B)}$ the phase of the pump before the source on Alice's (Bob's) side and $\chi_{A(B)}$ the respective phase acquired by the photon traveling from the source to the central station [see Ref. [7] for the derivation of Eq. (1) and a more complete discussion]. The first conceptual challenge of this scheme is to prove entanglement within the $\{|0\rangle, |1\rangle\}$ subspace. This is possible using photon detection techniques preceded by weak displacement operations [14–19], as described in the following.

Displacement-based measurement.—We introduce the bosonic annihilation and creation operators a_i and $a_i^\dagger$ with $i \in \{1, 2\}$ acting on the photonic modes on Alice's ($i = 1$) and Bob's ($i = 2$) sides. We assume non-photon-number-resolving detectors, that is, only two different measurement results can be produced in each run. A "no-click" event is modeled by a projection on the vacuum state $|0\rangle\langle 0|$ whereas a "click" event corresponds to the projection into the orthogonal subspace $\mathbb{1} - |0\rangle\langle 0|$. If we attribute the outcome $+1$ to a no-detection and -1 to a conclusive detection, the observable including the displacement operation $D(\alpha_i) = e^{\alpha_i a_i^\dagger - \alpha_i^* a_i}$ on mode i is given by

$$\sigma_{\alpha_i}^{(i)} = D^\dagger(\alpha_i)(2|0\rangle\langle 0| - \mathbb{1})D(\alpha_i). \tag{2}$$

In the qubit subspace $\{|0\rangle, |1\rangle\}$, $\sigma_0^{(i)}$ corresponds exactly to the Pauli matrix σ_z on mode i. When α increases in amplitude, the positive operator valued measure (POVM) elements associated with outcomes $+1$ get closer to projections in the $x-y$ plane of the Bloch sphere [14]. For $\alpha = 1$ ($\alpha = i$), these POVM elements are projections along non-unit vectors pointing in the $x(y)$ direction.

Entanglement certification.—Building upon the displacement-based measurement, we now elaborate on the theory behind the witness that we developed to optimally certify path entanglement even in a lossy environment. The certification of entanglement for the state $|\psi\rangle_{AB}$ requires access to the coherence terms $|01\rangle\langle 10|$ and $|10\rangle\langle 01|$ as well as to the probabilities P_{ij} to have i photons on the first mode and j photons on the second mode. A good entanglement witness for our state is the observable

$$\hat{\mathcal{W}} = \sigma_{\alpha_1}^{(1)} \otimes \sigma_{\alpha_2}^{(2)}, \tag{3}$$

which is phase averaged according to

$$\hat{W} = \frac{1}{2\pi}\int_0^{2\pi} d\phi \left(\prod_{i=1}^{2} e^{i\phi \hat{a}_i^\dagger \hat{a}_i}\right) \hat{\mathcal{W}} \left(\prod_{i=1}^{2} e^{-i\phi \hat{a}_i^\dagger \hat{a}_i}\right) \tag{4}$$

to take into account that from experimental run to run, the global phase of the displacement parameter is arbitrary. Thus, the only remaining coherence terms in $\hat{W}$ are exactly the desired ones between $|01\rangle$ and $|10\rangle$.

In order to demonstrate entanglement we use the Peres-Horodecki criterion [20] stating that separable two-qubit states have a positive partial transpose (PPT). Considering the observable $\hat{W}$, we first compute its maximum expectation value w_{ppt} (see Supplemental Material Sec. II [21]) for separable two-qubit states ρ_{qubit}, i.e., $\rho_{\mathrm{qubit}} \geq 0$ and $\mathrm{tr}(\rho_{\mathrm{qubit}}) = 1$:

$$\begin{aligned} w_{\mathrm{ppt}} &= \max_{\rho_{\mathrm{qubit}}} \mathrm{tr}(\rho_{\mathrm{qubit}} \hat{W}) \\ \text{s.t. } &(i)\, \rho_{\mathrm{qubit}}^{T_1} \geq 0, \\ &(ii)\, \rho_{i,i} = P_{ii}, \end{aligned} \tag{5}$$

where $\rho_{i,i}$ denote the diagonal elements of ρ_{qubit}. The advantage of using this witness together with condition (ii) rather than a fixed linear combination of observables as done in Ref. [13] is that we use all our knowledge of the diagonal elements of the density matrix. This is equivalent to considering a witness constructed from all possible linear combinations of $\sigma_{\alpha_1}^{(1)} \otimes \sigma_{\alpha_2}^{(2)}$, $\sigma_0^{(1)} \otimes \sigma_0^{(2)}$, $\sigma_0^{(1)} \otimes \mathbb{1}$ and $\mathbb{1} \otimes \sigma_0^{(2)}$ which can detect more entangled states. If we restrict ourselves to qubit states, the quantities P_{ij} are given by the measured quantities $P_{\mathrm{nc,nc}}$, $P_{\mathrm{nc,c}}$, $P_{\mathrm{c,nc}}$ and $P_{\mathrm{c,c}}$ without displacement fields where, for example, $P_{\mathrm{nc,c}}$ is the joint probability of having a "no-click" event on the detector on mode 1 and a "click" event on mode 2. If the measured value of $\langle \hat{W} \rangle$ is larger than w_{ppt}, we can conclude that our state is entangled.

To elaborate on the robustness of our witness, let us consider the state $\rho_\eta = (1-\eta)|00\rangle\langle 00|_{AB} + \eta|\psi\rangle\langle\psi|_{AB}$ which corresponds to adding losses on the state $|\psi\rangle_{AB}$. One can easily check that there always exist settings α_1 and α_2 such that $\mathrm{tr}(\rho_\eta \hat{W}) > w_{\mathrm{ppt}}$ for all efficiencies η different than 0 (see Supplemental Material Sec. II [21]). This means that $\hat{W}$ has the ability to detect entanglement for arbitrary loss on the state. Note the fact that we considered detectors with unit efficiencies is still a valid description of

our measurement apparatus since one can transfer the inefficiency of the detector to loss on the state (see Supplemental Material Sec. IV [21]).

In practice, the amplitude of displacement operations may vary from run to run which could lead to false witness violations. To take into account those fluctuations, we first bound them experimentally and then maximize w_{ppt} accordingly, which leads to $\tilde{w}_{\mathrm{ppt}} \geq w_{\mathrm{ppt}}$ (see Supplemental Material Sec. III [21]). Note that in order to reduce the impact of amplitude fluctuations we choose the mean amplitudes such that $\partial^2 w_{\mathrm{ppt}}/\partial\alpha_1\partial\alpha_2 = 0$, which in our case holds true for $\alpha_1 = \alpha_2 \approx 0.83$.

So far, we derived the maximum expectation value w_{ppt} a separable two-qubit state can achieve. To remove the assumption on the dimension and hence to obtain a state-independent entanglement witness, we derive a general bound for all separable states (see Supplemental Material Sec. III [21])

$$w_{\mathrm{ppt}}^{\mathrm{max}} = \tilde{w}_{\mathrm{ppt}} + p_1^* + p_2^* + 2\beta\sqrt{(p_1^* + p_2^*)(1 - p_1^* - p_2^*)}, \tag{6}$$

where $\beta = 2\alpha_1\alpha_2 e^{-(\alpha_1^2+\alpha_2^2)}\sqrt{2(\alpha_1^4+\alpha_2^4)}$ with $\alpha_i \in \mathbb{R}^+$ and p_i^* denote upper bounds on the probabilities of having more than one photon in mode i. The latter can be bounded in practice by measuring twofold coincidences after a 50/50 beam splitter. We can thus conclude about entanglement in an arbitrary state ρ if $\mathrm{tr}(\rho\hat{W}) > w_{\mathrm{ppt}}^{\mathrm{max}}$.

Experiment.—A schematic overview of the experimental implementation is presented in Fig. 2. We use two nonlinear crystals as type-II SPDC sources pumped by a pulsed laser at $\lambda_p = 771.7$ nm to create nondegenerate photons at $\lambda_s = 1541.3$ (signal) and $\lambda_i = 1546.1$ nm (idler). The photon pair creation probability per pump pulse for each crystal is kept at $P_{\mathrm{pair}} \approx 3 \times 10^{-3}$ in order to keep the probability of having double-pair emissions sufficiently low. Signal and idler modes are separated after their generation at the polarizing beam splitters (PBS) and coupled into single-mode optical fibers. The idler photons are then sent to a 50/50 beam splitter (BS) and are spectrally filtered by a dense wavelength division multiplexer (DWDM) with a 100 GHz passband (ITU channel 39). We therefore ensure high-purity heralded signal photons and achieve a spectral overlap of 99.9% between idler photons originating from the two independent sources (see Supplemental Material Sec. VIII [21]). To reduce the photon noise due to residual seed-pulse photons (see below), and unwanted optical reflections, arriving before the heralding idler photons, a gate of 2 ns is generated by an electro-optic intensity modulator (EOM) to temporally filter before the detector. The EOM has an insertion loss of 5.0 dB and an extinction ratio of 33 dB.

In order to perform the displacement-based measurement on the state shared between Alice and Bob, we generate a

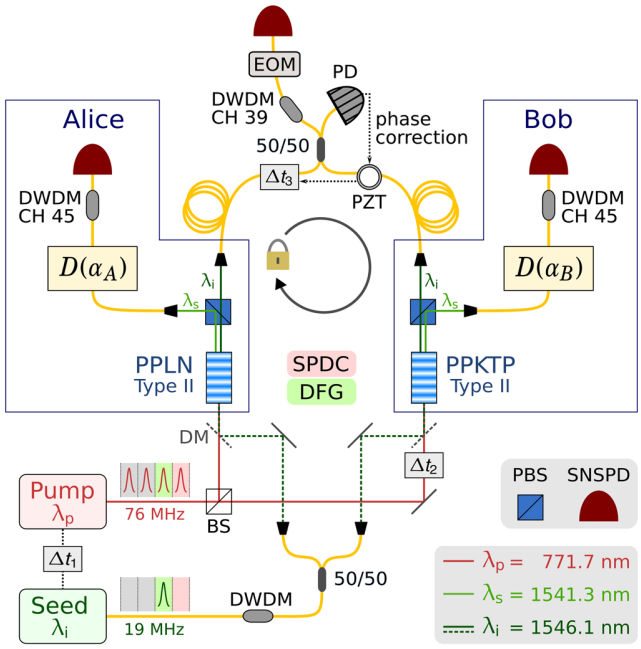

FIG. 2. Simplified schematic of the experimental setup for the heralded distribution and certification of single-photon path entanglement. A periodically poled lithium niobate (PPLN) and a periodically poled potassium titanyl phosphate (PPKTP) bulk nonlinear crystal are pumped by a pulsed Ti:sapphire laser at λ_p in the picosecond regime with a repetition rate of 76 MHz for collinear type-II SPDC and seeded by a pulsed DFB laser at λ_i with a repetition rate of 19 MHz for DFG. The idler photons are sent to the central station and herald entanglement distribution. The signal photons and coherent states are sent to Alice and Bob, respectively, in order to perform the displacement-based measurement. Photons are detected by three superconducting nanowire single-photon detectors (SNSPD).

coherent state with the same spectral, temporal, and polarization properties as the single photon signal via a difference frequency generation (DFG) process by stimulating the nonlinear crystals with a pulsed distributed feedback (DFB) seed laser at a wavelength $\lambda_i = 1546.1$ nm and repetition rate 19 MHz. The seed laser is driven from well below to above the lasing threshold each cycle to phase randomize the coherent state. For the implementation of the displacement-based measurement (see Supplemental Material Sec. VII [21]), the single-photon and the coherent states are temporally brought to coincidence in an asymmetric Mach-Zehnder interferometer (AMZI) followed by a PBS to project the single-photon and the coherent states into the same temporal and polarization modes, which realizes the displacement operation [15]. We increase the spectral overlap between single-photon and coherent states by local filtering with DWDMs (100 GHz passband at ITU channel 45).

To fulfill the phase stability requirement (see Supplemental Material Sec. VI [21]), the central interferometer is phase locked using the residual seed laser pulses at

the central station. A piezoelectric fiber stretcher (PZT) with a half-wavelength voltage of $V_\pi = 0.18$ V and an optical delay range of about 0.57 ps is actively controlled such that the seed power at the second output port of the 50/50 BS, measured with a photodiode (PD), is maximized. Note that we do not require phase-coherent pump pulses (see Supplemental Material Sec. VI [21]). Additionally, and specific to our implementation of the displacement-based measurement, the phase difference between the AMZIs is stabilized (see Supplemental Material Sec. VII [21]).

In order to demonstrate the feasibility of long-distance entanglement distribution, we extend the central interferometer arm lengths from initially $l = 42$ m to $l = 1.0$ km by inserting two fiber coils. This change additionally requires active polarization control before the 50/50 BS as well as active compensation of slow relative drifts in optical length between the two interferometer arms. Therefore, electronic polarization controllers (Phoenix Photonics PSC) are inserted after the fiber coils to minimize the seed power at the second output ports of the fiber PBSs whose first output ports are connected to the polarization maintaining 50/50 BS at the end of the central interferometer. The slow relative optical length drifts are compensated by actively setting Δt_3 (see Fig. 2) with a motorized delay line such that the voltage applied to the PZT is kept in range. In this way, we achieve long-term phase stabilization as shown in Fig. 3 for a duration of 8 h.

The photons are detected by three in-house-developed MoSi superconducting nanowire single-photon detectors (SNSPD) with efficiencies $\eta_d > 60\%$ and recovery times $\tau_{\mathrm{rec}} < 35$ ns. Time correlated single-photon counting (ID Quantique ID900) is used to register the events of a signal photon detected by Alice, by Bob, and coincidences conditioned on the detection of an idler photon at the central station within a 400 ps window with respect to the 19 MHz clock signal. In the α-basis, we monitor the displacement amplitudes by tracking the detection rates caused by coherent states arriving 1 cycle (52 ns) later than the expected signal photons.

Results.—A measurement of the witness as a function of the relative phase between Alice's and Bob's displacement operations is shown in Fig. 4. After the relative phase is set to $(\theta_B - \theta_A) = 0$, counts were acquired in the α-basis for 1 h and subsequently in the z-basis for 2.5 h by blocking the coherent state paths in the measurement interferometers. From the "click"-"no-click" events recorded by Alice and Bob, the corresponding joint probabilities are deduced (see Supplemental Material Sec. IX [21]). We separately determined the probability of having more than one photon locally in a Hanbury Brown–Twiss experiment for both Alice and Bob. Together with the joint probabilities measured in the z-basis as well as the displacement parameter amplitudes used in the α-basis measurement, we compute the estimator (see Supplemental Material Sec. V [21]) for the maximal separable bound $w_{\mathrm{ppt}}^{\max}$ according to Eq. (6). The experimental value for the expectation value $w_\rho^{\exp}$ of the witness $\hat{W}$ is computed from the measured joint probabilities in the α-basis by

$$w_\rho^{\exp} = (P_{\mathrm{nc,nc}} + P_{\mathrm{c,c}} - P_{c,\mathrm{nc}} - P_{\mathrm{nc,c}})|_{\alpha_1,\alpha_2}. \tag{7}$$

For the analysis of uncertainties on the separable bound $\sigma_{\mathrm{ppt}}^{\max}$ and on the experimental value of the witness $\sigma_\rho^{\exp}$ we assume the coincidence probabilities to be independent and identically distributed (i.i.d.) random variables (see Supplemental Material Sec. V [21]). The obtained results, as shown in Table I, certify a violation of the entanglement witness by more than 5 standard deviations at a heralding rate of at least 1.4 kHz for fiber distances of $l = 42$ m and

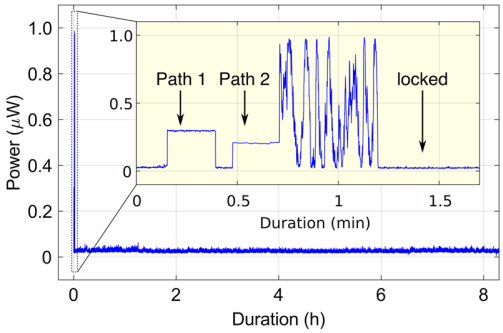

FIG. 3. Characterization measurement of the central interferometer phase locking for $l = 1.0$ km. The graph shows the measured seed power at the 50/50 BS output port 1 over a duration of 8 h. The active feedback on the piezoelectric fiber stretcher and the time delay feedback are turned on after 1.2 min (inset). During the initial 1.2 min, first path 1 of the interferometer is left open only, then path 2, and afterwards both paths are opened leading to interference.

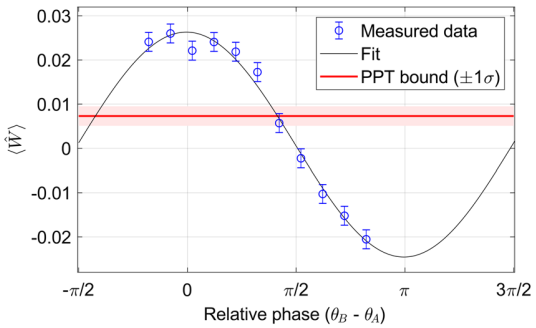

FIG. 4. Expectation value and PPT bound $w_{\mathrm{ppt}}^{\max}$ of the entanglement witness as a function of the relative phase $(\theta_B - \theta_A)$ between the displacement measurements for Alice and Bob with $l = 1.0$ km. Values of $\langle \hat{W} \rangle$ larger than $w_{\mathrm{ppt}}^{\max}$ demonstrate entanglement. For each phase setting, counts were acquired for 200 s in the α-basis with $\alpha_1 = 0.818^{+0.004}_{-0.003}$ and $\alpha_2 = 0.830^{+0.006}_{-0.007}$ indicating the mean, maximum, and minimum displacement amplitudes. Error bars of the measured data represent 1 standard deviation.

TABLE I. Measured value w_ρ^{exp} and calculated separable bound $w_{\mathrm{ppt}}^{\mathrm{max}}$ of the entanglement witness for fibers of length l inserted in each arm of the central interferometer at an observed heralding rate ν_h and signal-to-noise ratio (SNR). The witness is violated by $k = (w_\rho^{\mathrm{exp}} - w_{\mathrm{ppt}}^{\mathrm{max}})/(\sigma_{\mathrm{ppt}}^{\mathrm{max}} + \sigma_\rho^{\mathrm{exp}})$ standard deviations.

l	ν_h (kHz)	SNR	w_ρ^{exp}	$w_{\mathrm{ppt}}^{\mathrm{max}}$	k
42 m	1.4	12	0.0206(8)	0.0071(16)	5.6
1.0 km	1.6	5	0.0253(7)	0.0071(22)	6.2

$l = 1.0$ km inserted in each arm of the central interferometer. The higher total heralding rate in the case of $l = 1.0$ km is due to an elevated noise contribution. The larger statistical significance of the result with $l = 1.0$ km compared to $l = 42$ m is mainly attributed to a different alignment setting in the measurement AMZIs leading to an increase of the transmission on the entangled state (see Supplemental Material Sec. IX [21]).

Discussion.—Single-photon quantum repeater schemes are promising for fiber-based long-distance entanglement distribution because of their favorable transmission loss scaling, their robustness to memory and detector inefficiencies and the need for fewer resources than protocols based on two-photon detections [5]. We demonstrated the feasibility of such a scheme by actively stabilizing the phase of an interferometer with arm lengths of 1.0 km and utilizing local displacement-based measurements for entanglement certification. In our scheme the phase difference between the AMZIs also needs to be stabilized (see Supplemental Material Sec. VII [21]), however, in a quantum repeater these AMZIs could be replaced, and the displacement performed, by quantum memories [25,26].

In principle, the scheme can be extended for real world applications by using two individual pump lasers, adding fiber before the sources to distribute the seed pulses and further increasing the size of the central interferometer. The main technical challenge in such an implementation is the increase of phase noise in a larger central interferometer [27]. This would not only degrade the entanglement, but also increase the leakage of residual seed laser pulse photons towards the heralding detector. Our solution to suppress them with an EOM introduces unwanted loss on the heralding photons, however, a better solution would be to develop a gated SNSPD for the central station.

In conclusion, we demonstrated the heralded distribution of single-photon path entanglement in a repeater-like architecture. For a fiber distance of 2×1.0 km inserted in the central interferometer we achieve a heralding rate of 1.6 kHz and we certify a violation of the entanglement witness by 6.2 standard deviations. These results highlight the feasibility and challenges associated with realizing DLCZ-like quantum repeater architectures.

The authors would like to thank C. Autebert, J.-D. Bancal, F. Bussières, C. Barreiro, A. Boaron, and P. Remy for useful discussions and technical support. This work was supported by the Swiss National Science Foundation SNSF (Grants No. 200021_159592, No. 200020_182664, and No. PP00P2-179109), COST (SBFI/SNF) IZCNZ0-174835, and the European Union's Horizon 2020 research and innovation programme under Grant Agreement No. 820445 (Quantum Internet Alliance).

P. C. and E. V. contributed equally to this work.

*Present address: Université Côte d'Azur, CNRS, Institut de Physique de Nice, Parc Valrose, F-06108 Nice Cedex 2, France.

†Robert.Thew@unige.ch

[1] H. J. Kimble, Nature (London) **453**, 1023 (2008).
[2] S. Wehner, D. Elkouss, and R. Hanson, Science **362**, eaam9288 (2018).
[3] H.-J. Briegel, W. Dür, J. I. Cirac, and P. Zoller, Phys. Rev. Lett. **81**, 5932 (1998).
[4] S. M. Tan, D. F. Walls, and M. J. Collett, Phys. Rev. Lett. **66**, 252 (1991).
[5] N. Sangouard, C. Simon, H. de Riedmatten, and N. Gisin, Rev. Mod. Phys. **83**, 33 (2011).
[6] L.-M. Duan, M. D. Lukin, J. I. Cirac, and P. Zoller, Nature (London) **414**, 413 (2001).
[7] C. Simon, H. de Riedmatten, M. Afzelius, N. Sangouard, H. Zbinden, and N. Gisin, Phys. Rev. Lett. **98**, 190503 (2007).
[8] L. Slodička, G. Hétet, N. Röck, P. Schindler, M. Hennrich, and R. Blatt, Phys. Rev. Lett. **110**, 083603 (2013).
[9] A. Delteil, Z. Sun, W. B. Gao, E. Togan, S. Faelt, and A. Imamoglu, Nat. Phys. **12**, 218 (2016).
[10] R. Stockill, M. J. Stanley, L. Huthmacher, E. Clarke, M. Hugues, A. J. Miller, C. Matthiesen, C. Le Gall, and M. Atatüre, Phys. Rev. Lett. **119**, 010503 (2017).
[11] P. C. Humphreys, N. Kalb, J. P. J. Morits, R. N. Schouten, R. F. L. Vermeulen, D. J. Twitchen, M. Markham, and R. Hanson, Nature (London) **558**, 268 (2018).
[12] Y. Yu, F. Ma, X.-Y. Luo, B. Jing, P.-F. Sun, R.-Z. Fang, C.-W. Yang, H. Liu, M.-Y. Zheng, X.-P. Xie, W.-J. Zhang, L.-X. You, Z. Wang, T.-y. Chen, Q. Zhang, X.-H. Bao, and J.-W. Pan, Nature (London) **578**, 240 (2020).
[13] F. Monteiro, V. C. Vivoli, T. Guerreiro, A. Martin, J.-D. Bancal, H. Zbinden, R. T. Thew, and N. Sangouard, Phys. Rev. Lett. **114**, 170504 (2015).
[14] V. C. Vivoli, P. Sekatski, J.-D. Bancal, C. C. W. Lim, A. Martin, R. T. Thew, H. Zbinden, N. Gisin, and N. Sangouard, New J. Phys. **17**, 023023 (2015).
[15] M. G. Paris, Phys. Lett. A **217**, 78 (1996).
[16] K. Banaszek and K. Wódkiewicz, Phys. Rev. Lett. **82**, 2009 (1999).
[17] A. Kuzmich, I. A. Walmsley, and L. Mandel, Phys. Rev. Lett. **85**, 1349 (2000).
[18] G. Björk, P. Jonsson, and L. L. Sánchez-Soto, Phys. Rev. A **64**, 042106 (2001).
[19] B. Hessmo, P. Usachev, H. Heydari, and G. Björk, Phys. Rev. Lett. **92**, 180401 (2004).
[20] M. Horodecki, P. Horodecki, and R. Horodecki, Phys. Lett. A **223**, 1 (1996).

[21] See Supplemental Material at http://link.aps.org/supplemental/10.1103/PhysRevLett.125.110506 for theoretical calculations, details on the experimental implementation and additional data to support the results, which includes Refs. [22–24].

[22] A. R. McMillan, L. Labonté, A. S. Clark, B. Bell, O. Alibart, A. Martin, W. J. Wadsworth, S. Tanzilli, and J. G. Rarity, Sci. Rep. **3**, 2032 (2013).

[23] P. J. Mosley, Generation of heralded single photons in pure quantum states, Ph.D. Thesis, University of Oxford, 2007.

[24] N. Bruno, A. Martin, and R. Thew, Opt. Commun. **327**, 17 (2014).

[25] P. Jobez, Stockage multimode au niveau quantique pendant une milliseconde, Ph. D. thesis, Université de Genève, 2015.

[26] K. Kutluer, E. Distante, B. Casabone, S. Duranti, M. Mazzera, and H. de Riedmatten, Phys. Rev. Lett. **123**, 030501 (2019).

[27] J. Minář, H. de Riedmatten, C. Simon, H. Zbinden, and N. Gisin, Phys. Rev. A **77**, 052325 (2008).

Supplemental Material: Heralded distribution of single-photon path entanglement

Patrik Caspar,[1,*] Ephanielle Verbanis,[1,*] Enky Oudot,[1,2] Nicolas Maring,[1] Farid Samara,[1] Misael Caloz,[1] Matthieu Perrenoud,[1] Pavel Sekatski,[2] Anthony Martin,[1,†] Nicolas Sangouard,[2,3] Hugo Zbinden,[1] and Rob Thew[1,‡]

[1] *Department of Applied Physics, University of Geneva, CH-1211 Genève, Switzerland*
[2] *Quantum Optics Theory Group, University of Basel, CH-4056 Basel, Switzerland*
[3] *Institut de physique théorique, Université Paris Saclay, CEA, CNRS, F-91191 Gif-sur-Yvette, France*

I. ENTANGLEMENT WITNESS

We consider a scenario where we have two protagonists, Alice and Bob, each of whom has a photonic mode labelled 1 and 2, respectively. We introduce the corresponding bosonic operators a_i and $a_i^\dagger$ with $i \in \{1,2\}$. We consider the observable

$$\hat{\mathcal{W}} = \sigma_{\alpha_1}^{(1)} \otimes \sigma_{\alpha_2}^{(2)} \tag{1}$$

where $\sigma_{\alpha_i}^{(i)}$ is realized on mode i with a single photon detector (non-photon-number-resolving detector) preceded by a displacement operation $D(\alpha) = e^{\alpha a_i^\dagger - \alpha^* a_i}$. The explicit expression of $\sigma_{\alpha_i}^{(i)}$ is given by

$$\sigma_{\alpha_i}^{(i)} = D^\dagger(\alpha_i)(2|0\rangle\langle 0| - \mathbb{1})D(\alpha_i) \tag{2}$$

if one assigns the outcomes $+1$ when the detector does not click and -1 if it clicks. Moreover we consider the phase averaging of our observable according to

$$\hat{W} = \frac{1}{2\pi}\int_0^{2\pi} d\phi \left(\prod_i^2 e^{i\phi a_i^\dagger a_i}\right) \hat{\mathcal{W}} \left(\prod_i^2 e^{-i\phi a_i^\dagger a_i}\right). \tag{3}$$

Additionally we perform measurements without displacement and thus have access to the probabilities $P_{\mathrm{nc,nc}}$, $P_{\mathrm{c,nc}}$, $P_{\mathrm{nc,c}}$, $P_{\mathrm{c,c}}$, where for example $P_{\mathrm{nc,c}}$ is the probability that the first detector on mode 1 does not click and the second one mode 2 clicks.

II. SEPARABLE BOUND IN QUBIT SPACE

We consider the qubit space $\{|0\rangle, |1\rangle\}$ made with the vaccum and the single photon number state. We want to find the maximum value of $\mathrm{tr}(\rho_{\mathrm{qubit}}^{\mathrm{sep}} \hat{W}_{\mathrm{qubit}})$ a separable 2-qubit state $\rho_{\mathrm{qubit}}^{\mathrm{sep}}$ can achieve. We use the Peres-Horodecki criterion (also refered to as PPT criterion) stating that any two qubit state having a positive partial transpose (PPT state) is separable and hence compute the maximum value of $\mathrm{tr}(\rho_{\mathrm{qubit}}^{\mathrm{sep}} \hat{W}_{\mathrm{qubit}})$ a PPT qubit state can achieve knowing the diagonal elements of $\rho_{\mathrm{qubit}}^{\mathrm{sep}}$. Let us note that $\hat{W}$ have a simple structure in this qubit space

$$\hat{W}_{\mathrm{qubit}} = \begin{pmatrix} w_{00} & 0 & 0 & 0 \\ 0 & w_{01} & wc_{01} & 0 \\ 0 & wc_{10} & w_{10} & 0 \\ 0 & 0 & 0 & w_{11} \end{pmatrix}. \tag{4}$$

We can thus write

$$\mathrm{tr}(\rho_{\mathrm{qubit}}^{\mathrm{sep}} \hat{W}_{\mathrm{qubit}}) = w_{00}P_{00} + w_{01}P_{01} + w_{10}P_{10} + w_{11}P_{11} + wc_{01}\langle 10|\rho_{\mathrm{qubit}}^{\mathrm{sep}}|01\rangle + wc_{10}\langle 01|\rho_{\mathrm{qubit}}^{\mathrm{sep}}|10\rangle \tag{5}$$

where $P_{ij} = \langle ij|\rho_{\mathrm{qubit}}^{\mathrm{sep}}|ij\rangle$ represents the probability to get i photons in mode 1 and j photons in mode 2.

---

* These authors contributed equally to this work.
† Present address: Université Côte d'Azur, CNRS, Institut de Physique de Nice, Parc Valrose, F-06108 Nice Cedex 2, France
‡ Electronic address: Robert.Thew@unige.ch

Furthermore, the positivity of $\rho^{\text{sep}}_{\text{qubit}}$ implies that $|\langle 01|\rho^{\text{sep}}_{\text{qubit}}|10\rangle| \leq \sqrt{P_{10}P_{01}}$. The positivity under partial transpose imposes that $|\langle 01|\rho^{\text{sep}}_{\text{qubit}}|10\rangle| \leq \sqrt{P_{00}P_{11}}$. The condition "$\rho^{\text{sep}}_{\text{qubit}}$ is a PPT state" thus imposes that

$$\text{tr}(\rho^{\text{sep}}_{\text{qubit}}\hat{W}_{\text{qubit}}) \leq w_{00}P_{00} + w_{01}P_{01} + w_{10}P_{10} + w_{11}P_{11} + (wc_{01} + wc_{10}) \cdot \min(\sqrt{P_{00}P_{11}}, \sqrt{P_{10}P_{01}}). \tag{6}$$

We observe that the separable states maximizing the witness satisfy $\sqrt{P_{00}P_{11}} < \sqrt{P_{10}P_{01}}$. Moreover, from eqs. (1) and (3) one easily sees that $(wc_{01} + wc_{10}) = 8\alpha_1\alpha_2 e^{-\alpha_1^2-\alpha_2^2}$ is non-negative. To simplify the expression we thus relax the separable bound using $\min(\sqrt{P_{00}P_{11}}, \sqrt{P_{10}P_{01}}) \leq \sqrt{P_{00}P_{11}}$. Computing all the coefficients w from Eqs. (1) and (3) we obtain

$$\begin{aligned}
\text{tr}(\rho^{\text{sep}}_{\text{qubit}}\hat{W}_{\text{qubit}}) \leq w_{\text{ppt}} = &\left(2e^{-\alpha_1^2} - 1\right)\left(2e^{-\alpha_2^2} - 1\right)P_{00} \\
&+ 8\alpha_1\alpha_2 e^{-\alpha_1^2-\alpha_2^2}\sqrt{P_{00}P_{11}} \\
&+ \left(2\alpha_1^2 e^{-\alpha_1^2} - 1\right)\left(2\alpha_2^2 e^{-\alpha_2^2} - 1\right)P_{11} \\
&+ \left(2\alpha_1^2 e^{-\alpha_1^2} - 1\right)\left(2e^{-\alpha_2^2} - 1\right)P_{10} \\
&+ \left(2e^{-\alpha_1^2} - 1\right)\left(2\alpha_2^2 e^{-\alpha_2^2} - 1\right)P_{01}.
\end{aligned} \tag{7}$$

where here $\alpha_i \in \mathbb{R}^+$ denote the displacement amplitudes. If the quantity $V = (\langle \hat{W}_{\text{qubit}}\rangle - w_{\text{ppt}})$ is positive, we can conclude that the measured state is entangled under the condition that it is a 2-qubit state.

To elaborate on the robustness of our witness with respect to losses on the state, let us consider the pure state

$$|\Psi^+\rangle = \frac{1}{\sqrt{2}}(|01\rangle + |10\rangle). \tag{8}$$

After traveling through a lossy channel with transmission η, this state becomes

$$\rho_\eta = (1-\eta)|00\rangle\langle 00| + \eta|\Psi^+\rangle\langle\Psi^+|. \tag{9}$$

For such a state we have

$$V = 8\alpha_1\alpha_2 e^{-\alpha_1^2-\alpha_2^2}\frac{\eta}{2} \tag{10}$$

which is positive for all amplitude of the displacements. This means that $\hat{W}$ has the ability to detect entanglement for arbitrary loss on the state $|\Psi^+\rangle$. This statement can easily be generalized to every state of the form $|\psi\rangle = (|01\rangle + e^{i\phi}|10\rangle)/\sqrt{2}$ by selecting the displacement parameters $\alpha_i \in \mathbb{C}$ in Eq. (1) accordingly. In the next section we extend this witness to the case of an arbitrary Hilbert space.

III. SEPARABLE BOUND OUTSIDE THE QUBIT SPACE

A. Bound on w_{ppt} for displacement with fluctuating amplitudes

In practice, the amplitude of the displacement might fluctuate during the experiment. Averaging the amplitudes for short times, we have access to a range of fluctuations $\alpha_1 \in \mathcal{I}_1$, $\alpha_2 \in \mathcal{I}_2$ with $\mathcal{I}_1, \mathcal{I}_2 \subset \mathbb{R}^+$. We thus simply consider

$$\begin{aligned}
w_{\text{ppt}} \leq \max_{\alpha_1\in\mathcal{I}_1,\alpha_2\in\mathcal{I}_2} \Bigg(&\left(2e^{-\alpha_1^2} - 1\right)\left(2e^{-\alpha_2^2} - 1\right)P_{00} \\
&+ 8\alpha_1\alpha_2 e^{-\alpha_1^2-\alpha_2^2}\sqrt{P_{00}P_{11}} \\
&+ \left(2\alpha_1^2 e^{-\alpha_1^2} - 1\right)\left(2\alpha_2^2 e^{-\alpha_2^2} - 1\right)P_{11} \\
&+ \left(2\alpha_1^2 e^{-\alpha_1^2} - 1\right)\left(2e^{-\alpha_2^2} - 1\right)P_{10} \\
&+ \left(2e^{-\alpha_1^2} - 1\right)\left(2\alpha_2^2 e^{-\alpha_2^2} - 1\right)P_{01}\Bigg).
\end{aligned} \tag{11}$$

In the case where we do not restrict ourselves to qubits, we replace P_{00} and P_{11} by $P_{\mathrm{c,c}}$ and $P_{\mathrm{nc,nc}}$. Furthermore we replace P_{10} and P_{01} by $(P_{\mathrm{c,nc}} - p_1^*)$ and $(P_{\mathrm{nc,c}} - p_2^*)$ if the maximization in Eq. (11) gives negative terms in front of P_{10} and P_{01} where $p_1^* > p(n_1 \geq 2)$ is a bound on the probability to get strictly more than one photon in mode 1 and similarly for p_2^*. If the maximization in Eq. (11) gives positive terms in front of P_{10} and P_{01}, we replace them by $P_{\mathrm{c,nc}}$ and $P_{\mathrm{nc,c}}$, respectively. We thus get

$$w_{\mathrm{ppt}} \leq C_1 P_{\mathrm{nc,nc}} + C_2\sqrt{P_{\mathrm{nc,nc}}P_{\mathrm{c,c}}} + C_3 P_{\mathrm{c,c}} + \max\left(C_4(P_{\mathrm{c,nc}} - p_1^*), C_4 P_{\mathrm{c,nc}}\right) + \max\left(C_5(P_{\mathrm{nc,c}} - p_2^*), C_5 P_{\mathrm{nc,c}}\right), \quad (12)$$

where C_1, C_2, C_3, C_4, and C_5 come from the maximization in Eq. (11).

B. Bound on $\langle \hat{W} \rangle$ for separable state outside the qubit space

We consider the observable $\hat{W}$ represented by

$$\hat{W} = \begin{pmatrix} A & B \\ B^\dagger & C \end{pmatrix} \quad (13)$$

and a state ρ of the form

$$\rho = \begin{pmatrix} a & b \\ b^\dagger & c \end{pmatrix}, \quad (14)$$

where a and A live in the two-qubit space $\mathcal{H}_Q$ spanned by $\{|0\rangle, |1\rangle\}$ and c and C live in a Hilbert space $\mathcal{H}_C$. We define P_2 as the trace of c so that the trace of a is equal to $(1 - P_2)$. The parts are now arranged such that

$$\mathrm{tr}(\rho\hat{W}) = \mathrm{tr}(aA) + \mathrm{tr}(b^\dagger B + bB^\dagger) + \mathrm{tr}(cC). \quad (15)$$

We are interested in particular in the maximum expectation value of $\hat{W}$ a separable state can achieve. We treated the part which belongs to the qubit space above. We thus only have to find tight upper bounds on the quantities $\mathrm{tr}(b^\dagger B + bB^\dagger)$ and $\mathrm{tr}(cC)$ that any state ρ satisfies.

Let us first deal with the term $\mathrm{tr}(cC)$, we have

$$\mathrm{tr}(c\,C) = \mathrm{tr}\left(\begin{pmatrix} 0 & 0 \\ 0 & c \end{pmatrix}\hat{W}\right) \leq P_2 ||\hat{W}||_1 = P_2, \quad (16)$$

where $||\hat{W}||_1$ is the maximal eigenvalue of $\hat{W}$, bounded by one by definition. This settles the issue.

Next, consider the term $\mathrm{tr}(bB^\dagger)$. We start with the singular value decomposition of b

$$\begin{pmatrix} 0 & b \\ 0 & 0 \end{pmatrix} = \begin{pmatrix} 0 & UDV^\dagger \\ 0 & 0 \end{pmatrix} = \sum_{i=1}^{L} d_i |a_i\rangle\langle c_i|, \quad (17)$$

where $\{|a_i\rangle\}$ and $\{|c_i\rangle\}$ are sets of orthonormal vectors on $\mathcal{H}_Q$ and $\mathcal{H}_C$ respectively, the singlular values d_i are nonnegative real numbers, and $L = \min\big(\dim(\mathcal{H}_Q), \dim(\mathcal{H}_C)\big) = 4$ in our case. Using Eq. (17) we can bound

$$|\mathrm{tr}(bB^\dagger)| = \sum_{i=1}^{L} d_i |\langle c_i|B^\dagger|a_i\rangle| \leq \left(\sum_{i=1}^{L} d_i\right) b_{\max}, \quad (18)$$

where $b_{\max}$ is the maximal singular value of $B^\dagger$, or equivalently of B, it can be easily obtained from the definition of the witness in Eq. (3), see later. It remains to upper-bound the term $(\sum_{i=1}^{L} d_i)$.

To do so define a set of orthonormal states $|\psi^i\rangle \in \mathcal{H}_Q \oplus \mathcal{H}_C$ as

$$|\psi^i\rangle = \cos(\theta)|a_i\rangle + \sin(\theta)|c_i\rangle \quad (19)$$

for some parameter θ. As $\sum_{i=1}^{L} |\psi^i\rangle\langle\psi^i| \leq \mathbb{1}$ we obtain the following inequality

$$1 \geq \sum_{i=1}^{L} \langle\psi^i|\rho|\psi^i\rangle = \cos^2(\theta)\left(\sum_{i=1}^{L}\langle\chi_A^i|a|\chi_A^i\rangle\right) + \sin^2(\theta)\left(\sum_{i=1}^{L}\langle\chi_C^i|c|\chi_C^i\rangle\right) + 2\cos(\theta)\sin(\theta)\sum_{i=1}^{L} d_i. \tag{20}$$

Finally, by rearranging the terms we get the desired bound

$$\begin{aligned}\sum_{i=1}^{L} d_i &\leq \frac{1-\cos^2(\theta)\left(\sum_i \langle\chi_A^i|a|\chi_A^i\rangle\right) - \sin^2(\theta)\left(\sum_i \langle\chi_C^i|c|\chi_C^i\rangle\right)}{2\cos(\theta)\sin(\theta)} \\ &\leq \frac{1-\cos^2(\theta)\mathrm{tr}(a) - \sin^2(\theta)\mathrm{tr}(c)}{2\cos(\theta)\sin(\theta)} = \frac{1-\cos^2(\theta)(1-P_2) - \sin^2(\theta)(P_2)}{2\cos(\theta)\sin(\theta)}\end{aligned} \tag{21}$$

for any value of θ. Minimizing the right hand side with respect to θ yields the final bound

$$\sum_{i=1}^{L} d_i \leq \sqrt{P_2(1-P_2)}. \tag{22}$$

We thus have access to the two following inequalities in order to bound w_{ppt},

$$\mathrm{tr}(cC) \leq P_2, \tag{23}$$

$$\mathrm{tr}(b^\dagger B + bB^\dagger) \leq 2\sqrt{P_2(1-P_2)}|b_{\max}|, \tag{24}$$

where P_2 is the probability to have strictly more than one photon in at least one mode. For our witness, the phase randomization kills all the terms in B except two, namely the photon-number preserving terms $2\sqrt{2}\alpha_1\alpha_2^3|11\rangle\langle 02|$ and $2\sqrt{2}\alpha_1^3\alpha_2|11\rangle\langle 20|$. We thus simply have

$$b_{\max} = 2\alpha_1\alpha_2 e^{-\alpha_1^2-\alpha_2^2}\sqrt{2\alpha_1^4 + 2\alpha_2^4} \tag{25}$$

for which we consider the maximum value in $\mathcal{I}_1$ and $\mathcal{I}_2$

$$\beta = \max_{\alpha_1\in\mathcal{I}_1,\alpha_2\in\mathcal{I}_2}\Big(b_{\max}\Big). \tag{26}$$

The last part is to find a bound on P_2 one can measure in the experiment. One has the probabilities

$$P_2 = p(n_1 \leq 1 \cap n_2 > 1) + p(n_1 > 1 \cap n_2 \leq 1) + p(n_1 > 1 \cap n_2 > 1), \tag{27}$$

$$p_1^* \geq p(n_1 > 1) = p(n_1 > 1 \cap n_2 \leq 1) + p(n_1 > 1 \cap n_2 > 1), \tag{28}$$

$$p_2^* \geq p(n_2 > 1) = p(n_1 \leq 1 \cap n_2 > 1) + p(n_1 > 1 \cap n_2 > 1), \tag{29}$$

where n_i denotes the number of photons in mode i. If we sum the two last quantities, we end up with an upper bound on P_2

$$\begin{aligned}p_1^* + p_2^* &\geq 2p(n_1 > 1 \cap n_2 > 1) + p(n_1 \leq 1 \cap n_2 > 1) + p(n_1 > 1 \cap n_2 \leq 1) \\ &= P_2 + p(n_1 > 1 \cap n_2 > 1) \\ &\geq P_2.\end{aligned} \tag{30}$$

In practice p_i^* can be obtained by measuring the probability of coincidence after a 50/50 beam splitter. All together with the first part, this implies that if a state ρ obeys

$$\begin{aligned}\mathrm{tr}(\rho\hat{W}) > {} & C_1 P_{\mathrm{nc,nc}} + C_2\sqrt{P_{\mathrm{nc,nc}}P_{\mathrm{c,c}}} + C_3 P_{\mathrm{c,c}} + \max\left(C_4(P_{\mathrm{c,nc}} - p_1^*), C_4 P_{\mathrm{c,nc}}\right) \\ & + \max\left(C_5(P_{\mathrm{nc,c}} - p_2^*), C_5 P_{\mathrm{nc,c}}\right) + p_1^* + p_2^* + 2\beta\sqrt{(p_1^*+p_2^*)(1-(p_1^*+p_2^*))}\end{aligned} \tag{31}$$

then ρ is entangled.

IV. NON UNIT DETECTION EFFICIENCY

We considered so far that the measurement are realized with non-photon-number-resolving detectors preceded by displacement operations in phase space. As explained in the main text, we assign the outcome $+1$ to a no-detection and -1 to a conclusive detection event. Given a state ρ in the mode 1 corresponding to the bosonic operators a_1 and $a_1^\dagger$, the probability to get a outcome $+1$ ($P_{\rm nc}$) using a displacement with argument α_1 is given by

$$P_{\rm nc} = {\rm tr}(D^\dagger(\alpha_1)|0\rangle\langle 0|D(\alpha_1)\rho). \tag{32}$$

In the case where the detector has a finite efficiency, we can model the detector inefficiency with a beam splitter having a transmission $\eta = \cos\varphi^2$, that is

$$P_{\rm nc} = {\rm tr}(D^\dagger(\alpha_1)U^\dagger|\bar{0}\rangle\langle\bar{0}|UD(\alpha_1)\rho) \tag{33}$$

with $U = e^{\varphi(a^\dagger c - c^\dagger a)}$, the auxiliary mode described by c and $c^\dagger$, being initially empty. The state $|\bar{0}\rangle$ corresponds to the projection onto the vacuum for both modes. Commuting the beam splitter and displacement operation leads to

$$P_{\rm nc} = {\rm tr}(U^\dagger D^\dagger(\alpha_1\sqrt{\eta})|\bar{0}\rangle\langle\bar{0}|D(\alpha_1\sqrt{\eta})U\rho). \tag{34}$$

This means that we can model the detection inefficiency as loss operating on the state that is measured if the amplitude of the displacement operation is changed accordingly. Hence, the fact that we consider detectors with unit efficiencies is still a valid description of our measurement apparatus where we do not need any assumptions on our state nor on the efficiency of our detectors.

V. FINITE STATISTIC ANALYSIS

All quantities that are measured are frequencies. We make the i.i.d hypothesis. For N clicks on the heralded detectors, n_a clicks on Alice detectors (and no clicks on Bob detector), n_b clicks on Bob detectors (and no clicks on Alice detectors) and n_d double clicks, we take the following estimators $\overline{P_{\rm c,nc}} = \frac{n_a}{N}$, $\overline{P_{\rm nc,c}} = \frac{n_b}{N}$, $\overline{P_{\rm c,c}} = \frac{n_d}{N}$ and $\overline{P_{\rm nc,nc}} = \left(1 - \frac{n_a+n_b+n_d}{N}\right)$. We proceed in the same way for the estimator of p_1^* and p_2^*. The corresponding standard deviations are

$$\sigma_{c,c} = \frac{\sqrt{\overline{P_{\rm c,c}}(1-\overline{P_{\rm c,c}})}}{\sqrt{N}}, \qquad \sigma_{c,nc} = \frac{\sqrt{\overline{P_{\rm c,nc}}(1-\overline{P_{\rm c,nc}})}}{\sqrt{N}}, \qquad \sigma_{p_1^*} = \frac{\sqrt{\overline{p_1^*}(1-\overline{p_1^*})}}{\sqrt{N}},$$
$$\sigma_{nc,nc} = \frac{\sqrt{\overline{P_{\rm nc,nc}}(1-\overline{P_{\rm nc,nc}})}}{\sqrt{N}}, \qquad \sigma_{nc,c} = \frac{\sqrt{\overline{P_{\rm nc,c}}(1-\overline{P_{\rm nc,c}})}}{\sqrt{N}}, \qquad \sigma_{p_2^*} = \frac{\sqrt{\overline{p_2^*}(1-\overline{p_2^*})}}{\sqrt{N}}.$$

When the dependence of the witness with respect to the probabilities is linear, then the standard deviations can be added straightforwardly. Let us focus on the terms $\sqrt{\overline{P_{\rm nc,nc}P_{\rm c,c}}}$. One cannot find an unbiased estimator for this term but one can bound it by a linear quantity

$$\sqrt{\overline{P_{\rm nc,nc}P_{\rm c,c}}} \leq \frac{P_{\rm nc,nc}\overline{P_{\rm c,c}} + P_{\rm c,c}\overline{P_{\rm nc,nc}}}{2\sqrt{\overline{P_{\rm c,c}}\ \overline{P_{\rm nc,nc}}}}. \tag{35}$$

The same holds for the term $\sqrt{(p_1^*+p_2^*)\ (1-(p_1^*+p_2^*))}$ which we bound according to

$$\sqrt{(p_1^*+p_2^*)\ (1-(p_1^*+p_2^*))} \leq \frac{(p_1^*+p_2^*) - 2(p_1^*+p_2^*)(\overline{p_1^*+p_2^*}) + (\overline{p_1^*+p_2^*})}{2\sqrt{(\overline{p_1^*+p_2^*})\ (1-(\overline{p_1^*+p_2^*}))}}. \tag{36}$$

Note that Ineq. (36) holds for $(p_1^*+p_2^*) \leq \frac{1}{2}$. The parts are now arranged such that an upper bound to the separable bound can be estimated according to

$$\begin{aligned}\overline{w}_{\rm ppt}^{\rm max} = {} & C_1\overline{P_{\rm nc,nc}} + C_2\frac{\overline{P_{\rm nc,nc}}\ \overline{P_{\rm c,c}} + \overline{P_{\rm c,c}}\ \overline{P_{\rm nc,nc}}}{2\sqrt{\overline{P_{\rm c,c}}\ \overline{P_{\rm nc,nc}}}} + C_3\overline{P_{\rm c,c}} + \max\left(C_4(\overline{P_{\rm c,nc}} - \overline{p_1^*}), C_4\overline{P_{\rm c,nc}}\right) \\ & + \max\left(C_5(\overline{P_{\rm nc,c}} - \overline{p_2^*}), C_5\overline{P_{\rm nc,c}}\right) + p_1^* + p_2^* + 2\beta\frac{(\overline{p_1^*+p_2^*}) - 2(\overline{p_1^*+p_2^*})(\overline{p_1^*+p_2^*}) + (\overline{p_1^*+p_2^*})}{2\sqrt{(\overline{p_1^*+p_2^*})\ (1-(\overline{p_1^*+p_2^*}))}}.\end{aligned} \tag{37}$$

With the assumption of independent measurements for each probability, the standard deviation of this estimator is upper bounded by

$$\begin{aligned}\sigma_{\text{ppt}}^{\max} = C_1\sigma_{nc,nc} + C_2\frac{\sigma_{nc,nc}\ \overline{P_{\text{c,c}}} + \sigma_{c,c}\ \overline{P_{\text{nc,nc}}}}{2\sqrt{\overline{P_{\text{c,c}}}\ \overline{P_{\text{nc,nc}}}}} + C_3\sigma_{c,c} + |C_4|(\sigma_{c,nc} + \sigma_{p_1^*}) + |C_5|(\sigma_{nc,c} + \sigma_{p_2^*}) \\ + \sigma_{p_1^*} + \sigma_{p_2^*} + 2\beta\frac{(\sigma_{p_1^*} + \sigma_{p_2^*}) - 2(\sigma_{p_1^*} + \sigma_{p_2^*})(\overline{p_1^* + p_2^*}) + (\overline{p_1^* + p_2^*})}{2\sqrt{(\overline{p_1^* + p_2^*})\ (1 - (\overline{p_1^* + p_2^*}))}}.\end{aligned} \tag{38}$$

In the same way, one can define an estimator for $\langle\hat{W}\rangle$

$$\overline{w}_\rho^{\text{exp}} = \overline{P_{\text{c,c}}} + \overline{P_{\text{nc,nc}}} - \overline{P_{\text{c,nc}}} - \overline{P_{\text{nc,c}}} \tag{39}$$

and the standard deviation of this estimator

$$\sigma_\rho^{\text{exp}} = \sigma_{c,nc} + \sigma_{nc,c} + \sigma_{c,c} + \sigma_{nc,nc}. \tag{40}$$

We then say that we observe a violation of our witness by k standard deviations if

$$\overline{w}_{\text{ppt}}^{\max} - \overline{w}_\rho^{\text{exp}} = k(\sigma_{\text{ppt}}^{\max} + \sigma_\rho^{\text{exp}}). \tag{41}$$

VI. PHASE LOCKING REQUIREMENT

In order to detect entanglement in a state of the form $|\psi\rangle = (|01\rangle + e^{i\phi}|10\rangle)/\sqrt{2}$, our witness makes use of displacement operations on both modes (see Eq. (1)). For such a measurement, the joint coincidence probabilities P_{ij} will depend on optical phases acquired in the experimental setup. In the following, we will calculate the expected joint probability P_{00} of having a no-click event in both modes for our experimental setup which will give rise to a phase-locking requirement if we want to be able to detect entanglement. The calculation for joint probabilities different than P_{00} would lead to the same requirement.

$$\begin{aligned}P_{00} &= |\langle 00|_{AB} D(\alpha_1)D(\alpha_2)|\psi\rangle_{AB}|^2 \\ &= \left|\langle 00|_{AB} D(\alpha_1)D(\alpha_2)\frac{1}{\sqrt{2}}\left(e^{i(\phi_A+\chi_A+\xi_{A,l})}|10\rangle_{AB} + e^{i(\phi_B+\chi_B+\xi_{B,l})}|01\rangle_{AB}\right)\right|^2 \\ &= \frac{1}{2}\left|e^{i(\phi_A+\chi_A+\xi_{A,l})}\langle 00|_{AB} D(\alpha_1)|1\rangle_A|\alpha_2\rangle_B + e^{i(\phi_B+\chi_B+\xi_{B,l})}\langle 00|_{AB} D(\alpha_2)|\alpha_1\rangle_A|1\rangle_B\right|^2,\end{aligned} \tag{42}$$

where $D(\alpha_{1(2)})$ denotes the displacement operator acting on mode $A(B)$ with displacement parameters $\alpha_{1(2)} = |\alpha_{1(2)}|e^{i(\phi_{A(B)} - \zeta_{A(B)} + \xi_{A(B),s})}$.

- $\phi_{A(B)}$ is the phase of the pump before the crystal,
- $\zeta_{A(B)}$ the phase of the seed laser before the crystal,
- $\chi_{A(B)}$ the phase picked up from the crystal to the central station,
- $\xi_{A(B),l(s)}$ the phase from the crystal to the detector through the long (short) arm of the AMZI

on Alice's (Bob's) side as shown in Fig. 1. This leads us to

$$\begin{aligned}P_{00} &= \frac{1}{2}\left|e^{i(\phi_A+\chi_A+\xi_{A,l})}e^{-|\alpha_2|^2/2}\langle -\alpha_1|1\rangle_A + e^{i(\phi_B+\chi_B+\xi_{B,l})}e^{-|\alpha_1|^2/2}\langle -\alpha_2|1\rangle_B\right|^2 \\ &= \frac{1}{2}\left|e^{i(\phi_A+\chi_A+\xi_{A,l})}e^{-(|\alpha_1|^2+|\alpha_2|^2)/2}(-\alpha_1^*) + e^{i(\phi_B+\chi_B+\xi_{B,l})}e^{-(|\alpha_1|^2+|\alpha_2|^2)/2}(-\alpha_2^*)\right|^2 \\ &= \frac{1}{2}e^{-|\alpha_1|^2-|\alpha_2|^2}\left|e^{i(\phi_A+\chi_A+\xi_{A,l})}|\alpha_1|e^{-i(\phi_A-\zeta_A+\xi_{A,s})} + e^{i(\phi_B+\chi_B+\xi_{B,l})}|\alpha_2|e^{-i(\phi_B-\zeta_B+\xi_{B,s})}\right|^2\end{aligned} \tag{43}$$

and setting $|\alpha| = |\alpha_1| = |\alpha_2|$ for simplicity yields

$$P_{00} = \frac{1}{2}|\alpha|^2 e^{-2|\alpha|^2}\left|e^{i(\zeta_A+\chi_A+\xi_{A,l}-\xi_{A,s})} + e^{i(\zeta_B+\chi_B+\xi_{B,l}-\xi_{B,s})}\right|^2. \tag{44}$$

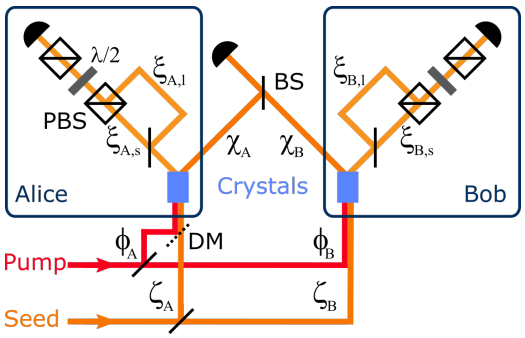

FIG. 1. Schematic of the experimental setup with the relevant phases. PBS, polarizing beam splitter; BS, beam splitter; DM, dichroic mirror; $\lambda/2$, half-wave plate.

We note that the phases of the pump before the crystals ϕ_A and ϕ_B cancel out. In order to keep P_{00} constant, we therefore require

$$\zeta_A + \chi_A + \xi_{A,l} - \xi_{A,s} = \zeta_B + \chi_B + \xi_{B,l} - \xi_{B,s} + \text{const.} \tag{45}$$

This can be achieved by locking the central interferometer according to

$$(\zeta_A + \chi_A) \mod 2\pi = \zeta_B + \chi_B + \pi \tag{46}$$

and the two asymmetric Mach-Zehnder interferometers (AMZI) for the displacement-based measurement such that

$$(\xi_{A,l} + \xi_{B,s}) \mod 2\pi = \xi_{A,s} + \xi_{B,l} + \pi. \tag{47}$$

VII. EXPERIMENTAL SETUP: PHASE LOCKING OF THE MEASUREMENT INTERFEROMETERS

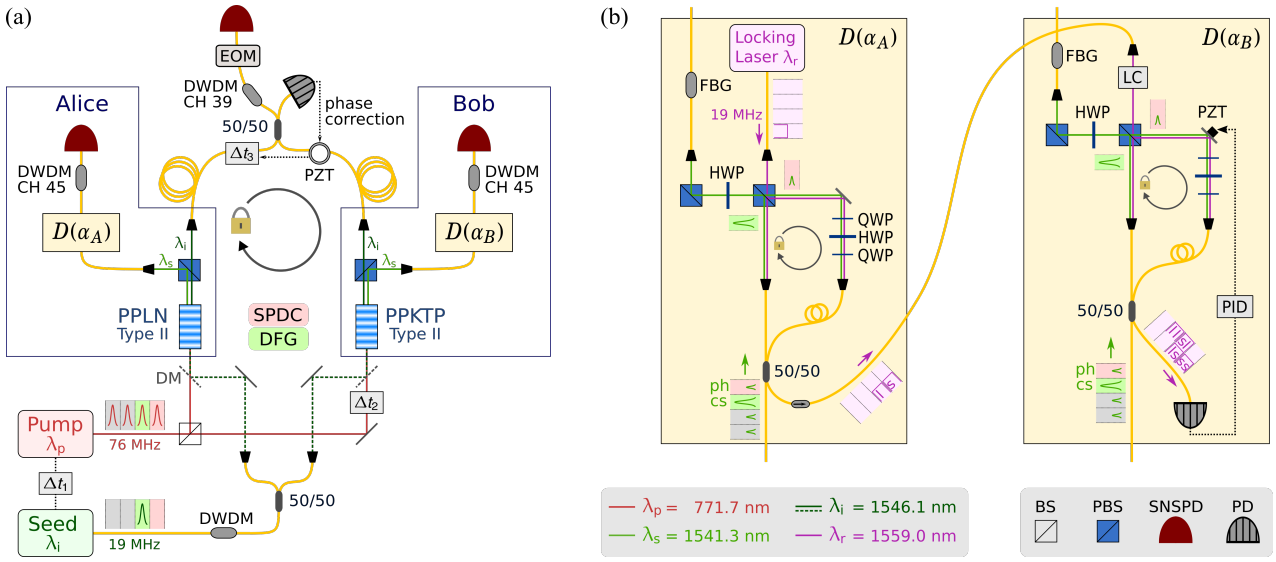

FIG. 2. (a) Simplified schematic of the experimental setup for the heralded distribution and certification of single-photon path entanglement. (b) Detailed schematic of the implementation for the displacement-based measurement using two asymmetric Mach-Zehnder interferometers (AMZI) with path difference corresponding to 13 ns. The phase-locking technique makes use of a pulsed DFB laser at $\lambda_r = 1559.0$ nm with a repetition rate of 19 MHz and pulse duration of about 10 ns.

A schematic overview of the experimental implementation is presented in Fig. 2(a). To fulfill the crucial phase stability requirement derived in Sec. VI, we need to phase-lock the central interferometer as described in the main text, and specific to our implementation of the displacement-based measurement, the phase difference between the AMZIs shown in Fig. 2(b).

We first note that in the common paths of the coherent state and the single-photon state, their short temporal separation of 13 ns intrinsically guarantees the phase stability since the phase changes occurring over this time scale are negligible. However, the phase has to be actively stabilized in the AMZIs which temporally bring the single-photon and coherent states to coincidence. We therefore inject distributed feedback (DFB) laser pulses at $\lambda_r = 1559.0$ nm of about 10 ns duration at a repetition rate of 19 MHz traveling in the reverse direction to the signal, first through Alice's AMZI, then through Bob's, as schematically shown in Fig. 2(b). The resulting averaged signal shows 50 % visibility interference fringes as a function of the phase difference between the long-short and short-long paths in the measurement AMZIs, which is kept at a constant set-point by controlling a piezo-actuated mirror in the long arm of Bob's AMZI.

The phase difference of the displacement fields between Alice and Bob is scanned and set with a liquid crystal (LC; Thorlabs LCC1111T-C) in the locking laser path before Bob's AMZI. The LC is aligned with the subsequent polarizing beam splitter (PBS) and therefore the signal in the long arm of Bob's AMZI is selectively retarded with respect to the signal in the short arm. In this way, the LC allows us to induce an additional relative phase between the displacement fields on Alice's and Bob's side over a range of π. In order to suppress unwanted reflections of the locking laser leaking to the detectors, we use fiber Bragg gratings (FBG) rejecting light at λ_r.

VIII. SPECTRAL OVERLAP AND TEMPORAL ALIGNMENT

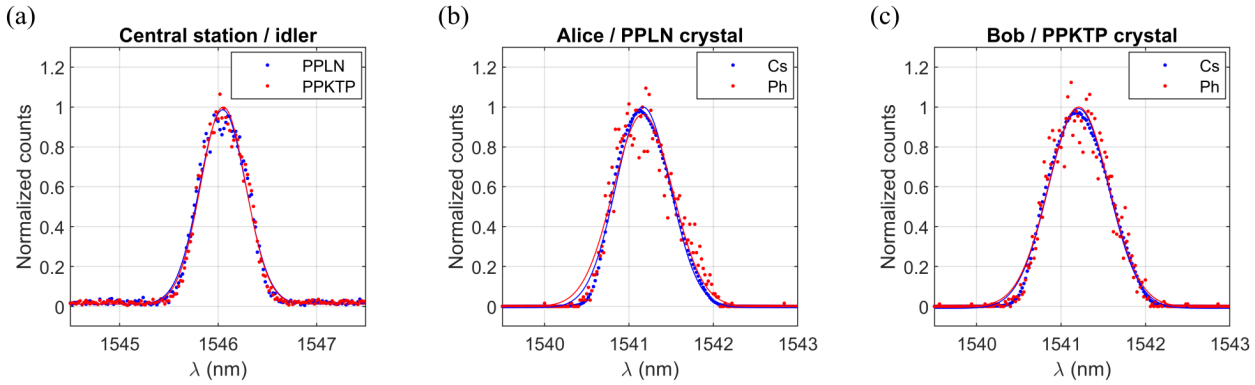

FIG. 3. Normalized measured spectra and Gaussian fit of (a) idler photons from independent sources before the heralding detector, (b) coherent state (Cs) and heralded signal photon (Ph) before Alice's detector and (c) before Bob's detector. All spectra are measured with a tunable grating filter with a FWHM of 0.2 nm inserted before the corresponding superconducting nanowire single-photon detector.

To ensure high-purity heralded signal photons, we spectrally filter the heralding idler photons [1] emitted from the PPLN crystal on Alice's side and from the PPKTP crystal on Bob's side after the 50/50 beam splitter by using a dense wavelength division multiplexer (DWDM) with a 100 GHz passband at ITU channel 39 ($\lambda = 1546.12$ nm). The expected HOM visiblity due to finite spectral overlap between the idler photons (see Fig. 3(a)) assuming Gaussian spectral distribution (see Eq. 5.14 in [2]) amounts to 99.9 %.

We also spectrally filter before Alice's and Bob's detectors with two DWDMs at channel 45 ($\lambda = 1541.35$ nm) and achieve a spectral overlap between the single-photon and coherent states [3] used for the displacement operation of more than 99 %, as shown in Figs. 3(b-c).

The fine temporal alignment of the central interferometer is achieved in the following way. First, the seed laser is replaced by a low coherence white light source and the motorized fiber delay line Δt_3 (see Fig. 2(a)) is set such that the observed interference visibility at the central station is maximized. Second, the white light source is exchanged by a cw laser at the signal wavelength λ_s such that together with the pulsed pump laser, a coherent state at the idler wavelength λ_i is created via difference frequency generation (DFG) in both crystals. The delay Δt_2 is then adjusted such that again the observed interference visibility at the central station is maximized. Third, the pulsed seed laser is put back in its place and the electronic delay Δt_1 is set such that pump and seed pulses overlap. This procedure ensures temporal indistinguishability of the idler photons from the two independent sources at the central station.

IX. RESULTS

The measured joint probabilities in the α- and z-basis as well as the local probability of having more than one photon locally p_i^* are given in Tab. I. In the case of $l = 42\,\mathrm{m}$ of optical fiber inserted in each arm of the central interferometer, we measured lower probabilities for $P_{\mathrm{c,nc}}$ and $P_{\mathrm{nc,c}}$ in the z-basis compared to the case of $l = 1.0\,\mathrm{km}$. These probabilities are direct measures of the signal photon transmissions. The difference can be explained by the realignment of the measurement AMZIs between the two experimental runs leading to an increase of the transmission on the signal photons in the case of $l = 1.0\,\mathrm{km}$.

The results of the entanglement witness are given in Tab. II. We detect photons at the central station at a heralding rate ν_h with the indicated signal-to-noise ration (SNR). The values for w_ρ^{exp} are computed from the joint probabilities in the α-basis. We further calculate the values for the PPT bound w_{ppt} according to Eq. 7, the bound including fluctuations of the displacement amplitudes $\widetilde{w}_{\mathrm{ppt}}$ according to the RHS of Ineq. 11 and the bound with additional contributions from outside the qubit space $w_{\mathrm{ppt}}^{\mathrm{max}}$ according to the RHS of Ineq. 31.

For $l = 42\,\mathrm{m}$, we measured at two different displacement amplitudes. The theoretical values for the amplitudes of the displacement parameters leading to the largest violation of our witness are $\alpha_1 = \alpha_2 = 1/\sqrt{2} \approx 0.71$, however, the witness is more robust to experimental fluctuations of the displacement parameter amplitudes if $\partial^2 w_{\mathrm{ppt}}/\partial\alpha_1\partial\alpha_2 = 0$, which in our case holds true for $\alpha_1 = \alpha_2 \approx 0.83$. This can be seen by comparing the difference between $\widetilde{w}_{\mathrm{ppt}}$ and w_{ppt} for the two α-settings.

We observe lower SNR for larger α as well as for longer fiber. We suspect this elevated noise background to be backward-scattered and forward-reflected Raman light that leaks through the DWDM before the heralding detector. One solution to this problem might be additional spectral filtering, however, leading to lower transmission on the heralding photons.

l	α_1	α_2	Basis	$P_{\mathrm{nc,nc}}$	$P_{\mathrm{nc,c}}$	$P_{\mathrm{c,nc}}$	$P_{\mathrm{c,c}}$	p_1^*	p_2^*
42 m	$0.720^{+0.014}_{-0.010}$	$0.710^{+0.008}_{-0.008}$	z	0.96834(4)	0.01431(3)	0.01735(3)	0.0000044(5)	$2.5(3)\times10^{-6}$	$5.1(4)\times10^{-6}$
			α	0.3604(2)	0.2305(2)	0.2407(2)	0.1684(2)		
	$0.804^{+0.010}_{-0.009}$	$0.819^{+0.003}_{-0.004}$	z	0.96935(5)	0.01515(3)	0.01550(3)	0.0000052(6)		
			α	0.2715(2)	0.2504(2)	0.2393(2)	0.2388(2)		
1.0 km	$0.819^{+0.005}_{-0.007}$	$0.837^{+0.006}_{-0.007}$	z	0.96142(5)	0.01881(4)	0.01977(4)	0.0000059(6)	$3.2(4)\times10^{-6}$	$1.25(8)\times10^{-5}$
			α	0.2575(2)	0.2504(2)	0.2370(2)	0.2552(2)		

TABLE I. Measured joint probabilities in the z- and α-basis for different fiber lengths l in each arm of the central interferometer. The displacement parameter amplitudes α_i are the mean amplitudes for the α-basis measurement with bounds on the minimum and maximum observed values during the 3600 s of measurement. The probabilities of having more than one photon p_1^* on Alice's side and p_2^* on Bob's side are separately determined for each experimental run by measuring the heralded $g^2(0)$. The uncertainties on all probabilities are 1 standard deviations as calculated in Sec. V.

l	ν_h (kHz)	SNR	α_1	α_2	w_ρ^{exp}	w_{ppt}	$\widetilde{w}_{\mathrm{ppt}}$	$w_{\mathrm{ppt}}^{\mathrm{max}}$	k
42 m	1.4	18	$0.720^{+0.014}_{-0.010}$	$0.710^{+0.008}_{-0.008}$	0.0576(8)	0.0391(2)	0.0451(2)	0.0472(14)	4.8
	1.4	12	$0.804^{+0.010}_{-0.009}$	$0.819^{+0.003}_{-0.004}$	0.0206(8)	0.0039(2)	0.0045(2)	0.0071(16)	5.6
1.0 km	1.6	5.0	$0.819^{+0.005}_{-0.007}$	$0.837^{+0.006}_{-0.007}$	0.0253(7)	0.0031(2)	0.0033(2)	0.0071(22)	6.2

TABLE II. Measured expectation value of the entanglement witness w_ρ^{exp} and calculated separable bound w_{ppt}, including fluctuations of the displacement amplitudes $\widetilde{w}_{\mathrm{ppt}}$ and additional contributions from outside the qubit space $w_{\mathrm{ppt}}^{\mathrm{max}}$ for fibers of length l inserted in each arm of the central interferometer at an observed heralding rate ν_h. The indicated heralding rate includes noise that we observe with the indicated signal-to-noise ratio (SNR). The witness is violated by $k = (w_\rho^{\mathrm{exp}} - w_{\mathrm{ppt}}^{\mathrm{max}})/(\sigma_{\mathrm{ppt}}^{\mathrm{max}} + \sigma_\rho^{\mathrm{exp}})$ standard deviations.

[1] A. R. McMillan, L. Labonté, A. S. Clark, B. Bell, O. Alibart, A. Martin, W. J. Wadsworth, S. Tanzilli, and J. G. Rarity, Scientific Reports **3**, 2032 (2013).
[2] P. J. Mosley, *Generation of Heralded Single Photons in Pure Quantum States*, Ph.D. thesis, University of Oxford (2007).
[3] N. Bruno, A. Martin, and R. Thew, Optics Communications **327**, 17 (2014).

P.2. Local and scalable detection of genuine multipartite single-photon path entanglement

Local and scalable detection of genuine multipartite single-photon path entanglement

Patrik Caspar[1], Enky Oudot[2], Pavel Sekatski[1], Nicolas Maring[1], Anthony Martin[1], Nicolas Sangouard[3], Hugo Zbinden[1], and Rob Thew[1]

[1]Department of Applied Physics, University of Geneva, CH-1211 Genève, Switzerland
[2]ICFO - Institut de Ciencies Fotoniques, The Barcelona Institute of Science and Technology, 08860 Castelldefels (Barcelona), Spain
[3]Institut de physique théorique, Université Paris Saclay, CEA, CNRS, F-91191 Gif-sur-Yvette, France

How can a multipartite single-photon path-entangled state be certified efficiently by means of local measurements? We address this question by constructing an entanglement witness based on local photon detections preceded by displacement operations to reveal genuine multipartite entanglement. Our witness is defined as a sum of three observables that can be measured locally and assessed with two measurement settings for any number of parties N. For any bipartition, the maximum mean value of the witness observable over biseparable states is bounded by the maximum eigenvalue of an $N \times N$ matrix, which can be computed efficiently. We demonstrate the applicability of our scheme by experimentally testing the witness for heralded 4- and 8-partite single-photon path-entangled states. Our implementation shows the scalability of our witness and opens the door for distributing photonic multipartite entanglement in quantum networks at high rates.

1 Introduction

The generation, distribution and certification of entanglement in multipartite quantum communication networks is of increasing importance as the size and complexity of networks grow beyond simple short-distance point-to-point scenarios [1, 2]. In general, multipartite entanglement enables applications such as enhanced sensing [3, 4] or multi-user quantum communication protocols [5, 6]. At the heart of the matter, the challenge is to find scalable solutions to realize these applications, which still remain experimentally feasible. On the one hand, the experimental limitations of probabilistic multi-photon sources, especially in terms of rates [7], represent fundamental obstacles for entangled state generation. On the other hand, for the state certification, the exponential scaling of measurements in tomography as the number of parties increases [8] makes it impractical already for a small number of parties.

In the case of generation and distribution of entanglement already for quantum repeaters, a shift away from photon-pair to heralded single-photon entanglement provided significant scaling benefits even for point-to-point communication schemes [9]. For example, as shown in Fig. 1(a), the distribution of entanglement between two remote parties through optical fiber can be realized efficiently by giving each party a source emitting signal-idler photon pairs, combining the idler modes into a beam splitter at a central station and placing two detectors at the output of the beam splitter. A photon detection by one of the two detectors heralds the sharing of a single photon between the signal modes – a single-photon path-entangled state [10, 11]. Although the realization of such schemes faces the challenge of active stabilization of the phase between the two parties [12], work addressing this issue has been reported [13–18], even over longer distances in optical fiber [19, 20].

More interestingly, this approach can be efficiently extended to the distribution of entanglement between multiple parties by simply replacing the two-port beam splitter by a multi-port beam splitter, see Fig. 1(b). This represents an efficient way of gen-

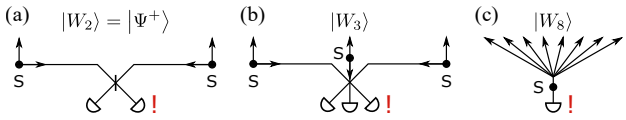

Figure 1: Heralded multipartite entanglement distribution. (a) Entanglement is distributed between two parties, each having a signal-idler photon pair source (S). The idler modes are combined on a beam splitter and the detection of a single photon after this beam splitter projects the signal modes into a single-photon entangled state. (b) Generalization of the scheme to tripartite states while keeping the local losses low. The aim of this work is to clarify on how entanglement can be detected in this setting. (c) Conceptual schematic of the experiment. Entanglement is distributed among several parties by locally splitting the signal mode into multiple spatial output modes.

Anthony Martin: Current address: Université Côte d'Azur, CNRS, Institut de Physique de Nice, Parc Valrose, F-06108 Nice Cedex 2, France
Rob Thew: Robert.Thew@unige.ch

erating a multipartite entangled state close to a W state [21]:

$$|W_N\rangle = \frac{1}{\sqrt{N}} \sum_{i=1}^{N} |0, ..., 0, 1_i, 0, ..., 0\rangle \tag{1}$$

with a single photon detection heralding its successful distribution remotely. Here, $|0\rangle$ denotes the vacuum state, $|1\rangle$ the single-photon number state and N the number of parties. Applications of this class of distributed states include long-baseline telescopes that can take advantage not only of a distribution over long distances but also the multipartite setting [22–24].

The certification of entanglement in such multipartite quantum communication networks is extremely challenging. Beyond tomography, even typical entanglement witnesses require multiple settings per party [25, 26], with the commensurate scaling that quickly ensures their infeasibility. Others have used certification techniques that require the recombination of optical modes [27, 28], which are impractical in communication scenarios where local measurements are required. These problems are further exacerbated in a distributed setting, where noisy and lossy channels also need to be addressed.

Here we develop an entanglement witness tailored to the W state, given in Eq. (1), to reveal genuine multipartite entanglement (GME) without postselection. We assume that the measurement apparatus is well characterized and that each party i holds a single optical mode with an associated bosonic annihilation operator a_i. There are no further assumptions. In particular, the photon number statistics are unknown and we do not assume that the same state is prepared in each run (i.i.d.). The witness is scalable as it only requires two different measurement settings, independently of the number of parties. Its applicability is demonstrated using an experimental setup in a configuration like in Fig. 1(c) where genuine 4- and 8-partite entangled states are heralded at high rates and successfully verified.

2 Theory

To certify the GME of N-partite single-photon path-entangled states, we build a witness using practical single-photon detectors, i.e. non-unit efficiency and non-photon number resolving. Such a detector can be modeled as a loss channel with transmission η (the detector efficiency) followed by a two-outcome measurement that perfectly distinguishes the vacuum $|0\rangle$ from all the other Fock states of the detected mode. In this model, the fixed loss can be interpreted as part of the state preparation degrading its entanglement. In the following, we therefore model the detector operating on party i with the positive operator valued measure (POVM) $\{E_c^i = \mathbb{1} - \Pi_0^{(i)}, E_0^i = \Pi_0^{(i)}\}$, E_c^i (E_0^i) corresponding to the POVM element associated to a click (c) (no-click (0)) event and $\Pi_0^{(i)} = |0\rangle\langle 0|$ is the projection on the vacuum. With such a detector, we thus have access to the weight of the vacuum component for each party from the no-click events, i.e. from $\mathrm{tr}(E_0^i\,\rho)$ where ρ denotes the N-mode state produced in the actual experiment. By probing each mode with such a detector, we can access the probability that more than one mode contain photons $\sum_{n\geq 2} P^n_{\mathrm{click}}$, where P^n_{click} is the probability that n detectors click. Let us define the POVM elements associated with these probabilities as $E_{n\geq 2}$ and E_n. Note that $p_0 = P^0_{\mathrm{click}} = \mathrm{tr}(|0\rangle\langle 0|^{\otimes N}\,\rho)$ is the probability that the state contains no photons. Furthermore, by probing the mode i with two such detectors after a 50/50 beam splitter, we can upper bound the probability that it contains more than one photon [26], that is $\mathrm{tr}(\Pi^{(i)}_{n_i\geq 2}\,\rho)$ with $\Pi^{(i)}_{n_i\geq 2} = \sum_{n_i\geq 2} |n_i\rangle\langle n_i|$. This allows us to upper bound the probability that the N-mode state ρ contains two or more photons, which we write as an operator inequality

$$\Pi_{n\geq 2} \leq E_{n\geq 2} + \sum_i \Pi^{(i)}_{n_i\geq 2}, \tag{2}$$

where $\Pi_{n\geq 2}$ is the projector on all the combinations of Fock states containing at least two photons in total. We then denote $p_* = \mathrm{tr}((E_{n\geq 2} + \sum_i \Pi^{(i)}_{n_i\geq 2})\,\rho)$.

In order to implement measurements that are sensitive to the coherence between different products of Fock states, the party i can perform a phase-space displacement operation $D(\alpha_i) = e^{\alpha_i a_i^\dagger - \alpha_i^* a_i}$ right before the detector [29]. As shown in Appendix A, the loss after the displacement operation, i.e. the detector inefficiency, can be permuted with the displacement by only adjusting the displacement amplitude α_i. This allows us to keep the POVM above and define a parametric family of local observables for each party $i \in \{1, ..., N\}$ [30]

$$\begin{aligned} \sigma^{(i)}_{\alpha_i} &= D^\dagger(\alpha_i)(E_0^i - E_c^i)D(\alpha_i) \\ &= D^\dagger(\alpha_i)(2|0\rangle\langle 0| - \mathbb{1})D(\alpha_i) \end{aligned} \tag{3}$$

by attributing the value $+1$ to a no-click and -1 to a click event. In principle, asking each party to perform such a measurement and combining the results allows us to define a global observable

$$\hat{O}_{\boldsymbol{\alpha}} = \sum_{i\neq j}^{N} \sigma^{(i)}_{\alpha_i} \otimes \sigma^{(j)}_{\alpha_j}, \tag{4}$$

where $\boldsymbol{\alpha} = (\alpha_1, \ldots, \alpha_N)$. To simplify the experimental realization, we consider the case where the local oscillators used by each party to perform the displacement operations are not phase-locked to the input state, so that the local displacements $\alpha_i \mapsto \alpha_i e^{\mathrm{i}\varphi}$ are only defined up to an arbitrary common phase φ, but the phase differences between the parties are well controlled and kept constant at zero. As a consequence,

we measure the observable

$$\hat{\mathcal{O}}_{\boldsymbol{\alpha}} = \frac{1}{2\pi}\int_0^{2\pi} \mathrm{d}\varphi\; e^{-\mathrm{i}\varphi\sum_{i=1}^N a_i^\dagger a_i}\; \hat{\mathcal{O}}_{\boldsymbol{\alpha}}\; e^{\mathrm{i}\varphi\sum_{i=1}^N a_i^\dagger a_i}. \tag{5}$$

Because of the phase averaging, the operator $\hat{\mathcal{O}}_{\boldsymbol{\alpha}} = \bigoplus_{n=0}^{\infty}\hat{\mathcal{O}}_{\boldsymbol{\alpha}}^{(n)}$ acts orthogonally on different total photon number subspaces $n = \langle\sum_{i=1}^N a_i^\dagger a_i\rangle$.

For displacement amplitudes chosen in the appropriate range [30], each two-body correlator $\sigma_{\alpha_i}^{(i)}\otimes\sigma_{\alpha_j}^{(j)}$ gathers the coherence $|1_i,0_j\rangle\langle 0_i,1_j| + h.c.$. This coherence is symptomatic of GME in the state $|W_N\rangle$, making the observable $\hat{\mathcal{O}}_{\boldsymbol{\alpha}}$ a natural candidate to witness this entanglement. However, $\hat{\mathcal{O}}_{\boldsymbol{\alpha}}$ is also sensitive to all higher photon number contributions, which are difficult to characterize. A simple way to circumvent this problem is to subtract the observable $N(N-1)\Pi_{n\geq 2}$ from $\hat{\mathcal{O}}_{\boldsymbol{\alpha}}$. On the one hand, for our state $\mathrm{tr}(\Pi_{n\geq 2}\,\rho)\approx 0$ and the expected value is not affected much by the subtraction. On the other hand, since $\|\hat{\mathcal{O}}_{\boldsymbol{\alpha}}\|\leq N(N-1)$, one can bound

$$\hat{\mathcal{O}}_{\boldsymbol{\alpha}} - N(N-1)\Pi_{n\geq 2} \leq \hat{\mathcal{O}}_{\boldsymbol{\alpha}}^{(0)}\oplus\hat{\mathcal{O}}_{\boldsymbol{\alpha}}^{(1)} \tag{6}$$

by an operator supported on a subspace with at most one photon.

We can now define the entanglement witness

$$\hat{\mathcal{W}}_{\boldsymbol{\alpha}} = \hat{\mathcal{O}}_{\boldsymbol{\alpha}} - N(N-1)\Pi_{n\geq 2} + M_{n\leq 1} - \mu E_{n\geq 2}, \tag{7}$$

where $M_{n\leq 1}$ is an operator diagonal in the product Fock basis and acting on the subspace with one photon at most, specified in Appendix B, and μ is a positive real parameter that one can tune. To show that the witness can reveal GME, let us start by computing the biseparable bound.

$$w_{\mathrm{bisep}} = \max_{\varrho_{\mathrm{bisep}}}\mathrm{tr}(\hat{\mathcal{W}}_{\boldsymbol{\alpha}}\varrho_{\mathrm{bisep}}), \tag{8}$$

i.e. the maximum value the witness takes on any biseparable state. A general biseparable state is a mixture of states that are product states for some bipartition (a partition of all modes into two groups). Formally,

$$\varrho_{\mathrm{bisep}} = \sum_{G_1|G_2} p(G_1|G_2)\,\rho_{G_1|G_2}. \tag{9}$$

Here, the sum runs over all partitions $G_1|G_2$ of the N parties where $G_1\cup G_2 = \{1,2,\ldots,N\}$ and $G_1\cap G_2 = \emptyset$. The probabilities of different partitions sum up to one $\sum_{G_1|G_2}p(G_1|G_2)=1$ and $\rho_{G_1|G_2}$ is a separable state with respect to the partition $G_1|G_2$. Since the set of biseparable states is convex, the maximum value that an observable takes on any biseparable state ϱ_{bisep}, including mixed states,

$$w_{\mathrm{bisep}} = \max_{G_1,G_2,|\Psi\rangle}\langle\Psi|\hat{\mathcal{W}}_{\boldsymbol{\alpha}}|\Psi\rangle, \tag{10}$$

is attained for a pure state $|\Psi\rangle = |\Psi_1\rangle_{G_1}|\Psi_2\rangle_{G_2}$ on some partition. Now, using Ineq. (6) we obtain a relaxation

$$w_{\mathrm{bisep}} \leq \max_{G_1,G_2,|\Psi\rangle}\langle\Psi|\widetilde{\mathcal{W}}|\Psi\rangle, \tag{11}$$

$$\widetilde{\mathcal{W}} = \hat{\mathcal{O}}_{\boldsymbol{\alpha}}^{(0)}\oplus\hat{\mathcal{O}}_{\boldsymbol{\alpha}}^{(1)} + M_{n\leq 1} - \mu E_{n\geq 2} \tag{12}$$

which simplifies the maximization problem enormously. Indeed, the operator $\widetilde{\mathcal{W}}$ is block diagonal, with restriction to the sector with two or more photons $-\mu E_{n\geq 2}$ that is negative. Thus, we can restrict the maximization to states $|\Psi_k\rangle_{G_k}$ which contain one photon at most and write

$$|\Psi_k\rangle_{G_k} = v_0^{(k)}|0\rangle_{G_k} + \sum_{i=1|j_i\in G_k}^{|G_k|} v_i^{(k)} a_{j_i}^\dagger|0\rangle_{G_k}. \tag{13}$$

For a fixed partition, the product states can be parametrized by normalized vectors $\boldsymbol{v}^{(1)}$ and $\boldsymbol{v}^{(2)}$, that can be taken to be real without loss of generality. This leaves us with a N-parameter optimization problem. In Appendix B, we show that for our witness this maximization can be reduced to a single parameter optimization

$$\begin{aligned}\widetilde{w}_{G_1,G_2} &= \max_{\boldsymbol{v}^{(1)},\boldsymbol{v}^{(2)}}\langle\Psi|\widetilde{\mathcal{W}}|\Psi\rangle \\ &= \max_{a\in[0,2\pi]}\left(\max\mathrm{eig}(\mathbb{M}(\lambda,\mu,\boldsymbol{\alpha},a))\right)\end{aligned} \tag{14}$$

of the maximum eigenvalue of a $N\times N$ matrix $\mathbb{M}(\lambda,\mu,\boldsymbol{\alpha},a)$, which can be solved efficiently with standard numerical tools. Here, λ (like μ) is a positive real parameter of the witness that can be tuned. We solve the optimization for all bipartitions to obtain a relaxation of the biseparable bound for the witness $\hat{\mathcal{W}}$

$$w_{\mathrm{bisep}} \leq \widetilde{w}_{\mathrm{bisep}} = \max_{G_1,G_2}(\widetilde{w}_{G_1,G_2}). \tag{15}$$

It remains to explain how we estimate the violation of the witness $\langle\hat{\mathcal{W}}_{\boldsymbol{\alpha}} - \widetilde{w}_{\mathrm{bisep}}\rangle$ on the multimode state ρ prepared in the experiment. In reality, the amplitudes $\boldsymbol{\alpha}$ of the displacements fluctuate within some range $\boldsymbol{\alpha}\in A$ that we characterize. The operator $\hat{\mathcal{W}}_{\boldsymbol{\alpha}}$ depends on these amplitudes both "physically" via the observable $\hat{\mathcal{O}}_{\boldsymbol{\alpha}}$, but also "algebraically" via the definition of the operator $M_{n\leq 1}(\boldsymbol{\alpha})$ and the value for the biseparable bound $\widetilde{w}_{\mathrm{bisep}}(\boldsymbol{\alpha})$. To remove the second dependence, we consider the worst-case scenario $w_{\mathrm{bisep}}^{\max} = \max_{\boldsymbol{\alpha}\in A}\widetilde{w}_{\mathrm{bisep}}(\boldsymbol{\alpha})$ and $\bar{M}_{n\leq 1} = \min_{\boldsymbol{\alpha}\in A}M_{n\leq 1}(\boldsymbol{\alpha})$. Then, defining the operator $\overline{\mathcal{W}}_{\boldsymbol{\alpha}}$, where we replace $M_{n\leq 1}$ by $\bar{M}_{n\leq 1}$ in the witness (Eq. (7)), implies

$$\hat{\mathcal{W}}_{\boldsymbol{\alpha}} - w_{\mathrm{bisep}} \geq \overline{\mathcal{W}}_{\boldsymbol{\alpha}} - w_{\mathrm{bisep}}^{\max}. \tag{16}$$

To prove GME it suffices to show that the average (over all rounds with fluctuating $\boldsymbol{\alpha}$) expected value of $\langle\overline{\mathcal{W}_{\boldsymbol{\alpha}}}\rangle$ on ρ, which we call $w_\rho^{\max}$, exceeds the constant $w_{\mathrm{bisep}}^{\max}$. As argued in Appendix C, $\langle\overline{\mathcal{W}_{\boldsymbol{\alpha}}}\rangle$ can be

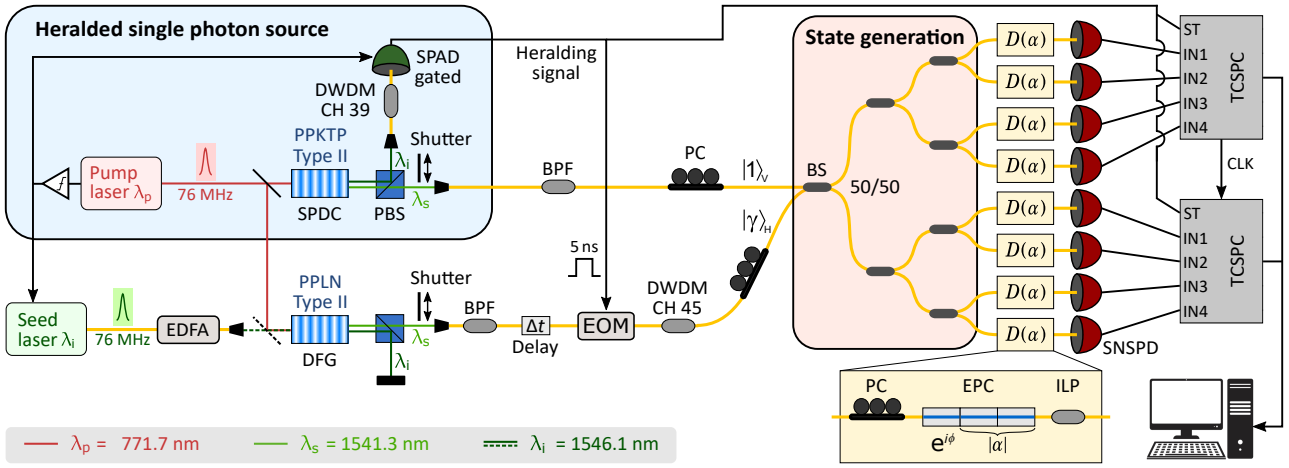

Figure 2: Experimental schematic: A heralded single photon, incident on a cascade of 50/50 fiber beam splitters (BS), is delocalized over spatial modes to generate an 8-partite path-entangled state. Weak coherent states in orthogonal polarization modes are co-propagated with the single-photon state to locally perform displacement-based measurements. See main text for details on the setup and notation.

estimated by combining the average values of three different observables measured independently in different runs of the experiment. These are, $\hat{\mathcal{O}}_{\boldsymbol{\alpha}}$ measured with displacement operations, $\mathcal{Z}$ as defined in Eq. (49) and measured without displacing and one detector per mode, and $\Sigma_{n\geq 2} = \sum_i \Pi^{(i)}_{n_i\geq 2}$ measured on a single mode with a 50/50 beam splitter and two detectors. Finally, in Appendix D we analyze the statistical significance of the observed violation of the witness. We use Hoeffding's theorem (1963) [31] to upper bound the p-value for the null-hypothesis that the state ρ is biseparable.

3 Experiment

The experimental setup is presented in Fig. 2. We use a heralded single photon source (HSPS) employing a periodically poled potassium titanyl phosphate (PPKTP) nonlinear crystal as a type-II spontaneous parametric down-conversion (SPDC) source. The crystal is pumped by a Ti:Sapphire laser at $\lambda_p = 771.7\,\text{nm}$ in the picosecond pulsed regime with a repetition rate of 76 MHz to create nondegenerate photon pairs at $\lambda_s = 1541.3\,\text{nm}$ (signal) and $\lambda_i = 1546.1\,\text{nm}$ (idler). The pair creation probability per pump pulse is kept at $p_{\text{pair}} \approx 2.7 \times 10^{-3}$ in order to minimize the impact of double-pair emissions. Signal and idler modes are separated after their generation by a polarizing beam splitter (PBS) and coupled into single-mode fibers (SMF). By spectrally filtering the heralding idler photon using a dense wavelength division multiplexer (DWDM) we ensure high-purity heralded signal photons.

Detection of one heralding photon by an InGaAs single-photon avalanche diode (SPAD – ID Quantique ID210) in gated mode with a detection efficiency of around 20 % heralds the presence of a fiber-coupled signal photon with a heralding efficiency of around 75 %. The heralded signal photon first encounters a band-pass filter (BPF) with a passband between 1528 nm and 1565 nm in order to further remove residual pump light and is subsequently sent to a cascade of 50/50 fiber beam splitters (BS) where it is delocalized to generate the targeted multipartite path-entangled state. In this manner, we herald the entangled state at a rate of 11.5 kcps where 0.6 kcps are attributed to dark counts, which effectively adds loss to the state.

To generate the coherent state with the same spectral and temporal properties as the signal photon for the displacement-based measurement (see Appendix E), we stimulate a difference frequency generation (DFG) process in a type-II quasi phase-matched periodically poled lithium niobate (PPLN) nonlinear crystal [32]. To this end, the crystal is pumped by the same laser pulses as the HSPS and seeded with pulses at the same repetition rate originating from a distributed feedback (DFB) laser at $\lambda_i = 1546.1\,\text{nm}$. The seed laser is driven from well below to above the lasing threshold each cycle to phase randomize the coherent state and in order to reach the required displacement amplitude, we amplify the pulses with an Erbium doped fiber amplifier (EDFA). We then couple the coherent state into SMF and further filter out residual pump light with a BPF before adjusting the time delay between the coherent state and the signal photon with a motorized delay line. Moreover, to avoid saturation of the detectors (see below), we select the coherent state pulses by passing them through an electro-optic (amplitude) modulator (EOM) with an extinction ratio of $\sim$ 30 dB triggered by a 5 ns gate upon successful detection of a heralding photon. Residual seed laser light is filtered with a DWDM at λ_s. The coherent state is then sent into the second

N	p_0	p_*	w_ρ^{exp}	$w_{\mathrm{bisep}}^{\mathrm{max}}$	p-value
4	0.6891(1)	$4.36(5)\cdot 10^{-4}$	2.993(2)	2.785	10^{-1952}
8	0.7319(1)	$3.40(4)\cdot 10^{-4}$	8.565(4)	8.358	10^{-87}

Table 1: Measured expectation values w_ρ^{exp} and calculated separable bounds $w_{\mathrm{bisep}}^{\mathrm{max}}$ of the N-partite entanglement witness for states with vacuum contributions p_0 and upper bounds p_* on the probability of having more than one photon, see Ineq. (2). The p-value for the null-hypothesis that the state ρ is biseparable is calculated according to Appendix D.

port of the first 50/50 BS where fiber polarization controllers (PC) are used to ensure orthogonal polarizations between coherent and single-photon states. The subsequent co-propagation passively guarantees stability of the relative optical phase between the coherent and single-photon states.

In order to perform the local displacement operations in an all-fiber configuration, the coherent and single-photon states are projected onto the same polarization mode using an in-line polarizer (ILP) preceded by a manual PC and a three-segment electronic polarization controller (EPC – Phoenix Photonics PSC). The first segment of the EPC allows for the control of the relative phase between the coherent and single-photon states (see Appendix E), whereas the second and third segments are used to control the displacement amplitude. In each spatial mode, the coherent state is set to have a mean photon number per pulse of roughly 13 before the polarizer to achieve a displacement amplitude of $\alpha \approx 0.83$. Drifts and fluctuations in the displacement amplitudes during the data acquisition are taken into account for the evaluation of the witness (see Appendix E). The photons are detected by eight in-house-developed MoSi superconducting nanowire single-photon detectors (SNSPD) with detection efficiencies between $75-82\,\%$ [33]. Time-correlated single-photon counting (TCSPC) using two clock-synchronized programmable time-to-digital converters (ID Quantique ID900) is then used to register detections conditioned on a successful heralding event.

After the alignment of the relative phases between the output modes, data for the witness is acquired in 20 sequences of 5 min. Each sequence measures the displacement amplitudes (1 min) and then ρ with and without displacement (2 min each). Shutters in the corresponding paths (see Fig. 2) are used to switch between the measurements. In order to estimate the probability of having more than one photon locally, we additionally perform a heralded autocorrelation measurement on one output mode by inserting a 50/50 BS before the detectors and acquire data for 6 h.

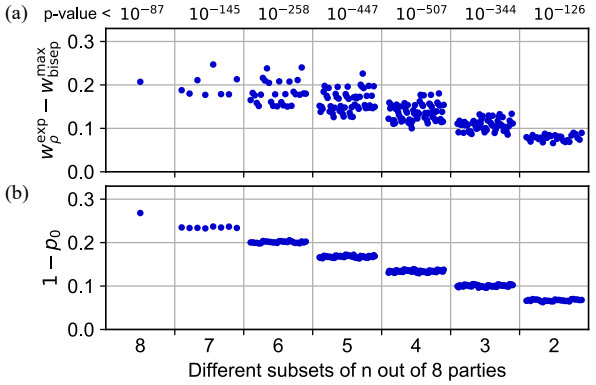

Figure 3: Results of the witness for $N = 8$. The witness is applied to all possible different subsets of n out of N parties where the discarded parties are traced out. The plots show (a) the violation of the witness $w_\rho^{\mathrm{exp}} - w_{\mathrm{bisep}}^{\mathrm{max}}$ with the maximum p-value for each fixed number of subsets indicated on top and (b) $1 - p_0$ where p_0 is the probability of the vacuum component for each subset of parties.

4 Results

The witness is measured for two different experimental configurations with $N = 4$ and 8 parties and the separable bound is violated in both cases, as shown in Tab. 1. In the case of $N = 8$ we have more loss on the state, mainly due to the insertion loss of another BS and the lower detection efficiencies of the four additional SNSPDs.

For $N = 8$ we further analyze the data by considering all $\sum_{n=2}^{N} \binom{N}{n} = 247$ possible subsets of $n \in \{2, ..., N\}$ out of N parties and calculating for each subset the expectation value and separable bound of the n-partite witness. The results are presented in Fig. 3. It is expected for our state that all subsets of parties show GME, however, these results suggest that also for a high probability of having vacuum for all parties p_0, our witness is suitable to detect GME. We attribute the fact that the witness violation $w_\rho^{\mathrm{exp}} - w_{\mathrm{bisep}}^{\mathrm{max}}$ varies for different choices of the same number of parties n to the difference in transmission and detection efficiencies for different parties (see Appendix E).

5 Discussion

Let us discuss the scalability of our witness with the number of parties N. First, we emphasize that our witness only relies on three measured quantities. Two of them, the measurement of p_0 and p_*, can be obtained with a single setting per party corresponding to no displacement. The last quantity is assessed with a second setting using displacement operations. This is in contrast with other methods where the overall number of settings grows polynomially with N, and in sharp contrast with techniques relying on state tomography where it grows exponentially with N. The

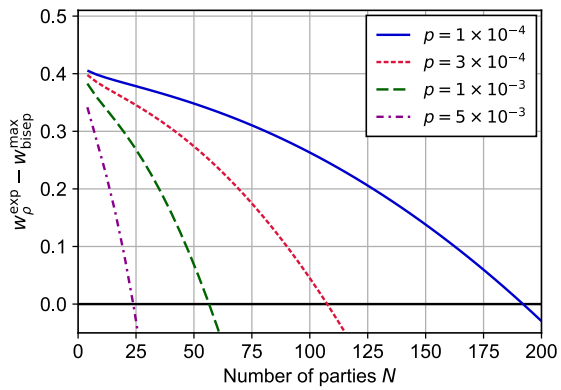

Figure 4: Calculation of the witness violation $w_\rho^{\exp} - w_{\text{bisep}}^{\max}$ as a function of the number of parties N for a state $\rho = (|1\rangle\langle 1| + p|2\rangle\langle 2|)/(1+p)$ input to a N-port beam splitter after undergoing a loss channel with transmission $\eta = 0.3$. The two-photon probability $p = 5 \times 10^{-3}$ is a good approximation for the state generated in the experiment. In this calculation, we assume a perfectly balanced state and fix the displacement amplitude for the measurement to $\alpha = \sqrt{\ln 2} \approx 0.83$ for each party, which is the most robust to fluctuations in α.

second aspect is the computational resources required to compute the biseparable bound. In our case, we only need to compute the maximum eigenvalue of an $N \times N$ matrix for each bipartition of the N parties in two groups. For any bipartition, the computational complexity of constructing the matrix and computing its maximum eigenvalue scales much better than the methods relying on a relaxation of a semi-definite optimization over the biseparable states of N qubits proposed earlier, e.g. [26]. Finally, the number of bipartitions to check grows exponentially $2^{N-1} - 1$ if all the amplitudes of displacement operations are different, however, this is reduced to $\lfloor N/2 \rfloor$ if all the displacement amplitudes can be assumed to be equal $\alpha_i = \alpha_j$. In our experimental implementation, this could be achieved by actively stabilizing the power of the coherent state before inserting it into the first beamsplitter. Further, active control of the EPCs as part of the local measurement setup would suppress drifts in the displacement amplitudes.

In the experiment, the main limiting factor for the demonstration of GME in large systems using the presented witness are contributions to the state with more than one photon in total, which we upper bound by p_*. In order to estimate the maximum number of parties N for which the witness still applies, we calculate the expected witness violation for a state $\rho = (|1\rangle\langle 1| + p|2\rangle\langle 2|)/(1+p)$ that undergoes a loss channel with transmission $\eta = 0.3$ and is then equally split into N modes, which is a good approximation of the state created in the experiment. As shown in Fig. 4, we see that the reduction of the probability of generating a two-photon state increases the number of parties for which our witness is able to detect GME. For a state similar to the one in the experiment, this would allow for the demonstration of GME for up to 23 parties. Furthermore, we show in Appendix F that our witness can be directly used in the presence of dark counts if one adds a term to the biseparable bound. We check that this does not affect the demonstration of GME in our experiment and further investigate the scalability under the presence of dark counts.

6 Conclusion

The developed witness is well suited for efficient certification of multipartite single-photon path entanglement in future quantum networks. Highly entangled multipartite states could be distributed at high rates in a scheme where each party holds a photon-pair source and one photon of each pair is sent to a central multi-port beam splitter that erases the which-path information. In this way, local losses can be kept low and the added distance between parties only reduces the heralding rate. In combination with quantum memories, such a scheme has potential for applications relying on distributed W states. The experimental challenge in such a scheme, however, remains the need for phase stability in long fiber links.

Acknowledgments

The authors would like to thank F. Bussières, M. Caloz and M. Perrenoud for the development of the SNSPDs and C. Barreiro for technical support. This work was supported by the Swiss National Science Foundation SNSF (Grant No. 200020_182664), the NCCR QSIT and by the European Union's Horizon 2020 research and innovation program under grant agreement No 820445 and project name Quantum Internet Alliance. E.O acknowledges support from the Government of Spain (FIS2020-TRANQI and Severo Ochoa CEX2019-000910-S), Fundació Cellex, Fundació Mir-Puig, Generalitat de Catalunya (CERCA, AGAUR SGR 1381) and from the ERC AdGCERQUT.

P.C. and E.O. contributed equally to this work.

A Non-unit detection efficiency

We considered that the measurements are realized with non-photon-number-resolving detectors preceded by displacement operations in phase space. As explained in the main text, we assign the outcome $+1$ to a no-detection and -1 to a conclusive detection event. Given a state ρ in a single bosonic mode with associated annihilation operator a and creation operator $a^\dagger$, the probability P_{nc} to get an outcome $+1$

using a displacement with argument α, is given by

$$P_{\rm nc} = {\rm tr}_a(D^\dagger(\alpha)|0\rangle\langle 0|D(\alpha)\rho). \tag{17}$$

In the case where the detector has a finite efficiency, we can model the detector inefficiency with a beam splitter having a transmission η, that is

$$P_{\rm nc} = {\rm tr}_a\Big(|0\rangle\langle 0|{\rm tr}_c(U_\eta(D(\alpha)\rho D^\dagger(\alpha))\otimes|0\rangle\langle 0|_c U_\eta^\dagger)\Big) \tag{18}$$

with $U_\eta = e^{\varphi(a^\dagger c - c^\dagger a)}$ for $\eta = \cos^2(\varphi)$, and the auxiliary mode described by c and $c^\dagger$, being initially empty. Using $U_\eta D(\alpha) = U_\eta D(\alpha) U_\eta^\dagger U_\eta$ together with $U_\eta D(\alpha) U_\eta^\dagger = D_a(\alpha\sqrt{\eta})D_c(\alpha\sqrt{1-\eta})$, we end up with

$$\begin{aligned} P_{\rm nc} = {\rm tr}_a\Big(&D_a^\dagger(\alpha\sqrt{\eta})|0\rangle\langle 0|D_a(\alpha\sqrt{\eta}) \\ &\cdot {\rm tr}_c(U_\eta\rho\otimes|0\rangle\langle 0|_c U_\eta^\dagger)\Big), \end{aligned} \tag{19}$$

where the displacement on mode c has been traced out. This means that we can model the detection inefficiency as loss operating on the measured state if the amplitude of the displacement operation is changed accordingly. Hence, the fact that we consider detectors with unit efficiencies is still a valid description of our measurement apparatus, where we do not need any assumptions on our state nor on the efficiency of our detectors.

B Genuine multipartite entanglement witness

Here we show how the calculation of the biseparable bound of our witness can be reduced to an single parameter optimization of the maximum eigenvalue of a $N\times N$-matrix. We start with the witness operator as presented in Eq. (7)

$$\hat{\mathcal{W}} = \hat{\mathcal{O}}_{\boldsymbol{\alpha}} + M_{n\leq 1} - N(N-1)\Pi_{n\geq 2} - \mu E_{n\geq 2}, \tag{20}$$

where $M_{n\leq 1}$ is an operator in the sector with not more than one photon and $E_{n\geq 2}\geq 0$ is in the sector with more than two photons. As argued in the main text, all our observables are block diagonal with respect to the total number of photons. In particular, $\hat{\mathcal{O}}_{\boldsymbol{\alpha}} = \hat{\mathcal{O}}_{\boldsymbol{\alpha}}^{n\leq 1}\oplus\hat{\mathcal{O}}_{\boldsymbol{\alpha}}^{n\geq 2}$. Furthermore, $\|\hat{\mathcal{O}}_{\boldsymbol{\alpha}}^{n\geq 2}\| \leq \|\hat{\mathcal{O}}\| = N(N-1)$ implies $\hat{\mathcal{O}}_{\boldsymbol{\alpha}}^{n\geq 2} - N(N-1)\Pi_{n\geq 2}\leq 0$ and

$$\begin{aligned} \hat{\mathcal{W}} &= (\hat{\mathcal{O}}_{\boldsymbol{\alpha}}^{n\leq 1} + M_{n\leq 1}) \\ &\quad\oplus (\hat{\mathcal{O}}_{\boldsymbol{\alpha}}^{n\geq 2} - N(N-1)\Pi_{n\geq 2} - \mu E_{n\geq 2}) \\ &\leq (\hat{\mathcal{O}}_{\boldsymbol{\alpha}}^{n\leq 1} + M_{n\leq 1}) \oplus (-\mu\, E_{n\geq 2}). \end{aligned} \tag{21}$$

To find the biseparable bound consider biseparable states of the form

$$|\Psi\rangle = |\Psi_1\rangle_{G_1}|\Psi_2\rangle_{G_2}, \tag{22}$$

defined over a bipartition given by two disjoint subsets $G_1\cup G_2 = \{1,\ldots,N\}$ of the N modes. The value that the witness takes over these states reads

$$\begin{aligned} \langle\Psi|\hat{\mathcal{W}}|\Psi\rangle \leq\ &\langle\Psi|\hat{\mathcal{O}}_{\boldsymbol{\alpha}}^{n\leq 1} + M_{n\leq 1}|\Psi\rangle \\ &- \mu\langle\Psi|E_{n\geq 2}|\Psi\rangle. \end{aligned} \tag{23}$$

As $\mu\langle\Psi|E_{n\geq 2}|\Psi\rangle$ is positive, to maximize the right-hand side one can restrict the consideration to states $|\Psi_{1(2)}\rangle$ with one photon at most. Hence, without loss of generality we take

$$|\Psi_k\rangle_{G_k} = v_0^{(k)}|0\rangle_{G_k} + \sum_{i=1|j_i\in G_k}^{|G_k|} v_i^{(k)} a_{j_i}^\dagger|0\rangle_{G_k}. \tag{24}$$

To compute the value of the witness on these states we need the explicit form of the operators $\hat{\mathcal{O}}_{\boldsymbol{\alpha}}^{n\leq 1}$ and $M_{n\leq 1}$. To compute $\hat{\mathcal{O}}_{\boldsymbol{\alpha}}^{n\leq 1}$ we use the restriction of σ_α to the subspace with not more than one photon $\{|0\rangle,|1\rangle\}$

$$\sigma_\alpha^{n\leq 1} = \begin{pmatrix} f(\alpha) & g(\alpha) \\ g(\alpha) & h(\alpha)\end{pmatrix}, \tag{25}$$

where we assumed a real α and denoted

$$f(\alpha) = \big(2e^{-\alpha^2} - 1\big), \tag{26}$$

$$g(\alpha) = 2\alpha e^{-\alpha^2}, \tag{27}$$

$$h(\alpha) = \big(2\alpha^2 e^{-\alpha^2} - 1\big), \tag{28}$$

see e.g. [30] for a derivation. For the product observable restricted to the subspace of interest we obtain

$$\begin{aligned} \Big(\sigma_{\alpha_i}^{(i)}\otimes\sigma_{\alpha_j}^{(j)}\Big)_{n\leq 1} &= f(\alpha_i)f(\alpha_j)|00\rangle\langle 00|_{i,j} + g(\alpha_i)g(\alpha_j)\big(|01\rangle\langle 10|_{i,j} + |10\rangle\langle 01|_{i,j}\big) \\ &\quad + f(\alpha_i)h(\alpha_j)|01\rangle\langle 01|_{i,j} + h(\alpha_i)f(\alpha_j)|10\rangle\langle 10|_{i,j}, \end{aligned} \tag{29}$$

remark that here and in the following $\sigma_{\alpha_i}^{(i)}\otimes\sigma_{\alpha_j}^{(j)}$ refers to the phase-averaged operator. Adding the identity on the remaining modes gives

$$\begin{aligned} \Big(\sigma_{\alpha_i}^{(i)}\otimes\sigma_{\alpha_j}^{(j)}\otimes\mathbb{1}_{\neg\{i,j\}}\Big)_{n\leq 1} &= f(\alpha_i)f(\alpha_j)\Big(|\bar{0}\rangle\langle\bar{0}| + \sum_{k\neq i,j}|1_k\rangle\langle 1_k|\Big) \\ + \Big(g(\alpha_i)g(\alpha_j)(|01\rangle\langle 10|_{i,j} + |10\rangle\langle 01|_{i,j}) + f(\alpha_i)h(\alpha_j)|01\rangle\langle 01|_{i,j} + h(\alpha_i)f(\alpha_j)|10\rangle\langle 10|_{i,j}\Big)&\otimes|\bar{0}\rangle\langle\bar{0}|_{\neg\{i,j\}}, \end{aligned} \tag{30}$$

with $|\bar{0}\rangle$ denoting the vacuum state of all involved modes and $|1_k\rangle = a_k^\dagger|\bar{0}\rangle$ denoting the state with one photon in mode k and vacuum elsewhere, and

$$\begin{aligned}\hat{\mathcal{O}}_{\boldsymbol{\alpha}}^{n\leq 1} &= \sum_{i\neq j}\left(\sigma_{\alpha_i}^{(i)}\otimes\sigma_{\alpha_j}^{(j)}\otimes\mathbb{1}_{\neg\{i,j\}}\right)_{n\leq 1}\\ &= \sum_{i\neq j} f(\alpha_i)f(\alpha_j)\left(|\bar{0}\rangle\langle\bar{0}| + \sum_{k\neq i,j}|1_k\rangle\langle 1_k|\right) + \sum_{i\neq j} g(\alpha_i)g(\alpha_j)\left(|1_i\rangle\langle 1_j| + |1_j\rangle\langle 1_i|\right)\\ &\quad + \sum_{i\neq j}\left(h(\alpha_i)f(\alpha_j)|1_i\rangle\langle 1_i| + h(\alpha_j)f(\alpha_i)|1_j\rangle\langle 1_j|\right).\end{aligned} \tag{31}$$

For $M_{n\leq 1}$ we chose

$$M_{n\leq 1} = \lambda|\bar{0}\rangle\langle\bar{0}| - \sum_{i\neq j} f(\alpha_i)f(\alpha_j)\left(|\bar{0}\rangle\langle\bar{0}| + \sum_{k\neq i,j}|1_k\rangle\langle 1_k|\right), \tag{32}$$

with a positive real parameter λ that one can tune, such that

$$\begin{aligned}\hat{\mathcal{O}}_{\boldsymbol{\alpha}}^{n\leq 1} + M_{n\leq 1} &= \lambda|\bar{0}\rangle\langle\bar{0}| + \sum_{i\neq j} g(\alpha_i)g(\alpha_j)\left(|1_i\rangle\langle 1_j| + |1_j\rangle\langle 1_i|\right)\\ &\quad + \sum_{i\neq j}\left(h(\alpha_i)f(\alpha_j)|1_i\rangle\langle 1_i| + h(\alpha_j)f(\alpha_i)|1_j\rangle\langle 1_j|\right).\end{aligned} \tag{33}$$

Finally for $E_{n\geq 2}$ we take the operators corresponding to the probability to find photons in more than one mode. We rewrite $v_0^{(1)} = c_a$ and $v_0^{(2)} = c_b$, where we use the short notation $c_{a(b)} = \cos\left(a(b)\right)$ and $s_{a(b)} = \sin\left(a(b)\right)$, such that $\boldsymbol{v}^{(1)} = \binom{c_a}{s_a\boldsymbol{v}'}$ and $\boldsymbol{v}^{(2)} = \binom{c_b}{s_b\boldsymbol{w}'}$ with normalized $\boldsymbol{v}'$ and $\boldsymbol{w}'$ which leads to

$$|\Psi\rangle = c_a c_b|\bar{0}\rangle + \sum_{i\in G_1} s_a c_b v_i'|1_i\rangle + \sum_{j\in G_2} c_a s_b w_j'|1_j\rangle + \sum_{i\in G_1}\sum_{j\in G_2} s_a s_b w_j' v_i'|1_i\rangle_{G_1}|1_j\rangle_{G_2}, \tag{34}$$

where $|1_j\rangle$ stands for one photon in mode j and vacuum in all the other modes. We thus have by Eq. (23)

$$\langle\Psi|\hat{\mathcal{W}}|\Psi\rangle \leq \lambda c_a^2 c_b^2 - \mu s_a^2 s_b^2 + 2\Big(\sum_{i\neq j} g(\alpha_i)g(\alpha_j)L_iL_j + f(\alpha_i)h(\alpha_j)L_j^2\Big), \tag{35}$$

where $\boldsymbol{L} = \binom{c_a s_b\boldsymbol{w}'}{s_a c_b\boldsymbol{v}'}$. We rewrite Eq. (35) in a matrix form

$$\langle\Psi|\hat{\mathcal{W}}|\Psi\rangle \leq \lambda c_a^2 c_b^2 - \mu s_a^2 s_b^2 + \boldsymbol{L}^T\begin{pmatrix} M_w & M_c\\ M_c^T & M_v\end{pmatrix}\boldsymbol{L}. \tag{36}$$

By arranging the entries of the matrix according to the defined bipartition, i.e. the block spanning the first $|G_2|$ rows and columns describes the modes in G_2, we can explicitly write down the matrix

$$\begin{pmatrix} M_w & M_c\\ M_c^T & M_v\end{pmatrix} = 2\begin{pmatrix} \sum_{i\neq 1} f(\alpha_i)h(\alpha_1) & g(\alpha_1)g(\alpha_2) & \cdots & g(\alpha_1)g(\alpha_N)\\ g(\alpha_2)g(\alpha_1) & \sum_{i\neq 2} f(\alpha_i)h(\alpha_2) & \cdots & g(\alpha_2)g(\alpha_N)\\ \vdots & \vdots & \ddots & \vdots\\ g(\alpha_N)g(\alpha_1) & g(\alpha_N)g(\alpha_2) & \cdots & \sum_{i\neq N} f(\alpha_i)h(\alpha_N)\end{pmatrix}. \tag{37}$$

We finally can write

$$\begin{aligned}\langle\Psi|\hat{\mathcal{W}}|\Psi\rangle &\leq \lambda c_a^2 c_b^2 - \mu s_a^2 s_b^2 + \begin{pmatrix} c_a s_b\boldsymbol{w}'\\ s_a c_b\boldsymbol{v}'\end{pmatrix}^T\begin{pmatrix} M_w & M_c\\ M_c^T & M_v\end{pmatrix}\begin{pmatrix} c_a s_b\boldsymbol{w}'\\ s_a c_b\boldsymbol{v}'\end{pmatrix}\\ &= \lambda c_a^2 c_b^2 - \mu s_a^2 s_b^2 + \begin{pmatrix} s_b\boldsymbol{w}'\\ c_b\boldsymbol{v}'\end{pmatrix}^T\begin{pmatrix} c_a^2 M_w & c_a s_a M_c\\ c_a s_a M_c^T & s_a^2 M_v\end{pmatrix}\begin{pmatrix} s_b\boldsymbol{w}'\\ c_b\boldsymbol{v}'\end{pmatrix}\\ &= \begin{pmatrix} s_b\boldsymbol{w}'\\ c_b\boldsymbol{v}'\end{pmatrix}^T\begin{pmatrix} c_a^2 M_w - s_a^2\mu\mathbb{1} & c_a s_a M_c\\ c_a s_a M_c^T & s_a^2 M_v + c_a^2\lambda\mathbb{1}\end{pmatrix}\begin{pmatrix} s_b\boldsymbol{w}'\\ c_b\boldsymbol{v}'\end{pmatrix}\\ &\leq \max\mathrm{eig}\begin{pmatrix} c_a^2 M_w - s_a^2\mu\mathbb{1} & c_a s_a M_c\\ c_a s_a M_c^T & s_a^2 M_v + c_a^2\lambda\mathbb{1}\end{pmatrix} = \max\mathrm{eig}\left(\mathbb{M}(\lambda,\mu,\boldsymbol{\alpha},a)\right),\end{aligned} \tag{38}$$

where in the last line "max eig" denotes the maximum eigenvalue of the Hermitian matrix $\mathbb{M}(\lambda, \mu, \boldsymbol{\alpha}, a)$.

The biseparable bound is thus given by the optimization

$$\widetilde{w}_{\text{bisep}} = \max_{G_1,G_2} w_{G_1,G_2} = \max_{G_1,G_2} \max_{a\in[0,2\pi]} \max \text{eig}\left(\mathbb{M}(\lambda, \mu, \boldsymbol{\alpha}, a)\right) \tag{39}$$

for well-chosen λ and μ. One notes that the optimization can be restricted to $a \in [0, \frac{\pi}{2}]$, as the transformation $(c_a^2, s_a^2, c_a s_a) \to (c_a^2, s_a^2, -c_a s_a)$ only changes the sign of the off-diagonal blocks of the matrix $\mathbb{M} \to \begin{pmatrix} 1 & \\ & -1 \end{pmatrix} \mathbb{M} \begin{pmatrix} 1 & \\ & -1 \end{pmatrix}$ which does not change its spectrum, as $\begin{pmatrix} 1 & \\ & -1 \end{pmatrix}$ is an orthogonal matrix (basis change).

C Measuring the witness

In this section, we explain how we estimate the expected value of the witness

$$\hat{\mathcal{W}}_{\boldsymbol{\alpha}} = \hat{\mathcal{O}}_{\boldsymbol{\alpha}} + M_{n\leq 1} - N(N-1)\Pi_{n\geq 2} - \mu E_{n\geq 2} \tag{40}$$

on the state ρ prepared in the experiment. It can be estimated from two observables, the one with displacement $\hat{\mathcal{O}}_{\boldsymbol{\alpha}}$ and one without $M_{n\leq 1} - N(N-1)\Pi_{n\geq 2} - \mu E_{n\geq 2}$.

In our case, given the limited number of detectors we actually use three different observables, because we split $\Pi_{n\geq 2}$ in two parts. To do so we note that the probability that any N-mode state ρ contains two or more photons satisfies $P_{n\geq 2}(\rho) = \text{tr}(\Pi_{n\geq 2}\,\rho) \leq p_*$, where

$$p_* = \sum_{n=2}^{N} P^n_{\text{click}} + \sum_{i=1}^{N} p_i^*. \tag{41}$$

Here, P^n_{click} is the joint probability that n detectors click and all the other detectors do not click when measured without displacement and p_i^* is an upper bound on the probability of having two or more photons in mode i, that we associate to an observable $\Pi^{(i)}_{n\geq 2}$. The value for p_i^* can be obtained in practice by measuring the probability of coincidence after a 50/50 beam splitter in mode i. On the level of the operators, we can write

$$\Pi_{n\geq 2} \leq E_{n\geq 2} + \sum_{i=1}^{N} \Pi^{(i)}_{n\geq 2} \tag{42}$$

with two parts that we measure independently. For the witness this implies

$$\begin{aligned} \hat{\mathcal{W}} \geq\ & \hat{\mathcal{O}}_{\boldsymbol{\alpha}} + M_{n\leq 1} - (N(N-1)+\mu)E_{n\geq 2} \\ & - N(N-1)\sum_{i=1}^{N} \Pi^{(i)}_{n\geq 2}. \end{aligned} \tag{43}$$

It is already clear how the observables $\hat{\mathcal{O}}_{\boldsymbol{\alpha}}$ and $\sum_{i=1}^{N} \Pi^{(i)}_{n\geq 2}$ can be measured, so let us now focus on the remaining terms. First, we note that

$$\begin{aligned} & -f(\alpha_i)f(\alpha_j)\left(|\bar{0}\rangle\langle\bar{0}| + \sum_{k\neq i,j} |1_k\rangle\langle 1_k|\right) \\ & \geq -\max\{f(\alpha_i)f(\alpha_j), 0\}|00\rangle\langle 00|_{ij} \end{aligned} \tag{44}$$

because the probability that there is no photon in the state or only one photon in some mode $k \neq i, j$, given by the POVM element $|\bar{0}\rangle\langle\bar{0}| + \sum_{k\neq i,j} |1_k\rangle\langle 1_k|$, is lower than the probability that there is no photons in the modes i and j given by $|00\rangle\langle 00|_{ij}$. We thus obtain

$$M_{n\leq 1} \geq \lambda|\bar{0}\rangle\langle\bar{0}| - \sum_{i\neq j} \max\{f(\alpha_i)f(\alpha_j), 0\}|00\rangle\langle 00|_{ij}. \tag{45}$$

In the experiment we do not have full information on the value of $\boldsymbol{\alpha}$ in a particular round, but rather a range of possible values $\boldsymbol{\alpha} = (\alpha_1, \ldots, \alpha_N) \in A$. Therefore, the following bound will be useful

$$M_{n\leq 1} \geq \bar{M}_{n\leq 1}, \tag{46}$$

$$\bar{M}_{n\leq 1} = \lambda|\bar{0}\rangle\langle\bar{0}| - \sum_{i\neq j} F_{ij}|00\rangle\langle 00|_{ij}, \tag{47}$$

$$\begin{aligned} F_{ij} &= \max_{\boldsymbol{\alpha}\in A} \max\{f(\alpha_i)f(\alpha_j), 0\} \\ &= \max\{0, \max_{\boldsymbol{\alpha}\in A} f(\alpha_i)f(\alpha_j)\}. \end{aligned} \tag{48}$$

To summarize we have shown that

$$\hat{\mathcal{W}}_{\boldsymbol{\alpha}} \geq \overline{\mathcal{W}}_{\boldsymbol{\alpha}} = \hat{\mathcal{O}}_{\boldsymbol{\alpha}} + \mathcal{Z} - N(N-1)\Sigma_{n\geq 2}, \tag{49}$$

$$\begin{aligned} \mathcal{Z} = \lambda|\bar{0}\rangle\langle\bar{0}| &- \sum_{i\neq j} F_{ij}|00\rangle\langle 00|_{ij} \\ &- (N(N-1)+\mu)E_{n\geq 2}, \end{aligned} \tag{50}$$

$$\Sigma_{n\geq 2} = \sum_{i=1}^{N} \Pi^{(i)}_{n\geq 2}. \tag{51}$$

In the experiment the values of the observables $\hat{\mathcal{O}}$, $\mathcal{Z}$ and $\Sigma_{n\geq 2}$ are measured independently. The observable $\Sigma_{n\geq 2}$ is independent of the displacement amplitudes $\boldsymbol{\alpha}$ while $\hat{\mathcal{O}}_{\boldsymbol{\alpha}}$ is physically determined by $\boldsymbol{\alpha}$. The observable $\mathcal{Z}$ is computed using the knowledge of the range A of possible values $\boldsymbol{\alpha} \in A$ for the coefficients F_{ij}, while the underlying physical measurement is performed without displacements.

To analyze the experimental data, we assume that the state preparation is identical in each run of the experiment, such that is the same N-mode state ρ is prepared repeatedly. On the other hand, the displacement amplitudes are subject to controlled fluctuations $\boldsymbol{\alpha} \in A$, with the possible range A determined experimentally, see Appendix E. Nevertheless, each round

k can be associated to some (unknown) value $\boldsymbol{\alpha}_k$. To prove that the state is GME it is sufficient to show that

$$\frac{1}{n}\sum_{k=1}^{n}\left\langle \hat{\mathcal{W}}_{\boldsymbol{\alpha}_k} - \widetilde{w}_{\text{bisep}}(\boldsymbol{\alpha}_k)\right\rangle_{\rho} > 0 \tag{52}$$

with $\langle X\rangle_\rho = \text{tr}(X\rho)$, since each $\boldsymbol{\alpha}_k$ yields a valid GME-witness. By defining the worst-case biseparable bound

$$w_{\text{bisep}}^{\max} = \max_{\boldsymbol{\alpha}\in A} \widetilde{w}_{\text{bisep}}(\boldsymbol{\alpha}), \tag{53}$$

and using the bound (49), we can relax the GME condition to

$$\frac{1}{n}\sum_{k=1}^{n}\left\langle \hat{\mathcal{O}}_{\boldsymbol{\alpha}_k} + \mathcal{Z} - N(N-1)\Sigma_{n\geq 2} - w_{\text{bisep}}^{\max}\right\rangle_{\rho} > 0, \tag{54}$$

where the left-hand side is a lower bound on $\frac{1}{n}\sum_{k=1}^{n}\left\langle \hat{\mathcal{W}}_{\boldsymbol{\alpha}_k} - w_{\text{bisep}}(\boldsymbol{\alpha}_k)\right\rangle_{\rho}$.

Before analyzing the statistical significance of our data, let us briefly sketch how GME can be guaranteed in the asymptotic limit $n\to\infty$. Then the average values of the observables $\mathcal{Z}$ and $\Sigma_{n\geq 2}$ converge to their expected values $\langle\mathcal{Z}\rangle$ and $\langle\Sigma_{n\geq 2}\rangle$. Similarly, for the random variables o_k as the value of $\hat{\mathcal{O}}_{\boldsymbol{\alpha}_k}$ observed in the round k (where it is measured), the observed average converges to the average expected value

$$\frac{1}{n}\sum_{k=1}^{n} o^{(k)} \to \frac{1}{n}\sum_{k=1}^{n}\mathbb{E}(o^{(k)}) = \frac{1}{n}\sum_{k=1}^{n}\langle\hat{\mathcal{O}}_{\boldsymbol{\alpha}_k}\rangle_\rho, \tag{55}$$

by Hoeffding's theorem (1963), see Appendix D. Hence, Eq. (54) can be directly guaranteed from the data. Note that in practice to estimate $\Sigma_{n\geq 2}$ we do not measure $\Pi^{(i)}_{n\geq 2}$ for each mode. Instead, we assume that it has the same expected value for each mode, such that

$$\langle\Sigma_{n\geq 2}\rangle_\rho = N\langle\Pi^{(1)}_{n\geq 2}\rangle_\rho, \tag{56}$$

and only estimate $\langle\Pi^{(1)}_{n\geq 2}\rangle_\rho$.

D Finite statistics analysis

In the experiment, three different measurements are performed, to each of which we associate a random variable. Let o_k be the random variable given the value of $\hat{\mathcal{O}}_{\boldsymbol{\alpha}_k}$ observed in the round $k=1,\dots,n$ (when it is measured). Analogously, define z_k associated to $\mathcal{Z}$ (for $k=1,\dots,m$) and s_k associated to $-N^2(N-1)\Pi^{(1)}_{n\geq 2}$ (for $k=1,\dots,\ell$). Note that all the variable are independent, furthermore the variables z_k and s_k are also identically distributed (for each k). From the definition of the corresponding observables (their spectrum) one directly sees that

$$o_k \in [-N(N-1), N(N-1)], \tag{57}$$

$$z_k \in [-\sum_{i\neq j} F_{ij} - N(N-1) - \mu, \lambda], \tag{58}$$

$$s_k \in [-N^2(N-1), 0], \tag{59}$$

from which we define

$$\Delta_o = 2N(N-1), \tag{60}$$

$$\Delta_z = \lambda + \sum_{i\neq j} F_{ij} + N(N-1) + \mu, \tag{61}$$

$$\Delta_s = N^2(N-1). \tag{62}$$

For each type of observables we define the average as

$$\bar{o} = \frac{1}{n}\sum_{k=1}^{n} o_k. \tag{63}$$

To analyze the statistical significance of our data, we use the following theorem by Hoeffding (1963) [31]: For any collection of independent random variables $x^{(1)},\dots,x^{(n)}$ with $x^{(k)}\in[a_k, a_k+\Delta_k]$ the following bound holds

$$\begin{aligned} &\text{P}\Big(\overline{x} - t \geq \mathbb{E}\left(\overline{x}\right)\Big) \leq \exp\left(-\frac{2n^2t^2}{\sum_{k=1}^{n}\Delta_k^2}\right) \\ &\text{for}\quad \overline{x} = \frac{1}{n}\sum_{i=1}^{n} x^{(k)}. \end{aligned} \tag{64}$$

To apply to our data consider the situation where the observable $o_k\in[a, a+\Delta_o]$ are measured in n rounds, $z_k\in[b, b+\Delta_z]$ are measured in m rounds, and $s_k\in[c, c+\Delta_s]$ are measured in ℓ rounds, the above theorem implies

$$\text{P}\Big(\bar{o}+\bar{z}+\bar{s} - t \geq \mathbb{E}\left(\bar{o}+\bar{z}+\bar{s}\right)\Big) \leq e^{-\frac{2(n+m+\ell)^2t^2}{n\Delta_o^2+m\Delta_z^2+\ell\Delta_s^2}}. \tag{65}$$

Now consider any state ρ_{bisep} that is not GME. We have shown that such a state does not violate the relaxed witness of Eq. (54). Thus, it gives rise to a collection of random variables, described in the beginning of the section, with

$$\begin{aligned} 0 &\geq \left\langle \frac{1}{n}\sum_{k=1}^{n}\hat{\mathcal{O}}_{\boldsymbol{\alpha}_k} + \mathcal{Z} - N(N-1)\Sigma_{n\geq 2} - w_{\text{bisep}}^{\max}\right\rangle_{\rho_{\text{bisep}}} \\ &= \mathbb{E}\left(\bar{o}+\bar{z}+\bar{s} - w_{\text{bisep}}^{\max}\right) \end{aligned} \tag{66}$$

Then, by Eq. (65) the probability that the observed averages satisfy

$$\bar{o}+\bar{z}+\bar{s} - w_{\text{bisep}}^{\max} \geq t, \tag{67}$$

i.e. a fake violation exceeding t is observed due to statistical fluctuation, is upper bounded by

$$\exp\left(-\frac{2(n+m+\ell)^2t^2}{n\Delta_o^2+m\Delta_z^2+\ell\Delta_s^2}\right). \tag{68}$$

Hence,

$$p = \exp\left(-\frac{2(n+m+\ell)^2(\bar{o}+\bar{z}+\bar{s}-w_{\text{bisep}}^{\max})^2}{n\Delta_o^2+m\Delta_z^2+\ell\Delta_s^2}\right) \tag{69}$$

N	λ	μ	$\overline{o}$	$\overline{z}$	$\overline{s}$	n	m	ℓ	$w_{\text{bisep}}^{\max}$	p-value
4	2.73	102	1.1525	1.8417	-0.0014	26747089	26755161	135905902	2.785	10^{-1952}
8	8.29	151	2.5762	5.9915	-0.0024	27611104	27576602	365370348	8.358	10^{-87}

Table 2: Evaluation of the witness for N parties with parameters λ and μ according to Eqs. (20) and (32). The mean values $\overline{o}$, $\overline{z}$ and $\overline{s}$ are associated to the observables $\hat{\mathcal{O}}_{\boldsymbol{\alpha}}$, $\mathcal{Z}$ and $-N^2(N-1)\Pi_{n\geq 2}^{(1)}$, respectively. The numbers n, m and ℓ indicate the number of evaluations of o, z and s. Together with the biseparable bound $w_{\text{bisep}}^{\max}$ according to Eq. (53), the p-value is calculated using Eq. (69). Note that in order to obtain a p-value of less than 10^{-10}, in the case of N=4 it would suffice to evaluate the observables $n = m = \ell = 4.9 \times 10^5$ times, corresponding to a total integration time of less than 130 s, and for N=8 it would require $n = m = \ell = 7.8 \times 10^6$ evaluations which could be achieved in less than 2100 s.

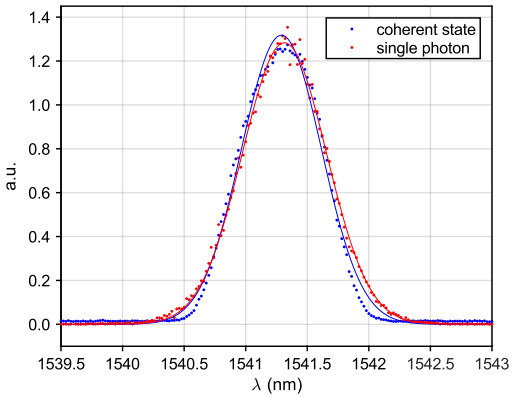

Figure 5: Normalized measured spectra and Gaussian fit of single-photon and coherent states. The spectra are measured with a tunable grating filter with a FWHM of 0.2 nm inserted before the SNSPD.

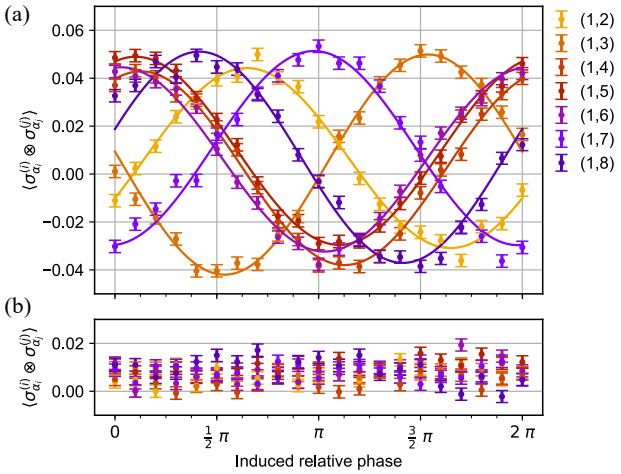

Figure 6: Phase alignment between mode 1 (reference) and all seven other modes. (a) The single-photon state is displaced with $\alpha \approx 0.83$ and the first segment of the electronic polarization controller is swept over its full range from 0 to 2π in each non-reference mode. Sinusoidal curves are fitted to the data. (b) Same measurement without the presence of the single-photon state.

can be interpreted as the p-value associated to our GME test. That is, p is an upper bound on the probability that a state ρ_{bisep} which is not GME produces a fake violation of $\overline{o} + \overline{z} + \overline{s} - w_{\text{bisep}}^{\max}$ or higher.

For the corresponding values in the experiment, see Tab. 2.

E Experimental methods and characterization

To ensure high-purity heralded signal photons, we spectrally filter the heralding idler photons emitted from the PPKTP crystal by using a dense wavelength division multiplexer (DWDM) with a 100 GHz passband at $\lambda_i = 1546.12$ nm (ITU channel 39).

Besides high single-photon purity, the single-photon and coherent states need to have a good spectral and temporal overlap in order to perform the targeted displacement operation. The measurement of the spectral overlap is shown in Fig. 5. The expected Hong-Ou-Mandel visibility due to the finite overlap of the fitted Gaussians is 99.2 % [34].

The temporal alignment between the single-photon and coherent states is done in the following way. The seed laser is switched to continuous mode and, together with the pulsed pump laser, difference frequency generation in both nonlinear crystals, PPKTP

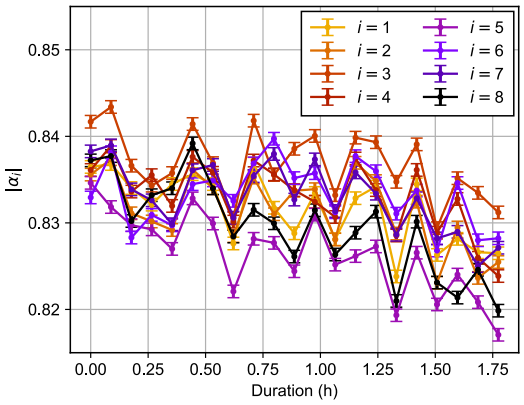

Figure 7: Measurement of the displacement amplitudes $|\alpha_i|$ for each spatial output mode i during the data acquisition. For each point, counts are acquired for 1 min.

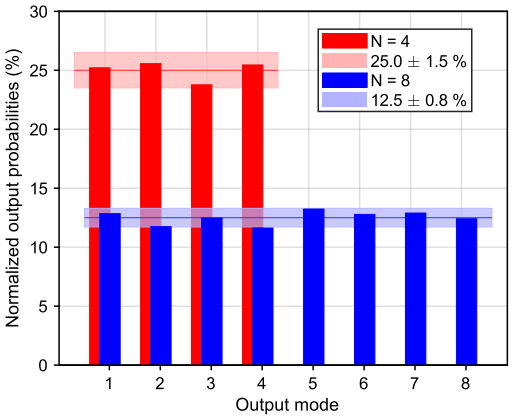

Figure 8: Normalized probabilities of detecting a photon in output mode $i \in \{1, ..., N\}$ in the measurement without displacement.

N	P^1_{click}	P^2_{click}	P^3_{click}	p^*_1
4	0.3106(1)	$3.21(4) \cdot 10^{-4}$	$1.5(8) \cdot 10^{-7}$	$2.89(5) \cdot 10^{-5}$
8	0.2678(1)	$2.96(4) \cdot 10^{-4}$	$1.5(8) \cdot 10^{-7}$	$5.4(1) \cdot 10^{-6}$

Table 3: Measured probabilities P^n_{click} that n detectors click in the case of preparing an N-partite state. Further, p^*_1 is an upper bound on the probability of having more than one photon locally in mode 1.

and PPLN, is used to generate coherent states at λ_s. First-order interference is observed at one of the output modes and the interference visibility is maximized by adjusting the delay of the motorized delay line.

In order to set the relative phases between single-photon and coherent states in each spatial mode, polarization is aligned with a polarization controller such that it enters the first segment of the electronic polarization controller on-axis which therefore allows for relative phase control locally, as shown in Fig. 6. The phase is then set in each mode such that its relative phase to the reference mode is zero.

After the phase alignment, data is acquired in intervals, as described in the main text. The displacement amplitudes are obtained by measuring the coherent state in the absence of the single-photon state and assuming Poissonian count statistics (see Fig. 7). For the calculation of the expectation value of the witness (see Eqs. (46) and (49)) and the biseparable bound according to Eq. (53), all the values $\boldsymbol{\alpha} \in A = \{(\alpha_1, \ldots, \alpha_8) \in \mathbb{R}^8 | \alpha_i^{\min} \leq \alpha_i \leq \alpha_i^{\max}\}$ are considered. Here, $\alpha_i^{\min}$ ($\alpha_i^{\max}$) denotes the minimum (maximum) value of α_i on mode i during the measurement shown in Fig. 7.

To determine the balance of the generated state, the counts in each mode in the measurement without displacement are normalized, as shown in Fig. 8. For the measurement where $N = 4$, the mode balance is $25.0 \pm 1.5\%$, where for $N = 8$ a balance of $12.5 \pm 0.8\%$ is achieved.

The values for the probabilities P^n_{click} that n detectors click when measuring the state are given in Tab. 3. Note that the probability p_0 indicated in Tab. 1 are $p_0 = P^0_{\text{click}} = 1 - \sum_{n \geq 1} P^n_{\text{click}}$.

F The effect of dark counts on the witness

Here we explain how the presence of detector dark counts can be in included in our GME witness. We will show that by adding a constant term $2N^2(N-1)p_{dc}$ to the biseparable bound, the violation of this shifted witness (exactly as described in the main text, but with detectors subject to dark counts) allows one to conclude that the measured state is GME. Before we start, recall that a usual model of dark counts for non-photon-number-resolving (NPNR) detectors is a classical noise which changes the outcome "no-click" to "click" with probability p_{dc}. Thus, "turning on" the dark counts on a detector modifies the click/no-click probabilities to

$$(p_0^{dc}, p_c^{dc}) = ((1 - p_{dc})p_0, p_{dc}\, p_0 + p_c). \tag{70}$$

The starting point is to consider an experiment where the expected value of the witness $\langle \hat{\mathcal{W}}_{dc} \rangle$ is estimated as described in the main text, but with detectors subject to dark counts. We now introduce a simple physical model that reproduces (almost) all the statistics of this experiment, but involves detectors without dark counts. To this end, consider a single-mode quantum channel S_{dc} which does nothing with probability $1 - p_{dc}$ and replaces a single mode state ϱ with a very bright Fock state $|M\rangle$ with probability p_{dc}

$$S_{dc} : \varrho \mapsto S_{dc}[\varrho] = (1 - p_{dc})\varrho + p_{dc}|M\rangle\langle M|. \tag{71}$$

The state $S_{dc}[\varrho]$ is then measured with the measurement described in the main text. We now have to distinguish between different measurements that we treat separately. (1) The measurements of the witness and (2) the estimation of p_*. More precisely, we need to distinguish measurements with one detector per mode and $g^{(2)}$ measurements with two detectors per mode.

In the case (1) all measurements involve a single lossy NPNR detector per mode, sometimes preceded by a displacement $D(\alpha)$. The probability distribution of the outcomes of this measurement is a mixture of two possibilities. With probability $1 - p_{dc}$ the state was unchanged and the measurement is performed on the original state ρ leading to the click/no-click probabilities (p_0, p_c). With probability p_{dc} the measurement is performed on the state $|M\rangle$, where we can always choose M large enough such that in this case a "click" outcome is observed with certainty $p_c = 1$.

The overall outcome probabilities are thus given by

$$\begin{aligned}(p_0^{dc}, p_c^{dc}) &= (1-p_{dc})(p_0, p_c) + p_{dc}(0,1)\\ &= ((1-p_{dc})p_0, (1-p_{dc})p_c + p_{dc})\\ &= ((1-p_{dc})p_0, p_{dc}p_0 + p_c).\end{aligned} \tag{72}$$

Hence, the N-mode state $\tilde{\rho} = S_{dc}^{\otimes N}[\rho]$ measured with detectors without dark-counts reproduces the statistics of the N-mode state ρ observed with detectors subject to dark counts whenever only one detector is used per mode.

Let us now consider the estimation of p_*, which is an upper bound on the probability of having two or more photons in the state. As defined in Eq. (41), p_* is composed of two contributions. The first term $\sum_{n=2}^{N} P^n_{\text{click}}$ is the probability to observe clicks on more than two modes gathered with a single detector per mode. Hence, for this term the above argumentation holds $P^n_{\text{click+dc}}[\rho] = P^n_{\text{click}}[\tilde{\rho}]$. The other term p_i^* is an upper bound on the probability of having two or more photons in a single mode. This is measured in a $g^{(2)}$ experiment – a single mode state ϱ is split on a 50/50 beam splitter, and each output is sent to a NPNR detector. The probability that the two detectors click p_{cc} is bounded by the probability that ϱ contains two or more photons $p_{cc} \leq p_i^* \leq 2p_{cc}$. And it is precisely the estimated p_{cc}, which is used to bound p_*. Let us now analyze how this probability is affected by dark counts. For a state ϱ we have

$$\begin{aligned}p_{cc}^{dc} &= p_{cc} + p_{dc}(p_{0c} + p_{c0}) + p_{dc}^2 p_{00}\\ &= p_{cc} + p_{dc}(p_{0c} + p_{c0} + p_{00}) - p_{dc}p_{00} + p_{dc}^2 p_{00}\\ &= p_{cc} + p_{dc}(1-p_{cc}) - p_{00}p_{dc}(1-p_{dc}).\end{aligned} \tag{73}$$

Now let us analyze the effect of the channel S_{dc} on this probability. For a state $\tilde{\varrho} = S_{dc}[\varrho]$ one has

$$\begin{aligned}\tilde{p}_{cc} &= (1-p_{dc})p_{cc} + p_{dc}\\ &= p_{cc} + p_{dc}(1-p_{cc})\\ &= p_{cc}^{dc} + p_{00}p_{dc}(1-p_{dc})\\ &\leq p_{cc}^{dc} + p_{dc}.\end{aligned} \tag{74}$$

Hence, for the state $\tilde{\rho}$ we get an upper bound

$$\tilde{p}_i^* \leq p_i^* + 2p_{dc}, \tag{75}$$

where p_i^* is the quantity estimated in the experiment with dark counts. Combining the above arguments and using Eq. (41) it follows that

$$\tilde{p}_* \leq p_*^{dc} + 2Np_{dc} \tag{76}$$

with p_*^{dc} the p_* estimated in the experiment with dark counts, is a valid upper bound on two (and more) photon contributions in the state $\tilde{\rho} = S_{cd}^{\otimes N}[\rho]$.

To summarize, the value of the witness estimated on an N-mode state ρ with detectors subject to dark counts

$$\langle \hat{\mathcal{W}}_{dc} \rangle = \text{tr}(\hat{\mathcal{W}}_{dc}\,\rho) = \text{tr}(\hat{\mathcal{W}}\, S_{dc}^{\otimes N}[\rho]) \tag{77}$$

corresponds to the values of the original witness (without dark counts) estimated on the state $S_{dc}^{\otimes N}[\rho]$. On the other hand, the biseparable bound for the state $S_{dc}^{\otimes N}[\rho]$ satisfies

$$\begin{aligned}\tilde{w}_{\text{bisep}}^{\max} &= w_{\text{bisep}} + \tilde{p}_* N(N-1)\\ &\leq w_{\text{bisep}} + p_*^{dc} N(N-1) + 2N^2(N-1)p_{dc},\end{aligned} \tag{78}$$

where we used Eq. (76). Here, $w_{\text{bisep}}^{\max+\text{dc}} = w_{\text{bisep}} + p_*^{dc}N(N-1)$ is the biseparable bound estimated in the real experiment (state ρ and dark counts). We can thus conclude that observing

$$\langle \hat{\mathcal{W}}_{dc} \rangle - w_{\text{bisep}}^{\max+\text{dc}} - 2N^2(N-1)p_{dc} \geq 0 \tag{79}$$

implies that the state $S_{dc}^{\otimes N}[\rho]$ is GME by our main result. Since the channel $S_{dc}^{\otimes N}$ describes noise acting locally on each mode and cannot create entanglement, the N-mode state ρ is also GME. This concludes our argument showing that if the detectors used in the experiment suffer from dark counts (that we did not include in their mode), the procedure described in the main text still allows to prove the GME of the measured state, but the observed violation $\langle \hat{\mathcal{W}}_{dc} \rangle - w_{\text{bisep}}^{\max+\text{dc}}$ has to exceed $2N^2(N-1)p_{dc}$. Note that since $\langle \hat{\mathcal{W}}_{dc} \rangle - w_{\text{bisep}}^{\max+\text{dc}}$ scales as N^2 in general, the penalty terms accounting for dark-count scales as $2Np_{dc}$.

In the experiment with $N = 8$, we measured $p_{dc} = 1.16(29) \times 10^{-6}$ for the detector with the highest dark count rate. Therefore, the measured witness violation of $\langle \hat{\mathcal{W}}_{dc} \rangle - w_{\text{bisep}}^{\max+\text{dc}} = 0.207(4)$ is reduced by $2N^2(N-1)p_{dc} = 0.0010(3)$, which still certifies GME with a p-value of 10^{-87}.

For the analysis of the scalability of the presented witness including detector dark counts, we consider a heralded single photon generated by a SPDC source, which state after heralding can be well approximated by

$$\rho = \frac{1}{1+p}(|1\rangle\langle 1| + p|2\rangle\langle 2|) \tag{80}$$

Since losses on the state commute with the beam splitter one can directly apply losses on ρ to account for finite efficiency and obtain ρ_η, which transforms to ρ_η^{BS} after the N-mode beam splitters. The idea in the following is to only consider the reduced density matrix to two modes

$$\sigma_{\{1,2\}} = \text{tr}_{\{3,\ldots,N\}}(\rho_\eta^{BS}), \tag{81}$$

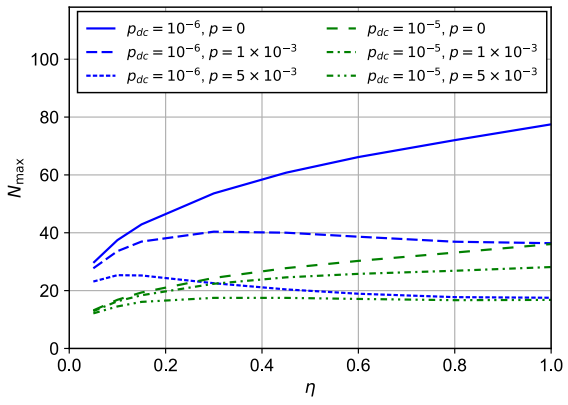

Figure 9: Maximum number of parties $N_{\max}$ for which the witness is still violated as a function of η for a state ρ_η. The scaling behavior is shown for input states $\rho = (|1\rangle\langle 1| + p|2\rangle\langle 2|)/(1+p)$ with $p \in \{0, 1\times10^{-3}, 5\times10^{-3}\}$ that are measured with detectors suffering from dark counts with probabilities per heralding event of $p_{dc} \in \{10^{-6}, 10^{-5}\}$.

which we use to compute

$$\begin{aligned} S_{dc}^{\otimes 2}[\sigma_{\{1,2\}}] &= (1-p_{dc})^2\sigma_{\{1,2\}} \\ &+ p_{dc}(1-p_{dc})(\sigma_1 \otimes |M\rangle\langle M| + |M\rangle\langle M| \otimes \sigma_1) \\ &+ p_{dc}^2 |M,M\rangle\langle M,M|. \end{aligned} \tag{82}$$

Since we consider a perfectly balanced beam splitter, we can evaluate almost all the terms in Eq. (77) only using $S_{dc}^{\otimes 2}[\sigma_{1,2}]$, where the only assumptions we make is that the 3-click events are always negligible over the 2-click events, which holds true for our state.

In Fig. 9, we show the maximum number of parties $N_{\max}$, for which the value $\langle \hat{\mathcal{W}}_{dc}\rangle - w_{\text{bisep}}^{\max+\text{dc}} - 2N^2(N-1)p_{dc}$ is still positive, as a function of η for a state ρ_η^{BS}. In the calculation, the displacement amplitude for the measurement is set to $\alpha = \sqrt{\ln 2} \approx 0.83$ for each party, which is experimentally the most robust to fluctuations in α. In the experiment, the probability of heralding a two-photon Fock state is $p \approx 4.9 \times 10^{-3}$ and the detector with the highest dark count rate has a dark count probability per heralding event of $p_{dc} = 1.16(29) \times 10^{-6}$, which is approximated in the plot by the line $(p, p_{dc}) = (5\times10^{-3}, 10^{-6})$. We notice that in this case for $\eta > 0.05$, we are able to detect GME for more than $N = 17$ parties. We further note that for higher dark count probabilities $N_{\max}$ decreases, and in the case of $p = 0$ the influence of dark counts can be substantial. The witness could be improved by using a different detector model including dark counts, which we leave for further work.

References

[1] H. J. Kimble. The quantum internet. *Nature*, 453(7198):1023–1030, 2008. DOI: 10.1038/nature07127.

[2] S. Wehner, D. Elkouss, and R. Hanson. Quantum internet: a vision for the road ahead. *Science*, 362(6412):eaam9288, 2018. DOI: 10.1126/science.aam9288.

[3] P. Kómár, E. M. Kessler, M. Bishof, L. Jiang, A. S. Sørensen, J. Ye, and M. D. Lukin. A quantum network of clocks. *Nature Physics*, 10(8):582–587, 2014. DOI: 10.1038/nphys3000.

[4] L.-Z. Liu, Y.-Z. Zhang, Z.-D. Li, R. Zhang, X.-F. Yin, Y.-Y. Fei, L. Li, N.-L. Liu, F. Xu, Y.-A. Chen, and J.-W. Pan. Distributed quantum phase estimation with entangled photons. *Nature Photonics*, 15(2):137–142, 2021. DOI: 10.1038/s41566-020-00718-2.

[5] G. Murta, F. Grasselli, H. Kampermann, and D. Bruß. Quantum Conference Key Agreement: A Review. *Advanced Quantum Technologies*, 3(11):2000025, 2020. DOI: 10.1002/qute.202000025.

[6] V. Lipinska, G. Murta, and S. Wehner. Anonymous transmission in a noisy quantum network using the W state. *Physical Review A*, 98(5):052320, 2018. DOI: 10.1103/PhysRevA.98.052320.

[7] H.-S. Zhong, Y. Li, W. Li, L.-C. Peng, Z.-E. Su, Y. Hu, Y.-M. He, X. Ding, W. J. Zhang, H. Li, L. Zhang, Z. Wang, L. X. You, X.-L. Wang, X. Jiang, L. Li, Y.-A. Chen, N.-L. Liu, C.-Y. Lu, and J.-W. Pan. 12-photon entanglement and scalable scattershot boson sampling with optimal entangled-photon pairs from parametric down-conversion. *Physical Review Letters*, 121(25):250505, 2018. DOI: 10.1103/PhysRevLett.121.250505.

[8] D. F. V. James, P. G. Kwiat, W. J. Munro, and A. G. White. Measurement of qubits. *Physical Review A*, 64(5):052312, 2001. DOI: 10.1103/PhysRevA.64.052312.

[9] N. Sangouard, C. Simon, H. de Riedmatten, and N. Gisin. Quantum repeaters based on atomic ensembles and linear optics. *Reviews of Modern Physics*, 83(1):33–80, 2011. DOI: 10.1103/RevModPhys.83.33.

[10] L.-M. Duan, M. D. Lukin, J. I. Cirac, and P. Zoller. Long-distance quantum communication with atomic ensembles and linear optics. *Nature*, 414(6862):413–418, 2001. DOI: 10.1038/35106500.

[11] C. Simon, H. de Riedmatten, M. Afzelius, N. Sangouard, H. Zbinden, and N. Gisin. Quantum repeaters with photon pair sources and multimode memories. *Phys. Rev. Lett.*, 98:190503, 19, 2007. DOI: 10.1103/PhysRevLett.98.190503.

[12] J. Minář, H. de Riedmatten, C. Simon, H. Zbinden, and N. Gisin. Phase-noise measurements in long-fiber interferometers for quantum-repeater applications. *Phys. Rev. A*, 77:052325, 5, 2008. DOI: 10.1103/PhysRevA.77.052325.

[13] C.-W. Chou, H. de Riedmatten, D. Felinto, S. V. Polyakov, S. J. Van Enk, and H. J. Kimble. Measurement-induced entanglement for excitation stored in remote atomic ensembles. *Nature*, 438(7069):828–832, 2005. DOI: 10.1038/nature04353.

[14] L. Slodička, G. Hétet, N. Röck, P. Schindler, M. Hennrich, and R. Blatt. Atom-atom entanglement by single-photon detection. *Phys. Rev. Lett.*, 110:083603, 8, 2013. DOI: 10.1103/PhysRevLett.110.083603.

[15] A. Delteil, Z. Sun, W. B. Gao, E. Togan, S. Faelt, and A. Imamoglu. Generation of heralded entanglement between distant hole spins. *Nature Physics*, 12(3):218–223, 2016. DOI: 10.1038/nphys3605.

[16] R. Stockill, M. J. Stanley, L. Huthmacher, E. Clarke, M. Hugues, A. J. Miller, C. Matthiesen, C. Le Gall, and M. Atatüre. Phase-tuned entangled state generation between distant spin qubits. *Phys. Rev. Lett.*, 119:010503, 1, 2017. DOI: 10.1103/PhysRevLett.119.010503.

[17] P. C. Humphreys, N. Kalb, J. P. J. Morits, R. N. Schouten, R. F. L. Vermeulen, D. J. Twitchen, M. Markham, and R. Hanson. Deterministic delivery of remote entanglement on a quantum network. *Nature*, 558(7709):268–273, 2018. DOI: 10.1038/s41586-018-0200-5.

[18] D. Lago-Rivera, S. Grandi, J. V. Rakonjac, A. Seri, and H. de Riedmatten. Telecom-heralded entanglement between multimode solid-state quantum memories. *Nature*, 594(7861):37–40, 2021. DOI: 10.1038/s41586-021-03481-8.

[19] P. Caspar, E. Verbanis, E. Oudot, N. Maring, F. Samara, M. Caloz, M. Perrenoud, P. Sekatski, A. Martin, N. Sangouard, H. Zbinden, and R. T. Thew. Heralded distribution of single-photon path entanglement. *Phys. Rev. Lett.*, 125:110506, 11, 2020. DOI: 10.1103/PhysRevLett.125.110506.

[20] Y. Yu, F. Ma, X.-y. Luo, B. Jing, P.-f. Sun, R.-z. Fang, C.-w. Yang, H. Liu, M.-Y. Zheng, X.-P. Xie, W.-J. Zhang, L.-X. You, Z. Wang, T.-Y. Chen, Q. Zhang, X.-H. Bao, and J.-W. Pan. Entanglement of two quantum memories via fibres over dozens of kilometres. *Nature*, 578(7794):240–245, 2020. DOI: 10.1038/s41586-020-1976-7.

[21] W. Dür, G. Vidal, and J. I. Cirac. Three qubits can be entangled in two inequivalent ways. *Physical Review A*, 62(6):062314, 2000. DOI: 10.1103/PhysRevA.62.062314.

[22] D. Gottesman, T. Jennewein, and S. Croke. Longer-Baseline Telescopes Using Quantum Repeaters. *Physical Review Letters*, 109(7):070503, 2012. DOI: 10.1103/PhysRevLett.109.070503.

[23] E. T. Khabiboulline, J. Borregaard, K. De Greve, and M. D. Lukin. Optical Interferometry with Quantum Networks. *Physical Review Letters*, 123(7):070504, 2019. DOI: 10.1103/PhysRevLett.123.070504.

[24] E. T. Khabiboulline, J. Borregaard, K. De Greve, and M. D. Lukin. Quantum-assisted telescope arrays. *Physical Review A*, 100(2):022316, 2019. DOI: 10.1103/PhysRevA.100.022316.

[25] O. Morin, J.-D. Bancal, M. Ho, P. Sekatski, V. D'Auria, N. Gisin, J. Laurat, and N. Sangouard. Witnessing trustworthy single-photon entanglement with local homodyne measurements. *Phys. Rev. Lett.*, 110:130401, 13, 2013. DOI: 10.1103/PhysRevLett.110.130401.

[26] F. Monteiro, V. C. Vivoli, T. Guerreiro, A. Martin, J.-D. Bancal, H. Zbinden, R. T. Thew, and N. Sangouard. Revealing genuine optical-path entanglement. *Phys. Rev. Lett.*, 114:170504, 17, 2015. DOI: 10.1103/PhysRevLett.114.170504.

[27] S. B. Papp, K. S. Choi, H. Deng, P. Lougovski, S. J. van Enk, and H. J. Kimble. Characterization of Multipartite Entanglement for One Photon Shared Among Four Optical Modes. *Science*, 324(5928):764–768, 2009. DOI: 10.1126/science.1172260.

[28] M. Gräfe, R. Heilmann, A. Perez-Leija, R. Keil, F. Dreisow, M. Heinrich, H. Moya-Cessa, S. Nolte, D. N. Christodoulides, and A. Szameit. On-chip generation of high-order single-photon W-states. *Nature Photonics*, 8(10):791–795, 2014. ISSN: 17494893. DOI: 10.1038/nphoton.2014.204.

[29] M. G. A. Paris. Displacement operator by beam splitter. *Physics Letters A*, 217(2):78–80, 1996. DOI: 10.1016/0375-9601(96)00339-8.

[30] V. C. Vivoli, P. Sekatski, J.-D. Bancal, C. C. W. Lim, A. Martin, R. T. Thew, H. Zbinden, N. Gisin, and N. Sangouard. Comparing different approaches for generating random numbers device-independently using a photon pair source. *New Journal of Physics*, 17(2):023023, 2015. DOI: 10.1088/1367-2630/17/2/023023.

[31] W. Hoeffding. Probability Inequalities for Sums of Bounded Random Variables. *Journal of the American Statistical Association*, 58(301):13–30, 1963. DOI: 10.1080/01621459.1963.10500830.

[32] N. Bruno, A. Martin, and R. T. Thew. Generation of tunable wavelength coherent states and heralded single photons for quantum optics applications. *Optics Communications*, 327:17–21, 2014. DOI: 10.1016/j.optcom.2014.02.025.

[33] M. Caloz, M. Perrenoud, C. Autebert, B. Korzh, M. Weiss, C. Schönenberger, R. J. Warburton, H. Zbinden, and F. Bussières. High-detection efficiency and low-timing jitter with amorphous superconducting nanowire single-photon detectors. *Applied Physics Letters*, 112(6), 2018. DOI: 10.1063/1.5010102.

[34] P. J. Mosley. *Generation of Heralded Single Photons in Pure Quantum States*. PhD thesis, University of Oxford, 2007. URL: https://ora.ox.ac.uk/objects/uuid:44c36e1e-11ee-41e2-ba29-611c932ce4ff.

P.3. Benchmarking single-photon sources from an auto-correlation measurement

Benchmarking single-photon sources from an auto-correlation measurement

Pavel Sekatski[1], Enky Oudot[2], Patrik Caspar[1], Rob Thew[1], and Nicolas Sangouard[3]

[1]Department of Applied Physics, University of Geneva, Geneva, Switzerland

[2]ICFO - Institut de Ciencies Fotoniques, The Barcelona Institute of Science and Technology, 08860 Castelldefels (Barcelona), Spain

[3]Université Paris-Saclay, CEA, CNRS, Institut de physique théorique, 91191, Gif-sur-Yvette, France

Here we argue that the probability that a given source produces exactly a single photon is a natural quantity to benchmark single-photon sources as it certifies the absence of multi-photon components and quantifies the efficiency simultaneously. Moreover, this probability can be bounded simply from an auto-correlation measurement – a balanced beam splitter and two photon detectors. Such a bound gives access to various non-classicality witnesses that can be used to certify and quantify Wigner-negativity, in addition to non-Gaussianity and P-negativity of the state produced by the source. We provide tools that can be used in practice to account for an imperfect beam splitter, non-identical and non-unit detection efficiencies, dark counts and other imperfections, to take finite statistical effects into account without assuming that identical states are produced in all rounds, and optionally allow one to remove the detector inefficiencies from the analysis. We demonstrate the use of the proposed benchmark, non-classicality witness and measure using a heralded single-photon source based on spontaneous parametric down-conversion. We report on an average probability that a single photon is produced $\geq 55\%$ and an average measure of the Wigner negativity ≥ 0.004 with a confidence level of $1-10^{-10}$.

1 Introduction

Single-photon sources [1, 2] are key resources for quantum communication [3], photonic quantum computation [4] or radiometry [5, 6]. Not all single-photon sources are alike and to be scaled up, most applications require efficient sources of true single photons (single-photon Fock/number states). The quality of single-photon sources is usually quantified from an auto-correlation measurement [7], that is, by sending the photons to a balanced beam splitter and checking that the ratio between the detected twofold coincidences and the product of singles vanishes, see Fig. 1 and the discussion in Appendix A. This ensures that the source produces no more than one photon. The result is, however, insensitive to loss as the efficiency cancels out of the ratio. These two aspects – the capacity of a source to produce no more than one photon and its efficiency – are thus considered separately. Both aspects are, however, important and are quantified jointly by the probability that the source actually produces exactly a single photon. Characterizing this probability is a direct and more complete way to benchmark single-photon sources.

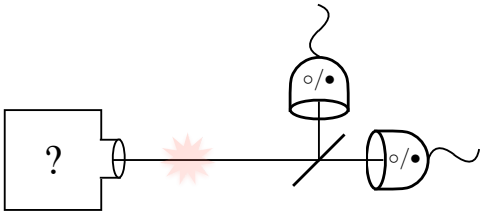

Figure 1: Schematic representation of the measurement that is considered to characterize an unknown photon source which supposedly produces single photons. It is realized with a beam splitter and two non-photon-number-resolving detectors, as in a standard auto-correlation measurement. At each round, each detector either clicks • or not ◦. By analyzing the frequency of these events, the probability that the source actually produces exactly a single photon can be lower bounded. Furthermore, if a single radiation mode is detected, various forms of non-classicality can be witnessed and quantified.

Interestingly, this probability can be bounded by reconsidering the statistics of detector counts in an auto-correlation measurement. This suggests a systematic way to benchmark the quality and quantify the efficiency of single-photon sources, and to witness and quantify their quantum nature. To motivate benchmarking single-photon sources by the probability that the source actually produces exactly a single photon, we provide a detailed analysis which includes a simple statistical tool to account for finite-size effects without assuming that identical states were produced in all rounds of the experiment. We show how to include imperfections in the measurements apparatus and how to remove the detector ef-

Pavel Sekatski: pavel.sekatski@unige.ch
Rob Thew: robert.thew@unige.ch

ficiencies from the analysis to facilitate the use of the proposed benchmark. An experimental demonstration is presented, illustrating the quality of heralded single-photon sources based on spontaneous parametric down-conversion.

The auto-correlation measurement is also known to be valuable for witnessing various forms of non-classicality, including the non-positivity of the P-distribution and quantum non-Gaussianity [8–10]. Here we show that for single-mode states or measurements a bound on the single-photon probability can be readily used to quantify the negativity of the Wigner representation [7], the strongest form of non-classicality, with respect to a measure proposed in [11]. We apply this method to verify Wigner-negativity in the reported experiments.

2 Measurement apparatus

The measurement apparatus we consider is similar to the one used for the second order auto-correlation measurement. It is a simple measurement consisting of sending the photonic state to be measured (labeled ρ) on to a beam splitter and recording the photon-count correlations between the two outputs, see Fig. 1. We consider that photon detections are made with typical non-photon-number-resolving detectors. In order to draw conclusions from such photon-counts, we introduce a simple quantum model for such a measurement setup. A non-photon-number-resolving detector of efficiency η can be modeled with a two element positive operator-valued measure (POVM) $\{E_\bullet, E_\circ\}$ corresponding to click ($\bullet$) and no-click ($\circ$) outcomes. When the measurement acts on a single mode characterized by bosonic operators a and $a^\dagger$, the POVM elements take the following form

$$E_\circ = (1-\eta)^{a^\dagger a}, \qquad E_\bullet = \mathbb{1} - (1-\eta)^{a^\dagger a}. \tag{1}$$

This model describes a non-photon-number-resolving detector, for which every incident photon can trigger the detection event with probability η. The no-click outcome then corresponds to the event where none of the incident photons triggered a click, and occurs with probability $p_\circ = \mathrm{tr}\,\rho\,(1-\eta)^{a^\dagger a}$, see e.g. [12]. From now on we assume that the detectors are accurately described by Eq. (1) for *some value* of η. In section 3.1.4 we will discuss how to account for small deviation from this model.

When two such detectors are placed after a beam splitter with reflectance r (transmittance t), it is straightforward to see that the four possible outcomes are given by the POVM elements

$$\begin{aligned} E_{\circ\circ} &= (1-\eta)^{a^\dagger a} \\ E_{\bullet\circ} &= (1-\eta\,t)^{a^\dagger a} - (1-\eta)^{a^\dagger a} \\ E_{\circ\bullet} &= (1-\eta\,r)^{a^\dagger a} - (1-\eta)^{a^\dagger a} \\ E_{\bullet\bullet} &= \mathbb{1} - E_{\circ\circ} - E_{\bullet\circ} - E_{\circ\bullet}, \end{aligned} \tag{2}$$

where the first (second) label $\circ/\bullet$ refers to the detector after the reflected (transmitted) output of the beam splitter, see Appendix B for a formal derivation. The events where a fixed detector does not click are modeled by the two POVM elements $E_{\circ\_} = E_{\circ\bullet} + E_{\circ\circ} = (1-\eta\,r)^{a^\dagger a}$ and $E_{\_\circ} = (1-\eta\,t)^{a^\dagger a}$. The corresponding probabilities are labeled $p_{\circ\_}$ and $p_{\_\circ}$. Note that the case where the two detectors do not have the same efficiency $\eta_R \neq \eta_T$ can be accounted for by replacing t with $t' = \frac{t\eta_T}{t\eta_T + r\eta_R}$, r with $r' = \frac{r\eta_R}{t\eta_T + r\eta_R}$, and setting $\eta = t\eta_T + r\eta_R$ in Eq. (2).

3 Benchmarking a single-photon source

For simplicity, through the main part of this section we will be considering the case of single-mode sources. In section 3.3, we show that all the presented tools also apply to multi-mode sources.

With the measurement we just described, any single-mode state ρ incident on the beam splitter can be associated with a probability vector

$$\boldsymbol{p} = (p_{\circ\circ}, p_{\bullet\circ}, p_{\circ\bullet}, p_{\bullet\bullet}) \tag{3}$$

governing the occurrence of clicks. Our goal is to construct an estimator $\hat{P}_1(\boldsymbol{p})$ that relates this vector $\boldsymbol{p}$ to the photon number statistics of the state and in particular to the weight of the single-photon component $P_1 = \langle 1|\,\rho\,|1\rangle$. Directly lower bounding P_1 is a natural way to benchmark a single-photon source. In particular, it sets a bound on the trace distance between the state ρ prepared by the source and an ideal single photon $|1\rangle$

$$\frac{1}{2}\,\|\rho - |1\rangle\langle 1|\,\|_1 \leq 1 - P_1, \tag{4}$$

which can be readily used to bound the errors for various applications of single-photon sources.

3.1 Measurement calibration independent benchmark

We proceed step by step, considering first an ideal measurement apparatus, then considering two identical non-unit detector efficiencies and finally focusing on the most imperfect measurement, where we consider an unbalanced beam splitter and two detectors having different efficiencies. At this point we only assume that the measurement is described by the POVM in Eq. (2) for *some* parameters η, t and r, that do not need to be known. The benchmark that we will derive in this section is thus independent of the calibration of the measurement apparatus. Finally, we show that by adding a small correction term our benchmark can be applied in situations where the POVM in Eq. (2) is only an approximate description of the measurement apparatus.

3.1.1 Ideal measurement apparatus

For clarity, we first assume that the source produces an identical state ρ at each round, the detectors have unit detection efficiency $\eta = 1$ and the beam splitter is balanced $t = r = 1/2$. In this ideal case, the probabilities $p_{\bullet\circ}$, $p_{\circ\bullet}$ are equal, and $\boldsymbol{p}$ is described by two independent real parameters. For convenience, we introduce $p_\bullet = p_{\bullet\circ} + p_{\circ\bullet}$ the probability to get exactly one click. The probabilities that a given detector does not click $p_{\circ\_} = p_{\circ\circ} + p_{\circ\bullet}$ and $p_{\_\circ} = p_{\circ\circ} + p_{\bullet\circ}$ are equal in the ideal case and in particular $p_{\circ\_} = p_{\_\circ} = p_{\circ\circ} + \frac{1}{2}p_\bullet$. This means that the probabilities of outcomes of the measurement of interest can be fully captured by $(p_{\circ\_}, p_{\circ\circ})$. Let

$$P_n = \langle n| \rho |n\rangle \tag{5}$$

be the weight of the n-photon Fock state component of the measured state. For $\eta = 1$, the no-click events can only come from the vacuum state $E_{\circ\circ} = |0\rangle\langle 0|$, hence the probabilities $(p_{\circ\_}, p_{\circ\circ})$ can be linked to the photon number distribution P_n. From Eqs. (2), one gets $p_{\circ\circ} = P_0$ and $p_{\circ\_} = \sum_n P_n \frac{1}{2^n}$.

The question we ask now is very simple – what are the values $(p_{\circ\_}, p_{\circ\circ})$ that are obtainable for states ρ satisfying $P_1 \leq P$, for some parameter $P \in [0, 1]$?

First, we note that $p_{\circ\_} \geq p_{\circ\circ}$ holds by definition. Furthermore, the points $(1, 1)$ and $(0, 0)$ are attained by the vacuum and the state with infinitely many photons, respectively. Thus, the line $p_{\circ\_} = p_{\circ\circ}$ is also attainable by mixtures of aforementioned states. Then, we look for the maximum value of $p_{\circ\_} = \sum_n P_n \frac{1}{2^n}$ for a fixed $p_{\circ\circ}$. We have to solve

$$\begin{aligned} p^{\uparrow}_{\circ\_}(p_{\circ\circ}, P) = \max_{\rho} & \sum_n P_n \frac{1}{2^n} \\ \text{such that} \quad & P_1 \leq P \\ & P_0 = p_{\circ\circ}. \end{aligned} \tag{6}$$

As $(1/2)^n$ is decreasing with n, the maximum is attained by saturating the values of P_n starting with P_0. Hence, it equals

$$p_{\circ\_} \leq p^{\uparrow}_{\circ\_}(p_{\circ\circ}, P) = \begin{cases} \frac{1+p_{\circ\circ}}{2} & 1 - p_{\circ\circ} \leq P \\ \frac{1+P+3p_{\circ\circ}}{4} & 1 - p_{\circ\circ} > P \end{cases} \tag{7}$$

The set of possible values $(p_{\circ\_}, p_{\circ\circ})$ is thus included in a convex polytope with four vertices $\boldsymbol{Q}_P = \text{Polytope}\{(0,0), \left(\frac{1+P}{4}, 0\right), \left(\frac{2-P}{2}, 1-P\right), (1,1)\}$, sketched in Fig. 2. The only nontrivial facet of this polytope is the edge connecting $\left(\frac{1+P}{4}, 0\right)$ and $\left(\frac{2-P}{2}, 1-P\right)$ which is associated to the inequality $4p_{\circ\_} - 3p_{\circ\circ} - 1 \leq P$, and is given by the colored lines in Fig. 2. Thus, without loss of generality, the condition $\langle 1| \rho |1\rangle \leq P$ implies that the elements of $\boldsymbol{p}$ satisfy the linear constraint

$$\hat{P}_1^T(\boldsymbol{p}) = 4p_{\circ\_} - 3p_{\circ\circ} - 1 \leq P. \tag{8}$$

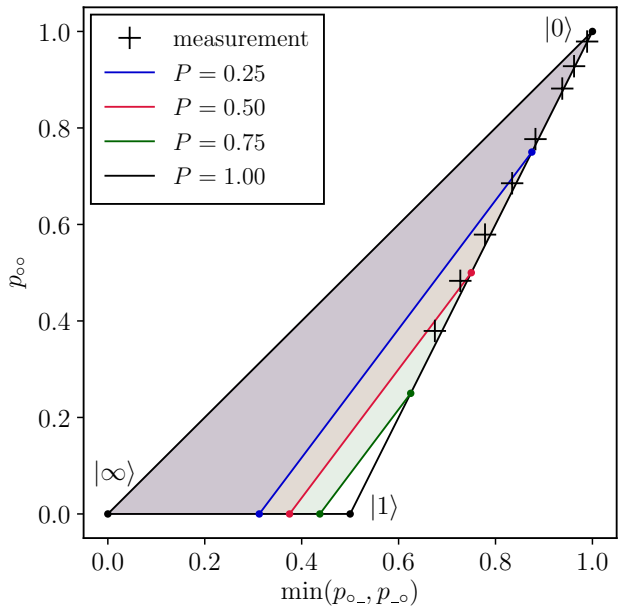

Figure 2: Representation of the polytopes $\boldsymbol{Q}_P$ (defined after Eq. (7)) containing all possible values $(\min(p_{\circ\_}, p_{\_\circ}), p_{\circ\circ})$ associated to states ϱ with $\langle 1| \varrho |1\rangle \leq P$. There are four polytopes $\boldsymbol{Q}_P$ for the values $P \in \{0.25, 0.5, 0.75, 1\}$. The physically possible region $\boldsymbol{Q}_{P=1}$ is given by the black triangle. The regions for $P = 0.25, 0.5, 0.75$ are given by the part of the black triangle above the corresponding colored line. The black crosses are measurements of $(\min(p_{\circ\_}, p_{\_\circ}), p_{\circ\circ})$ for a heralded single photon undergoing different added attenuation corresponding to transmission efficiencies of $\eta_{\text{att}} \in \{1.0, 0.83, 0.68, 0.51, 0.36, 0.19, 0.12, 0.034\}$.

Conversely, by measuring the pair $(p_{\circ\_}, p_{\circ\circ})$ and by computing the resulting value of $\hat{P}_1^T$, we can guarantee that for any value of P such that $\hat{P}_1^T > P$, $\langle 1| \rho |1\rangle > P$ holds, that is we get a lower bound on the probability that the source to be benchmarked produces exactly a single photon.

3.1.2 Identical non-unit efficiency detectors

To move away from the ideal case, we still consider a perfectly balanced beam splitter and focus on a situation where non-unit efficiency detectors are used. We consider the case where the detector efficiency η is unknown. In the measurement setup shown in Fig. 1, non-unit efficiency detectors can be modeled by taking ideal detectors and placing a beam splitter with transmission η before the balanced beam splitter. As a consequence, observing a violation of Ineq. (8) proves that the state produced by the single-photon source *and undergoing losses* satisfies $\langle 1| \varrho |1\rangle \geq \hat{P}_1^T(\boldsymbol{p})$. This provides a valid benchmark even though the intrinsic quality of the source is estimated with a lossy measurement apparatus. It is interesting to note that for any state ρ with $P_1 \geq 2/3$, the probability of the single-photon weight P_1 can only decrease with loss, see Appendix C. Therefore, showing that $P_1 \geq 2/3$ with lossy detectors implies that the original state also

satisfies $P_1 \geq \frac{2}{3}$. This is not the case when $P_1 < 2/3$, i.e. for specific states the single-photon weight P_1 can be increased by loss (an intuitive example is the two-photon Fock state).

3.1.3 Unbalanced beam splitter and different non-unit efficiency detectors

We now relax the assumptions that the beam splitter is balanced and the detector efficiencies are the same, i.e. we consider the case with a measurement performed with a beam splitter having an unknown transmission t and reflection $r = 1 - t$ and two detectors having different efficiencies labeled η_R and η_T. In this case, the observed statistics would be equivalently obtained with a beam splitter having a transmission coefficient $t' = t\eta_T/(t\eta_T + r\eta_R)$ and two detectors with the same efficiency $\eta = t\eta_T + r\eta_R$, as already mentioned below Eq. (2). This means that the measurement can be modeled with a first unbalanced beam splitter with transmission coefficient η corresponding to loss on the state to be characterized, an unbalanced beam splitter with transmission t' and two detectors with unit detection efficiency. In this case, the relation between $p_{\circ\circ}$ and P_0 is unchanged, i.e. $p_{\circ\circ} = P_0$. The probabilities $p_{\circ\_} = p_{\circ\bullet} + p_{\circ\circ}$ and $p_{\_\circ} = p_{\bullet\circ} + p_{\circ\circ}$ are however no longer the same. They are now given by $p_{\circ\_} = \sum_n P_n(1-r')^n$ and $p_{\_\circ} = \sum_n P_n(1-t')^n$. Hence, the quantity $\sum_n P_n \frac{1}{2^n}$ is no longer directly related to the probability $\boldsymbol{p}$. Nevertheless, it can be bounded from observable quantities, as $\sum_n P_n \frac{1}{2^n} \geq \min(p_{\circ\_}, p_{\_\circ})$.

We introduce $\hat{P}_1^R(\boldsymbol{p})$ which is defined analogously to $\hat{P}_1^T(\boldsymbol{p})$ by $\hat{P}_1^R(\boldsymbol{p}) = 4p_{\_\circ} - 3p_{\circ\circ} - 1$. Using the definition of $p_{\circ\_}$ and $p_{\_\circ}$, we rewrite them in terms of probabilities of disjoint events as

$$\begin{aligned} \hat{P}_1^T(\boldsymbol{p}) &= 4p_{\circ\bullet} + p_{\circ\circ} - 1 \\ \hat{P}_1^R(\boldsymbol{p}) &= 4p_{\bullet\circ} + p_{\circ\circ} - 1. \end{aligned} \tag{9}$$

With this notation in hand, we conclude that the quantity

$$\hat{P}_1(\boldsymbol{p}) = \min\{\hat{P}_1^T(\boldsymbol{p}), \hat{P}_1^R(\boldsymbol{p})\} \tag{10}$$

is a benchmark for single-photon sources, without assumptions on the detector efficiencies and on the fact that the beam splitter is balanced. This means that from the outcome probabilities $\boldsymbol{p}$ of a usual auto-correlation measurement, we can compute $\hat{P}_1^T(\boldsymbol{p})$ and $\hat{P}_1^R(\boldsymbol{p})$, deduce their minimum $\hat{P}_1(\boldsymbol{p})$ and guarantee the tested source produces states with the weight of the single-photon component satisfying $P_1 = \langle 1|\,\rho\,|1\rangle \geq \hat{P}_1(\boldsymbol{p})$.

3.1.4 Dark counts and other imperfections

Finally let us briefly consider general passive detectors described by a POVM

$$\tilde{E}_\circ = \sum_{n\geq 0} e_\circ(n)\,|n\rangle\langle n| \quad \text{and} \quad \tilde{E}_\bullet = \sum_{n\geq 0} e_\bullet(n)\,|n\rangle\langle n|\,, \tag{11}$$

where $e_\circ(n)+e_\bullet(n) = 1$. Consider combining two such detectors in the $g^{(2)}$ setup, with the POVM $\{\tilde{E}_{\circ/\bullet}\}$ performed on the transmitted mode and $\{\tilde{E}'_{\circ/\bullet}\}$ on the reflected one. The resulting POVM elements for $a, b = \circ, \bullet$ read

$$\tilde{E}_{ab} = \sum_{n\geq 0}\sum_{k=0}^{n} \mathrm{P}_{\mathrm{BS}}(k|n)\, e_a(k)e'_b(n-k)\,|k, n-k\rangle\langle k, n-k|\,. \tag{12}$$

with $\mathrm{P}_{\mathrm{BS}}(k|n) = \binom{n}{k} t^k r^{n-k}$.

Now let us assume these detectors are not too different from the textbook single-photon detector model of Eq. (1). Concretely we assume that for some η, t and r

$$\left|\mathrm{tr}\big(\tilde{E}_{ab} - E_{ab}\big)\rho\right| \leq \Delta, \tag{13}$$

where ρ can be any state susceptible to be prepared in the experiment. In particular, consider the case where both detectors satisfy

$$\begin{aligned} |e_\circ(n) - (1-\eta)^n| &\leq \delta \\ |e'_\circ(n) - (1-\eta')^n| &\leq \delta' \end{aligned} \tag{14}$$

for some η, η', and all n on which the input state is supported. For $a = b = \circ$ we then find $|e_\circ(k)e'_\circ(n-k) - (1-\eta)^k(1-\eta')^{n-k}| \leq \delta + \delta' + \delta\delta'$ in Eq. (12). Similar inequalities hold for the other possible outcomes $\circ\bullet$,$\bullet\circ$ and $\bullet\bullet$, and lead to the bound of Eq. (13) with

$$\Delta = \delta + \delta' + \delta\delta'. \tag{15}$$

It follows that the probabilities $\tilde{\boldsymbol{p}} = (\tilde{p}_{\circ\circ}, \tilde{p}_{\circ\bullet}, \tilde{p}_{\bullet\circ}, \tilde{p}_{\bullet\bullet})$ observed with these detectors described by $\{\tilde{E}_{\circ/\bullet}\}$ and $\{\tilde{E}'_{\circ/\bullet}\}$, are close to the probabilities $\boldsymbol{p} = (p_{\circ\circ}, p_{\circ\bullet}, p_{\bullet\circ}, p_{\bullet\bullet})$ that would have been observed with textbook detectors, concretely

$$|\tilde{p}_{ab} - p_{ab}| \leq \Delta. \tag{16}$$

With the help of Eq. (9) it is then straightforward to lower bound the value of the benchmark

$$\hat{P}_1(\boldsymbol{p}) \geq \min\{\hat{P}_1^T(\tilde{\boldsymbol{p}}), \hat{P}_1^R(\tilde{\boldsymbol{p}})\} - 5\Delta. \tag{17}$$

given the coincidence probabilities $\tilde{\boldsymbol{p}}$ observed with any detectors abiding to Eq. (13).

Here, it is worth noting that the POVM model of Eq. (1) does not account for dark counts. These can be modeled by setting a nonzero click probability for the vacuum $e_\bullet(0) = p_{\mathrm{dc}}$, implying $|e_\circ(n) - (1-\eta)^n| \leq$

$\delta = p_{\mathrm{dc}}$. Then accordingly to Eqs. (15,17), to account for the effect of dark counts one can use the bound

$$\hat{P}_1(\boldsymbol{p}) \geq \min\{\hat{P}_1^T(\tilde{\boldsymbol{p}}), \hat{P}_1^R(\tilde{\boldsymbol{p}})\} - 10\, p_{\mathrm{dc}}, \tag{18}$$

where we only took the leading order correction in p_{dc}, which is typically fairly small.

3.2 Measurement calibration dependent benchmark

The benchmark we proposed relies on no assumption on the characteristics of the beam splitter or the two detectors used in the auto-correlation measurement. This prevents a miscalibration of the measurement apparatus that could result in an overestimation of the quality of the single-photon source. Nevertheless, as one would expect, the bound on the quality of the tested source (see Eq. (10)) is reduced when using an unbalanced beam splitter or inefficient detectors. We now discuss a way to characterize the intrinsic quality of the source by making additional assumptions on the measurement apparatus. The basic idea is to exploit estimations of different losses in photonic experiments. In particular, we assume that the detector efficiencies $\eta_{R(T)}$ and the beam splitter reflectivity r are bounded, that is $\eta_{R(T)} \leq \hat{\eta}_{R(T)}$ and $r \in [1-\hat{t}, \hat{r}]$. We show in Appendix D that the condition $\langle 1|\,\rho\,|1\rangle \leq P$ implies that the two following inequalities hold

$$\begin{aligned}
\hat{P}_1^{T*}(\boldsymbol{p}) &= C_1(\hat{t}, \hat{\eta}_T) p_{\circ\bullet} - C_2(\hat{t}, \hat{\eta}_T, \hat{\eta}_R) p_{\bullet\bullet} \leq P, \\
\hat{P}_1^{R*}(\boldsymbol{p}) &= C_1(\hat{r}, \hat{\eta}_R) p_{\bullet\circ} - C_2(\hat{r}, \hat{\eta}_R, \hat{\eta}_T) p_{\bullet\bullet} \leq P,
\end{aligned} \tag{19}$$

where the coefficients C_1 and C_2, defined as

$$\begin{aligned}
C_1(x, \eta) &= \frac{1}{x\,\eta} \\
C_2(x, \eta_1, \eta_2) &= \frac{1}{x\,\eta_1}\left(\frac{2 - x\,\eta_1}{2(1-x)\eta_2} - 1\right)
\end{aligned} \tag{20}$$

have been optimized such that $\hat{P}_1^{T*}(\boldsymbol{p})$ and $\hat{P}_1^{R*}(\boldsymbol{p})$ give the tightest bound on P. Finally, one can choose the best among the two bounds, giving rise to the benchmark

$$\hat{P}_1^*(\boldsymbol{p}) = \max\{\hat{P}_1^{T*}(\boldsymbol{p}), \hat{P}_1^{R*}(\boldsymbol{p})\} \leq P_1 \tag{21}$$

for the single-photon probability, which takes advantage of the additional experimental knowledge.

Again we can account for deviations of the POVMs $\{\tilde{E}_{\circ/\bullet}\}$ and $\{\tilde{E}'_{\circ/\bullet}\}$ describing the detectors form the textbook model of Eq. (1), as quantified by Eq. (15). Repeating the analysis of Sec. 3.1.4, we obtain the bounds

$$\begin{aligned}
\hat{P}_1^{T*}(\boldsymbol{p}) &\geq \hat{P}_1^{T*}(\tilde{\boldsymbol{p}}) - (C_1(\hat{t}, \hat{\eta}_T) + |C_2(\hat{t}, \hat{\eta}_T, \hat{\eta}_R)|)\Delta \\
\hat{P}_1^{R*}(\boldsymbol{p}) &\geq \hat{P}_1^{R*}(\tilde{\boldsymbol{p}}) - (C_1(\hat{r}, \hat{\eta}_R) + |C_2(\hat{r}, \hat{\eta}_R, \hat{\eta}_T)|)\Delta.
\end{aligned} \tag{22}$$

To account for dark counts one may use $\Delta = 2p_{\mathrm{dc}}$. Recall that here $\tilde{\boldsymbol{p}} = (\tilde{p}_{\circ\circ}, \tilde{p}_{\circ\bullet}, \tilde{p}_{\bullet\circ}, \tilde{p}_{\bullet\bullet})$ is the vector of probabilities observed with the real detectors, while $\boldsymbol{p}$ gives the probabilities that would have been observed with the textbook model and that are used in the benchmark.

3.3 Multi-mode sources

We have so far considered sources emitting light in a single mode, or equivalently that the emitted light is filtered in all the auxiliary degrees of freedom so that a single mode of light is detected. We will now briefly consider the situation where the detected state is multi-mode, each mode being associated to an annihilation operator a_k satisfying $[a_k, a_\ell^\dagger] = \delta_{k\ell}$. The no-click and click events for a multi-mode input are associated to the POVM elements $E_\circ = \bigotimes_k (1-\eta)^{a_k^\dagger a_k}$ and $E_\bullet = \mathbb{1} - E_\circ$ – a detector does not click only if none of the modes triggers a click. To a multi-mode state ρ one associates the distribution P_n of the *total photon number* operator $\hat{n} = \sum_k a_k^\dagger a_k$. Assuming that the beam splitter acts identically on all modes, the measurement apparatus is only sensitive to the total number of photons $\hat{n}$. That is, the POVM elements $\{E_{\circ\circ}, E_{\circ\bullet}, E_{\bullet\circ}, E_{\bullet\bullet}\}$ are given by Eq. (2) albeit with $a^\dagger a$ replaced by $\hat{n}$, see Appendix B. We thus conclude that the quantities $\hat{P}_1(\boldsymbol{p})$ and $\hat{P}_1^*(\boldsymbol{p})$ that have been derived, can be readily used to benchmark the probability that a multi-mode source emits a single photon

$$P_1 = \mathrm{tr}\left(\varrho \sum_k a_k^\dagger\, |0\rangle\langle 0|\, a_k\right). \tag{23}$$

It is worth noting that a high P_1 for a multi-mode source does not guarantee that the single-photon probability is high in any of the individual modes. As a practical example, consider the multi-mode single-photon state

$$\varrho = \frac{1}{N}\sum_{j=1}^{N} a_j^\dagger\, |0\rangle\langle 0|\, a_j. \tag{24}$$

This state has exactly one photon in total $\hat{n} = 1$. Nevertheless, it is not a good *single-mode* single-photon state. The probability to find exactly one photon in any single mode is only $1/N$, therefore two such states would only exhibit a limited two-photon interference (bunching). In other words ϱ is not a pure single-photon state $|1\rangle\langle 1|_1$, the degree of freedom that distinguishes between the different modes is in a highly mixed states. Depending on the application, the mode-purity (or single-mode character) of the source may be either irrelevant (e.g. for some quantum random number generators) if the interference between different sources plays no role, or crucial (e.g. quantum repeaters, boson sampling or photonic quantum computation) if it is at the heart of the task.

In Appendix G, we show that one can guarantee that the source produces a single-mode state with high P_1 if it is reasonable to assume that the multi-mode state is a product $\varrho = \bigotimes_k \rho_k$. In general, however, the auto-correlation measurement is intrinsically insensitive to the multi-mode characteristics of the source, as illustrated by the example of Eq. (24). In principle, it is possible to extract a single-mode state from a multi-mode source by filtering the auxiliary degrees of freedom, e.g. using a single-mode fiber for spatial degrees of freedom and a spectral filter for frequency domain. In any case, the mode-purity of the detected state has to be verified with a different set of measurements, e.g. via Hong-Ou-Mandel interference [13] or based on a physical model of the source. For example, in the case of a heralded single-photon source, the spectral purity can be determined by measuring the signal-idler joint spectral intensity [14], as will be explained in Sec. 6.3.

A systematic analysis of the characterization of the mode-purity of a source is beyond the scope of this paper. Nevertheless, it is worth mentioning that with the additional information on the multi-mode characteristics of the source and the knowledge of the total single-photon probability P_1 it is possible to bound the probability to find a single photon in the mode of interest $P_1^{[1]}$ (denoted mode 1). In particular, given a bound on the probability that all the modes but one are empty $\operatorname{tr} \varrho(\mathbb{1}_1 \otimes |0\rangle\langle 0|_2 \otimes \cdots \otimes |0\rangle\langle 0|_N) \geq 1-\varepsilon$, one can conclude that

$$P_1^{[1]} = \operatorname{tr} |1\rangle\langle 1|_1 \, \rho_k \geq P_1 - \varepsilon, \tag{25}$$

since the maximal contribution to P_1 from the other modes is ε. Here, $\rho_1 = \operatorname{tr}_{2,\ldots,N} \varrho$ is the marginal state of the first mode, which can in principle be filtered from the source. A bound on $P_1^{[1]}$ can then be used to, e.g., quantify the Wigner-negativity of the state ρ_1, see Sec. 5.

4 Finite statistics

In this section, we analyze finite size effects for the benchmark.

We sketch an analysis to account for finite statistics in any experiment aiming to evaluate $\hat{P}_1(\boldsymbol{p})$, the benchmark for single-photon sources derived in Sec. 3. For a measurement round described by $\boldsymbol{p}$ we associate a random variable X_T that takes different real values depending on the measurement result

$$X_T = \begin{cases} 3 & (\circ\bullet) \\ 0 & (\circ\circ) \\ -1 & (\bullet\circ) \text{ or } (\bullet\bullet) \end{cases} \tag{26}$$

This random variable satisfies $\mathbb{E}(X_T) = \hat{P}_1^T(\boldsymbol{p})$ in Eq. (9) (here and further $\mathbb{E}$ denotes the expected value of a random variable). Analogously, we define X_R by exchanging the role of the two detectors, such that it satisfies $\mathbb{E}(X_R) = \hat{P}_1^R(\boldsymbol{p})$.

In general, the source may prepare a different state $\rho^{(i)}$ at each round, corresponding to different probabilities $\boldsymbol{p}^{(i)}$ of the measurement outcomes. This means that in each round, we sample different random variables $X_T^{(i)}$ and $X_R^{(i)}$, which are independent between rounds given the sequence of states $\rho^{(1)}, \ldots, \rho^{(n)}$ produced in the experiment. In this case, a reasonable figure of merit is the average quality of the state prepared by the source $\bar{P}_1 = \frac{1}{n}\sum_{i=1}^n P_1^{(i)}$ where $P_1^{(i)}$ is the probability of the single-photon component of the state $\rho^{(i)}$. Because the transmission and reflection coefficients of the beam splitter can be considered to be constant, either $\mathbb{E}(X_T^{(i)}) \geq \mathbb{E}(X_R^{(i)})$ or $\mathbb{E}(X_T^{(i)}) \leq \mathbb{E}(X_R^{(i)})$ holds for all i. This means that the average single-photon weight fulfills

$$\bar{P}_1 \geq \min\{\mathbb{E}(\bar{X}_T), \mathbb{E}(\bar{X}_R)\}, \tag{27}$$

where $\bar{X}_{T(R)} = \frac{1}{n}\sum_{i=1}^n X_{T(R)}^{(i)}$. Finally, we use the Hoeffding 1963 theorem [15] to show that

$$\hat{q}_\alpha = \min\{\bar{X}_T, \bar{X}_R\} - \sqrt{\frac{16\log(1/\alpha)}{2n}} \tag{28}$$

is a one-sided confidence interval on $\bar{P}_1$ with confidence α (see Appendix F). Precisely, with probability $1-\alpha$ the observed value of $\hat{q}_\alpha$ lower bounds $\bar{P}_1$. It might be convenient to note that the quantity $\min\{\bar{X}_T, \bar{X}_R\}$ of this confidence interval can be computed using

$$\min\{\bar{X}_T, \bar{X}_R\} = \frac{4\min\{n_{\circ\bullet}, n_{\bullet\circ}\} - n_{\circ\bullet} - n_{\bullet\circ} - n_{\bullet\bullet}}{n} \tag{29}$$

with e.g. $n_{\bullet\bullet}$ counting the number of outcomes $\bullet\bullet$.

Analogously, one can derive a one-sided confidence intervals associated to the calibration-dependent benchmark derived in Sec. 3.2. With very similar arguments one can show that both

$$\begin{aligned} \hat{q}_\alpha^{(T)*} &= \frac{C_1(\hat{t},\hat{\eta}_T)n_{\circ\bullet} - C_2(\hat{t},\hat{\eta}_T,\hat{\eta}_R)n_{\bullet\bullet}}{n} \\ &\quad - (C_1(\hat{t},\hat{\eta}_T) + C_2(\hat{t},\hat{\eta}_T,\hat{\eta}_R))\sqrt{\frac{\log(1/\alpha)}{2n}}, \\ \hat{q}_\alpha^{(R)*} &= \frac{C_1(\hat{r},\hat{\eta}_R)n_{\bullet\circ} - C_2(\hat{r},\hat{\eta}_R,\hat{\eta}_T)n_{\bullet\bullet}}{n} \\ &\quad - (C_1(\hat{r},\hat{\eta}_R) + C_2(\hat{r},\hat{\eta}_R,\hat{\eta}_T))\sqrt{\frac{\log(1/\alpha)}{2n}}, \end{aligned} \tag{30}$$

where the functions C_1 and C_2 defined in Eq. (20) are confidence intervals for $\bar{P}_1$. Since they are derived from the same data, for a statistically meaningful statement one has to chose parameter α before computing the confidence interval. On the other hand, it is straightforward to see that

$$\hat{q}_{2\alpha}^* = \max\{q_\alpha^{(T)*}, q_\alpha^{(R)*}\} \tag{31}$$

is also a confidence interval at confidence level $1-2\alpha$. See App. F for a detailed derivation.

5 Relation to the non-classicality of the source

The data obtained from auto-correlation type measurements are known to be valuable for witnessing and quantifying various forms of non-classicality, including the non-positivity of the P-function and quantum non-Gaussianity [8–10]. We now show that the knowledge of P_1 in a single bosonic mode (as e.g. provided by our benchmarks $\hat{P}_1(\boldsymbol{p})$ and $\hat{P}_1^*(\boldsymbol{p})$) can reveal Wigner-negativity [16], arguably the strongest form of non-classically for a bosonic mode. In particular, Wigner-negativity implies the non-positivity of the P-function [17]. Similarly, it implies that the corresponding state is non-Gaussian, as a Gaussian state has a Gaussian (and thus positive) Wigner function[1]. Thus, demonstrating Wigner-negativity for a light source brings evidence of its strong quantum nature. Note that it has been shown recently that witnesses of Wigner-negativity can be derived systematically using a hierarchy of semidefinite programs [19]. Our contribution is more specific and aims at witnessing Wigner-negativity simply and directly from $\hat{P}_1(\boldsymbol{p})$ or $\hat{P}_1^*(\boldsymbol{p})$ observed on a single mode.

5.1 Wigner-negativity witness

The Wigner function is a representation of a single-mode state ρ in terms of the following quasi-probability distribution [20]

$$W_\rho(\beta) = \frac{2}{\pi}\mathrm{Tr}(\mathrm{D}_\beta(-1)^{a^\dagger a}\mathrm{D}_\beta^\dagger\,\rho), \tag{32}$$

with $\int \mathrm{d}\beta^2 W_\rho(\beta) = 1$. Here, $\mathrm{D}_\beta = e^{a^\dagger\beta - a\beta^*}$ is the displacement operator with a complex amplitude β. Applying Eq. (32) to a Fock state gives [17]

$$W_{|n\rangle\langle n|}(\beta) = \frac{2(-1)^n}{\pi}e^{-2|\beta|^2}L_n\left(4|\beta|^2\right) \tag{33}$$

where L_n is the Laguerre polynomial. Note that the following bound on the Laguerre polynomials $e^{-x/2}|L_n(x)| \leq 1$, see e.g. Eq. (18.14.8) in [21], leads to a bound on the Wigner function of Fock states $|W_{|n\rangle\langle n|}(\beta)| \leq \frac{2}{\pi}$. Note also that $L_1(x) = 1-x$.

With the help of Eq. (33), the upper bound on the Wigner function of Fock states and the definition of the Laguerre polynomial $L_1(x)$, it is easy to see that the Wigner function of any mixture of Fock states $\rho = \sum p_n\,|n\rangle\langle n|$ satisfies [2]

$$\begin{aligned} W_\rho(\beta) &= P_1 W_{|1\rangle\langle 1|}(\beta) + \sum_{n\neq 1} P_n W_{|n\rangle\langle n|}(\beta) \\ &\leq \frac{2}{\pi}\left(-P_1(1-4|\beta|^2)e^{-2|\beta|^2} + (1-P_1)\right). \end{aligned} \tag{34}$$

Focusing on the origin $\beta = 0$, we get $W_\rho(0) \leq 2\frac{1-2P_1}{\pi}$ which is negative if P_1 is larger than $\frac{1}{2}$. Hence, if one concludes from the measurement of $\boldsymbol{p}$ that $\hat{P}_1(\boldsymbol{p}) > \frac{1}{2}$, one can conclude that the measured state is Wigner-negative (recall that we assumed that the state ρ is single-mode).

5.2 Wigner-negativity measure

A natural way to quantify the negativity of the Wigner representation of a given state ρ is to measure the total quasi-probability for which the function $W_\rho(\beta)$ takes negative values [11], i.e.

$$N_W(\rho) = \int \mathrm{d}\beta^2 \frac{|W_\rho(\beta)| - W_\rho(\beta)}{2}, \tag{35}$$

which is manifestly zero for states with a positive Wigner function. In the Appendix E we show that $N_W(\rho)$ is non-increasing under Gaussian operations, which justifies its use as a measure of Wigner-negativity. Note that with the help of Ineq. (34), we show that $N_W(\rho)$ satisfies

$$\begin{aligned} N_W(\rho) \geq F(P_1) &= \begin{cases} \frac{3(1-P_1)\left(4w^2+3\right)}{8w} + P_1 - 2 & P_1 > \frac{1}{2} \\ 0 & P_1 \leq \frac{1}{2} \end{cases} \\ \text{with} \quad w &= w_0\left(\frac{\sqrt{e}}{2}\frac{1-P_1}{P_1}\right), \end{aligned} \tag{36}$$

where w_0 is the principal branch of the Lambert W function. The function $F(P_1)$ is non-decreasing. Hence, from the measurement of $\boldsymbol{p}$, we get a lower bound $\hat{P}_1(\boldsymbol{p})$ on P_1 that can be used to lower bound $N_W(\rho)$ using $F(\hat{P}_1(\boldsymbol{p}))$. The bound (36) is tight by construction in the ideal case $N_W(|1\rangle) = F(1) = \frac{9}{4\sqrt{e}} - 1 \approx 0.36$.

By computing $F''(P_1) \geq 0$ we show that the function $F(P_1)$ in Eq. (36) is convex. This property will be used in the following section, where we discuss the finite statistics effects.

[1] In addition, Hudson's theorem [18] tells us that any pure state with a positive Wigner function is Gaussian.

[2] For a general state $\varrho = \sum_{nm} c_{nm}\,|n\rangle\langle m|$ with Wigner function $W_\varrho(\beta)$, one can always define the corresponding Fock state mixture $\rho = \sum_n P_n\,|n\rangle\langle n|$ with $p_n = c_{nn}$. Its Wigner function reads $W_\rho(\beta) = W_\rho(|\beta|) = \int \mathrm{d}\varphi W_\varrho(|\beta|e^{\mathrm{i}\varphi}) = \langle W_\varrho(|\beta|e^{\mathrm{i}\varphi})\rangle_\varphi$. The two functions coincide at the origin $W_\rho(0) = W_\varrho(0)$. Furthermore, W_ρ can only be non-positive if W_ϱ is non-positive, and $N_{W_\rho} \leq N_{W_\varrho}$ (introduced at the end of the section) follows from $|\langle W(|\beta|e^{\mathrm{i}\varphi})\rangle_\varphi| \leq \langle |W(|\beta|e^{\mathrm{i}\varphi})|\rangle_\varphi$.

5.3 p-value to witness Wigner-negativity

We now present the extension of finite statistics analysis presented in Sec. 4 to the task of Wigner-negativity detection and quantification.

First, let us now consider the witness of Wigner-negativity discussed in Sec. 5.1, that is $W_\rho(0) \geq 0 \implies \hat{P}_1(\boldsymbol{p}) \leq 1/2$, and quantify the statistical significance of its contrapositive given the measurement data. This can be done by computing the p-value associated to the hypothesis that the Wigner function of the state is positive. As before, we consider the general case where a different state $\rho^{(i)}$ may be prepared at each run. Nevertheless, at each round the bound $W_{\rho^{(i)}}(0) \leq \frac{2}{\pi}(1-2P_1^{(i)})$ holds. Therefore, for the sequence of states prepared in the experiment, the average Wigner function at the origin satisfies

$$\bar{W}(0) = \frac{1}{n}\sum_{i=1}^{n} W_{\rho^{(i)}}(0) \leq \frac{2}{\pi}(1-2\bar{P}_1), \tag{37}$$

and is negative if $\bar{P}_1 > \frac{1}{2}$. Given some value of $\min\{\bar{X}_T, \bar{X}_R\}$ recorded after n measurement rounds, we show in Appendix F that for any collection of n states with $\bar{W}(0) \geq 0$, the probability that the results are equal or exceed the observed value of $\min\{\bar{X}_T, \bar{X}_R\}$ is given by

$$\text{p-value} \leq \exp\left(-\frac{2n\left(\min\{\bar{X}_T, \bar{X}_R\} - \frac{1}{2}\right)^2}{16}\right), \tag{38}$$

for $\min\{\bar{X}_T, \bar{X}_R\} > \frac{1}{2}$. In other words, given the observed value of $\min\{\bar{X}_T, \bar{X}_R\}$, the probability that it is coming from states that are Wigner-positive on average is bounded by the right-hand side of Ineq. (38). In App. F one finds a bound on the p-value for the calibration-dependent setting.

5.4 Confidence interval on the measure of Wigner-negativity

Finally, the convexity of the function $F(P_1)$ in Eq. (36) implies that the average Wigner-negativity satisfies $\bar{N}_W = \frac{1}{n}\sum_i N_W(\rho^{(i)}) \geq \frac{1}{n}\sum_i F(P_1^{(i)}) \geq F(\bar{P}_1)$. Therefore, a confidence interval q_α for $\bar{P}_1$

$$n w_\alpha = F(q_\alpha) \tag{39}$$

is a one-sided confidence interval on $\bar{N}_W$, that is, with probability $1-\alpha$, the average Wigner-negativity as quantified by $\bar{N}_W$ is lower bounded by $n w_\alpha = F(q_\alpha)$. This can be used both in the calibration-independent $n\hat{w}_\alpha = F(\hat{q}_\alpha)$ and calibration-dependent $n\hat{w}^*_\alpha = F(\hat{q}^*_\alpha)$ settings.

5.5 The crucial role of the single-mode hypothesis

It is important to emphasize that the single-mode hypothesis is crucial in order to relate P_1 (or its estimated value $\hat{P}_1(\boldsymbol{p}), \hat{P}^*_1(\boldsymbol{p})$) to Wigner-negativity. In particular, the multi-mode single-photon state ϱ of Eq. (24) becomes Wigner-positive for $N > 2$. In section 3.3 we have discussed how the single-mode character of the emitted radiation can be verified in practice. Here we merely recall that a bound of the form $P_1^{[1]} \geq P_1 - \varepsilon$, where $P_1^{[1]}$ is the single photon probability for a given mode, can be readily used to verify Wigner-negativity. One simply has

$$\begin{aligned} & n w_\alpha^{[1]} \geq F(q_\alpha - \varepsilon) \\ & \text{p-value} \leq \exp\left(-\frac{2n\left(\min\{\bar{X}_T, \bar{X}_R\} - \varepsilon - \frac{1}{2}\right)^2}{16}\right), \end{aligned} \tag{40}$$

if $\min\{\bar{X}_T, \bar{X}_R\} > \frac{1}{2} + \varepsilon$, for Wigner-negativity of the said mode.

It is worth mentioning that a possibility to ensure that the detected radiation is single-mode is to perform homodyne measurements. In such a measurement the incoming beam is mixed with a strong local oscillator on a beam splitter, the intensity of the output beams are then measured with linear detectors and subtracted. Under the assumption that the local oscillator is single-mode[3] the obtained signal is only sensitive to the single input mode identified by the local oscillator. Photon number statistics, and P_1 in particular, can be reconstructed from the statistics of a phase-averaged quadrature measurement [22], i.e. a homodyne measurement with a phase-randomized local oscillator. This offers the possibility to use our bound on the Wigner-negativity $N_W(\rho)$ in Eq. (36) with measurements that are guaranteed to pick up a single mode.

6 Experiment

To demonstrate the feasibility of our tools, we experimentally benchmark, witness and quantify the nonclassical nature of a heralded single-photon source [23] that is optimized for high efficiency of the heralded photon [24]. A periodically poled potassium titanyl phosphate (PPKTP) crystal is pumped by a Ti:Sapphire laser at $\lambda_p = 771.8\,\text{nm}$ in the picosecond pulsed regime with a repetition rate of 76 MHz to create nondegenerate photon pairs at $\lambda_s = 1541.3\,\text{nm}$ (signal) and $\lambda_i = 1546.1\,\text{nm}$ (idler) via type-II spontaneous parametric down-conversion (SPDC). The pair creation probability per pump pulse is set to $P_{\text{pair}} \approx 1.0 \times 10^{-3}$ and high-purity heralded signal photons are ensured by spectrally filtering the heralding idler photons using a dense wavelength division multiplexer

[3] Note that the situation where n modes $a_1, \ldots, a_n$ are prepared in coherent states $|\alpha_1\rangle|\alpha_2\rangle\ldots|\alpha_n\rangle$ with fixed phase relations, can be viewed as a coherent state of the mode $\bar{a} = \frac{\sum_k a_k \alpha_k}{\sqrt{\sum_k |\alpha_k|^2}}$, plus $n-1$ modes in the vacuum states.

at ITU channel 39. From a joint spectral intensity measurement [14], we estimate the spectral purity of the heralded photon to be $98.59\% \pm 0.04\%$. In this way, we herald signal photons at a rate of 19.1 kcps.

For the heralded auto-correlation measurement, the signal photon is sent to a 50/50 fiber coupler (AFW FOBC). All photons are detected by MoSi superconducting nanowire single-photon detectors [25] and time-correlated single-photon counting in a programmable time-to-digital converter (ID Quantique ID900) is used to register the detection events. Data are acquired for 200 s in order to evaluate $\boldsymbol{p} = (p_{\circ\circ}, p_{\bullet\circ}, p_{\circ\bullet}, p_{\bullet\bullet})$ for the signal photons after the 50/50 beam splitter.

The dark count probabilities of the detectors we used for the auto-correlation measurement are fairly small, $p_{\mathrm{dc}} \leq 4 \times 10^{-7}$, and can be completely neglected. That is, the dark count corrections ($\approx 4 \times 10^{-6}$) to the estimated values of the benchmark in Eqs. (18,22) are more than two orders of magnitude lower than the statistical noise, see Tables 1 and 3.

6.1 Calibration-independent benchmark

In a first step we apply our benchmark to the experimental results without taking the splitting ratio of the beam splitter and the detector efficiencies into account. The overall efficiency is 25 % for the heralding idler photons and 62 % for the heralded signal photons. In order to simulate a less efficient single-photon source, we introduce loss by inserting a fiber coupled variable attenuator (JDS Uniphase MV47W) into the heralded photon path before the 50/50 beam splitter and repeat the auto-correlation measurement for eight different transmission efficiencies η_{att}. Each transmission efficiency leads to a value for the pair $(\min(p_{\circ\_}, p_{\_\circ}), p_{\circ\circ})$ that is represented by a black cross in Fig. 2. In the same figure, we represent the polytope $\boldsymbol{Q}_P$ (defined after Eq. (7)) containing all possible values $(\min(p_{\circ\_}, p_{\_\circ}), p_{\circ\circ})$ associated to states ϱ with $\langle 1|\,\varrho\,|1\rangle \leq P$. Four polytopes are represented corresponding to the values $P \in \{0.25, 0.5, 0.75, 1\}$. A measurement result associated to a black cross lying outside a polytope $\boldsymbol{Q}_P$ is guaranteed to come from a state with a single-photon component satisfying $P_1 > P$.

$\eta_{\mathrm{s,tot}}$	$\hat{P}_1^T$	$\hat{P}_1^R$	$\hat{q}_{\alpha=10^{-10}}$
62 %	0.561(1)	0.678(1)	0.554
52 %	0.460(1)	0.573(1)	0.453
42 %	0.376(1)	0.465(1)	0.369

Table 1: Results of the measurement for the three highest transmission efficiencies $\eta_{\mathrm{s,tot}}$ of the heralded single-photon state. The values for $\hat{P}_1^T$ and $\hat{P}_1^R$ are calculated according to Eq. (9). For the finite statistics analysis we calculate the confidence interval $\hat{q}_\alpha \leq \bar{P}_1$ from Eq. (28) for the confidence level $1 - \alpha = 1 - 10^{-10}$.

Mode	η_{tot}	η_c	η_f		η_t	η_d
Idler	25 %	80 %	50 %		83 %	75 %
Signal	62 %	80 %	-	R	43 %	92 %
				T	44 %	85 %

Table 2: Characterization of the loss for idler (heralding) and signal (heralded) modes. η_{tot}, total efficiency; η_c, fiber coupling efficiency; η_f, spectral filter transmission; η_t, fiber transmission including the insertion loss of the 50/50 fiber coupler, connectors and telecom fiber isolators for further pump rejection; η_d, detector efficiency.

For the measurements with the three highest transmission efficiencies, we give the results of our benchmark in Tab. 1. We conclude for the highest transmission for example, that the measured states have on average a single-photon component with a weight $\bar{P}_1 \geq 0.554$ with a confidence level of $1 - 10^{-10}$.

6.2 Calibration-dependent benchmark

To compute the value of the calibration-dependent benchmark one needs to estimate the detector efficiencies and the reflection/transmission coefficient of the beam splitter. In order to characterize the detectors, we use the standard method, see e.g. [25] for a detailed description. For our setup we find that the beam splitter coefficients are bounded by $\hat{r} \in [0.49, 0.50]$ and the detector efficiencies are upper bounded by $(\hat{\eta}_R, \hat{\eta}_T) = (0.95, 0.88)$. The upper bounds for the detector efficiencies are obtained from results of the measured detection efficiencies given in Tab. 2 by adding three times the measurement uncertainty of around 0.01, see Supplementary Material of [25].

Under the assumptions that the $(\hat{r}, \hat{\eta}_R, \hat{\eta}_T)$ belong to these intervals, the values of $\hat{P}_1^{T*}(\boldsymbol{p})$ and $\hat{P}_1^{R*}(\boldsymbol{p})$ as measured in our experiment are given in Tab. 3 for the three highest transmission efficiencies. The confidence interval $\hat{q}_\alpha^* \leq \bar{P}_1$ is also reported for a confidence level of $1 - \alpha = 1 - 10^{-10}$.

$\eta_{\mathrm{s,tot}}$	$\hat{P}_1^{T*}$	$\hat{P}_1^{R*}$	$\hat{q}^*_{\alpha=10^{-10}}$
62 %	0.658(1)	0.683(1)	0.677
52 %	0.544(1)	0.573(1)	0.566
42 %	0.444(1)	0.466(1)	0.459

Table 3: Results of the measurement including the imperfect beam splitter ratio with $(1 - \hat{t}, \hat{r}) = (0.49, 0.50)$ and the non-unit detection efficiencies by using the upper bounds $(\hat{\eta}_R, \hat{\eta}_T) = (0.95, 0.88)$. The values for $\hat{P}_1^{T*}$ and $\hat{P}_1^{R*}$ are calculated with Eq. (19). The confidence intervals $\hat{q}_\alpha^* \leq \bar{P}_1$ in the finite statistics analysis are calculated for a confidence level of $1 - \alpha = 1 - 10^{-10}$.

6.3 Non-classicality of the source

As already mentioned, there is no guarantee that the single-mode assumption is exactly satisfied in our experiment, hence we have to estimate the mode purity of the source. We assume that the spatial mode purity is guaranteed by coupling the photons into a single-mode fiber. The polarization-purity is ensured by the fact that the signal and idler photons are separated with a polarizing beam splitter. To estimate the spectral purity, we apply the standard approach that relies on a physical model of the source, which we believe to properly describe the experiment. Precisely, we assume that the SPDC process responsible for the generation of the photon pairs is of the form

$$H_{\mathrm{SPDC}} \propto \int \mathrm{d}w_s \mathrm{d}w_i f(w_s, w_i) a^\dagger(w_s) b^\dagger(w_i), + \mathrm{h.c.}, \tag{41}$$

where $a(w_s)$ and $b(w_i)$ are the frequency field-modes of the signal/idler photons with $[a(w), a^\dagger(w')] = [b(w), b^\dagger(w')] = \delta(w - w')$. At low pumping power, we reconstruct $f(w_s, w_i)$ with a signal-idler joint spectral intensity measurement. Via a 2D-Gaussian fit we perform a singular value decomposition of $f(w_s, w_i)$ to rewrite the interaction in the form

$$H_{\mathrm{SPDC}} \propto \sum_k \sqrt{\lambda_k} a_k^\dagger b_k^\dagger + \mathrm{h.c.}, \tag{42}$$

where $[a_k, a_\ell^\dagger] = [b_k, b_\ell^\dagger] = \delta_{k\ell}$ now describe discrete spectral modes. With this procedure the largest Schmidt coefficient λ_1 is computed to be $\lambda_1 = 0.992\,92(18)$, where the standard deviation $\sigma_{\lambda_1} = 1.8 \times 10^{-4}$ is obtained from a Monte Carlo method assuming Poissonian count statistics in the joint spectral intensity measurement. Therefore, assuming that the efficiency of the trigger detector is the same for all idler modes, we obtain the leading order estimate

$$1 - \varepsilon \approx \lambda_1 - 3\,\sigma_{\lambda_1} = 99.24\%, \tag{43}$$

of the probability that the modes $a_{k\geq 2}$ are empty conditional to the detection of an idler photon. This corresponds to the mode-purity of $\sum_k \lambda_k^2 \approx 98.59\%$.

With the help of Eq. (25) we can take this into account for the quantification of Wigner-negativity, resulting in $\hat{nw}_{\alpha=10^{-10}} = 0.0046$ for the case of no added loss on the heralded single-photon state and no assumptions on the calibration of the measurement apparatus. The corresponding p-value and the results for the measurement-apparatus-dependent case are given in Tab. 4.

$\eta_{\mathrm{s,tot}}$	$\hat{nw}_{\alpha=10^{-10}}$	p-value	$\hat{nw}^*_{\alpha=10^{-10}}$	p-value*
62 %	0.0046	10^{-603}	0.053	10^{-6420}
52 %	0	×	0.0072	10^{-894}
42 %	0	×	0	×

Table 4: Wigner-negativity in our experiment for the three highest transmission efficiencies $\eta_{\mathrm{s,tot}}$ of the heralded single-photon state. The confidence interval on the measure of Wigner-negativity $\hat{nw}_\alpha \leq \bar{N}_W$ is obtained from Eq. (39) for the confidence level $\alpha = 10^{-10}$, assuming the reduced single-mode $P_1^{[1]}$ as given in Eq. (25). Further, we give the p-value according to Eq. (38) associated with the hypothesis that the measured states are on average Wigner-positive. The quantities with a * are taking the detector efficiencies into account and are obtained accordingly from Eqs. (19) and (25).

7 Conclusion

Auto-correlation measurements are commonly used to assess the quality and the quantum nature of single-photon sources, that is, they are used to check that a given source does not emit more than one photon and its emission is non-classical in the sense that its P-distribution is non-positive or that its state is non-Gaussian. We have shown that the statistics obtained from these measurements is actually richer. They can be used to lower bound the probability that a given source actually produces a single photon. We argued that this probability is a good benchmark for single-photon sources as it captures both its quality and its efficiency. Moreover, we showed that if the mode purity of the source can be assessed the lower bound on the single-photon emission probability can be used to witness and quantify the negativity of the Wigner function, a stronger form of non-classicality than the negativity of the P-distribution and the non-Gaussianity. We have proposed practical tools to benchmark single-photon sources and characterize its Wigner-negativity this way. With this material in hand, we hope that the community which is developing single-photon sources could exploit the statistics of their auto-correlation measurements in a more enlightening way.

Acknowledgments

We thank R.J. Warburton for fruitful discussions at an early stage of the project. This work was supported by the Swiss National Science Foundation (SNSF) under Grant No. 200020-182664. E.O acknowledges support from the Government of Spain (FIS2020-TRANQI and Severo Ochoa CEX2019-000910- S), Fundació Cellex, Fundació Mir-Puig, Generalitat de Catalunya (CERCA, AGAUR SGR 1381) and from the ERC AdGCERQUT.

Data availability

The data supporting the experimental results within this paper are available on the Zenodo data repository [26].

A Auto-correlation function and auto-correlation measurement

Here we briefly recall the definitions of the auto-correlation function $g^{(2)}$. We will use the notation introduced in Section 2, 3 and 3.1.1 of the main text, and assume that the beam splitter is balanced and the two detectors have equal efficiency, i.e. $t = r = \frac{1}{2}$ in Eq. (2).

Historically [27], the auto-correlation function was defined as the ratio

$$g^{(2)} = \frac{\langle a^{\dagger 2} a^2 \rangle}{\langle a^\dagger a \rangle^2} = \frac{\langle (a^\dagger a)^2 \rangle - \langle a^\dagger a \rangle}{\langle a^\dagger a \rangle^2} \tag{44}$$

and the efficiency of the source can be characterized by the average number of photons it emits $I = \langle a^\dagger a \rangle$. Then it is not difficult to see that the bound

$$P_1 \geq 2\langle a^\dagger a \rangle - \langle (a^\dagger a)^2 \rangle = I - I^2 g^{(2)} \tag{45}$$

is a tight benchmark. To see this note that in the $\left(\langle a^\dagger a \rangle, \langle (a^\dagger a)^2 \rangle\right)$ plane the quantity $w = 2\langle a^\dagger a \rangle - \langle (a^\dagger a)^2 \rangle$ measures the distance from the line connecting the points $(0,0)$ and $(2,4)$ corresponding to Fock states $|0\rangle$ and $|2\rangle$. With $w = 1$ for the point $(1,1)$ corresponding to the single-photon state $|1\rangle$. In practice, one can not directly measure $\langle (a^\dagger a)^2 \rangle$ and $\langle a^\dagger a \rangle$, but can approximate these values by increasing the loss artificially, as $E_{\bullet -} = \frac{a^\dagger a}{2}\eta + O(\eta^2)$ and $E_{\bullet\bullet} = \frac{a^{\dagger 2} a^2}{4}\eta^2 + O(\eta^3)$ for $\frac{1}{\eta} \gg a^\dagger a$ (recall that $E_{\bullet -} = E_{\bullet\bullet} + E_{\bullet\circ}$). Such an approach thus requires a precise control of the efficiency η and is statistically inefficient, since additional losses are introduced.

Alternatively [28], the auto-correlation function can by directly defined as

$$\tilde{g}^{(2)} = \frac{\langle E_{\bullet\bullet} \rangle}{\langle E_{\bullet -} \rangle \langle E_{- \bullet} \rangle}. \tag{46}$$

The efficiency can also be characterized by probability that a source produces a click $\tilde{I} = \langle E_{\bullet\bullet} + E_{\bullet\circ} + E_{\circ\bullet} \rangle$. Given the two values $\tilde{g}^{(2)}$ and $\tilde{I}$ it is then possible to reconstruct the full probability distribution $\boldsymbol{p} = (\langle E_{\circ\circ} \rangle, \langle E_{\bullet\circ} \rangle, \langle E_{\circ\bullet} \rangle, \langle E_{\bullet\bullet} \rangle)$, since we assumed $\langle E_{\bullet\circ} \rangle = \langle E_{\circ\bullet} \rangle$ so that $\mathbf{p}$ is defined by two parameters. As argued above the two functions coincide $g^{(2)} = \tilde{g}^{(2)}$ in the limit $\eta \to 0$.

In both cases the auto-correlation measurements relies on the setup of the Fig. 1. The measurement data can thus be readily used to estimate $\boldsymbol{p}$ and compute the benchmarks proposed in this paper.

To finish the discussion of the auto-correlation functions we recall that both $g^{(2)}$ and $\tilde{g}^{(2)}$ are witnesses of the non-classicality of the state ρ [28], i.e. $g^{(2)}, \tilde{g}^{(2)} < 1$ is only possible for states whose P-function admits negative values. In fact, this is true in a more general context, as given by the following observation.

Observation. *For any two binary POVMs $\{M_\bullet, M_\circ\}$ and $\{M'_\bullet, M'_\circ\}$ measured at the two outputs of a beam splitter (Fig. 1), the inequality*

$$G^{(2)} = \frac{\langle M_\bullet \otimes M'_\bullet \rangle}{\langle M_\bullet \otimes \mathbb{1} \rangle \langle \mathbb{1} \otimes M'_\bullet \rangle} < 1 \tag{47}$$

is a witness of non-classicality (P-function taking negative values), as long as the POVM element of individual detectors are only functions of the number of photons $\langle n | M_\bullet | m \rangle = \delta_{n,m} p_\bullet(|n\rangle)$ and the click probabilities are increasing functions of the photon number $p_\bullet(|n\rangle) \geq p_\bullet(|m\rangle)$ for $n \geq m$ (and the same for $M'_\bullet$).

For the sake of completeness we prove the above statement here. A coherent state splits into two coherent states on a beam splitter $|\alpha\rangle \mapsto_{BS} |\sqrt{r}\alpha\rangle |\sqrt{t}\alpha\rangle$. Hence for a coherent state

$$\begin{aligned} \langle M_\bullet \otimes M'_\bullet \rangle &= \left\langle \sqrt{r}\alpha \right| M_\bullet \left| \sqrt{r}\alpha \right\rangle \left\langle \sqrt{t}\alpha \right| M'_\bullet \left| \sqrt{t}\alpha \right\rangle \\ &= p_\bullet(\sqrt{r|\alpha|^2})\, p'_\bullet(\sqrt{t|\alpha|^2}) \\ &= \langle M_\bullet \otimes \mathbb{1} \rangle \langle \mathbb{1} \otimes M'_\bullet \rangle \end{aligned} \tag{48}$$

and $G^{(2)} = 1$. Then for any mixture of coherent states $\rho_{cl} = \int d^2\alpha \mathrm{P}(\alpha) |\alpha\rangle\langle\alpha|$ one finds

$$\langle M_\bullet \otimes M'_\bullet \rangle = \int d^2\alpha \mathrm{P}(\alpha) p_\bullet(\sqrt{r|\alpha|^2}) p'_\bullet(\sqrt{t|\alpha|^2}). \tag{49}$$

To shorten the equations let us denote $z = |\alpha|$, $f(z) = p_\bullet(\sqrt{r|\alpha|^2})$, $g(z) = p'_\bullet(\sqrt{t|\alpha|^2})$, $\mu(z) = 2z \int \mathrm{d}\varphi \mathrm{P}\left(ze^{\mathrm{i}\varphi}\right)$ and $\mathrm{d}\mu(z) = \mathrm{d}z\mu(z)$ with $\int \mathrm{d}\mu(z) = 1$, such that

$$\begin{aligned} \langle M_\bullet \otimes M'_\bullet \rangle &= \int \mathrm{d}\mu(z) f(z) g(z) \\ &= \int \mathrm{d}\mu(z) \mathrm{d}\mu(z') \frac{1}{2}(f(z)g(z) + f(z')g(z')), \\ \langle M_\bullet \otimes \mathbb{1} \rangle \langle \mathbb{1} \otimes M'_\bullet \rangle &= \int \mathrm{d}\mu(z) f(z) \int \mathrm{d}\mu(z') g(z') \\ &= \int \mathrm{d}\mu(z) \mathrm{d}\mu(z') \frac{1}{2}(f(z)g(z') + f(z')g(z)). \end{aligned} \tag{50}$$

Without loss of generality consider $z' \geq z$, by $p_\bullet(|n\rangle) \geq p_\bullet(|m\rangle)$ for $n \geq m$ it follows that $f(z') \geq f(z)$ for $z' \geq z$ (using the fact that a coherent state has a Poissonian photon number distribution). Hence, one can write

$$\begin{aligned} f(z') &= f(z) + \Delta_f \qquad \Delta_f \geq 0 \\ g(z') &= g(z) + \Delta_g \qquad \Delta_g \geq 0 \end{aligned} \tag{51}$$

and

$$\begin{aligned} &(f(z)g(z) + f(z')g(z')) - (f(z)g(z') + f(z')g(z)) \\ &= \Delta_f \Delta_g \geq 0 \end{aligned} \tag{52}$$

for each z and z'. Therefore the inequality is also true for the integrals

$$\langle M_\bullet \otimes M'_\bullet \rangle \geq \langle M_\bullet \otimes \mathbb{1} \rangle \langle \mathbb{1} \otimes M'_\bullet \rangle. \tag{53}$$

Showing that $G^{(2)} \geq 1$ for any state with a positive P-function. Notably, the same proof works if both $\langle n| M_\bullet |n\rangle$ and $\langle n| M'_\bullet |n\rangle$ are decreasing functions of n, e.g. if they are replaced with $M_\circ$ and $M'_\circ$. The above observation has been used to propose an experiment where non-classicality of light would be demonstrated by directly using human eyes as detectors [29].

B POVM corresponding to photon detection preceded by a beam splitter

Since two single-photon detectors after a beam splitter cannot detect any coherence between Fock states of an incoming state, we can consider a state $\rho = \sum_n \frac{c_n}{n!} (a^\dagger)^n |0\rangle \langle 0| a^n$ without loss of generality. The state ρ arrives at a beam splitter with transmittance t, the resulting state is (ignoring again the coherence between the Fock states)

$$\rho_r = \sum_{n,k} c_n \binom{n}{k} (t^k)(1-t)^{n-k} |k, n-k\rangle \langle k, n-k| . \tag{54}$$

One can then compute the probability of the different events for the state ρ_r, for example

$$P_{\circ\bullet} = \mathrm{Tr}(\mathrm{E}_\circ \otimes \mathrm{E}_\bullet \rho_r) = \mathrm{Tr}(\mathrm{E}_\circ \rho_r) - \mathrm{Tr}(\mathrm{E}_\circ \otimes \mathrm{E}_\circ \rho_r) \tag{55}$$

where

$$\begin{aligned}\mathrm{Tr}(\mathrm{E}_\circ \otimes \mathrm{E}_\circ \rho_r) &= \sum_n c_n^2 (1-\eta)^n \sum_{k=0}^n \binom{n}{k} t^k (1-t)^{n-k} \\ &= \sum_n c_n^2 (1-\eta)^n \\ &= \mathrm{Tr}((1-\eta)^{a^\dagger a} \rho)\end{aligned}$$

and

$$\begin{aligned}\mathrm{Tr}(\mathrm{E}_\circ \rho_r) &= \sum_n c_n^2 \sum_{k=0}^n \binom{n}{k} t^k (1-t)^{n-k} (1-\eta)^k \\ &= \sum_n c_n^2 (1-t\eta)^n \\ &= \mathrm{Tr}((1-t\eta)^{a^\dagger a} \rho).\end{aligned}$$

The resulting POVM is thus $\mathrm{E}_{\circ\bullet} = (1-t\eta)^{a^\dagger a} - (1-\eta)^{a^\dagger a}$.

Let us consider a two-mode state (generalization to n modes is straightforward) $\rho = \sum_{n_1,n_2} \frac{c_{n_1,n_2}}{n_1! n_2!} (a_1^\dagger)^{n_1} (a_2^\dagger)^{n_2} |0\rangle \langle 0| a_1^{n_1} a_2^{n_2}$. The POVM element corresponding to no-clicks after the beam splitter on each mode now reads $\mathrm{E}_\circ^{(2)} = \mathrm{E}_\circ \otimes \mathrm{E}_\circ$. The state after the beam splitter is now

$$\begin{aligned}\rho_r = &\sum_{n_1,k_1,n_2,k_2} C_{n_1,k_1,n_2,k_2} \\ &|k_1, n_1-k_1, k_2, n_2-k_2\rangle \langle k_1, n_1-k_1, k_2, n_2-k_2|\end{aligned} \tag{56}$$

where $C_{n_1,k_1,n_2,k_2} = \binom{n_1}{k_1}\binom{n_2}{k_2} t^{k_1+k_2}(1-t)^{n_1+n_2-k_1-k_2}$. We focus on the event click on the first detector and no click on the second

$$\begin{aligned}&\mathrm{Tr}(\mathrm{E}_\circ^2 \otimes \mathrm{E}_\circ^2 \rho_r) \\ &= \sum_{n_1,n_2} c_{n_1,n_2}^2 (1-\eta)^{n_1+n_2} \\ &\sum_{k_1,k_2=0}^{n_1,n_2} \binom{n_2}{k_2}\binom{n_1}{k_1} t^{k_1+k_2} (1-t)^{n_1+n_2-k_1-k_2} \\ &= \sum_n c_n^2 (1-\eta)^{n_1+n_2} \\ &= \mathrm{Tr}((1-\eta)^{\hat{n}} \rho)\end{aligned}$$

similarly

$$\mathrm{Tr}(\mathrm{E}_\circ^2 \rho_r) = \mathrm{Tr}((1-t\eta)^{\hat{n}} \rho). \tag{57}$$

We retrieve that the POVM elements in the multimode case are given by

$$\begin{aligned}E_{\circ\circ} &= (1-\eta)^{\hat{n}} \\ E_{\bullet\circ} &= (1-\eta\, t)^{\hat{n}} - (1-\eta)^{\hat{n}} \\ E_{\circ\bullet} &= (1-\eta\, r)^{\hat{n}} - (1-\eta)^{\hat{n}} \\ E_{\bullet\bullet} &= \mathbb{1} - E_{\circ\circ} - E_{\bullet\circ} - E_{\circ\bullet}.\end{aligned} \tag{58}$$

C The effect of loss on P_1

We show here that the set of states ρ with $P_1 \geq \frac{2}{3}$ is closed under losses. Consider a state ρ associated with a single-photon component $P_1 = P$. Let us apply infinitesimal transmission losses $\eta = 1 - \mathrm{d}\epsilon$. After the loss, the photon number distribution $P_n = \langle n|\rho|n\rangle$ reads

$$P_n(\epsilon) = (1 - n\mathrm{d}\epsilon) P_n + \mathrm{d}\epsilon (n+1) P_{n+1}. \tag{59}$$

In particular,

$$\begin{aligned}\frac{\mathrm{d}}{\mathrm{d}\epsilon} P_1 &= -P_1 + 2P_2 \\ &\leq -P + 2(1-P) \\ &= 2 - 3P\end{aligned} \tag{60}$$

which is negative for $P \geq 2/3$.

On the other hand, there are states with $P_1 < 2/3$ for which the single-photon probability can be increased substantially by losses. Consider a channel with transmission efficiency η and apply it to the state

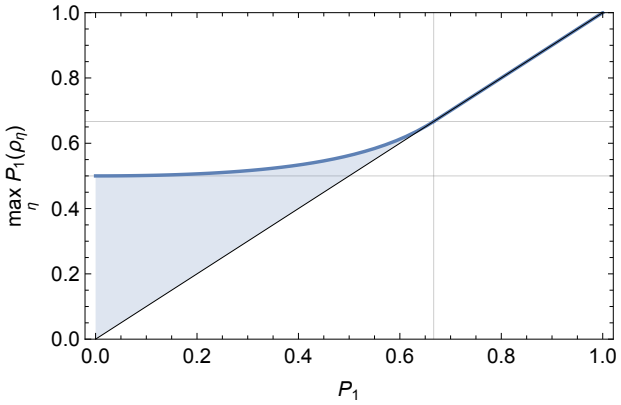

Figure 3: Consider the sate $\rho = P_1 |1\rangle\langle 1| + (1-P_1)|2\rangle\langle 2|$, which is transformed intro ρ_η by a loss channel of transmission η. Fro any P_1 there is a value of η which maximize the single-photon probability $P_1(\rho_\eta)$ after losses, see Eq. (62). The blue line depicts $\max_\eta P_1(\rho_\eta)$ as the function P_1, and the black line is simply P_1. One sees that for this example the single-photon component can be increased by losses if $P_1 < 2/3$, as illustrated by the shaded area. Conversely, we show that for any single-mode state ρ' with $P_1 \geq 2/3$, the single-photon component can not be increased by losses.

$\rho = P_1 |1\rangle\langle 1| + (1-P_1)|2\rangle\langle 2|$. This leads to a state ρ_η having a single-photon component

$$P_1(\rho_\eta) = \eta P_1 + 2\eta(1-\eta)(1-P_1). \tag{61}$$

This quantity is maximized at

$$\max_\eta P_1(\rho_\eta) = \begin{cases} \frac{(2-P_1)^2}{8(1-P_1)} & P_1 \leq \frac{2}{3} \\ P_1 & P_1 > \frac{2}{3}, \end{cases} \tag{62}$$

the maximum being depicted in Fig. 3 as a function of P_1. To give a concrete example, for the initial $\rho = \frac{1}{2}(|1\rangle\langle 1| + |2\rangle\langle 2|)$, the weight of the single-photon component can be increased to $P_1(\rho_{\eta=3/4}) = 1/2 + 1/16 = 0.562$ while for the Fock state $\rho = |2\rangle\langle 2|$, it is possible to reach $P_1(\rho_{\eta=1/2}) = 1/2$.

D Parameter dependent witness

We consider the case where the two detectors have efficiencies η_T and η_R and the beam splitter has reflectance r and transmittance t (with $t + r = 1$). For an incoming Fock state $|n\rangle$ the probabilities of clicks are given by

$$\begin{aligned} f_n = p_{\circ\bullet}^{|n\rangle} &= (1-\eta_R r)^n - (1-\eta_T t - \eta_R r)^n \\ h_n = p_{\bullet\circ}^{|n\rangle} &= (1-\eta_T t)^n - (1-\eta_R r - \eta_T t)^n \\ g_n = p_{\bullet\bullet}^{|n\rangle} &= 1 + (1-\eta_R r - \eta_T t)^n + \\ &\quad - (1-\eta_R r)^n - (1-\eta_T t)^n. \end{aligned} \tag{63}$$

For a mixture of Fock states $\rho = \sum_n P_n |n\rangle\langle n|$ one has

$$p_{\circ\bullet} = \sum_{n=1}^{\infty} P_n f_n, \tag{64}$$

from which we get

$$P_1 = \frac{1}{f_1}\left(p_{\circ\bullet} - \sum_{n\geq 2} P_n f_n\right). \tag{65}$$

In order to set a lower bound on P_1 we thus need to upper bound the term $\sum_{n\geq 2} P_n f_n$. We also have

$$p_{\bullet\bullet} = \sum_{n\geq 2} P_n g_n. \tag{66}$$

Therefore, to derive a benchmark for P_1 we are looking for a function $f_*(p_{\bullet\bullet})$ such that

$$\begin{aligned} f_*(p_{\bullet\bullet}) = \max_{\mathbf{p}>\mathbf{0}} &\sum_{n\geq 2} P_n f_n \\ \text{s.t.} &\sum_{n\geq 2} P_n g_n = p_{\bullet\bullet} \end{aligned} \tag{67}$$

To find $f_*(p_{\bullet\bullet})$ we define $q_n = P_n g_n$, so that the maximization can be rewritten as

$$\begin{aligned} f_*(p_{\bullet\bullet}) = \max &\sum_{n\geq 2} q_n \frac{f_n}{g_n} \\ \text{s.t.} &\sum_{n\geq 2} q_n = p_{\bullet\bullet}. \end{aligned} \tag{68}$$

Using $\sum_n q_n \frac{f_n}{g_n} \leq (\sum_n q_n)\left(\max_n \frac{f_n}{g_n}\right)$ we see that the solution of Eq. (67) satisfies

$$f_*(p_{\bullet\bullet}) \leq p_{\bullet\bullet}\left(\max_{n\geq 2} \frac{f_n}{g_n}\right). \tag{69}$$

We prove right after that the maximum is achieved for $n = 2$. By plugging $\sum_{n\geq 2} P_n f_n \leq f_*(p_{\bullet\bullet}) \leq p_{\bullet\bullet}\frac{f_2}{g_2}$ in Eq. (65), we get the desired inequality

$$P_1 \geq \frac{1}{f_1}\left(p_{\circ\bullet} - p_{\bullet\bullet}\frac{f_2}{g_2}\right). \tag{70}$$

The same bound holds with $p_{\bullet\circ}$ instead of $p_{\circ\bullet}$ and h_n instead of f_n. The right-hand side of these two inequalities are a function of the observed probabilities $\boldsymbol{p}$ and a lower bound on P_1, hence defining two benchmarks

$$\begin{aligned} \hat{P}_1^{T*}(\boldsymbol{p}) &= \frac{1}{f_1}p_{\circ\bullet} - \frac{f_2}{f_1 g_2}p_{\bullet\bullet}, \\ \hat{P}_1^{R*}(\boldsymbol{p}) &= \frac{1}{h_1}p_{\bullet\circ} - \frac{h_2}{h_1 g_2}p_{\bullet\bullet}. \end{aligned} \tag{71}$$

The best option is to consider the larger value of $p_{\bullet\circ}$ and $p_{\circ\bullet}$.

The proof of $\max_n \frac{f_n}{g_n} = \frac{f_2}{g_2}$. To maximize the ratio $\frac{f_n}{g_n}$ express it as

$$\begin{aligned} \frac{f_n}{g_n} &= \frac{(1-\eta_R r)^n - (1-\eta_T t - \eta_R r)^n}{1 - (1-\eta_T t)^n - (1-\eta_R r)^n + (1-\eta_R r - \eta_T t)^n} \\ &= \frac{1}{\frac{1-(1-\eta_T t)^n}{(1-\eta_R r)^n - (1-\eta_R r - \eta_T t)^n} - 1}. \end{aligned} \tag{72}$$

Manifestly, maximizing $\frac{f_n}{g_n}$ is equivalent to minimizing $\frac{1-(1-\eta_T t)^n}{(1-\eta_R r)^n-(1-\eta_R r-\eta_T t)^n}$. In other words we want to show that for $n \geq 2$ the fraction

$$\frac{1^n-(1-x)^n}{y^n-(y-x)^n}, \tag{73}$$

with $x=\eta_T t$ and $y=1-\eta_R r$ satisfying $0<x<y<1$, is minimized at $n=2$. However, it is enough to show that the expression $\frac{1^n-(1-x)^n}{y^n-(y-x)^n}$ is increasing with n. To do so, let us derive this quantity with respect to n. We have

$$\begin{aligned}\frac{\mathrm{d}}{\mathrm{d}n}\frac{1-(1-x)^n}{y^n-(y-x)^n} &= \frac{1}{(y^n-(x-y)^n)^2}\\ &\times\Big((1-x)^n-1\big)\left(y^n\log(y)-(y-x)^n\log(y-x)\right)\\ &-(1-x)^n\log(1-x)(y^n-(y-x)^n)\Big).\end{aligned} \tag{74}$$

To show that it is positive we can omit the denominator $(y^n-(x-y)^n)^2$. Labeling $a=(1-x)^n, b=y^n, c=(y-x)^n$ and noting that $\log\left(x^{\frac{1}{n}}\right)=\frac{1}{n}\log(x)$ we get

$$\frac{\mathrm{d}}{\mathrm{d}n}\frac{1-(1-x)^n}{y^n-(y-x)^n}\geq 0 \Longleftrightarrow f(a,b,c)\geq 0,$$

with

$$f(a,b,c)=(a-1)(b\log(b)-c\log(c))-a\log(a)(b-c). \tag{75}$$

It remains to show that the function $f(a,b,c)$ is positive for $a,b>c$. Note that it is a decreasing function of c, as

$$\begin{aligned}\frac{\mathrm{d}}{\mathrm{d}c}f(a,b,c) &= (1-a)(\log(c)+1)+a\log(a)\\ &\leq (1-a)(\log(a)+1)+a\log(a)\\ &= 1-a+\log(a)\\ &\leq 0\end{aligned} \tag{76}$$

using a standard inequality for the logarithm $\log(a)\leq 1-a$. We can thus only verify the positivity of the function for the maximal possible value of c. There are, however, two possibilities $a\geq b$ and $b>a$. For $a\geq b$ we set $c=b$ and obtain

$$f(a,b,c)\geq f(a,b,b)=0. \tag{77}$$

For $b>a$ we set $c=a$ and get

$$\begin{aligned}f(a,b,c) &\geq f(a,b,a)\\ &= (1-b)a\log(a)-(1-a)b\log(b).\end{aligned} \tag{78}$$

To show that the last expression is positive, we divide it by $(1-a)(1-b)$ to get

$$\frac{a}{1-a}\log(a)-\frac{b}{1-b}\log(b), \tag{79}$$

and note that the function $\frac{x}{1-x}\log(x)$ is decreasing ($\frac{\mathrm{d}}{\mathrm{d}x}\frac{x}{1-x}\log(x)=\frac{1-x+\log(x)}{(1-x)^2}\leq 0$ by Eq. (76)). Therefore, $b\geq a$ implies

$$\frac{a}{1-a}\log(a)-\frac{b}{1-b}\log(b)\geq 0 \implies f(a,b,c)\geq 0. \tag{80}$$

Hence, the fraction $\frac{1-(1-x)^n}{y^n-(y-x)^n}$ is increasing with n and attains its minimum at the boundary $n=2$ of the interval $[2,\infty)$. Therefore, $\frac{f_n}{g_n}$ is maximized at $n=2$, which concludes the proof.

E Wigner-negativity measure

For a single-mode state ρ, the Wigner function $W_\rho(\beta)$ is a quasi-probability distribution satisfying $\int \mathrm{d}\beta^2\, W_\rho(\beta)=1$. The negativity of the Wigner function ($W(\beta)<0$ for some $\beta\in\mathbb{C}$) is an important non-classical feature of the state, as argued in the main text. A natural way to quantify this negativity is to measure the total quasi-probability where the function W_ρ takes negative values, that is to compute

$$N_W(\rho)=\int \mathrm{d}\beta^2\frac{|W_\rho(\beta)|-W_\rho(\beta)}{2}. \tag{81}$$

This intuitive quantity was introduced in [11]. We now show that $N_W(\rho)$ is a good "measure" of Wigner negativity in the sense that it can not be increased by Gaussian operations.

Pure Gaussian operations are displacements $\mathrm{D}_\gamma=e^{\gamma a^\dagger-\gamma^* a}$, single-mode squeezing $\mathrm{SMS}_g=e^{\frac{g}{2}(a^{\dagger 2}-a^2)}$, phase rotations $e^{i\varphi a^\dagger a}$, or combination thereof. Consider a single-mode state ρ with its Wigner function $W_\rho(\beta)$ and its Wigner negativity measure $N_W(\rho)$. The effect of a displacement $\varrho=\mathrm{D}_\gamma\rho\mathrm{D}_\gamma^\dagger$ on the Wigner function is a mere translation in phase space $W_\varrho(\beta)=W_\rho(\beta-\gamma)$, which does not affect the Wigner negativity measure $N_W(\rho)=N_W(\varrho)$. The same goes for a phase rotation, which merely transform $W_\varrho(\beta)=W_\rho(\beta e^{\mathrm{i}\varphi})$. For a squeezing operation $\varrho=\mathrm{SMS}_g\rho\mathrm{SMS}_g^\dagger$, the Wigner function is transformed as

$$W_\varrho(\beta)=W_\rho(\tilde{\beta}) \tag{82}$$

where $\beta=\beta'+\mathrm{i}\beta''$ and $\tilde{\beta}=e^g\beta'+e^{-g}\mathrm{i}\beta''$. This implies for the Wigner negativity measure that

$$\begin{aligned}N_W(\varrho) &= \frac{1}{2}\int \mathrm{d}\beta^2\left(|W_\varrho(\beta)|-W_\varrho(\beta)\right)\\ &= \frac{1}{2}\int \mathrm{d}\beta'\,\mathrm{d}\beta''\left(|W_\rho(\tilde{\beta})|-W_\rho(\tilde{\beta})\right)\\ &= \frac{1}{2}\int e^{-g}\mathrm{d}\tilde{\beta}'\,e^{g}\mathrm{d}\tilde{\beta}''\left(|W_\rho(\tilde{\beta})|-W_\rho(\tilde{\beta})\right)\\ &= \frac{1}{2}\int \mathrm{d}\tilde{\beta}^2\left(|W_\rho(\tilde{\beta})|-W_\rho(\tilde{\beta})\right)\\ &= N_W(\rho).\end{aligned} \tag{83}$$

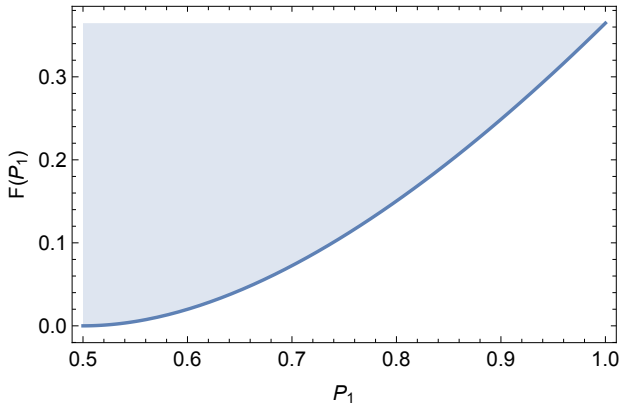

Figure 4: A sketch of the function $F(P_1)$ in Eq. (89) that lower bounds the Wigner-negativity of a state $N_W(\rho)$, for $P_1 = \langle 1|\,\rho\,|1\rangle \in [0.5, 1]$. Any single-mode state ρ with single-photon probability P_1 (or higher) has Wigner-negativity $N_W(\rho)$ above the blue line, as illustrated by the shaded area.

Hence, $N_W(\rho)$ is also unchanged by squeezing. Moreover, the quantity

$$N_W(p_1\rho_1 + p_2\rho_2) \leq p_1 N_W(\rho_1) + p_2 N_W(\rho_2) \tag{84}$$

is manifestly convex as $|p_1 W_1(\beta) + p_2 W_2(\beta)| \leq p_1|W_1(\beta)| + p_2|W_2(\beta)|$. Hence, $N_W(\rho)$ is non-increasing under mixtures of pure Gaussian operations. We conclude that $N_W(\rho)$ is a reasonable measure of Wigner negativity.

Let us now show how the Wigner negativity measure of a given state can be related to the weight of its single-photon component. The Wigner function for an arbitrary Fock state $|n\rangle$ reads [17]

$$W_n(\beta) = \frac{2(-1)^n}{\pi} e^{-2|\beta|^2} L_n\left(4|\beta|^2\right), \tag{85}$$

with $|W_n(\beta)| \leq \frac{2}{\pi}$ since $e^{-x/2}|L_n(x)| \leq 1$ (L_n are Laguerre polynomials). Hence, for any mixture of Fock states $\rho = \sum P_n\,|n\rangle\langle n|$, we have

$$\begin{aligned} W_\rho(\beta) &= P_1 W_1(\beta) + \sum_{n\neq 1} P_n W_n(\beta) \\ &\leq -\frac{2}{\pi}\left(P_1(1-4|\beta|^2)e^{-2|\beta|^2} - (1-P_1)\right). \end{aligned} \tag{86}$$

For $P_1 \geq 1/2$, the Wigner function is negative in the phase-space region with

$$\begin{aligned} (1-4|\beta|^2)e^{-2|\beta|^2} > \frac{1-P_1}{P_1} \iff \\ |\beta|^2 < \underbrace{\frac{1}{4}\left(1 - 2\,w_0\left(\frac{\sqrt{e}}{2}\frac{1-P_1}{P_1}\right)\right)}_{\equiv \ell(P_1)}, \end{aligned} \tag{87}$$

where $w_0(x)$ is the principal branch of the Lambert W function. Eq. (87) defines a disk

$$\text{disk}(P_1) = \left\{\beta \in \mathbb{C}\,\middle|\, |\beta|^2 \leq \ell(P_1)\right\} \tag{88}$$

in phase-space centered at the origin, where the Wigner function is negative. We can now compute the integral over this region

$$\begin{aligned} N_W(\rho) &\geq \int_{\text{disk}(P_1)} \mathrm{d}\beta^2 |W_\rho(\beta)| \\ &= \int_0^{\sqrt{\ell(P_1)}} 2\pi r \mathrm{d}r\, |W_\rho(r)| \\ &\geq 4\int_0^{\sqrt{\ell(P_1)}} r\mathrm{d}r \left(P_1(1-4r^4)e^{-2r^2} - (1-P_1)\right) \\ &= F(P_1) = \frac{3(1-P_1)\left(4w^2+3\right)}{8w} + P_1 - 2 \\ &\text{with} \quad w = w_0\left(\frac{\sqrt{e}}{2}\frac{1-P_1}{P_1}\right) \quad \text{for} \end{aligned} \tag{89}$$

that is plotted in Fig. 4. Notably, for $P_1 = 1$ the bound becomes tight $N_W(|1\rangle) = F(1) = \frac{9}{4\sqrt{e}} - 1 \approx 0.36$. To show that the function $F(P_1)$ is convex, one computes

$$F''(P_1) = \frac{3w\,(4w\,(w+2)+5)}{8\,(1-P_1)\,P_1^2\,(w+1)^3}, \tag{90}$$

which is positive since $w \geq 0$. In the main text, we defined the function $F(P_1)$ continued on the whole interval $P_1 \in [0,1]$ by simply setting $F(P_1) = 0$ for $P_1 \leq \frac{1}{2}$. Obviously, the continued function remains convex. Furthermore, at $P_1 = \frac{1}{2}$ the derivative of the function F is zero $F'(1/2) = 0$, and since $F''(P_1) \geq 0$ we can conclude that $F(P_1)$ is non-decreasing on the whole interval.

F Finite statistics

Consider n independent random variables $X^{(i)} \in [a,b]$ with its mean $\mathbb{E}(\bar{X}) = \mathbb{E}(\frac{1}{n}\sum X^{(i)})$. The Hoeffding theorem [15] gives a simple bound on the deviation of the observed average $\bar{X}$ after n trails from the expected value $\mathbb{E}(\bar{X})$

$$\mathrm{P}\left(\bar{X} - t \geq \mathbb{E}(\bar{X})\right) \leq \exp\left(-\frac{2nt^2}{(b-a)^2}\right). \tag{91}$$

In our case, the observables $X^{(i)}$ takes values in the interval $[-1,3]$ so that $(b-a)^2 = 16$.

Let us now defined $X^{(i)}$ as the minimum of two variables $X^{(i)} = \min\{X_T^{(i)}, X_R^{(i)}\}$ such that $\bar{X} = \min\{\bar{X}_T, \bar{X}_R\}$. We have for the probability

$$\begin{aligned} \mathrm{P}\left(\bar{X} \geq x\right) &= \mathrm{P}\left(\bar{X}_T \geq x \text{ and } \bar{X}_R \geq x\right) \\ &\leq \mathrm{P}\left(\bar{X}_T \geq x\right), \mathrm{P}\left(\bar{X}_R \geq x\right). \end{aligned} \tag{92}$$

We now use $\bar{P}_1 + t \geq x = \min\{\mathbb{E}(\bar{X}_T), \mathbb{E}(\bar{X}_R)\} + t$ such that

$$\mathrm{P}\Big(\bar{X} \geq \bar{P}_1 + t\Big) \leq \mathrm{P}\Big(\bar{X} \geq \min\{\mathbb{E}(\bar{X}_T), \mathbb{E}(\bar{X}_R)\} + t\Big) \tag{93}$$

and consider two cases.

If $\mathbb{E}(\bar{X}_T) \leq \mathbb{E}(\bar{X}_R)$ we use

$$\begin{aligned} &\mathrm{P}\Big(\bar{X} \geq \min\{\mathbb{E}(\bar{X}_T), \mathbb{E}(\bar{X}_R)\} + t\Big) \\ &= \mathrm{P}\Big(\bar{X} \geq \mathbb{E}(\bar{X}_T) + t\Big) \\ &\leq \mathrm{P}\Big(\bar{X}_T \geq \mathbb{E}(\bar{X}_T) + t\Big) \\ &\leq \exp\left(-\frac{2nt^2}{16}\right). \end{aligned} \tag{94}$$

Otherwise, we do the same with $\bar{X}_R$. For both cases we find that

$$\mathrm{P}\Big(\min\{\bar{X}_T, \bar{X}_R\} - t \geq \bar{P}_1\Big) \leq \exp\left(-\frac{2nt^2}{16}\right) \tag{95}$$

or equivalently

$$\mathrm{P}\Big(\min\{\bar{X}_T, \bar{X}_R\} - t < \bar{P}_1\Big) \geq 1 - \exp\left(-\frac{2nt^2}{16}\right). \tag{96}$$

Writing the last expression in the form

$$\mathrm{P}\Big(\hat{q}_\alpha(\bar{X}_T, \bar{X}_R) < \bar{P}_1\Big) \geq 1 - \alpha \tag{97}$$

we find

$$\hat{q}_\alpha(\bar{X}_T, \bar{X}_R) = \min\{\bar{X}_T, \bar{X}_R\} - \sqrt{\frac{16\log(1/\alpha)}{2n}}, \tag{98}$$

the latter being a confidence interval for $\bar{P}_1$.

For the calibration-dependent benchmark, one naturally defines the random variable

$$Z_T = \begin{cases} C_1(\hat{t}, \hat{\eta}_T) & (\circ\bullet) \\ 0 & (\circ\circ) \text{ or } (\bullet\circ) \\ -C_2(\hat{t}, \hat{\eta}_T, \hat{\eta}_R) & (\bullet\bullet) \end{cases} \tag{99}$$

for the quantity $\hat{P}_1^{T*}(\boldsymbol{p})$ of Eq. (19), with positive constants $C_1, C_2 \geq 0$ giving rise to the confidence interval

$$\hat{q}_\alpha^{T*} = \bar{Z}_T - (C_1(\hat{t}, \hat{\eta}_T) + C_2(\hat{t}, \hat{\eta}_T, \hat{\eta}_R))\sqrt{\frac{\log(1/\alpha)}{2n}} \tag{100}$$

on the average single-photon weight $\bar{P}_1$. Defining Z_R similarly (with detector's roles exchanged) gives rise to the confidence interval

$$\hat{q}_\alpha^{R*} = \bar{Z}_R - (C_1(\hat{r}, \hat{\eta}_R) + C_2(\hat{r}, \hat{\eta}_R, \hat{\eta}_T))\sqrt{\frac{\log(1/\alpha)}{2n}}, \tag{101}$$

by exchanging the roles of the detectors. Both are confidence intervals on $\bar{P}_1$, that is

$$\mathrm{P}\left(\hat{q}_\alpha^{T(R)*} < \bar{P}_1\right) \geq 1 - \alpha. \tag{102}$$

It follows that

$$\begin{aligned} &\mathrm{P}\left(\max\{\hat{q}_\alpha^{T*}, \hat{q}_\alpha^{R*}\} < \bar{P}_1\right) \\ &= \mathrm{P}\left(\hat{q}_\alpha^{T*} < \bar{P}_1 \,\&\, \hat{q}_\alpha^{R*} < \bar{P}_1\right) \\ &= \mathrm{P}\left(\hat{q}_\alpha^{T*} < \bar{P}_1\right) \\ &\quad - \mathrm{P}\left(\hat{q}_\alpha^{T*} < \bar{P}_1 \,\&\, \hat{q}_\alpha^{R*} \geq \bar{P}_1\right) \\ &\geq \mathrm{P}\left(\hat{q}_\alpha^{T*} < \bar{P}_1\right) - \mathrm{P}\left(\hat{q}_\alpha^{R*} \geq \bar{P}_1\right) \\ &\geq 1 - 2\alpha, \end{aligned} \tag{103}$$

hence

$$\hat{q}_\alpha^{*} = \max\{\hat{q}_{\alpha/2}^{T*}, \hat{q}_{\alpha/2}^{R*}\} \tag{104}$$

is also a confidence interval on $\bar{P}_1$ with confidence level $1 - \alpha$.

Finally, let us discuss the witness of Wigner negativity. First, we label by Q the measured value of $\min\{\bar{X}_T, \bar{X}_R\}$ after n measurement rounds and consider the case $Q > 1/2$. Given that $W_{\rho^{(i)}}(0) \leq \frac{1}{\pi}(1 - 2P_1^{(i)})$ for each state, for any collection of states that have a positive average Wigner function at the origin $\bar{W}(0) = \frac{1}{n}\sum_{i=1}^n W_{\rho^{(i)}}(0) \geq 0$, the average single-photon weight is $\bar{P}_1 \leq \frac{1}{2}$. For such a collection we thus have

$$\begin{aligned} &\mathrm{P}\Big(\min\{\bar{X}_T, \bar{X}_R\} \geq Q\Big) \\ &\leq \mathrm{P}\Big(\min\{\bar{X}_T, \bar{X}_R\} - Q \geq \bar{P}_1 - \frac{1}{2}\Big) \\ &\leq \mathrm{P}\Big(\min\{\bar{X}_T, \bar{X}_R\} - \Big(Q - \frac{1}{2}\Big) \geq \bar{P}_1\Big) \\ &\leq \exp\left(-\frac{2n\left(Q - \frac{1}{2}\right)^2}{16}\right) \end{aligned} \tag{105}$$

by virtue of Eq. (95). In other words, for any collection of states with $\bar{W}(0) \geq 0$ the probability to get a benchmark value exceeding the observation $Q > 1/2$ is upper bounded by

$$\text{p-value} \leq \exp\left(-\frac{2n\left(\min\{\bar{X}_T, \bar{X}_R\} - \frac{1}{2}\right)^2}{16}\right). \tag{106}$$

In the calibration-dependent setting with the same argument, the p-value can be obtained analogously. For any value Q and an ensemble of random variables $Z_T^{(1)}, \ldots, Z_T^{(n)}$ such that $\bar{P}_1 \leq \frac{1}{2}$ one has

$$\begin{aligned} &\mathrm{P}\Big(\bar{Z}_T \geq Q\Big) \\ &\leq \mathrm{P}\Big(\bar{Z}_T - Q \geq \bar{P}_1 - \frac{1}{2}\Big) \\ &\leq \mathrm{P}\Big(\bar{Z}_T - \Big(Q - \frac{1}{2}\Big) \geq \bar{P}_1\Big) \\ &\leq \exp\left(-\frac{2n\left(Q - \frac{1}{2}\right)^2}{(C_1 + C_2)^2}\right). \end{aligned} \tag{107}$$

Hence, the hypothesis $\bar{P}_1 \leq 1/2$ is associated to the p-value

$$\text{p-value} \leq \exp\left(-\frac{2n(\bar{Z}_T - \frac{1}{2})^2}{(C_1(\hat{t},\hat{\eta}_T) + C_2(\hat{t},\hat{\eta}_T,\hat{\eta}_R))^2}\right), \tag{108}$$

where $\bar{Z}_T$ is now the value of $\bar{Z}_T = \frac{1}{n}\sum_{i=1}^n Z_T^{(i)}$ observed in the experiment. Exchanging the roles of the detectors we also obtain

$$\text{p-value} \leq \exp\left(-\frac{2n(\bar{Z}_R - \frac{1}{2})^2}{(C_1(\hat{r},\hat{\eta}_R) + C_2(\hat{r},\hat{\eta}_R,\hat{\eta}_T))^2}\right). \tag{109}$$

Given the observed data $(n_{\circ\circ}, n_{\bullet\circ}, n_{\circ\bullet}, n_{\bullet\bullet})$ both bounds are valid statements about all collections of states with $\bar{P}_1 \leq \frac{1}{2}$. One can then simply choose the most favorable bound, that is

$$\begin{aligned}&\text{p-value}\\ &\leq \min\Big\{\exp\left(-\frac{2n(\bar{Z}_T - \frac{1}{2})^2}{(C_1(\hat{t},\hat{\eta}_T) + C_2(\hat{t},\hat{\eta}_T,\hat{\eta}_R))^2}\right),\\ &\qquad \exp\left(-\frac{2n(\bar{Z}_R - \frac{1}{2})^2}{(C_1(\hat{r},\hat{\eta}_R) + C_2(\hat{r},\hat{\eta}_R,\hat{\eta}_T))^2}\right)\Big\}\end{aligned} \tag{110}$$

where $\bar{Z}_T = \frac{1}{n}(C_1(\hat{t},\hat{\eta}_T)n_{\circ\bullet} - C_2(\hat{t},\hat{\eta}_T\hat{\eta}_R)n_{\bullet\bullet})$ and $\bar{Z}_R = \frac{1}{n}(C_1(\hat{r},\hat{\eta}_R)n_{\bullet\circ} - C_2(\hat{r},\hat{\eta}_R\hat{\eta}_T)n_{\bullet\bullet})$.

G Multi-mode product states

We now consider multi-mode product states of the form

$$\varrho = \bigotimes_k \rho_k, \tag{111}$$

where the state of each mode $\rho^{[k]}$ is associated to a probability vector $\boldsymbol{p}^{[k]}$, as defined by the expected values of the operators in Eq. (2). For multi-mode states, we do not have access to individual values of $\boldsymbol{p}^{[k]}$. Instead, a detector does not click if none of the modes triggers a click. Hence, for the state ϱ, the observed probabilities satisfy $p_{\circ\circ} = \prod_k p_{\circ\circ}^{[k]}$, $p_{\_\circ} = \prod_k p_{\_\circ}^{[k]}$, and $p_{\circ\_} = \prod_k p_{\circ\_}^{[k]}$. Denote $P_1^{[k]} = \langle 1|\,\rho_k\,|1\rangle$ the single-photon probability for the mode k. Under the assumption that the beam splitter is balanced $p_{\_\circ}^{[k]} = p_{\circ\_}^{[k]} = \sum_n P_n^{[k]}\frac{1}{2^n}$ we will show in the next section that

$$\widetilde{P}_1^T(\boldsymbol{p}) = \frac{1}{2}(12\,p_{\circ\_} - 9\,p_{\circ\circ} - 4) \leq \max_k P_1^{[k]}. \tag{112}$$

The case of unbalanced beam splitter is analogous with the single-mode case, we introduce $\widetilde{P}_1^R(\boldsymbol{p})$ which is obtained from the definition of $\widetilde{P}_1^T(\boldsymbol{p})$ (given in Eq. (112)) by replacing $p_{\circ\_}$ by $p_{\_\circ}$. Since either $p_{\circ\_}^{[k]} \geq p_{\_\circ}^{[k]}$ or $p_{\circ\_}^{[k]} \leq p_{\_\circ}^{[k]}$ holds for all modes k, the minimum of $p_{\circ\_}^{[k]}$ and $p_{\_\circ}^{[k]}$ is a lower bound on $\sum_n P_n^{[k]}(\lambda)\frac{1}{2^n}$. We deduce that

$$\max_k P_1^{[k]} \geq \widetilde{P}_1(\boldsymbol{p}) = \min\{\widetilde{P}_1^T(\boldsymbol{p}), \widetilde{P}_1^R(\boldsymbol{p})\}. \tag{113}$$

Under the assumption that the source produces a multi-mode product state ϱ of the form given in Eq. (111), we thus deduce that there is a mode k_*, that can in principle be filtered out, such that the corresponding state $\rho^{[k_*]}$ satisfies $\langle 1|\rho^{[k_*]}|1\rangle \geq \widetilde{P}_1(\boldsymbol{p})$.

G.1 The proof of Eq. (112)

Consider a multi-mode product state $\varrho = \bigotimes_k \rho_k$ with $P_1^{[k]} \leq P$ in each mode. We label $(p_{\circ\_}^{[k]}, p_{\circ\circ}^{[k]})$ the statistics associated to ρ_k and $(p_{\circ\_}, p_{\circ\circ})$ the statistics associated to ρ. For a balanced beam splitter, we have $(p_{\circ\_}^{[k]}, p_{\circ\circ}^{[k]}) \in \boldsymbol{Q}_P$, with

$$\begin{aligned}\boldsymbol{Q}_P = \text{Polytope}\Big\{&(0,0), \left(\frac{1+P}{4}, 0\right),\\ &\left(\frac{2-P}{2}, 1-P\right), (1,1)\Big\}.\end{aligned}$$

The probabilities $p_{\circ\_}$ and $p_{\circ\circ}$ satisfy

$$\begin{aligned}p_{\circ\_} &= \prod_{k=1}^n p_{\circ\_}^{[k]},\\ p_{\circ\circ} &= \prod_{k=1}^n p_{\circ\circ}^{[k]}.\end{aligned} \tag{114}$$

Our first aim is to analyze the possible set of values $\boldsymbol{Q}_P^\infty = \{(p_{\circ\_}, p_{\circ\circ})\}$ for all n from 1 to ∞ and in particular, to show that $\boldsymbol{Q}_P^\infty \subset \boldsymbol{Q}_P$ for $P \geq \frac{1}{2}$. Naturally, we are interested in the extreme points of this set. Eq. (114) is linear in all points $(p_{\circ\_}^{[k]}, p_{\circ\circ}^{[k]})$, hence the extreme points of $\boldsymbol{Q}_P^\infty$ are obtained by combining the vertices of $\boldsymbol{Q}_P$.

Whenever a single vertex $(p_{\circ\_}^{[k]}, p_{\circ\circ}^{[k]}) = (0,0)$ appears in the product of Eq. (114), it results in $(p_{\circ\_}, p_{\circ\circ}) = (0,0)$. Similarly, if the vertex $(p_{\circ\_}^{[k]}, p_{\circ\circ}^{[k]}) = \left(\frac{1+P}{4}, 0\right)$ is chosen for at least one mode k, $p_{\circ\circ} = 0$ and $p_{\circ\_} = \frac{1+P}{4}\prod_{j\neq k} p_{\circ\_}^{[j]} \leq \frac{1+P}{4}$. This means that the point $(p_{\circ\_}, p_{\circ\circ} = 0)$ remains inside the original polytope $\boldsymbol{Q}_P$. We can thus remember that $(0,0)$ and $\left(\frac{1+P}{4}, 0\right)$ are points of $\boldsymbol{Q}_P^\infty$, but ignore these vertices in the further construction. Analogously, all modes with $(p_{\circ\_}^{[k]}, p_{\circ\circ}^{[k]}) = (1,1)$ do not change the value of the product, and we can also ignore this vertex. Hence, the only products in Eq. (114) that are potentially not in $\boldsymbol{Q}_P$ are of the form

$$(p_{\circ\_}, p_{\circ\circ})_n = \left(\left(\frac{2-P}{2}\right)^n, (1-P)^n\right) \tag{115}$$

for $n \geq 2$. Let us first consider the point $(p_{\circ\_}, p_{\circ\circ})_2$.

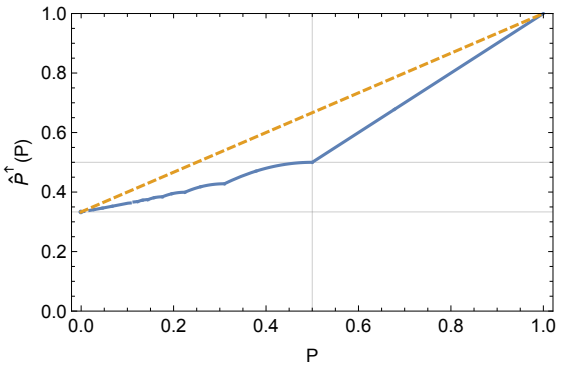

Figure 5: (Full line) Representation of $\hat{P}_1^{T\uparrow}(P)$ as a function of P (full blue line) and an upper-bound (dashed orange line) given by a simple linear function of the form $\frac{1}{3}+\frac{2}{3}P \geq \hat{P}_1^{T\uparrow}(P)$.

It remains inside $\boldsymbol{Q}_P$ if and only if

$$\begin{aligned} 4p_{\circ\_} - 3p_{\circ\circ} - 1 &\leq P \\ 4\left(\frac{2-P}{2}\right)^2 - 3(1-P)^2 - 1 &\leq P \\ P - 2P^2 &\leq 0 \\ P &\geq \frac{1}{2}. \end{aligned} \tag{116}$$

Naturally, if $(p_{\circ\_}, p_{\circ\circ})_2 \in \boldsymbol{Q}_P$ the next points $(p_{\circ\_}, p_{\circ\circ})_n$ are also in $\boldsymbol{Q}_P$. Therefore, $\boldsymbol{Q}_P^\infty \subset \boldsymbol{Q}_P$ for $P \geq \frac{1}{2}$. This means that for any state of the form $\varrho = \bigotimes_k \rho_k$, with $P_1^{[k]} \leq 1/2 \leq P$, $4p_{\circ\_} - 3p_{\circ\circ} - 1 \leq P$.

In order to extend the analysis to any value of P, we would need to analyze $\boldsymbol{Q}_P^\infty$ for a arbitrary P, which is cumbersome. Instead, we analyze the maximal value that $\hat{P}_1^T(\boldsymbol{p})$ takes on $\boldsymbol{Q}_P^\infty$. We know that it takes its maximum value on one of the vertices $(p_{\circ\_}, p_{\circ\circ})_n$, and denote these values

$$\hat{P}_1^T(n) = 4\left(\frac{2-P}{2}\right)^n - 3(1-P)^n - 1, \tag{117}$$

for $n \geq 1$. Its maximal value in $\boldsymbol{Q}_P^\infty$ is thus given by

$$\begin{aligned} \hat{P}_1^{T\uparrow}(P) &= \sup_{\boldsymbol{p}\in\boldsymbol{Q}_P^\infty} \hat{P}_1^T(\boldsymbol{p}) \\ &= \sup_{n\geq 1} \hat{P}_1^T(n). \end{aligned} \tag{118}$$

Let us now look at $\hat{P}_1^T(n)$ as a function of a continuous parameter $n \in [0, \infty)$, and compute its derivative

$$\frac{d}{dn}\hat{P}_1^T(n) = 4X^n \log(X) - 3Y^n \log(Y) \tag{119}$$

with $X = \frac{2-P}{2}$ and $Y = 1-P$. $\hat{P}_1^T(n)$ admits a unique local extremum $\frac{d}{dn}\hat{P}_1^T(n) = 0$ at

$$n_* = \frac{\log\left(\frac{4\log(X)}{3\log(Y)}\right)}{\log(X) - \log(Y)}. \tag{120}$$

Furthermore, one easily sees that $\hat{P}_1^T(0) = 0$, $\hat{P}_1^T(\infty) = -1$ and $\hat{P}_1^T(1) = P$ and hence $\hat{P}_1^T(n_*)$ is the global maximum of the function.

Next, we recall that n can only take integer values. Thus, the maximal value reads

$$\hat{P}_1^{T\uparrow}(P) = \max\{\hat{P}_1^T(\lfloor n_* \rfloor), \hat{P}_1^T(\lfloor n_* + 1 \rfloor)\}. \tag{121}$$

It is quite an irregular function, as can be seen in Fig. 5. The boundary value $\hat{P}_1^{T\uparrow}(0) = \lim_{P\to 0}\hat{P}_1^{T\uparrow}(P) = \frac{1}{3}$ can be computed analytically. We show numerically that it is upper-bounded by a simple linear function

$$\hat{P}_1^T(\boldsymbol{p}) \leq \hat{P}_1^{T\uparrow}(P) \leq \frac{1}{3} + \frac{2}{3}P, \tag{122}$$

also can be seen in Fig. 5. By inverting the last inequality we find that

$$\begin{aligned} &\widetilde{P}_1^T(\boldsymbol{p}) \leq P \qquad \text{for} \\ &\widetilde{P}_1^T(\boldsymbol{p}) = \frac{3\hat{P}_1^T(\boldsymbol{p}) - 1}{2} = \frac{1}{2}(12p_{\circ\_} - 9p_{\circ\circ} - 4). \end{aligned} \tag{123}$$

Therefore, for any value P such that $\widetilde{P}_1^T(\boldsymbol{p}) > P$, we can conclude that at least one mode satisfies $\max_k \langle 1|\rho^{[k]}|1\rangle > P$.

G.2 Finite statistics

Here, in order to obtain a confidence interval we define an independent random variable

$$Y_T = \begin{cases} 4 & (\circ\bullet) \\ -1/2 & (\circ\circ) \\ -2 & (\bullet\circ) \text{ or } (\bullet\bullet) \end{cases}, \tag{124}$$

with $\mathbb{E}(Y_T) = \widetilde{P}_1^T(\boldsymbol{p})$. Similarly, we define Y_R by exchanging the role of the two detectors and get $\mathbb{E}(Y_R) = \widetilde{P}_1^R(\boldsymbol{p})$ with $Y_{T(R)} \in [-2, 4]$. The same exact analysis as above yields a one-sided confidence interval

$$\widetilde{q}_\alpha(\bar{Y}_T, \bar{Y}_R) = \min\{\bar{Y}_T, \bar{Y}_R\} - \sqrt{\frac{36\log(1/\alpha)}{2n}} \tag{125}$$

on the quantity $\max_k P_1^{[k]}$ averaged over all states produced by the source. In the general multi-mode case, the same quantity is a one-sided interval on the quantity $\sum_\lambda p(\lambda)\max_k P_1^{[k]}(\lambda)$ averaged over all states produced by the source.

References

[1] M. D. Eisaman, J. Fan, A. Migdall, and S. V. Polyakov. Invited review article: Single-photon sources and detectors. *Review of Scientific Instruments*, 82(7):071101, 2011. DOI: 10.1063/1.3610677.

[2] Sarah Thomas and Pascale Senellart. The race for the ideal single-photon source is on. *Nature Nanotechnology*, 16(4):367–368, 2021. DOI: 10.1038/s41565-021-00851-1.

[3] Nicolas Sangouard and Hugo Zbinden. What are single photons good for? *Journal of Modern Optics*, 59(17):1458–1464, 2012. DOI: 10.1080/09500340.2012.687500.

[4] Pieter Kok, W. J. Munro, Kae Nemoto, T. C. Ralph, Jonathan P. Dowling, and G. J. Milburn. Linear optical quantum computing with photonic qubits. *Rev. Mod. Phys.*, 79:135–174, Jan 2007. DOI: 10.1103/RevModPhys.79.135.

[5] Christopher J. Chunnilall, Ivo Pietro Degiovanni, Stefan Kück, Ingmar Müller, and Alastair G. Sinclair. Metrology of single-photon sources and detectors: a review. *Optical Engineering*, 53(8):081910–081910, July 2014. DOI: 10.1117/1.oe.53.8.081910.

[6] Stefan Kück. Single photon sources for absolute radiometry – a review about the current state of the art. *Measurement: Sensors*, 18:100219, 2021. ISSN 2665-9174. DOI: 10.1016/j.measen.2021.100219.

[7] D. F. Walls and Gerard J. Milburn. *Quantum Optics*. Springer, Berlin, Heidelberg, 2 edition, 2008. ISBN 978-3-540-28574-8. DOI: 10.1007/978-3-540-28574-8.

[8] Miroslav Ježek, Ivo Straka, Michal Mičuda, Miloslav Dušek, Jaromír Fiurášek, and Radim Filip. Experimental test of the quantum non-gaussian character of a heralded single-photon state. *Phys. Rev. Lett.*, 107:213602, Nov 2011. DOI: 10.1103/PhysRevLett.107.213602.

[9] Ana Predojević, Miroslav Ježek, Tobias Huber, Harishankar Jayakumar, Thomas Kauten, Glenn S. Solomon, Radim Filip, and Gregor Weihs. Efficiency vs. multi-photon contribution test for quantum dots. *Opt. Express*, 2014. DOI: 10.1364/OE.22.004789.

[10] Ivo Straka, Ana Predojević, Tobias Huber, Luká š Lachman, Lorenz Butschek, Martina Miková, Michal Mičuda, Glenn S. Solomon, Gregor Weihs, Miroslav Ježek, and Radim Filip. Quantum non-gaussian depth of single-photon states. *Phys. Rev. Lett.*, 113:223603, Nov 2014. DOI: 10.1103/PhysRevLett.113.223603.

[11] Anatole Kenfack and Karol Życzkowski. Negativity of the wigner function as an indicator of non-classicality. *Journal of Optics B: Quantum and Semiclassical Optics*, 6(10):396, 2004. DOI: 10.1088/1464-4266/6/10/003.

[12] Alan Migdall, Sergey V Polyakov, Jingyun Fan, and Joshua C Bienfang. *Single-photon generation and detection: physics and applications*. Academic Press, 2013. ISBN 978-0-12-387695-9.

[13] Katiúscia N Cassemiro, Kaisa Laiho, and Christine Silberhorn. Accessing the purity of a single photon by the width of the hong–ou–mandel interference. *New Journal of Physics*, 12(11):113052, 2010. DOI: 10.1088/1367-2630/12/11/113052.

[14] Kevin Zielnicki, Karina Garay-Palmett, Daniel Cruz-Delgado, Hector Cruz-Ramirez, Michael F. O'Boyle, Bin Fang, Virginia O. Lorenz, Alfred B. U'Ren, and Paul G. Kwiat. Joint spectral characterization of photon-pair sources. *Journal of Modern Optics*, 65(10):1141–1160, Jun 2018. DOI: 10.1080/09500340.2018.1437228.

[15] Wassily Hoeffding. Probability Inequalities for Sums of Bounded Random Variables. *Journal of the American Statistical Association*, 58(301):13–30, mar 1963. DOI: 10.1080/01621459.1963.10500830.

[16] E. Wigner. On the quantum correction for thermodynamic equilibrium. *Phys. Rev.*, 40:749–759, Jun 1932. DOI: 10.1103/PhysRev.40.749.

[17] Werner Vogel and Dirk-Gunnar Welsch. *Quantum optics*. John Wiley & Sons, 2006. DOI: 10.1002/3527608524.

[18] R. L. Hudson. When is the wigner quasi-probability density non-negative? *Reports on Mathematical Physics*, 6(2):249–252, 1974. ISSN 0034-4877. DOI: 10.1016/0034-4877(74)90007-X.

[19] U. Chabaud, PE. Emeriau, and F. Grosshans. Witnessing wigner negativity. *Quantum*, 471: 230503, Jun 2021. DOI: 10.22331/q-2021-06-08-471.

[20] Antoine Royer. Wigner function as the expectation value of a parity operator. *Phys. Rev. A*, 15:449–450, Feb 1977. DOI: 10.1103/PhysRevA.15.449.

[21] F. W. J. Olver, A. B. Olde Daalhuis, D. W. Lozier, B. I. Schneider, R. F. Boisvert, C. W. Clark, B. R. Miller, B. V. Saunders, H. S. Cohl, M. A. McClain, and eds. Nist digital library of mathematical functions. `http://dlmf.nist.gov/`, Release 1.1.3 of 2021-09-15.

[22] M. Munroe, D. Boggavarapu, M. E. Anderson, and M. G. Raymer. Photon-number statistics from the phase-averaged quadrature-field distribution: Theory and ultrafast measurement. *Phys. Rev. A*, 52:R924–R927, Aug 1995. DOI: 10.1103/PhysRevA.52.R924.

[23] N. Bruno, A. Martin, T. Guerreiro, B. Sanguinetti, and R. T. Thew. Pulsed source of spectrally uncorrelated and indistinguishable photons at telecom wavelengths. *Optics Express*, 22(14): 17246, jul 2014. DOI: 10.1364/OE.22.017246.

[24] T. Guerreiro, A. Martin, B. Sanguinetti, N. Bruno, H. Zbinden, and R. T. Thew. High efficiency coupling of photon pairs in practice. *Optics Express*, 21(23):27641, nov 2013. DOI: 10.1364/OE.21.027641.

[25] Misael Caloz, Matthieu Perrenoud, Claire Autebert, Boris Korzh, Markus Weiss, Christian

Schönenberger, Richard J. Warburton, Hugo Zbinden, and Félix Bussières. High-detection efficiency and low-timing jitter with amorphous superconducting nanowire single-photon detectors. *Applied Physics Letters*, 112(6), 2018. DOI: 10.1063/1.5010102.

[26] P. Sekatski, E. Oudot, P. Caspar, R.T. Thew, and N. Sangouard. Benchmarking single-photon sources from an auto-correlation measurement [data set]. 2022. DOI: 10.5281/zenodo.7245446.

[27] Marlan O Scully and M Suhail Zubairy. *Quantum optics*. American Association of Physics Teachers, 1999. DOI: 10.1017/CBO9780511813993.

[28] Pavel Sekatski, N Sangouard, Félix Bussieres, Christoph Clausen, Nicolas Gisin, and Hugo Zbinden. Detector imperfections in photon-pair source characterization. *Journal of Physics B: Atomic, Molecular and Optical Physics*, 45(12):124016, 2012. DOI: 10.1088/0953-4075/45/12/124016.

[29] A. Dodel, A. Mayinda, E. Oudot, A. Martin, P. Sekatski, J.-D. Bancal, and N. Sangouard. Proposal for witnessing non-classical light with the human eye. *Quantum*, 1:7, April 2017. ISSN 2521-327X. DOI: 10.22331/q-2017-04-25-7.

P.4. High-efficiency photon-number-resolving detector for improving heralded single-photon sources

Quantum Science and Technology

High efficiency photon number resolving detector for improving heralded single-photon sources

To cite this article before publication: Lorenzo Stasi *et al* 2023 *Quantum Sci. Technol.* in press https://doi.org/10.1088/2058-9565/ace54b

High-efficiency photon-number-resolving detector for improving heralded single-photon sources

Lorenzo Stasi,[1, 2, *] Patrik Caspar,[1] Tiff Brydges,[1] Hugo Zbinden,[1] Félix Bussières,[2] and Rob Thew[1]

[1] *Department of Applied Physics, University of Geneva, CH-1211 Geneva, Switzerland*
[2] *ID Quantique SA, CH-1227 Geneva, Switzerland*

(Dated: July 3, 2023)

Heralded single-photon sources (HSPS) intrinsically suffer from multiphoton emission, leading to a trade-off between the source's single-photon quality and the heralding rate. A solution to this problem is to use photon-number-resolving (PNR) detectors to filter out the heralding events where more than one photon pair is created. Here, we demonstrate an improvement of a HSPS by heralding photons using a high-efficiency parallel superconducting nanowire single-photon detector (P-SNSPD) with PNR power. Specifically, we show a reduction in the $g^{(2)}(0)$ of the heralded single photon by $(26.9 \pm 0.1)\,\%$ for a fixed pump power, or alternatively, an increase in the heralding rate by a factor of 1.368 ± 0.002 for a fixed $g^{(2)}(0)$. We also demonstrate that such a PNR device can reveal thermal photon-number statistics of unheralded photons, which is enabled by our ability to construct its full input-output response function. These results are possible thanks to our P-SNSPD architecture that ensures non-latching operation with no electrical crosstalk, which are essential conditions necessary to obtain the correct photon-number statistics and also faster recovery times, therefore enabling fast heralding rates. These results show that our efficient photon-number-resolving P-SNSPD architecture can significantly improve the performance of HSPSs and can precisely characterize them, making these detectors a useful tool for a wide range of optical quantum information protocols.

I. INTRODUCTION

Over the past decades, there have been remarkable developments in the field of quantum technologies. In particular, photonic systems employing single photons have been used in a variety of applications, ranging from quantum communication and repeater protocols [1, 2] to linear optical quantum computing [3–5] and Gaussian boson sampling [6–8]. A convenient and versatile tool to generate single photons are heralded single-photon sources (HSPS) [9, 10]. They have the advantage of operating at room temperature, are wavelength and bandwidth tunable, and can produce indistinguishable and pure photons [11–13].

The photon generation mechanism in HSPSs is, however, probabilistic and multi-photon events can also occur. Such events are undesired, leading to a decrease in the single-photon fidelity [14]. Therefore, to minimize their impact, HSPSs are often used in the low-squeezing regime ($\mu \ll 1$, where μ is the mean photon-pair number per pump pulse). However, in such a regime the probability of emitting vacuum states increases, reducing the generation rate of single photons.

A possible solution to this problem is to use a photon-number resolving (PNR) detector as the heralding detector. In this way, it is possible to filter out events when more than one photon is detected, therefore lowering the multi-photon contribution in the heralded state. In principle, such a scheme would allow one to work with a higher μ, making it possible to increase the heralding rate towards the theoretical limit of 25 % of the pump rate [15].

Transition-edge sensors (TES), have shown to be able to distinguish high numbers of photons with high probability [16, 17]. However, the long recovery time of several microseconds precludes their application in high rate experiments, limiting their operation to the hundreds of kHz regime. In addition, TESs need ultra-low temperatures ($< 100\,\mathrm{mK}$) which requires a complex cryogenic system.

Recently, superconducting nanowire single-photon detectors (SNSPD) have demonstrated few-photon PNR capability based on the signal's slew rate [18] or on the amplitude of the voltage pulse when used in combination with an impedance-matching taper [19]. Both methods have been employed in recent experiments to improve the heralded $g^{(2)}(0)$ measurement of HSPSs [20, 21]. In the first approach, one can either fit the waveform's rising edge or use a differentiating circuit to retrieve the photon-number event, which requires detectors with very low timing jitter. In the second scenario, the impedance-matching taper acts as a kinetic inductive element, which increases the recovery time of the overall detector, potentially limiting its usage at high repetition rates. Additionally, to be able to resolve photon-number states, photons need to arrive with minimum delay between each other, limiting light pulses to tens of ps [19].

A promising alternative technology is based on SNSPDs in a parallel configuration (P-SNSPD) [22–24]. This consists of an array of several pixels (the single SNSPD element) which are electrically connected in parallel. With respect to an array of independent pixels, which would require one coaxial cable per pixel for the read-out, a P-SNSPD requires only one, which is a practical advantage. In fact, information on the number of pixels that clicked can be extracted directly from the sig-

* Corresponding author: lorenzo.stasi@idquantique.com

nal amplitude's only, so a full digitalization and analysis of the trace or fast and precise electronics are not necessary, which can ease the photon-number discrimination process. Hence, a P-SNSPD can be used with any discriminator-based time-tagging device. In addition, the active detection area covered by the P-SNSPD is the same as a single-meander SNSPD, resulting in pixels of shorter length that can recover faster thanks to the lower kinetic inductance.

However, ensuring that a P-SNSPD operates correctly is not a trivial task. In fact, many effects can occur which would alter the experimental results: thermal crosstalk, electrical crosstalk and latching. The common solution is to operate the detector at a lower bias current to mitigate the thermal crosstalk and the current redistribution effect that causes the electrical crosstalk (and possibly latching). However, such a solution is not effective at high count rates and, more importantly, it lowers the system detection efficiency of the device, which is clearly non-ideal for optimal operation of a HSPS. In order to solve these problems altogether, we developed a novel P-SNSPD design that can reach high detection efficiency and high detection rate in a latch-free regime, while operating the detector at the optimal bias current value. Detailed information of this architecture can be found in Ref. [23]. We also investigated the PNR performance of our novel P-SNSPD design in Ref. [24], where the full input-output response function of the detector is obtained thanks to the development of a new analytical model that describes the multi-photon detection probabilities. Therefore, thanks to such developments, our P-SNSPD can be used to measure photon-number statistics in high repetition rate regimes.

Another important aspect regarding single-photon sources is the characterization of their emission statistics. More generally speaking, it is paramount to understand if a particular quantum system may suffer from multi-photon emission (as a thermal source does) and to quantify it [25–27]. To this end, one needs a PNR detector with a fully mapped input-output response function that displays a clear distinction between the different generated signals in order to correctly assign each one of them to the corresponding photon-count event (as a P-SNSPD does). In fact, it is only in this way that it is possible to correctly reconstruct the emitting light statistics of a source.

This paper reports on the improvements to a HSPS that can be achieved through the use of a high ($> 80\,\%$) single-photon-efficiency P-SNSPD, when used to distinguish multi-photon detection events. We first introduce the theoretical tools that we use to describe the employed source and the detectors. Then we conduct two experiments, first we show the improvement from using the P-SNSPD as a heralding detector as part of a HSPS with regard to improving the $g^{(2)}(0)$ of the heralded single-photon state. Second, we show that a P-SNSPD can be used to correctly measure and reconstruct the thermal statistics of the HSPS. We benchmark our result by retrieving the unconditional $g^{(2)}(0)$ on a single spatial mode. This result demonstrates that our P-SNSPD can be used as a quantum metrology tool for source characterization [25–27].

II. THEORY

The ideal state generated by a spontaneous parametric down-conversion (SPDC) source is a two-mode squeezed vacuum (TMSV) state described by [28]

$$\begin{aligned} |\Psi\rangle_{si} &= \sqrt{1-\lambda^2}\sum_{n=0}^{\infty}\lambda^n\,|nn\rangle_{si} \\ &= \sum_{n=0}^{\infty}\sqrt{\frac{\mu^n}{(\mu+1)^{n+1}}}\,|nn\rangle_{si}\,, \end{aligned} \tag{1}$$

where $\lambda = \tanh r$ with the squeezing parameter r and the mean photon number $\mu = \sinh^2 r = \lambda^2/(1-\lambda^2)$. Note that the marginal states of the signal (s) and idler (i) modes are thermal states with photon-number probability distribution

$$p_n = \frac{\mu^n}{(\mu+1)^{n+1}}. \tag{2}$$

A standard measurement to probe a SPDC source is represented by the second-order autocorrelation function [28]

$$g^{(2)}(0) = \frac{\langle\hat{n}(\hat{n}-1)\rangle}{\langle\hat{n}\rangle^2} = \frac{\sum_n n(n-1)p_n}{\left(\sum_n np_n\right)^2}, \tag{3}$$

where $\hat{n}$ is the photon-number operator and p_n the photon-number probability distribution of the state. To this end, two different measurements can be performed on a SPDC source, unconditional and heralded $g^{(2)}(0)$. The former is measured on one mode of the state and gives information on the statistical nature of a source and on the spectral purity of the generated photons. The latter instead is measured on one mode given a heralding detection on the other mode of the state and quantifies the amount of multi-photon pairs that are generated from the SPDC source.

First, we consider the scenario shown in Fig. 1(a), in which the signal photon is sent to a P-SNSPD acting as a heralding detector, $\mathrm{D_h}$, and the idler photon is sent to a 50/50 beam splitter followed by two threshold SNSPDs, $\mathrm{D_a}$ and $\mathrm{D_b}$, which are only able to distinguish between 0 or at least one photon. In order to obtain analytical equations describing the single and coincidence detection probabilities per pump pulse, we use the approach of Ref. [29]. In this formalism, the TMSV state $\rho = |\Psi\rangle\langle\Psi|_{si}$ can be expressed as 4×4 covariance matrix with μ as a single free parameter. Furthermore, the action of beam splitters can be modeled by Gaussian unitary operations. The formalism additionally allows modes to be traced out, and so we are able to model transmission loss on

a given mode by introducing an auxiliary mode, applying a beam splitter operation between the two modes, and finally tracing out the auxiliary mode. Moreover, the formalism also allows for calculation of the expectation value of a given Gaussian state after projection onto vacuum. Therefore, we can model threshold detectors described by positive-operator-valued measure (POVM) elements $E_0 = |0\rangle\langle 0|$ corresponding to a no-click outcome and $E_c = \mathbb{1} - |0\rangle\langle 0|$ to a click outcome. To obtain a model for the P-SNSPD, we note that each of the N pixels of the detector is a threshold detector. Therefore, a physically intuitive model for the P-SNSPD consists of a sequence of beam splitters, with splitting ratios corresponding to the characterized pixel efficiencies, and N threshold detectors (see Appendix A for further details).

To additionally take account of the non-unit spectral purity of our source, we assume a multimode state $\rho = \varrho_1 \otimes \cdots \otimes \varrho_M$. Here $\varrho_k = |\Psi\rangle\langle\Psi|_k$, as defined in Eq. (1), describes a single Schmidt mode with mean photon number $\lambda_k \mu$, where the Schmidt coefficients are normalized such that $\sum_k \lambda_k = 1$. In the case of a SPDC source, the Schmidt coefficients can be estimated by a measurement of the joint spectral intensity [30]. In this way, we obtain a model to accurately describe the expected single and coincidence detection probabilities per pump pulse and the heralded $g^{(2)}(0)$

$$g^{(2)}_{\mathrm{h}}(0) \approx \frac{p_{\mathrm{h}} p_{\mathrm{hab}}}{p_{\mathrm{ha}} p_{\mathrm{hb}}}, \tag{4}$$

where p_{h} is the probability of a heralding detection, $p_{\mathrm{ha(b)}}$ the probability of a coincidence detection between detectors $\mathrm{D_h}$ and $\mathrm{D_a}$ ($\mathrm{D_b}$), and p_{hab} the triple-coincidence probability between $\mathrm{D_h}$, $\mathrm{D_a}$, and $\mathrm{D_b}$. For details on the derivation and the explicit formulas for the probabilities, see Appendix A.

Similarly, the unconditional $g^{(2)}(0)$ on one spatial mode of the TMSV state can be evaluated as

$$g^{(2)}_{\mathrm{unc.}}(0) \approx \frac{p_{\mathrm{ab}}}{p_{\mathrm{a}} p_{\mathrm{b}}}, \tag{5}$$

where $p_{\mathrm{a(b)}}$ is the probability of a detection on $\mathrm{D_a}$ ($\mathrm{D_b}$) and p_{ab} the probability of a coincidence detection between $\mathrm{D_a}$ and $\mathrm{D_b}$. We note that in the case where we have direct access to the photon-number probability distribution p_n of the state, e.g. by measuring it with a PNR detector, one can also use Eq. (3) to obtain $g^{(2)}_{\mathrm{unc.}}(0)$.

III. EXPERIMENT

In a first experiment, as illustrated in Fig. 1(a), we employ a P-SNSPD as the heralding detector in a HSPS and assess its performance by measuring $g^{(2)}_{\mathrm{h}}(0)$ for different pump power settings. We use the P-SNSPD in two different configurations: as a threshold detector, where all the $(n \geq 1)$-click events are considered as a (single) detection, and as a PNR detector, where only $(n = 1)$-click events are considered.

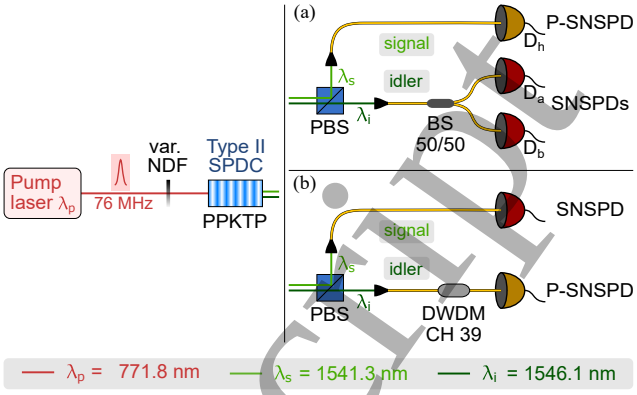

Figure 1. Experimental setups used for the two different measurements of (a) heralded $g^{(2)}(0)$ and (b) unconditional $g^{(2)}(0)$. A Ti:sapphire laser in the picosecond pulsed regime at $\lambda_p = 771.8$ nm with a repetition rate of 76 MHz is used to pump a 30 mm long periodically poled potassium titanyl phosphate (PPKTP) bulk nonlinear crystal with poling period $\Lambda = 46.2\,\mu$m. In this way, non-degenerate signal ($\lambda_s = 1541.3$ nm) and idler ($\lambda_i = 1546.1$ nm) photon pairs are generated via type-II SPDC, where the pump power can be varied with a reflective variable neutral density filter (NDF). Signal and idler photons are separated by a polarizing beam splitter (PBS) and coupled into single-mode optical fibers. (a) The heralding signal photons are detected by the P-SNSPD while the idler photons are sent to a 50/50 beam splitter (BS) and detected by threshold SNSPDs. (b) The idler photons are spectrally filtered by a dense wavelength division multiplexer (DWDM) channel 39 and detected by the P-SNSPD for the reconstruction of the thermal photon number statistics.

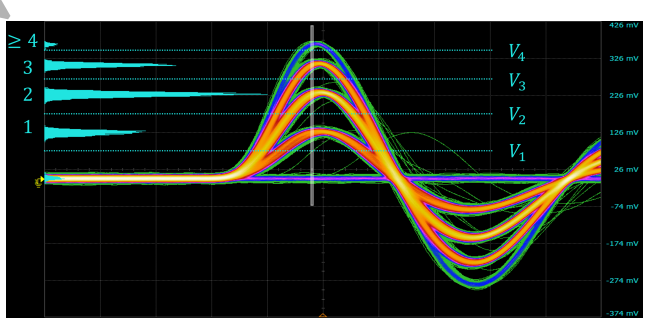

Figure 2. Oscilloscope persistence traces of the electrical signals generated by the P-SNSPD (500 ps/div and 100 mV/div). On the left, are reported the waveforms histograms corresponding to each n-click event, taken from the vertical white slice. The n-click events are discriminated by setting different voltage thresholds on the time tagger.

In a second experiment, shown in Fig. 1(b), we replace the 50/50 beam splitter and the two standard SNSPDs by a single P-SNSPD to reconstruct the photon-number probability distribution. Using Eq. (3) we calculate $g^{(2)}_{\mathrm{unc.}}(0)$ and compare it to the values obtained when using the more standard method, where a 50/50 beam splitter and two threshold detectors are used, via Eq. (5). Here, we additionally filter the idler mode with a dense wavelength division multiplexer (DWDM) in order to ob-

tain spectrally pure photons and suppress leaking signal photons due to the finite extinction ratio of the polarizing beam splitter which separates the signal and idler photons.

The spectral purity of the heralded single photons is characterized by a joint spectral intensity measurement [30, 31] and was found to be $\sim 84\,\%$. For increasing pump power, we observe a decrease in purity due to spectral broadening of the pump light caused by the non-linearity of the spatial mode cleaning fiber (Coherent 780-HP, 9 cm long) before the PPKTP crystal. We take this into account for our theory model by fitting Eq. (5) to the experimental data with the purity P as a fit parameter, see Appendix A.

The total efficiencies (including transmission, coupling and detection efficiencies) are measured in the setup shown in Fig. 1(a) at low pump power ($\mu \approx 5 \times 10^{-4}$) using the method described in [32]. We obtain the values $\eta_\mathrm{h} = (C_\mathrm{ha} + C_\mathrm{hb})/(C_\mathrm{a} + C_\mathrm{b}) = 0.6348(5)$, $\eta_\mathrm{a} = 2C_\mathrm{ha}/C_\mathrm{h} = 0.6293(6)$ and $\eta_\mathrm{b} = 2C_\mathrm{hb}/C_\mathrm{h} = 0.5809(6)$, where C denotes the (coincidence) counts (conditioned on the pump pulse in 1 ns window) on the corresponding detectors within 3 min of integration time. Note that the efficiencies η_a and η_b do not include the 50/50 beam splitter. Dark counts are negligible (<100 counts per second for all detectors) and do not affect the measurements.

The two standard threshold detectors are in-house developed single-pixel SNSPDs made from molybdenum silicide (MoSi) and have system detection efficiencies of about 85 % and 83 %, respectively. The P-SNSPD consists of four adjacent MoSi pixels, where the amplitude of the electrical readout signal is dependent on the number of pixels that click in the detection process. To avoid electrical and thermal crosstalk between the pixels, we employed the architecture developed in Ref. [23]. In order to characterize the full input-output response function of the P-SNSPD, light with known statistics (Poissonian with $\mu = 1$, in our case) is sent onto the detector. The photon-counting statistics are collected and, by employing the analytical model described in Ref. [24], one can obtain the conditional probability matrix $\mathbf{P}$. Its elements P_{nm} denote the probabilities of registering an n-click event when m photons are incident on the detector. Therefore, an initial photon-number probability distribution p_m leads to an n-click probability recorded by the P-SNSPD of $q_n = \sum_{m=0}^{\infty} P_{nm}\, p_m$. Even though m can go to infinity, practically it is stopped at a finite value M. Therefore, $\mathbf{P}$ has dimension $(N+1)\times(M+1)$, where N is the number of pixels of the P-SNSPD. By inverting $\mathbf{P}$, the incident photon-number probability distribution p_m can be reconstructed from the detected click probability distribution q_n. In our case for $N = 4$ and $M = 9$, we measured $P_{11} = 84\,\%$, $P_{12} = 55\,\%$, $P_{22} = 42\,\%$, $P_{13} = 31\,\%$ and $P_{14} = 17\,\%$ (the full $\mathbf{P}$ matrix can be found in Appendix B). The time taken for a full recovery of the efficiency after a detection is < 40 ns and is obtained by measuring the probability distribution of the time between two consecutive detections [24].

For the photon-number discrimination, the electrical readout signal of the P-SNSPD is separated in two by a coaxial power splitter and discriminated by a time controller (ID Quantique, ID900) at two different voltage thresholds, corresponding to a detection of $n \geq 1$ photons and $n \geq 2$ photons (see Fig. 2). In the second experiment, where the photon-number probability distribution is reconstructed, we also use a third discrimination level corresponding to a detection of $n \geq 3$ photons. The time controller additionally takes the electrical pickup signal from the pump laser and the readout signals from the threshold SNSPDs. All detection events are taken within a 1 ns time window with respect to the pump pulses to reduce dark count contributions, and their timestamps are saved for the data analysis.

IV. RESULTS

The results of the first experiment (see Fig. 1(a)), where we use the P-SNSPD as the heralding detector for the HSPS, are shown in Fig. 3. We calculate the mean photon number μ from the measured probability of detecting a heralding photon, p_h, in the threshold configuration together with the characterized total efficiency of the heralding photons η_h and the Schmidt coefficients λ_k obtained from a fit of Eq. (5) to the corresponding measured data (see Eq. (A1) in Appendix A). The values for $g_\mathrm{h}^{(2)}(0)$ are calculated according to Eq. (4), where the blue points correspond to the threshold configuration of the P-SNSPD and the red points to the PNR configuration. The solid lines are obtained from the theoretical model described in Sec. II with the characterized total efficiencies η_h, η_a, η_b and λ_k as defined in Sec. III. The shaded areas around the solid lines mark the regions with a difference in spectral purity of $\pm 4\,\%$ and the dashed lines show the theory calculation for a spectrally pure source.

The ratio between the blue and the red data is $g^{(2)}_{\mathrm{h,thr}}(0)/g^{(2)}_{\mathrm{h,PNR}}(0)$ which is the factor by which the heralding rate can be increased when switching from threshold to PNR heralding mode while keeping a fixed $g_\mathrm{h}^{(2)}(0) \ll 1$. In our experiment, we obtain 1.368 ± 0.002, averaged across all μ values, which inversely corresponds to a reduction in $g_\mathrm{h}^{(2)}(0)$ of 26.9(1) %. It should be noted that, in this demonstration, no spectral filtering of the heralding photons has been performed, in order to show the maximum achievable improvement in $g_\mathrm{h}^{(2)}(0)$ with our PNR detector.

As described in Sec. III, in the second experiment (see Fig. 1(b)) we reconstruct the photon-number probability distribution of one mode of the TMSV state by measuring the click probability distribution with the P-SNSPD. We then calculate $g^{(2)}_{\mathrm{unc.}}(0)$ using Eq. (3) and compare it to the value obtained by the standard method using Eq. (5). The results for different mean photon numbers are shown in Fig. 4 and display $g^{(2)}_{\mathrm{unc.}}(0) \approx 2$ which confirms the thermal nature of our source.

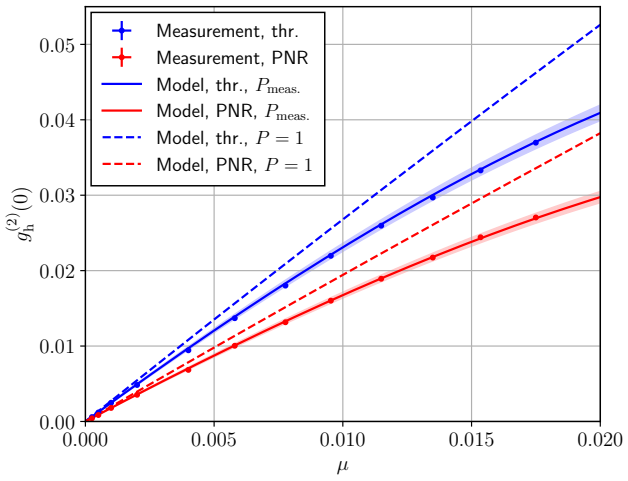

Figure 3. Heralded second-order autocorrelation function as a function of the mean photon number μ. The blue points correspond to the case where the P-SNSPD operates in threshold configuration (thr.), whereas the red points show the measurements for PNR configuration. The solid lines are obtained from the theoretical model with the same purity as in the experiment, where the shaded areas mark the spectral purity interval of $\pm 4\,\%$. The dashed lines show the behavior for a source with purity $P = 1$.

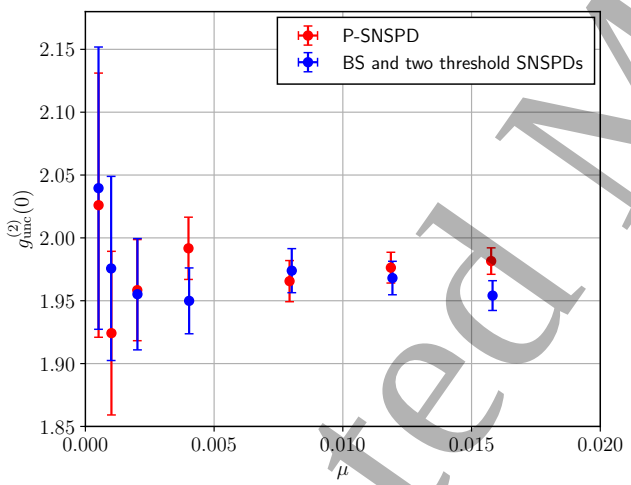

Figure 4. Unconditional second-order autocorrelation measurement on the spectrally filtered idler mode of the SPDC source. The red data correspond to the measurement with the P-SNSPD, whereas the blue data are obtained with the standard method using a beam splitter and two threshold detectors.

The error bars for the P-SNSPD were calculated through a Monte Carlo method with 10^3 iterations. In each iteration, to characterize $\mathbf{P}$, the Poissonian input state used for the detector characterization is randomly picked from a Gaussian distribution centered at $\mu = 1$ (the experimental value) with a standard deviation of $\sigma = 0.05$. In this way, we take into account the uncertainties of our characterization setup (see Ref. [24] for more details). The obtained matrix $\mathbf{P}$ is then used to reconstruct the light input statistics p_m of the SPDC source from the experimental photon-counting distribution of the P-SNSPD. As a last step in each iteration, the value $g_{\text{unc.}}^{(2)}(0)$ is computed from the reconstructed statistics using Eq. (3).

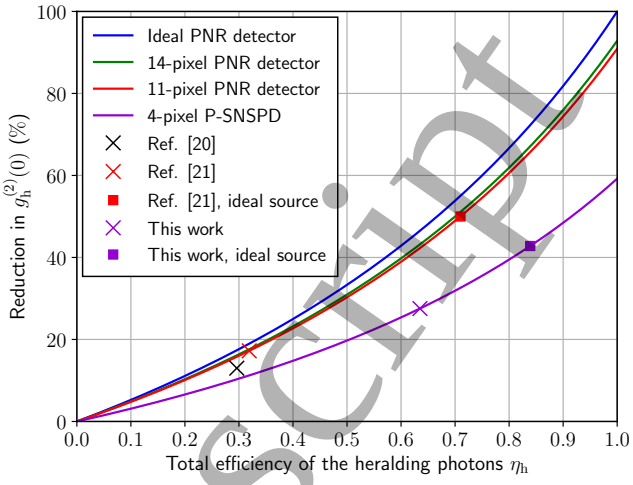

Figure 5. Reduction in $g_{\text{h}}^{(2)}(0)$ as a function of the total efficiency of the heralding photons η_{h}. The solid lines are obtained from the theoretical model for a spectrally pure source with fixed $\mu = 10^{-3}$. For the 14- and 11- pixel PNR detectors, we assume uniform light distribution across the pixels. The crosses are calculated from the measured values and the squares are obtained by assuming unit efficiency on the source side, i.e. $\eta_{\text{h}} = P_{11}$.

V. DISCUSSION

In order to improve the HSPS, the most important parameters to optimize are the PNR capability of the detector and the total efficiency of the heralding photons η_{h}, i.e. transmission through optical elements, coupling and detection efficiency [20]. As shown in Fig. 5, for a pure SPDC source combined with an ideal PNR heralding detector ($\mathbf{P} = \mathbb{1}$), the reduction in $g_{\text{h}}^{(2)}(0)$, that is $1 - g_{\text{h,PNR}}^{(2)}(0)/g_{\text{h,thr}}^{(2)}(0)$, reaches $100\,\%$ for $\eta_{\text{h}} = 1$. It achieves a value of $50\,\%$ for $\eta_{\text{h}} = 0.67$ and surpasses $90\,\%$ for $\eta_{\text{h}} = 0.95$. For $\eta_{\text{h}} = 0.635$, as measured in our experiment, a perfect PNR detector would achieve a reduction of $46.5\,\%$, however, our reported value of $26.9(1)\,\%$ lies significantly lower. This is due to the fact that the PNR capability of the detector to correctly detect an incoming higher-photon-number state is still limited by the non-resolvability of two photons hitting the same pixel. Another possible cause is the non-unity efficiency of the detector: it is possible that if two photons arrive on two different pixels, only one is detected. In order to increase the PNR capability of our P-SNSPD, the number of pixels needs to be increased while still maintaining good

Table I. Comparison of different parameters between PNR SNSPDs used to improve a HSPS. The heralded single-photon rates R_{hsp} are calculated from a fit to the measured data at $\mu = 0.005$ and have been estimated for the other references. For Ref. [20], we assume η_{a} and η_{b} equal to η_{h}, since their values were not reported.

Ref.	PNR method	P_{11}	P_{12}	P_{22}	Full recovery time	η_{h}	$g_{\mathrm{h}}^{(2)}(0)$ reduction	R_{hsp} (kcps)	Pump rate (MHz)
[20]	Slew rate	80-86 %	—	—	< 100 ns	29.6 %	13 %	4.4	10
[21]	Slew rate	71 %	45.8 %	45.8 %	100 ns	31.9 %	20 %	0.64	1
This work	Signal's amplitude	84 %	55%	42 %	< 40 ns	63.5 %	26 %	146	76

amplitude discrimination of the electrical readout signal between different photon-number detection events. In addition, a uniform light distribution over the pixels can be obtained by exploiting an interleaved design, which reduces the probability of having more photons arriving at the same pixel [33] (e.g. for the same single-photon-detection-efficiency, the P_{22} would become 53 %). To give more context, by exchanging our P-SNSPD with the recently reported multi-pixel detector [34] composed of 14 interleaved pixels, the achievable $g_{\mathrm{h}}^{(2)}(0)$ reduction would be 47 %.

Lastly, we show that P-SNSPDs can correctly reconstruct the thermal statistics of an SPDC source thanks to our access to the full $\mathbf{P}$ matrix and the clear distinction between each photon-count signal. To validate our results, we retrieve the unconditional $g^{(2)}(0)$ values via Eq. (3). As it can be seen from the results, the $g_{\mathrm{unc.}}^{(2)}(0)$ obtained with the two different techniques match very well, both in the absolute value and in the amplitude of the error bars. This result demonstrates that P-SNSPDs can effectively replace a 50/50 beam splitter and two detectors used in the standard method, simplifying the overall experimental apparatus. Hence, they can for example be applied in protocols which require upper bounds on the probability of having more than one photons in each spatial mode [2, 35]. It is important to note that the approach does not rely on an accurate absolute characterization of the P-SNSPD efficiency, keeping the $g_{\mathrm{unc.}}^{(2)}(0)$ measurement efficiency-independent as in the case of the more common-place method which uses two detectors. However, this is not the case for the reconstructed photon-number distribution, p_n.

In Table I, and additionally in Fig. 5, we compare the main results of this work with Ref. [20] and [21], which also employ a PNR SNSPD to improve a HSPS. We report a significant $g_{\mathrm{h}}^{(2)}(0)$ reduction thanks to the high value of η_{h} in our experiment and the good P_{22} value of the P-SNSPD. Furthermore, our heralded single-photon rate (R_{hsp}) for a value of $\mu = 0.005$ is over 30 times higher than the rates reported in the previous works. This result is mainly due to the high pump repetition rate assisted by the fast detector recovery time that the P-SNSPD can sustain in the operationally relevant low squeezing regime. Increasing the number of pixels could further improve the results we obtain, both in terms of P_{22} and recovery time, which would reflect in a better $g_{\mathrm{h}}^{(2)}(0)$ reduction and higher heralded single-photon rate.

VI. CONCLUSION

We have shown the benefit for a HSPS that a PNR detector, such as a P-SNSPD, can bring when combined with a SPDC source. Even though P-SNSPDs do not possess perfect PNR capability, we already demonstrate a significant reduction in the heralded $g^{(2)}(0)$ of 26.9(1) %, compared to the threshold configuration. In addition, the PNR capability of the P-SNSPD is not limited by the timing jitter as in the case of a slew rate discrimination, or by super-short light pulses (tens of ps) as in the impedance-matching taper approach. Lastly, to improve our results further, the number of pixels of the P-SNSPD need to be increased. In that case, not only a better photon-number discrimination can be achieved, but also an overall faster recovery time, thanks to the shorter meanders of the P-SNSPD structure. This result marks a first step towards high-rate generation of single photons which could be of use in repeater protocols [36]. We further show the usefulness of our P-SNSPD for the task of reconstructing the photon-number probability distribution of pulsed light by measuring a thermal state. We demonstrated that we can estimate $g^{(2)}(0)$ with a single detector, which replaces a beam splitter and two threshold detectors used in more common methods. Therefore, such a PNR detector can be of great help in quantum protocols, metrology applications, and source characterization.

ACKNOWLEDGMENTS

We thank Giovanni V. Resta and Gaëtan Gras for useful discussions. This work was supported by the Swiss National Science Foundation SNSF (Grant No. 200020_-182664). L.S. is part of the AppQInfo MSCA ITN which received funding from the EU Horizon 2020 research and

innovation program under the Marie Sklodowska-Curie grant agreement No. 956071.

L.S. and P.C. contributed equally to this work.

Appendix A: Theoretical model

We use a characteristic function based approach to model our SPDC source and to derive the single and coincidence detection probabilities [29]. We start with the covariance matrix of a TMSV state and apply Gaussian unitary operations corresponding to the action of the beam splitters in our model as shown in Fig. 6. On each mode, we apply a loss channel with the corresponding transmittance $\eta_\mathrm{a}, \eta_\mathrm{b}$ and η_h. Each detector is described by a positive operator valued measure (POVM) with element $E_0 = |0\rangle\langle 0|^{\otimes M}$ corresponding to a no-click outcome and $E_c = \mathbb{1} - |0\rangle\langle 0|^{\otimes M}$ corresponding to a click outcome over all the spectral modes M. This leads to the following detection probability of a detecting a heralding photon per pump pulse

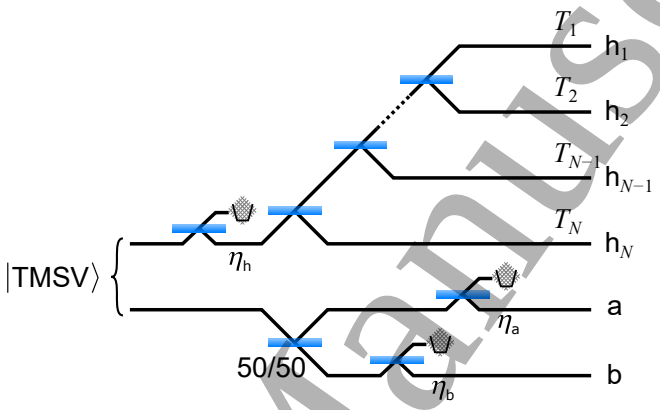

Figure 6. Schematic representation of the theory model to calculate the single and coincidence detection probabilities. The heralding mode of the two-mode squeezed vacuum (TMSV) state is subject to loss (η_h) and is then split into N modes before being detected by threshold detectors (h_1 to h_N) on each mode. The other mode of the TMSV state is sent to a 50/50 beam splitter and further undergoes loss channels (η_a and η_b) before reaching the threshold detectors $\mathrm{D_a}$ and $\mathrm{D_b}$.

$$p_\mathrm{h} = \sum_{k=1}^{N} \mathrm{tr}\rho\left(\mathbb{1}_\mathrm{a} \otimes \mathbb{1}_\mathrm{b} \otimes E_{c,\mathrm{h}_k} \otimes E_{0,\mathrm{h}_{\neg k}}^{\otimes(N-1)}\right) = \sum_{k=1}^{N}\left(\prod_m \frac{1}{1+(1-T_k)\eta_\mathrm{h}\lambda_m\mu}\right) - N\prod_m \frac{1}{1+\eta_\mathrm{h}\lambda_m\mu}, \tag{A1}$$

where $\{\lambda_m\}_{m=1}^{M}$ denote the Schmidt coefficients (with $\sum_m \lambda_m = 1$) and T_k is the fraction of the light that reaches pixel k of the heralding detector with $\sum_k T_k = 1$. Note that here and in the following, taking $\{T_k\}_{k=1}^{N}$ models a single-photon detection event on the P-SNSPD, but by setting $N = 1$ and $T_1 = 1$ one obtains the behavior for the detector in threshold configuration, i.e. detecting one or more photons.

Similarly to p_h, we obtain the probability of a coincidence detection between the heralding detector $\mathrm{D_h}$ and detector $\mathrm{D_a}$ after the 50/50 beam splitter on the heralded mode

$$\begin{aligned} p_\mathrm{ha} &= \sum_{k=1}^{N} \mathrm{tr}\rho\left(E_{c,\mathrm{a}} \otimes \mathbb{1}_\mathrm{b} \otimes E_{c,\mathrm{h}_k} \otimes E_{0,\mathrm{h}_{\neg k}}^{\otimes(N-1)}\right) \\ &= p_\mathrm{h} - \sum_{k=1}^{N}\left(\prod_m \frac{2}{2+[(1-T_k)(2-\eta_\mathrm{a})\eta_\mathrm{h}+\eta_\mathrm{a}]\lambda_m\mu}\right) + N\prod_m \frac{2}{2+[(2-\eta_\mathrm{a})\eta_\mathrm{h}+\eta_\mathrm{a}]\lambda_m\mu} \end{aligned} \tag{A2}$$

and the three-fold coincidence probability

$$\begin{aligned} p_\mathrm{hab} &= \sum_{k=1}^{N} \mathrm{tr}\rho\left(E_{c,\mathrm{a}} \otimes E_{c,b} \otimes E_{c,\mathrm{h}_k} \otimes E_{0,\mathrm{h}_{\neg k}}^{\otimes(N-1)}\right) \\ &= p_\mathrm{ha} + p_\mathrm{hb} - p_\mathrm{h} + \sum_{k=1}^{N}\left(\prod_m \frac{2}{2+[(1-T_k)(2-\eta_\mathrm{a}-\eta_\mathrm{b})\eta_\mathrm{h}+\eta_\mathrm{a}+\eta_\mathrm{b}]\lambda_m\mu}\right) \\ &\quad - N\prod_m \frac{2}{2+[(2-\eta_\mathrm{a}-\eta_\mathrm{b})\eta_\mathrm{h}+\eta_\mathrm{a}+\eta_\mathrm{b}]\lambda_m\mu}. \end{aligned} \tag{A3}$$

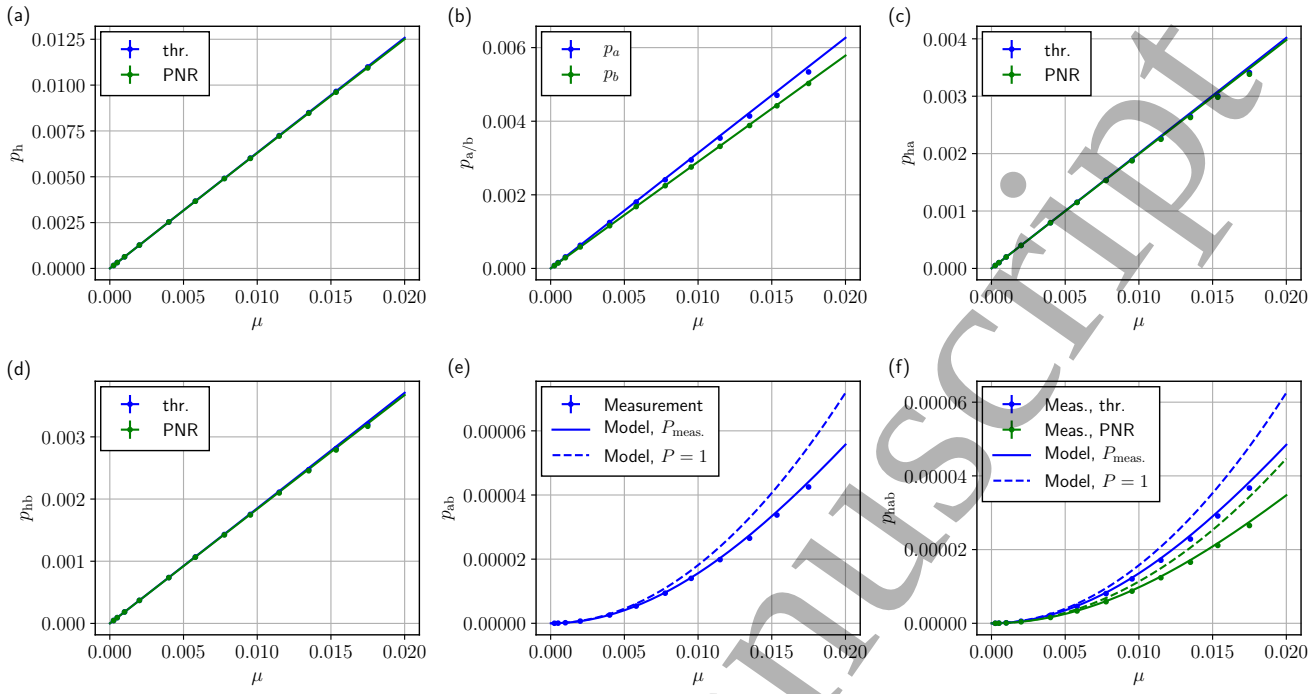

Figure 7. Measurement and theory model for the single and coincidence detection probabilities. The solid lines are obtained from the theory model including the non-unit purity of our SPDC source whereas the dashed lines describe the behavior for a pure source. (a) Probability of a heralding detection per pump pulse for the threshold and PNR configurations. (b) Detection probabilities for detectors D_a and D_b. (c) Coincidence probability between detectors D_h and D_a. (d) Coincidence probability between detectors D_h and D_b. (e) Coincidence probability for detections on D_a and D_b. (f) Triple-coincidence probability between detectors D_h, D_a and D_b.

The detection probability of detector D_a (and similarly for detector D_b) is given by

$$p_a = \sum_{k=1}^{N} \mathrm{tr}\rho\left(E_{c,a} \otimes \mathbb{1}_b \otimes \mathbb{1}_h^{\otimes N}\right) = 1 - \prod_m \frac{1}{1+\eta_a \lambda_m \mu} \tag{A4}$$

and the coincidence probability between detector D_a and D_b by

$$p_{ab} = \sum_{k=1}^{N} \mathrm{tr}\rho\left(E_{c,a} \otimes E_{c,b} \otimes \mathbb{1}_h^{\otimes N}\right) = 1 - \prod_m \frac{2}{2+\eta_a \lambda_m \mu} - \prod_m \frac{2}{2+\eta_b \lambda_m \mu} + \prod_m \frac{2}{2+(\eta_a+\eta_b)\lambda_m \mu}. \tag{A5}$$

Those formulas are then used to calculate the theory values for the second-order autocorrelation functions according to Eqs. (4) and (5). In Fig. 7, the theory model for all the different probabilities is shown together with the experimental data.

For a spectrally pure source (i.e. $\lambda_1 = 1$), the derived formulas (A1-A5) simplify. In the case of non-unit spectral purity $P = \sum \lambda_k^2 < 1$, but still $P > \frac{1}{2}$, we estimate P by fixing two Schmidt coefficients $\lambda_{1,2} = \frac{1}{2} \pm \sqrt{\frac{P}{2} - \frac{1}{4}}$ and fitting $g^{(2)}_{\mathrm{unc.}}(0) \approx p_{ab}/p_a p_b$ to the experimental value. In our case, we find that the purity of the source decreases as a function of μ, therefore a second-order polynomial is fitted to the purity values obtained from $g^{(2)}_{\mathrm{unc.}}(0)$ to get the function $P_{\mathrm{meas.}}(\mu)$ which is then used throughout in the theoretical model. We attribute the decrease in purity for increasing pump power to the nonlinearity of the spatial mode cleaning fiber in our setup before the nonlinear crystal. This behavior is confirmed by the measurement of the pump spectrum as a function of pump power and a simulation of the corresponding joint spectral amplitude of the down-converted photon pairs [30, 37, 38].

Appendix B: PNR characterization

Here, we report the results of the PNR characterization of the four-pixel P-SNSPD and the full $\mathbf{P}$ matrix that we obtain following the method described in Ref. [24]:

$$\mathbf{P} = \begin{bmatrix} 1 & 0.161 & 0.026 & 0.004 & 0 & 0 & 0 & 0 & 0 & 0 \\ 0 & 0.839 & 0.557 & 0.312 & 0.170 & 0.093 & 0.051 & 0.028 & 0.015 & 0.008 \\ 0 & 0 & 0.417 & 0.600 & 0.640 & 0.619 & 0.576 & 0.526 & 0.478 & 0.433 \\ 0 & 0 & 0 & 0.084 & 0.183 & 0.269 & 0.338 & 0.392 & 0.432 & 0.463 \\ 0 & 0 & 0 & 0 & 0.007 & 0.019 & 0.035 & 0.054 & 0.075 & 0.096 \end{bmatrix}, \tag{B1}$$

where each column indicates the number of photon sent to the detector and each row the number of detected ones.

The single-pixel efficiencies are 3.48 %, 33.53 %, 41.25 % and 5.64 %. Since the pixels are distributed one next to the other, the outer ones are naturally less exposed to light (due to the Gaussian beam profile of light in single-mode fibers), thus displaying lower efficiency. These values are used in the theoretical model to calculate η_{h} and the normalized splitting ratios T_i.

[1] N. Gisin and R. Thew. Quantum communication. *Nature photonics*, 1(3):165–171, 2007. doi: 10.1038/nphoton.2007.22.

[2] N. Sangouard, C. Simon, H. De Riedmatten, and N. Gisin. Quantum repeaters based on atomic ensembles and linear optics. *Reviews of Modern Physics*, 83(1): 33, 2011. doi:10.1103/RevModPhys.83.33.

[3] E. Knill, R. Laflamme, and G. J. Milburn. A scheme for efficient quantum computation with linear optics. *nature*, 409(6816):46–52, 2001. doi:10.1038/35051009.

[4] P. Kok, W. J. Munro, K. Nemoto, T. C. Ralph, J. P. Dowling, and G. J. Milburn. Linear optical quantum computing with photonic qubits. *Reviews of modern physics*, 79(1):135, 2007. doi: 10.1103/RevModPhys.79.135.

[5] S. Slussarenko and G. J. Pryde. Photonic quantum information processing: A concise review. *Applied Physics Reviews*, 6(4):041303, 2019. doi:10.1063/1.5115814.

[6] J. B. Spring, B. J. Metcalf, P. C. Humphreys, W. S. Kolthammer, X.-M. Jin, M. Barbieri, A. Datta, N. Thomas-Peter, N. K. Langford, D. Kundys, et al. Boson sampling on a photonic chip. *Science*, 339(6121): 798–801, 2013. doi:10.1126/science.1231692.

[7] M. Bentivegna, N. Spagnolo, C. Vitelli, F. Flamini, N. Viggianiello, L. Latmiral, P. Mataloni, D. J. Brod, E. F. Galvão, A. Crespi, et al. Experimental scattershot boson sampling. *Science advances*, 1(3):e1400255, 2015. doi:10.1126/sciadv.1400255.

[8] H.-S. Zhong, Y. Li, W. Li, L.-C. Peng, Z.-E. Su, Y. Hu, Y.-M. He, X. Ding, W. Zhang, H. Li, et al. 12-photon entanglement and scalable scattershot boson sampling with optimal entangled-photon pairs from parametric down-conversion. *Physical review letters*, 121(25):250505, 2018. doi:10.1103/PhysRevLett.121.250505.

[9] S. Castelletto and R. Scholten. Heralded single photon sources: a route towards quantum communication technology and photon standards. *The European Physical Journal-Applied Physics*, 41(3):181–194, 2008. doi: 10.1051/epjap:2008029.

[10] M. D. Eisaman, J. Fan, A. Migdall, and S. V. Polyakov. Invited review article: Single-photon sources and detectors. *Review of Scientific Instruments*, 82(7):071101, 2011. doi:10.1063/1.3610677.

[11] P. J. Mosley, J. S. Lundeen, B. J. Smith, P. Wasylczyk, A. B. U'Ren, C. Silberhorn, and I. A. Walmsley. Heralded generation of ultrafast single photons in pure quantum states. *Physical Review Letters*, 100(13):133601, 2008. doi:10.1103/PhysRevLett.100.133601.

[12] N. Bruno, A. Martin, T. Guerreiro, B. Sanguinetti, and R. T. Thew. Pulsed source of spectrally uncorrelated and indistinguishable photons at telecom wavelengths. *Optics Express*, 22(14):17246, 2014. doi:10.1364/OE.22.017246.

[13] F. Graffitti, P. Barrow, M. Proietti, D. Kundys, and A. Fedrizzi. Independent high-purity photons created in domain-engineered crystals. *Optica*, 5(5):514–517, 2018. doi:10.1364/optica.5.000514.

[14] E. Meyer-Scott, C. Silberhorn, and A. Migdall. Single-photon sources: Approaching the ideal through multiplexing. *Rev. Sci. Instrum*, 91(4):041101, 2020. doi: 10.1063/5.0003320.

[15] A. Christ and C. Silberhorn. Limits on the deterministic creation of pure single-photon states using parametric down-conversion. *Phys. Rev. A*, 85:023829, 2012. doi: 10.1103/PhysRevA.85.023829.

[16] A. E. Lita, A. J. Miller, and S. W. Nam. Counting near-infrared single-photons with 95% efficiency. *Optics express*, 16(5):3032–3040, 2008. doi:10.1364/OE.16.003032.

[17] L. A. Morais, T. Weinhold, M. P. de Almeida, A. Lita, T. Gerrits, S. W. Nam, A. G. White, and G. Gillett. Precisely determining photon-number in real-time. *arXiv preprint arXiv:2012.10158*, 2020. doi: 10.48550/arXiv.2012.10158.

[18] C. Cahall, K. L. Nicolich, N. T. Islam, G. P. Lafyatis, A. J. Miller, D. J. Gauthier, and J. Kim. Multi-photon

detection using a conventional superconducting nanowire single-photon detector. *Optica*, 4(12):1534–1535, 2017.

[19] D. Zhu, M. Colangelo, C. Chen, B. A. Korzh, F. N. Wong, M. D. Shaw, and K. K. Berggren. Resolving photon numbers using a superconducting nanowire with impedance-matching taper. *Nano Letters*, 20(5):3858–3863, 2020.

[20] S. Sempere-Llagostera, G. S. Thekkadath, R. B. Patel, W. S. Kolthammer, and I. A. Walmsley. Reducing $g^{(2)}(0)$ of a parametric down-conversion source via photon-number resolution with superconducting nanowire detectors. *Optics Express*, 30(2):3138, 2022. doi: 10.1364/OE.450172.

[21] S. I. Davis, A. Mueller, R. Valivarthi, N. Lauk, L. Narvaez, B. Korzh, A. D. Beyer, O. Cerri, M. Colangelo, K. K. Berggren, M. D. Shaw, S. Xie, N. Sinclair, and M. Spiropulu. Improved heralded single-photon source with a photon-number-resolving superconducting nanowire detector. *Phys. Rev. Appl.*, 18:064007, 2022. doi:10.1103/PhysRevApplied.18.064007.

[22] F. Marsili, D. Bitauld, A. Fiore, A. Gaggero, R. Leoni, F. Mattioli, A. Divochiy, A. Korneev, V. Seleznev, N. Kaurova, et al. Superconducting parallel nanowire detector with photon number resolving functionality. *Journal of Modern Optics*, 56(2-3):334–344, 2009. doi: 10.1080/09500340802220729.

[23] M. Perrenoud, M. Caloz, E. Amri, C. Autebert, C. Schönenberger, H. Zbinden, and F. Bussières. Operation of parallel snspds at high detection rates. *Superconductor Science and Technology*, 34(2):024002, 2021. doi: 10.1088/1361-6668/abc8d0.

[24] L. Stasi, G. Gras, R. Berrazouane, M. Perrenoud, H. Zbinden, and F. Bussières. Fast high-efficiency photon-number-resolving parallel superconducting nanowire single-photon detector. *Physical Review Applied*, 19(6):064041, 2023.

[25] M. Schmidt, M. Von Helversen, M. López, F. Gericke, E. Schlottmann, T. Heindel, S. Kück, S. Reitzenstein, and J. Beyer. Photon-number-resolving transition-edge sensors for the metrology of quantum light sources. *Journal of Low Temperature Physics*, 193:1243–1250, 2018.

[26] M. Von Helversen, J. Böhm, M. Schmidt, M. Gschrey, J.-H. Schulze, A. Strittmatter, S. Rodt, J. Beyer, T. Heindel, and S. Reitzenstein. Quantum metrology of solid-state single-photon sources using photon-number-resolving detectors. *New Journal of Physics*, 21(3): 035007, 2019.

[27] N. Tomm, S. Mahmoodian, N. O. Antoniadis, R. Schott, S. R. Valentin, A. D. Wieck, A. Ludwig, A. Javadi, and R. J. Warburton. Photon bound state dynamics from a single artificial atom. *Nature Physics*, pages 1–6, 2023.

[28] D. Walls and G. J. Milburn. *Quantum Optics*. Springer Berlin Heidelberg, Berlin, Heidelberg, 2008. ISBN 978-3-540-28573-1. doi:10.1007/978-3-540-28574-8.

[29] M. Takeoka, R.-B. Jin, and M. Sasaki. Full analysis of multi-photon pair effects in spontaneous parametric down conversion based photonic quantum information processing. *New Journal of Physics*, 17(4):043030, 2015. doi:10.1088/1367-2630/17/4/043030.

[30] K. Zielnicki, K. Garay-Palmett, D. Cruz-Delgado, H. Cruz-Ramirez, M. F. O'Boyle, B. Fang, V. O. Lorenz, A. B. U'Ren, and P. G. Kwiat. Joint spectral characterization of photon-pair sources. *Journal of Modern Optics*, 65(10):1141–1160, 2018. doi: 10.1080/09500340.2018.1437228.

[31] F. Graffitti, J. Kelly-Massicotte, A. Fedrizzi, and A. M. Brańczyk. Design considerations for high-purity heralded single-photon sources. *Physical Review A*, 98(5):053811, 2018. doi:10.1103/PhysRevA.98.053811.

[32] D. N. Klyshko. Use of Two-Photon Light for Absolute Calibration of Photoelectric Detectors. *Soviet journal of quantum electronics*, 7(9):1112–1116, 1980. doi: 10.1070/qe1980v010n09abeh010660.

[33] W. Zhang, J. Huang, C. Zhang, L. You, C. Lv, L. Zhang, H. Li, Z. Wang, and X. Xie. A 16-pixel interleaved superconducting nanowire single-photon detector array with a maximum count rate exceeding 1.5 ghz. *IEEE Transactions on Applied Superconductivity*, 29(5):1–4, 2019.

[34] F. Grünenfelder, A. Boaron, G. V. Resta, M. Perrenoud, D. Rusca, C. Barreiro, R. Houlmann, R. Sax, L. Stasi, S. El-Khoury, et al. Fast single-photon detectors and real-time key distillation enable high secret-key-rate quantum key distribution systems. *Nature Photonics*, pages 1–5, 2023.

[35] P. Caspar, E. Oudot, P. Sekatski, N. Maring, A. Martin, N. Sangouard, H. Zbinden, and R. Thew. Local and scalable detection of genuine multipartite single-photon path entanglement. *Quantum*, 6:671, 2022. doi:10.22331/q-2022-03-22-671.

[36] N. Sangouard, C. Simon, J. Minář, H. Zbinden, H. de Riedmatten, and N. Gisin. Long-distance entanglement distribution with single-photon sources. *Physical Review A*, 76(5):050301, 2007. doi: 10.1103/PhysRevA.76.050301.

[37] T. Guerreiro, A. Martin, B. Sanguinetti, N. Bruno, H. Zbinden, and R. T. Thew. High efficiency coupling of photon pairs in practice. *Optics Express*, 21(23):27641, 2013. doi:10.1364/OE.21.027641.

[38] D. Ljunggren and M. Tengner. Optimal focusing for maximal collection of entangled narrow-band photon pairs into single-mode fibers. *Physical Review A*, 72(6):062301, 2005. doi:10.1103/PhysRevA.72.062301.